



HAL
open science

Non-hydrolytic sol-gel synthesis of TiO₂-based electrode materials for Li-ion batteries

Angel Manuel Escamilla Perez

► To cite this version:

Angel Manuel Escamilla Perez. Non-hydrolytic sol-gel synthesis of TiO₂-based electrode materials for Li-ion batteries. Other. Université Montpellier, 2017. English. NNT : 2017MONTT181 . tel-01866697

HAL Id: tel-01866697

<https://theses.hal.science/tel-01866697>

Submitted on 3 Sep 2018

HAL is a multi-disciplinary open access archive for the deposit and dissemination of scientific research documents, whether they are published or not. The documents may come from teaching and research institutions in France or abroad, or from public or private research centers.

L'archive ouverte pluridisciplinaire **HAL**, est destinée au dépôt et à la diffusion de documents scientifiques de niveau recherche, publiés ou non, émanant des établissements d'enseignement et de recherche français ou étrangers, des laboratoires publics ou privés.

THÈSE POUR OBTENIR LE GRADE DE DOCTEUR DE L'UNIVERSITÉ DE MONTPELLIER

En Chimie et Physico-Chimie des Matériaux

École doctorale ED 459 Sciences Chimiques Balard

Unité de recherche UMR 5253 - Institut Charles Gerhardt de Montpellier,
équipe Chimie Moléculaire et Organisation du Solide

Non-hydrolytic sol-gel synthesis of TiO₂-based electrode materials for Li-ion batteries

Présentée par Angel Manuel ESCAMILLA PÉREZ
Le vendredi 13 octobre 2017

Sous la direction d'Hubert MUTIN
et Bruno BOURY

Devant le jury composé de

Mme. Bénédicte LEBEAU-TALAMONA, Directeur de Recherche, IS2M-Mulhouse

Mme. Liliane GUERLOU-DEMOURGUES, Professeur, ICMCB-Bordeaux

M. Cédric BOISSIÈRE, Directeur de Recherche, UPMC-Paris

M. Hubert MUTIN, Directeur de Recherche, ICGM-Montpellier

M. Nicolas BRUN, Chargé de Recherche, ICGM-Montpellier

M. Nicolas LOUVAIN, Maître de Conférences, ICGM-Montpellier

Rapporteur

Rapporteur

Président

Directeur de thèse

Co-encadrant de thèse

Examineur



UNIVERSITÉ
DE MONTPELLIER

“Life is not easy for any of us... But what of that? We must have perseverance and above all confidence in ourselves. We must believe that we are gifted for something, and that this thing, at whatever cost, must be attained.”

-Marie Curie

To Carmen

Beloved mother and source of inspiration

Remerciements

Cette thèse a été réalisée au sein de l'Institut Charles Gerhardt de Montpellier (ICGM) dans l'équipe Chimie Moléculaire et Organisation du Solide (CMOS) en collaboration avec l'équipe Agrégats, Interfaces et Matériaux pour l'Énergie (AIME). Je tiens à remercier Jean-Marie Devoisselle, directeur de l'ICGM d'avoir permis la réalisation de cette thèse, ainsi qu'au CONACYT Mexique pour la bourse qui a financé mes études en France.

Je remercie vivement les membres du jury d'avoir accepté la lecture de ce manuscrit de thèse, pour leur évaluation et leurs commentaires enrichissants lors de la soutenance. Je remercie plus particulièrement Bénédicte Lebeau-Talamona, Directeur de Recherche à l'IS2M de Mulhouse et Liliane Guerlou-Demourgues, Professeur à l'ICMCB de Bourdeaux qui m'ont fait l'honneur d'être rapporteurs de ce travail, ainsi qu'à Cédric Boissière, Directeur de Recherche à l'UPMC de Paris qui a présidé ce jury.

Je tiens à remercier Hubert Mutin, directeur de cette thèse ; Bruno Boury, co-directeur et Nicolas Brun et Olivier Fontaine co-encadrants de ce projet. Je remercie également Nicolas Louvain pour la collaboration que nous avons développée. Merci à vous tous pour votre temps, vos conseils et les discussions que nous avons eues ; le travail ensemble de ce groupe hétérogène a enrichi le produit final présenté dans ce manuscrit. Travailler avec vous a été un grand plaisir et votre expérience m'a permis de grandir et d'améliorer mes compétences scientifiques.

Merci Hubert de m'avoir permis l'accomplissement d'un rêve : la réalisation de ma thèse en France. Tu es un excellent être humain, je te remercie infiniment d'avoir cru en moi, pour ta patience et tes conseils. Ton expérience dans le domaine de sol-gel non-hydrolytique a été un des piliers du projet. Je ne pourrais jamais oublier ces trois ans de travail avec toi.

Bruno, un gros merci pour les moments de discussion ensemble. Ta rigueur et tes conseils m'ont permis de m'améliorer et dépasser mes capacités. Je tiens à remercier aussi ton enthousiasme pendant la correction du manuscrit.

Nicolas Brun, merci pour être toujours disponible et à l'écoute, tu a été un grand support pendant la thèse. En plus, comment oublier mon arrivée à Montpellier, les premières nuits au grenier et le déluge sur la ville. Merci aussi pour m'avoir introduit au monde de la divulgation scientifique avec Pint of Science, j'ai trop aimé le brassage de la BAFLAB.

Nicolas Louvain, un grand merci pour ton engagement dans le projet. Tu m'as appris beaucoup de choses côté électrochimique et c'était toujours un plaisir d'aller discuter les résultats avec toi. Je remercie profondément ton aide tout au long de la thèse. Je pense que sans toi je n'aurais pas pu obtenir beaucoup de résultats concernant les batteries.

Je remercie aussi tout le personnel du plateau technique de l'ICGM, de l'UM et l'IEM qui m'ont aidé avec la réalisation de certains analyses et caractérisations. Dominique Granier pour la formation et discussions par rapport à la diffraction aux rayons X ; Léa Daenens pour la spectroscopie Raman ; Philippe Gaveau pour la réalisation des spectres RMN solide ; Didier Cot, Bertrand Rebière et Frédéric Fernandez pour les images MEB et analyses EDX et Aurélien Lebrun pour la RMN liquide. Je tiens à remercier Claudia Cammarano et Radu Andrei de l'équipe MACS pour les caractérisations NH₃-TPD, de même que Laure

Monconduit, Romain Berthelot, Julien Fullenwarth, Bernard Fraisse et Nicolas Bibent de l'équipe AIME pour les facilités lors des essais électrochimiques.

Je tiens à remercier aussi au personnel administratif et technique de l'équipe CMOS Christian, Serge, Christine, Fatima, Magali, Aurélie, Tzvetelina, Sylvain, Karim, Xavier vous avez été toujours là que ce soit pour une commande de produit, des soucis avec le software, les appareils ou l'inscription aux congrès. Merci à tous.

Il est important de noter que ces trois années ne seraient pas les mêmes sans la compagnie de mes chers collègues thésards et post-docs : Adèle, Chiara, Clémence, Clément, Aurélien, Maroua, Hussein, Mohamed, Sanghoon, Mich, JB, Mathieu, Walaa, Rosa, Rajesh, Chikis et Carlos, sans oublier le team Sikémia, Guillaume et Adeline. Que ce soit le partage du bureau, de la paillasse ou le fait de se croiser dans les couloirs vous m'avez fait passer des moments inoubliables. Je garderai toujours dans ma mémoire les discussions, les repas de midi, les randonnées, les sorties canoë, l'escalade, les laser et escape games, j'ai même connu la neige grâce à vous et fait mes premiers pas au ski, les raclettes, les crêpes, les afterworks au Ranch et les soirées qui finissaient toujours aux Coulisses, au Sound Station ou au Rockstore. Merci pour trois années folles et remplies de très agréables souvenirs.

Merci aussi au team du Pint of Science : Anaïs, Eva, Estelle et Sarah. Ça a été vraiment chouette de travailler avec vous tout au long de la préparation du festival en développant des nouvelles capacités et en partageant des soirées intéressantes et amusantes.

Merci aussi aux potes fêtards Lérays, Loïc, Riccardo et Amandine. Je ne m'imagine pas I love Techno, Platja, Plages électroniques, Berlin, les lundis au Scarabée et les mercredis Couleur de Bières sans vous. Johan la soirée tequila restera inoubliable de même que les cours de natation qui étaient plus amusants avec tes commentaires sur la faune marine (le canard, le dauphin, la tortue).

Comment ne pas mentionner JF, co-responsable des étudiants avec moi. Nous avons fait un excellent travail ensemble. Je me souviendrai aussi des sorties à la plage, de la bouée tractée, de la clime qui rafraichissait et facilitait la rédaction, de la visite à Metz et surtout de l'halloween à Amsterdam. Céline ma chère collègue de bureau, que de bons souvenirs : I follow rivers et Melody les chansons de la thèse, les soirées en boîte (l'Amnésia, l'Austra et la Villa), le saut en parachute (le seul moment où je n'ai pas de tout rigolé), Strasbourg et sa cathédral, une journée d'émotions extrêmes à Europa-Park et le célèbre « VRAIMENT prends ma montre !!! ».

Un immense merci à ma famille : Mamel, Paco, Anita, Doris, Angelita, Mariana, Cecilia, Kika, Fer y Mafer. Vous m'avez supporté pour entreprendre cette aventure et malgré la distance physique vous avez été toujours à mes côtés. Vous êtes les meilleurs et je vous aime trop. Finalement, merci Carmelita, merci Crucy vous me donnez toujours la force de poursuivre mes rêves, de dépasser mes limites et de ne pas me laisser tomber.

MERCI À VOUS TOUS !!!

Glossary

BET	Brunauer-Emmett-Teller method
BJH	Barret-Joyner-Halenda method
CB	Carbon black
CMOS	Chimie Moléculaire et Organisation du Solide
CNT(s)	Carbon nanotube(s)
CP-MAS	Cross polarization magic angle spinning
DMC	Dimethyl carbonate
EC	Ethylene carbonate
EDX	Energy-dispersive X-ray spectroscopy
EV(s)	Electric vehicle(s)
FEC	Fluoroethylene carbonate
FTIR	Fourier transform infrared spectroscopy
FWHM	Full width at half maximum
HEV(s)	Hybrid-electric vehicle(s)
HSG	Hydrolytic sol-gel
ICGM	Institut Charles Gerhardt Montpellier
IPE/ⁱPr₂O	Diisopropyl ether
ⁱPrOH	Iso-propanol
IUPAC	International Union of Pure and Applied Chemistry
LIB(s)	Lithium-ion battery(ies)
LTO	Lithium titanium oxide (Li ₄ Ti ₅ O ₁₂)
NH₃-TPD	Ammonia temperature programmed desorption
NHSG	Non-hydrolytic sol-gel
NMP	N-methyl-2-pyrrolidone
NMR	Nuclear magnetic resonance
PC	Propylene carbonate
PEIS	Potential electrochemical impedance spectroscopy
PVDF	Polyvinylidene difluoride
RS2E	Réseau sur le stockage électrochimique de l'énergie
SEI	Solid electrolyte interface
SEM	Scanning electron microscopy
SIB(s)	Sodium-ion battery(ies)
SSNMR	Solid state nuclear magnetic resonance
^tBuOH	Tert-butanol
TCD	Thermal conductivity detector
TGA	Thermogravimetric analyses
THF	Tetrahydrofuran
UV-vis	Ultraviolet-visible
VC	Vinylene carbonate
XRD	X-ray diffraction

Contents

Remerciements	i
Glossary.....	iii
Contents.....	iv
List of Figures	vii
List of Tables.....	xii
List of Schemes	xiv
General Introduction	1
1 Bibliography.....	3
1.1 Non-hydrolytic sol-gel chemistry	3
1.1.1 Hydrolytic sol-gel: history and concepts.....	3
1.1.2 Introduction to non-hydrolytic sol-gel	4
1.1.3 Non-hydrolytic sol-gel mechanisms.....	5
1.1.3.1 Alkyl halide elimination	6
1.1.3.2 Ether, ester and acetamide elimination	8
1.2 Lithium-ion batteries (LIBs).....	8
1.2.1 Negative electrode materials	10
1.2.2 Towards ideal anode materials for lithium-ion batteries.....	14
1.3 Titanium dioxide (TiO ₂)	15
1.3.1 Polymorphs.....	16
1.3.2 State of art of TiO ₂ as anode for Li-ion batteries	19
2 Experimental part: Synthesis, characterizations and evaluation of performances	21
2.1 Principle of the main characterizations techniques	21
2.1.1 X-ray diffraction.....	21
2.1.2 Molecular nitrogen physisorption	23
2.1.3 Electrochemical cycling	26
2.2 Protocols of synthesis and analyses.....	28
2.2.1 Materials.....	28
2.2.2 Synthesis.....	29
2.2.2.1 TiO ₂ and TiO ₂ -V ₂ O ₅ mixed oxides prepared by NHSG ⁱ Pr ₂ O route	29
2.2.2.2 TiO ₂ prepared by NHSG ⁱ PrOH and ^t BuOH routes and TiO ₂ -V ₂ O ₅ mixed oxides prepared by NHSG ⁱ PrOH route	30
2.2.2.3 TiO ₂ /C nanocomposites prepared by NHSH ⁱ Pr ₂ O or NHSG THF routes	31

2.2.3	Xerogels impregnation with a FeCl ₃ solution	32
2.2.4	Preparation of electrodes and assemblage of coin cells	32
2.2.5	Devices characteristics	34
3	TiO ₂ -V ₂ O ₅ Mixed Oxides.....	37
3.1	Evaluation of the influence of vanadium over the properties of TiO ₂ prepared by the NHSH ¹ Pr ₂ O route	39
3.1.1	Published Article: <i>J. Sol-Gel Sci. Technol.</i> , 2016, 79, 270-278.....	39
3.1.2	Complementary characterizations of the samples from the published article: <i>J. Sol-Gel Sci. Technol.</i> , 2016, 79, 270-278.....	51
3.1.2.1	Thermogravimetric analysis of TiO ₂ -V ₂ O ₅ xerogels	51
3.1.2.2	Wettability analysis of electrodes by contact angle measurements	52
3.1.2.3	PEIS evaluation of mechanically prepared TiO ₂ -V ₂ O ₅ mixed oxides and galvanostatic cycling of a commercial TiO ₂	53
3.1.3	Optimization of synthesis conditions and influence of the heat treatment temperature over the anatase-rutile TiO ₂ phase transformation.....	55
3.1.3.1	Influence of the synthesis time over the preparation of TiO ₂	55
3.1.3.2	Influence of calcination temperature over crystallinity and texture of TiO ₂ and TiO ₂ -V ₂ O ₅ mixed oxides	59
3.1.3.3	Electrochemical performance of TiO ₂ calcinated at different temperatures (<i>i.e.</i> 350-650 °C).....	63
3.1.4	Electrochemical performance of NHSG TiO ₂ and TiO ₂ -V ₂ O ₅ mixed oxides <i>versus</i> sodium.....	65
3.1.5	Electrochemical performance of TiO ₂ over different potential ranges	68
3.2	TiO ₂ and TiO ₂ -V ₂ O ₅ mixed oxides prepared by NHSG alcohol routes	75
3.2.1	Influence of the oxygen donor, alcohol <i>versus</i> ether, over the TiO ₂ properties. 75	
3.2.2	Structural and textural characterization of TiO ₂ -V ₂ O ₅ mixed oxides prepared by NHSG ¹ PrOH route.....	78
3.3	Chapter Conclusion	81
4	TiO ₂ /C Nanocomposites.....	83
4.1	Evaluation of oxygen donors over the carbon formation	84
4.1.1	Submitted article: <i>J. Mater. Chem. A</i> , 2017	84
4.1.2	Electrochemical performances at higher current densities (above C).....	102
4.1.3	Spectroscopic analyses for further insights to the carbon coating formation mechanism.....	105
4.2	Catalytic graphitization of the NHSG organic byproducts by FeCl ₃ impregnation	109
4.3	Chapter conclusion	115

General Conclusion	117
Résumé en Français.....	119
Synthèse par chimie sol-gel non-hydrolytique de matériaux d'électrodes pour batteries Li-ion à base de TiO_2	119
Synthèse des oxydes mixtes ($\text{TiO}_2\text{-V}_2\text{O}_5$) par chimie sol-gel non-hydrolytique pour des applications comme matériaux d'anode de batteries Li-ion.....	120
Élaboration des nanocomposites TiO_2/C par chimie sol-gel non-hydrolytique où le donneur d'oxygène est également la source de carbone du composite. Analyse de leur performances électrochimiques vis-à-vis l'insertion de lithium.....	125
Conclusions	129
References	131

List of Figures

Chapter 1 - Bibliography

Figure 1.1 Overview of the sol-gel process, principal steps to control the final morphology of the product. Figure taken from [9].	3
Figure 1.2 Scheme of components of Li-ion batteries. Figure taken from [95].	9
Figure 1.3 Voltage <i>versus</i> capacity for positive- and negative-electrode materials used in Li-based cells. The output voltage values for Li-ion cells and Li-metal cells are also represented. Figure taken from [96].	10
Figure 1.4 Structural changes observed during lithiation/delithiation processes in Li-ion batteries electrodes; black, blue and yellow circles correspond to voids in crystal structure, metal and lithium respectively. Figure taken from [92].	12
Figure 1.5 Crystal structures of (a) Rutile, (b) Anatase, (c) Bronze, (d) Brookite, (e) Columbite, (f) Hollandite, (g) Baddeleyite, and (h) Ramsdellite phases; red spheres correspond to oxygen, titanium is inside green octahedra. Figure taken from [168].	16
Figure 1.6 (a) Phase diagram of the Li composition in TiO ₂ anatase as function of particle size (α , β and γ correspond to anatase, lithium titanate and LiTiO ₂ respectively); and (b) scheme of phase transition upon Li insertion in anatase TiO ₂ . Figures taken from [184] (a) and [185] (b).	18

Chapter 2 - Experimental part: Synthesis, characterizations and evaluation of performances

Figure 2.1 Scheme corresponding to Bragg's law. Figure taken from [222].	22
Figure 2.2 Classification of isotherms according to IUPAC. Figure taken from [223].	23
Figure 2.3 Hysteresis classification according to IUPAC. Figure taken from [223].	25
Figure 2.4 Scheme of excitation (left) and response (right) of galvanostatic cycling (cycling chronopotentiometry). Figure taken from [229].	26
Figure 2.5 (a) Galvanostatic charge/discharge profile of a TiO ₂ sample <i>vs.</i> Li ⁺ /Li and (b) its rate performance at different current densities. Figure taken from [230].	27
Figure 2.6 Nyquist plot for an electrochemical system evidencing the kinetic and mass transfer control regions at high and low frequencies respectively. Figure taken from [229].	28
Figure 2.7 Picture of the IPE and THF derived TiO ₂ xerogels and final products after heat treatment.	31
Figure 2.8 (a) As tape casted slurry visual aspect and (b) dried film visual aspect.	32
Figure 2.9 Visual aspect of TiO ₂ -THF electrodes with and without acetylene black.	33
Figure 2.10 Scheme of coin cell assemblage.	34

Chapter 3 - TiO₂-V₂O₅ Mixed Oxides

Fig. 1 Powder X-ray diffraction patterns of the TiO ₂ and TiO ₂ -V ₂ O ₅ samples.	43
Fig. 2 SEM images of TiO ₂ (a-c), TiV5 (d-f), and TiV20 (g-i) at different magnifications.	44
Fig. 3 (a) N ₂ physisorption isotherms and (b) BJH pore size distribution (desorption branch) of TiO ₂ and TiO ₂ -V ₂ O ₅ samples. Filled and open symbols refer to adsorption and desorption, respectively.	45

Fig. 4 Conductivity spectra of the as-synthesized TiO ₂ and TiO ₂ -V ₂ O ₅ samples at 293 K. The insert shows the complex plane (Nyquist) plot.....	45
Fig. 5 (a) Initial (first cycle) charge/discharge profiles at a current rate of 16.8 mA·g ⁻¹ (C/20) of TiO ₂ and TiO ₂ -V ₂ O ₅ electrodes <i>versus</i> Li; (b) cycling performances at different C rates (C = 335.6 mA·g ⁻¹) for a voltage window of 1.2-2.6 V <i>versus</i> Li ⁺ /Li (filled and open symbols refer to reduction (discharge) and oxidation (charge), respectively).....	47
Fig. S1 Raman spectra of the TiO ₂ and TiO ₂ -V ₂ O ₅ samples.....	50
Fig. S2 Complex impedance plots of TiO ₂ , TiV5, TiV10, TiV15, and TiV20 electrodes in half-cells <i>versus</i> lithium. Plots were obtained in potentiostatic mode at 1.8 V vs Li ⁺ /Li after 2 h relaxation time before the lithiation. The equivalent circuit used for the analysis of the complex impedance plots is shown on the top right hand corner.....	51
Figure 3.1 Thermogravimetric analysis of xerogels of TiO ₂ and TiO ₂ -V ₂ O ₅ mixed oxides.....	52
Figure 3.2 Contact angle measured after deposition of a water drop (bleu section) or an electrolyte drop (white section) over glass, copper sheet (current collector) and electrode films; two images corresponding to the droplet deposition (water up and electrolyte down) over TiV10 electrode film are presented on the right side.....	53
Figure 3.3 Complex impedance plots of TiO ₂ -V ₂ O ₅ mechanically mixed electrodes in half-cells <i>versus</i> lithium. Plots were obtained in potentiostatic mode at 1.8 V vs Li ⁺ /Li after 2 h relaxation time before the lithiation. The equivalent circuit used for the analysis of the complex impedance plots is shown on the top right hand corner.....	54
Figure 3.4 NHSG and commercial TiO ₂ cycling performances at different C rates (C=335.6 mA·g ⁻¹) for a voltage window of 1.2-2.6 V <i>versus</i> Li ⁺ /Li (filled and open symbols refer to reduction (discharge) and oxidation (charge), respectively).....	55
Figure 3.5 Powder X-ray diffraction patterns of TiO ₂ xerogels (a) and calcinated TiO ₂ (b) for different reaction times.....	56
Figure 3.6 Thermogravimetric analysis of TiO ₂ xerogels for different reaction times.....	57
Figure 3.7 SEM micrographs at different magnifications of NHSG ¹ Pr ₂ O derived TiO ₂ after 1 day (a-c) and 8 days (d-f) of synthesis.....	57
Figure 3.8 (a) Molecular nitrogen physisorption isotherms and (b) BJH pore size distribution (desorption branch) of TiO ₂ prepared at different reaction times. Filled and open symbols refer to adsorption and desorption, respectively.....	58
Figure 3.9 Powder X-ray diffraction patterns of TiO ₂ (a), TiV10 (b) and TiV20 (c) xerogels and calcinated samples.....	60
Figure 3.10 Mechanism proposed for the TiO ₂ anatase (A) to rutile (R) transformation. Figure taken from [236].....	62
Figure 3.11 (a) Molecular nitrogen physisorption isotherms and (b) BJH pore size distribution (desorption branch) of TiO ₂ after different heat treatments. Filled and open symbols refer to adsorption and desorption, respectively.....	63
Figure 3.12 Cycling performances at a current rate of 16.8 mA·g ⁻¹ (C/20; C=335.6 mA·g ⁻¹) of TiO ₂ calcinated at different temperatures (xerogel and commercial TiO ₂ also included) for a voltage window of 1.2-2.5 V <i>versus</i> Li ⁺ /Li (filled and open symbols refer to reduction (discharge) and oxidation (charge), respectively).....	64
Figure 3.13 Initial galvanostatic charge/discharge profiles at a current rate of 16.8 mA·g ⁻¹ (C/20; C=335.6 mA·g ⁻¹) of different temperature heat-treated TiO ₂ electrodes for a voltage window of 1.2-2.5 V <i>versus</i> Li ⁺ /Li.....	65
Figure 3.14 Galvanostatic charge/discharge profiles at a current rate of 16.8 mA·g ⁻¹ (C/20) of TiO ₂ and TiO ₂ -V ₂ O ₅ electrodes <i>versus</i> Na, (a) 1 st cycle and (b) 20 th cycle; (c) cycling performances and (d) coulombic efficiency at different C rates (C = 335.6 mA·g ⁻¹) for a voltage window of 0.0-2.5 V <i>versus</i> Na ⁺ /Na (filled and open symbols refer to reduction – discharge– and oxidation –charge–, respectively).....	67

Figure 3.15 Cycling performances at a current rate of $67.2 \text{ mA} \cdot \text{g}^{-1}$ ($C/5$) of TiO_2 from NHSG $^1\text{Pr}_2\text{O}$ ether route calcinated at $350 \text{ }^\circ\text{C}$ for different voltage windows <i>versus</i> Li^+/Li	69
Figure 3.16 Powder X-ray diffractograms of $^1\text{Pr}_2\text{O}$ and THF derived TiO_2 calcinated at different temperatures (<i>i.e.</i> $350 \text{ }^\circ\text{C}$ and $500 \text{ }^\circ\text{C}$).....	70
Figure 3.17 (a) Molecular nitrogen physisorption isotherms and (b) BJH pore size distribution (desorption branch) of $^1\text{Pr}_2\text{O}$ and THF derived TiO_2 calcinated at $350 \text{ }^\circ\text{C}$ and $500 \text{ }^\circ\text{C}$. Filled and open symbols refer to adsorption and desorption, respectively.	71
Figure 3.18 NH_3 -TPD profiles of the TiO_2 samples prepared by NHSG ether routes.....	72
Figure 3.19 Cycling performances at a current rate of $67.2 \text{ mA} \cdot \text{g}^{-1}$ ($C/5$) of TiO_2 from NHSG ether route (<i>i.e.</i> $^1\text{Pr}_2\text{O}$ and THF; both heat treatments 350 and $500 \text{ }^\circ\text{C}$ in air) for different voltage windows <i>versus</i> Li^+/Li (filled and open symbols refer to reduction (discharge) and oxidation (charge), respectively).....	73
Figure 3.20 Galvanostatic charge/discharge profiles at a current density rate of $67.2 \text{ mA} \cdot \text{g}^{-1}$ ($C/5$) of TiO_2 from NHSG ether route (<i>i.e.</i> $^1\text{Pr}_2\text{O}$ and THF; both heat treatments 350 and $500 \text{ }^\circ\text{C}$ in air) for different voltage windows <i>versus</i> Li^+/Li (a) 1 st cycle; (b) 11 th cycle; (c) 21 st cycle and (d) 31 st cycle (<i>i.e.</i> 1 st cycles after changing the potential window; Figure 3.19).	73
Figure 3.21 Powder X-ray diffraction patterns of TiO_2 from different oxygen donors.	76
Figure 3.22 (a) Molecular nitrogen physisorption isotherms and (b) BJH pore size distribution (desorption branch) of TiO_2 from $^1\text{Pr}_2\text{O}$, $^1\text{PrOH}$ and $^1\text{BuOH}$ route. Filled and open symbols refer to adsorption and desorption, respectively.	76
Figure 3.23 Initial galvanostatic charge/discharge profiles at a current rate of $16.8 \text{ mA} \cdot \text{g}^{-1}$ ($C/20$; $C=335.6 \text{ mA} \cdot \text{g}^{-1}$) of different oxygen donors TiO_2 electrodes for a voltage window of 1.2 - 2.5 V <i>versus</i> Li^+/Li	77
Figure 3.24 Powder X-ray diffraction patterns of $^1\text{PrOH}$ derived mixed oxides.....	78
Figure 3.25 SEM micrographs of TiV5-OH (a), TiV10-OH (b), TiV15-OH (c) and TiV20-OH (d-e) from the NHSG $^1\text{PrOH}$ route.	79
Figure 3.26 (a) Molecular nitrogen physisorption isotherms and (b) BJH pore size distribution (desorption branch) of TiO_2 and $\text{TiO}_2\text{-V}_2\text{O}_5$ from the NHSG $^1\text{PrOH}$ route. Filled and open symbols refer to adsorption and desorption, respectively.	80

Chapter 4 - TiO_2/C Nanocomposites

Figure 1. (a) N_2 physisorption isotherms of TiO_2 and TiO_2/C samples (filled and open symbols refer to adsorption and desorption, respectively); (b) BJH pore size distribution (desorption branch).....	90
Figure 2. Powder X-ray diffraction patterns of TiO_2 and TiO_2/C samples. Additionally to typical TiO_2 reflections; XRD patterns show the presence of two weak reflections around 45° 2θ . Both of them have been correlated to the PTFE of the support used during analysis.....	90
Figure 3. Raman spectra of TiO_2/C samples (graphite region).....	92
Figure 4. Solid-state ^{13}C CP-MAS NMR spectra of dried xerogels and TiO_2/C nanocomposites. Spectra were normalized. The background signal was removed by subtracting the spectrum obtained without the sample.....	92
Figure 5. Scanning electron micrographs of TiO_2 -IPE (a,b), TiO_2 -THF (c,d), TiO_2/C -IPE (e,f), TiO_2/C -THF (g,h) at different magnifications.....	93
Figure 6. Transmission electron micrographs and HAADF images of TiO_2/C -IPE (a,b) and TiO_2/C -THF (c,d) samples.....	93
Figure 7. Cycling performance at different C rates ($C=335.6 \text{ mAh} \cdot \text{g}^{-1}$) of (a) electrodes prepared with IPE-based samples and (b) electrodes prepared with THF-based samples. Voltage window of 1.2 - 2.5 V <i>versus</i> Li^+/Li . Filled and open symbols refer to reduction	

(discharge) and oxidation (charge) respectively. The intrinsic and/or extrinsic carbon content of the electrodes is given in Table 1.....	94
Figure SI1. Thermogravimetric analysis in air of xerogels and TiO ₂ /C composites.....	99
Figure SI2. Powder X-ray diffraction patterns of TiO ₂ /C nanocomposites pyrolyzed at different temperatures: IPE derived samples (a) and THF derived ones (b).....	99
Figure SI3. Raman spectra of TiO ₂ and TiO ₂ /C composites in the 100-800 cm ⁻¹ range.....	100
Figure SI4. Comparison of Raman spectra of TiO ₂ /C-THF and of a mixture of TiO ₂ -THF with carbon black. The amount of carbon for each sample was 18 wt%.....	100
Figure SI5. EDX analysis over different sections of the TiO ₂ /C-IPE sample: (a) carbon coating; (b) TiO ₂ nanoparticle.....	100
Figure SI6. EDX analysis over different areas of the TiO ₂ /C-THF sample: (a) carbon coating; (b) TiO ₂ nanoparticle.....	101
Figure SI7. Columbic efficiency of electrodes cycled at different C rates (C=335.6 mAh g ⁻¹) for a voltage window of 1.2-2.5 V versus Li ⁺ /Li; (a) electrodes prepared with IPE-based samples and (b) electrodes prepared with THF-based samples. It is worth reminding that electrodes contain different carbon amounts (<i>i.e.</i> intrinsic and/or extrinsic carbon; Table 1).	101
Figure SI8. Initial (first cycle) charge/discharge profiles at a current rate of 16.8 mA g ⁻¹ (C/20) of IPE (a) and THF (b) based electrodes versus Li.....	101
Figure 4.1 Cycling performances of THF derived TiO ₂ at different C rates (C; 2C and 5C; C=335.6 mA·g ⁻¹) for a voltage window of 1.2-2.5 V versus Li ⁺ /Li (filled and open symbols refer to reduction –discharge– and oxidation –charge–, respectively) (a); galvanostatic charge/discharge profiles after varying the C rate at a current rate of 336 mA·g ⁻¹ , <i>i.e.</i> cycle 1 (b) and at a current rate of 672 mA·g ⁻¹ , <i>i.e.</i> cycle 51 (c).....	102
Figure 4.2 Complex impedance plots of TiO ₂ -THF and TiO ₂ /C-THF(IPE) electrodes with a total amount of 18 wt% of C in half-cells versus lithium. Plots were obtained in potentiostatic mode at 1.8 V versus Li ⁺ /Li (a) and 1.2 V versus Li ⁺ /Li (b) after 2 h relaxation time before the lithiation. The equivalent circuit used for the analysis of the complex impedance plots is shown on the top right hand corner.....	104
Figure 4.3 Raman spectra of Xer-THF and Xer-IPE.....	105
Figure 4.4 ¹ H NMR spectrum in CDCl ₃ , 300 MHz of byproducts of Xer-THF after washing with CHCl ₃ , full range (a) and aliphatic region (b). ¹³ C NMR spectrum of the same sample (c).	106
Figure 4.5 UV-vis spectra of solvents used for washing Xer-IPE (a) and Xer-THF (b); solutions diluted 600 times before analysis.....	107
Figure 4.6 Solvents after washing Xer-IPE (filled symbols) and Xer-THF (open symbols); each box correspond to the same solvent: CH ₂ Cl ₂ (black), CHCl ₃ (red) and THF (blue).	108
Figure 4.7 FTIR spectra of dried xerogels and pyrolysed samples in the 900-1800 and 2700-3100 cm ⁻¹ ranges.	108
Figure 4.8 Powder X-ray patterns of TiO ₂ /C nanocomposites after Fe impregnation (different concentrations and time) under Ar (a) and Ar-H ₂ (b) atmospheres.	110
Figure 4.9 Raman spectra of TiO ₂ /C nanocomposites (a-b) TiO ₂ region and (c-d) graphite region. Samples pyrolyzed under Ar atmosphere are presented in (a, c), while under Ar-H ₂ atmosphere are presented in (b, d).....	111
Figure 4.10 (a-b) Molecular nitrogen physisorption isotherms and (c-d) BJH pore size distribution (desorption branch) of TiO ₂ /C nanocomposites after impregnation treatment. Filled and open symbols refer to adsorption and desorption, respectively. Samples pyrolyzed under Ar atmosphere (a, c) and samples pyrolyzed under Ar-H ₂ atmosphere (b, d).	113
Figure 4.11 Cycling performances of THF derived TiO ₂ /C nanocomposites at different current densities for a voltage window of 1.2-2.5 V versus Li ⁺ /Li (filled and open symbols refer to	

reduction –discharge– and oxidation –charge–, respectively) (a); initial galvanostatic charge/discharge profiles at a current rate of $16.8 \text{ mA} \cdot \text{g}^{-1}$ versus lithium. (12h impregnation).
 114

Résumé en Français

Figure R. 1	Diffractogrammes du TiO_2 et des oxydes mixtes ($\text{TiO}_2\text{-V}_2\text{O}_5$).	121
Figure R. 2	Micrographies MEB de TiO_2 (a-c), TiV_5 (d-f) et TiV_{20} (g-i) à différents grossissements (x10k, x25k et x150k).	122
Figure R. 3	(a) Isothermes d'adsorption-désorption d'azote et (b) distribution BJH de la taille des pores déterminée à partir de la courbe de désorption du TiO_2 et des oxydes mixtes $\text{TiO}_2\text{-V}_2\text{O}_5$. Les symboles pleins et ouverts correspondent aux courbes d'adsorption et desorption respectivement.	123
Figure R. 4	(a) Profils galvanostatiques correspondant au premier cycle (charge-décharge) des électrodes de TiO_2 et de $\text{TiO}_2\text{-V}_2\text{O}_5$ avec une densité de courant égal à $16,8 \text{ mA} \cdot \text{g}^{-1}$ ($C/20$) par rapport au lithium ; (b) performances électrochimiques correspondant au cyclage avec différents densités de courant ($C=335,6 \text{ mA} \cdot \text{g}^{-1}$) pour une fenêtre de potentiel de 1,2-2,5 V versus Li^+/Li (les symboles pleins et ouverts correspondent à la réduction –décharge– ou à l'oxydation –charge– respectivement).	124
Figure R. 5	Diffractogrammes des xérogels, TiO_2 et TiO_2/C nanocomposites.....	126
Figure R. 6	Micrographies MEB de $\text{TiO}_2\text{-IPE}$ (a,b), $\text{TiO}_2\text{-THF}$ (c,d), $\text{TiO}_2/\text{C-IPE}$ (e,f), $\text{TiO}_2/\text{C-THF}$ (g,h) à différents grossissements (x25k et x150k).	127
Figure R. 7	Micrographies MET de $\text{TiO}_2/\text{C-IPE}$ (a-d) et $\text{TiO}_2/\text{C-THF}$ (e-h) ; (b, d, f, h) ont été prises en champ noir annulaire à angle élevé.	127
Figure R. 8	Spectre Raman des nanocomposites TiO_2/C dans la région de 900 à 2000 cm^{-1} .128	
Figure R. 9	Performances électrochimiques correspondant au cyclage avec différents densités de courant ($C=335.6 \text{ mA} \cdot \text{g}^{-1}$) pour une fenêtre de potentiel de 1.2-2.5 V versus Li^+/Li (les symboles pleins et ouverts correspondent à la réduction –décharge– ou à l'oxydation –charge– respectivement).	129

List of Tables

Chapter 1 - Bibliography

Table 1.1 Examples of oxides and mixed oxides obtained by alkyl halide elimination routes.	7
Table 1.2 Summary comparing common materials used as Li-ion batteries anodes according to their type classification; advantages and disadvantages are also presented. Table based on reference [99].	13
Table 1.3 Structural and lithiation properties of TiO ₂ polymorphs. Table based on references [168, 190].	18

Chapter 2 - Experimental part: Synthesis, characterizations and evaluation of performances

Table 2.1 Reagents used in the synthesis of TiO ₂ , V ₂ O ₅ and TiO ₂ -V ₂ O ₅ samples by NHSG ¹ Pr ₂ O route.	30
Table 2.2 Reagents used in the synthesis of TiO ₂ and TiO ₂ -V ₂ O ₅ samples by NHSH alcohol routes.	31
Table 2.3 Summary of samples nomenclature for TiO ₂ /C composites.	32
Table 2.4 Theoretical percentage values from electrodes films (TiO ₂ /C nanocomposite series).	33

Chapter 3 - TiO₂-V₂O₅ Mixed Oxides

Table 1 Reactants used in the synthesis of TiO ₂ and TiO ₂ -V ₂ O ₅ samples and experimental V content (derived from EDX analysis).	41
Table 2 Crystallite size and textural data for the TiO ₂ and TiO ₂ -V ₂ O ₅ samples.	43
Table 3. Performances of selected nanostructured anatase TiO ₂ materials as anode in lithium batteries.	48
Table S1. Fitted resistance values from impedance plots of TiO ₂ , TiV5, TiV10, TiV15, and TiV20 electrodes in half-cell versus lithium.	51
Table 3.1 Fitted resistance values from impedance plots of TiO ₂ -V ₂ O ₅ mechanically mixed electrodes in half-cell <i>versus</i> lithium.	54
Table 3.2 Organic content present in xerogels, crystallite size of both xerogels and calcinated TiO ₂ and textural data of TiO ₂ from different synthesis periods.	56
Table 3.3 Crystallite size and textural data for TiO ₂ and TiO ₂ -V ₂ O ₅ samples after different heat treatments.	61
Table 3.4 Comparison of TiO ₂ and mixed oxides reduction specific capacities of galvanostatic cycling versus Li and Na.	68
Table 3.5 Crystallite size, textural data and NH ₃ uptake for TiO ₂ from different oxygen donors (<i>i.e.</i> ¹ Pr ₂ O and THF) and different calcination temperatures (<i>i.e.</i> 350 °C and 500 °C).	70
Table 3.6 Crystallite size and textural data for TiO ₂ prepared by NHSG using different oxygen donors.	75
Table 3.7 Crystallite size and textural data for TiO ₂ and TiO ₂ -V ₂ O ₅ samples from the ¹ PrOH NHSG route.	79

Chapter 4 - TiO₂/C Nanocomposites

Table 1. Nominal active material, carbon black, and PVDF content of the electrode films, and TiO ₂ and intrinsic C content calculated from the films composition and from the pyrolytic C content of the TiO ₂ /C nanocomposites (6.6 wt% C for TiO ₂ /C-IPE and 18.9 wt% C TiO ₂ /C-THF).....	87
Table 2. Carbon content for TiO ₂ /C composites prepared by reaction at different temperature, then pyrolyzed at 750 °C under argon. The C content was determined by TGA from the weight loss between 300 and 1000 °C (Figure SI1).....	88
Table 3. Textural data and TiO ₂ crystallite size for the composite and oxide samples; ^a specific surface area, ^b total pore volume; ^c BJH average pore diameter calculated from the desorption branch; ^d crystallite size determined by the Scherrer equation.....	89
Table SI1. Textural data for TiO ₂ /C composites prepared at 180 °C and pyrolyzed at 750 or 800 °C, ^a temperature of pyrolysis, ^b specific surface area, ^c total pore volume.....	99
Table 4.1 Fitted resistance values from impedance plots of TiO ₂ -THF and TiO ₂ /C-THF(IPE) electrodes in half-cell versus lithium.	104
Table 4.2 Crystallite size and textural data for TiO ₂ after impregnation treatment and pyrolysis under Ar or Ar-H ₂	110

Résumé en Français

Tableau 1 Contenu expérimental de vanadium, taille de cristallite et information de la texture du TiO ₂ et des oxides mixtes (TiO ₂ -V ₂ O ₅).....	121
Tableau 2 Taille de cristallite et information de la texture du TiO ₂ et des TiO ₂ /C nanocomposites.	126
Tableau 3 Composition des électrodes.....	128

List of Schemes

Scheme 1.1 Main reactions of the sol–gel process using metal or silicon alkoxides (represented by M–OR).....	4
Scheme 1.2 Different NHSG reactions involved in alkyl halide elimination routes.	6
Scheme 1.3 Non-hydrolytic condensation involving ether, ester and acetamide elimination. ..	8
Scheme 1.4 Reaction mechanisms observed in anodes for Li-ion batteries.	11
Scheme 1.5 Reaction of lithiation/delithiation processes of TiO_2 ; x taking values between 0 and 1.	16
Scheme 3.1 Global overview of samples prepared in chapter 3: TiO_2 - V_2O_5 mixed oxides.	38
Scheme 1 ideal reaction scheme for the synthesis of TiO_2 - V_2O_5 samples.....	42
Scheme 3.2 Global balance for ideal reaction synthesis of TiO_2 by NHSG alcohol routes.....	75
Scheme 4.1 Global overview of samples prepared in chapter 4: TiO_2/C nanocomposites.....	83
Scheme 1. Ideal reaction scheme for the NHSG synthesis of TiO_2 from IPE and THF.....	88
Schéma 1 Bilan réactionnel idéal de la synthèse d’oxydes mixtes TiO_2 - V_2O_5	121
Schéma 2 Bilan réactionnel idéal de la synthèse des xérogels donnant les nanocomposites TiO_2/C	125

General Introduction

Oxide compounds are ubiquitous; they compose most of the Earth's crust (*e.g.* ~66 wt% of SiO₂) making them interesting materials for study due to their abundance. Furthermore, their diverse properties offer a wide range of possibilities for applications in different fields such as energy storage systems (*e.g.* electrodes for Li-ion batteries), catalysts, pigments, energy harvesting devices (*e.g.* piezo and pyroelectric nanogenerators), biomedical devices (*e.g.* implants, targeted drug delivery, magnetic resonance imaging and magnetic hyperthermia), photovoltaic devices (*e.g.* solar cells) and optoelectronic applications (*e.g.* light emitting diodes), for citing some of them.

One interesting example of versatility of metal oxides is the case of titanium dioxide (TiO₂). This compound, also known as titania, has been widely studied and employed in an array of industrial applications due to its singular properties including high refractive index, photocatalytic activity, and semiconductivity. Considerable efforts have been devoted to controlling various parameters such as morphology, particle size, crystallinity and porosity for specific applications. Interestingly, TiO₂ has been considered a promising substitute to replace graphite anodes in lithium-ion batteries, mainly due to its competitive theoretical specific capacity (335.6 mAh·g⁻¹), low cost and good chemical stability. Nevertheless, TiO₂ presents poor electronic conductivity and low ion diffusion coefficient; those issues can be limited by reducing the distance of ions diffusion (*e.g.* by using nanoporous structures), improving the electronic conductivity of TiO₂ (*e.g.* by metal atoms doping) or improving the electronic transport (*e.g.* by using carbon-titania composites).

Metal oxides, including TiO₂, usually are obtained by high temperature methods; however, complex oxides or nanostructured oxides could not be obtained that way. In order to overcome this limitation, researchers started looking for new and innovative methods to produce metastable metal oxides by low temperature wet synthesis processes such as sol-gel, co-precipitation, hydrothermal and solvothermal methods.

The non-hydrolytic sol-gel (NHSG) technique, a variant of the conventional hydrolytic sol-gel (HSG) method, started its development in the early 1990s. The main difference between HSG and NHSG is that NHSG uses organic oxygen donors (commonly ethers, alkoxides or alcohols) instead of water. NHSG has been widely used for the production of oxides, mixed oxides and organic-inorganic hybrids materials. It proved particularly successful for the synthesis of nanoparticles, bringing the advantages of better control over size, shape and crystallinity, and for the preparation of mesoporous oxides in one-step, avoiding the use of templates.

The group Chimie Moléculaire et Organisation du Solide (CMOS) of the Institut Charles Gerhardt Montpellier (ICGM) is a pioneer in the NHSG field. The laboratory has more than 25 years of experience with this synthesis methodology, notably for the production of catalytic materials. Exploiting the expertise of the CMOS group in NHSG, this PhD thesis focuses on the synthesis of TiO₂ based materials with potential applications in the Li-ion battery field. Two different approaches have been explored in order to improve the electronic conductivity of TiO₂, either by synthesizing TiO₂-V₂O₅ mixed oxides or TiO₂/carbon nanocomposites.

These two approaches will be presented in this PhD dissertation, following the plan detailed below.

Chapter 1: Bibliography

This first chapter delimits the main topics of this study by bringing a general literature overview of the essential concepts and notions. Discussion starts with a survey concerning the non-hydrolytic sol-gel chemistry, passing by the principal reaction mechanisms. Then, the notions of lithium-ion batteries and anode materials are treated. Finally, a third part is dedicated to titanium dioxide and its properties; a scope of TiO₂ applications in the Li-ion battery field is also explored.

Chapter 2: Experimental part: Synthesis, characterizations and evaluation of performances

This chapter briefly describes the principle of the main characterization methods employed in this work (*i.e.* X-ray diffraction, N₂ physisorption and electrochemical cycling). Materials, experimental protocols and devices characteristics are also presented in this chapter.

Chapter 3: TiO₂-V₂O₅ Mixed Oxides

This chapter focuses on the preparation of TiO₂ and TiO₂-V₂O₅ mixed oxides with different Ti/V ratios using the NHSG ether route in the absence of solvent or additives. The structure, texture and electrochemical properties are studied and compared to the literature. The effect of the heat treatment temperature is also evaluated focusing on the anatase to rutile transformation. Besides, the electrochemical stability of TiO₂ is monitored at different potential windows. This chapter also presents the results of TiO₂-V₂O₅ mixed oxides prepared by NHSG alcohol route.

It is worth mentioning that the main results of this chapter were published in reference [1].

Chapter 4: TiO₂/C Nanocomposites

This chapter describes the development of TiO₂/C nanocomposites using NHSG chemistry and pyrolysis under an inert atmosphere. Different oxygen donors have been tested, acting also as carbon source. The discussion is based on the comparison of the TiO₂/C nanocomposites with their TiO₂ counterparts obtained by calcination in air. Moreover, the mechanisms of formation of the carbon coating have been investigated by several methods. As in the former chapter, the texture, structure, and electrochemical properties of the materials has been thoroughly investigated. In a second part, discussion focuses on the catalytic graphitization of the residual organic byproducts in xerogels in presence of an iron salt, *i.e.* FeCl₃.

It is worth mentioning that the main results of this chapter were already submitted for their publication.

1 Bibliography

1.1 Non-hydrolytic sol-gel chemistry

Before talking about non-hydrolytic sol-gel (NHSG) chemistry, it is necessary to explain some notions about conventional (or hydrolytic) sol-gel (HSG).

1.1.1 Hydrolytic sol-gel: history and concepts

The “Chimie Douce” or “Soft Chemistry” term was first introduced by French chemists Jacques Livage and Jean Rouxel in 1970s [2, 3]. This concept puts together a group of reactions allowing materials synthesis at low temperatures, thus giving access to final products that could not be synthesized in the classical way. Syntheses carried out under these conditions do not provide enough energy to the system, giving as results metastable and porous materials [2, 4, 5]. Wet soft chemistry methods take advantage of the involvement of a liquid phase into the system, improving homogeneity and providing heat control [6, 7]. Furthermore, they allow the synthesis of complex mixed oxides by mixing different precursors in solution, while the composition of the final product can be controlled by varying the molar ratio of reactants [8].

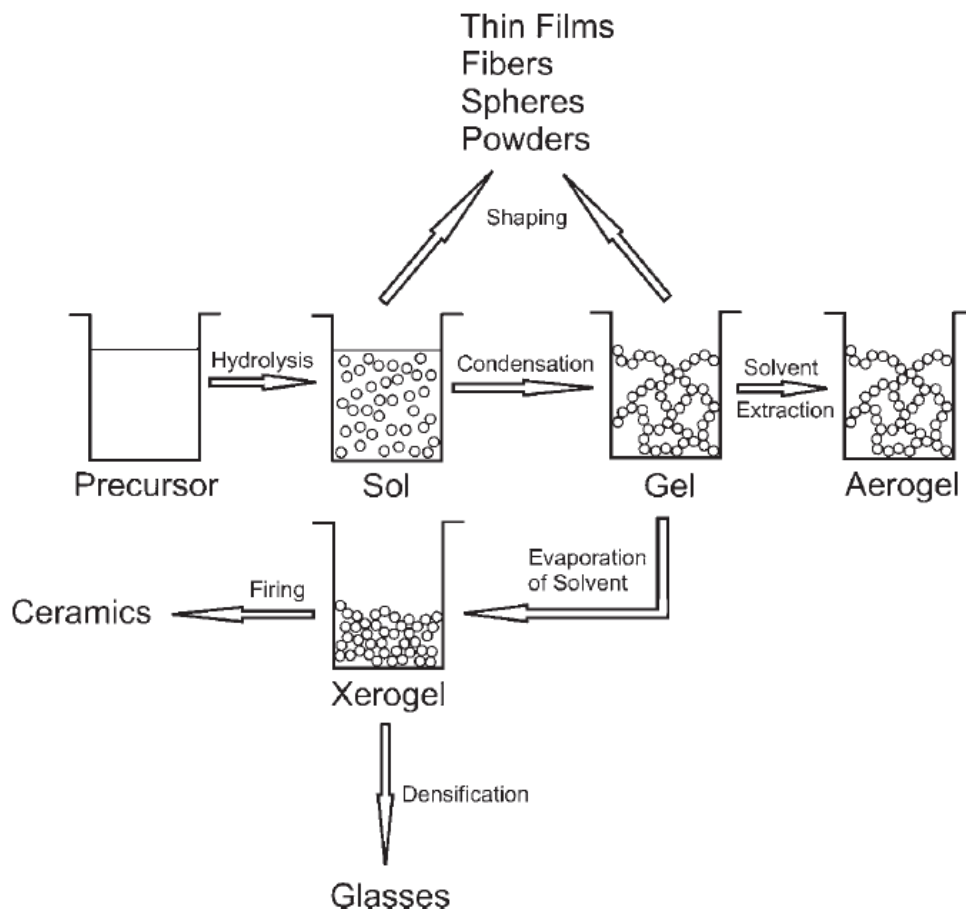


Figure 1.1 Overview of the sol-gel process, principal steps to control the final morphology of the product. Figure taken from [9].

The sol-gel method is one of the oldest wet soft chemistry techniques to be developed which lead to the synthesis of technologically important ceramic and glasses [5]. Actually, Ebelmen obtained the first metal alkoxide in 1846 from silicon tetrachloride (SiCl_4) and alcohol. He observed that the product of this reaction gelled when exposed under atmosphere with normal humidity, thus marking a point for the following researches in the colloidal gel field. However, alkoxides were not widely industrially applied until 1930s, when they were used as precursors for the formation of oxide films [10, 11]. The versatility of this method, as shown in Figure 1.1, lies on the possibilities of shaping the sol or the gel, leading to powders, nanoparticles, films, fibers or monoliths. Dense ceramics or glasses can be obtained after a high temperature heat treatment [9]. Alternatively, if this final treatment is avoided, the sol-gel process allows the preparation of organic-inorganic hybrid materials. Nowadays, alkoxides have become the main precursors in the conventional sol-gel process. The two main reactions involved in conventional sol-gel are hydrolysis and condensation (presented in Scheme 1.1) [3, 10-13].

Hydrolysis



Condensation



Scheme 1.1 Main reactions of the sol-gel process using metal or silicon alkoxides (represented by M-OR).

Hydrolysis takes place through a nucleophilic water attack leading to the formation of hydroxylated species. During the condensation step, there is the formation of oxo-bridges (oxolation) and release of water or alcohol, leading to the formation of an inorganic network. These reactions initially lead to a colloidal dispersion of particles in the solvent (usually a water-alcohol mixture), the “sol”. Further reaction leads to a solid network confining a continuous liquid phase, the “gel”.

At that point, one can mention the main difficulty encountered in the hydrolytic sol-gel process, namely the control over hydrolysis and condensation rates. This issue becomes particularly important when working with metal alkoxide precursors (*e.g.* titanium alkoxides) that have extremely high reaction rates, and when working with several alkoxide precursors to prepare multicomponent oxides. Different strategies have been employed to modify the hydrolysis and condensation rates, including playing on the concentration and/or nature of precursors, the mode of addition of water, modification of the most reactive alkoxide (*e.g.* with carboxylic acids or acetylacetonate), pre-hydrolysis of the least reactive alkoxide, regulation of pH, and elaborated mixing methods. Those parameters also have an influence over the size and morphology of the particles obtained, or over the texture and structure of the xerogel formed [3, 9-14].

1.1.2 Introduction to non-hydrolytic sol-gel

Non-hydrolytic sol-gel process presents an alternative to conventional sol-gel synthesis. This technique, as its hydrolytic counterpart, also belongs to the wet soft chemistry methods. Interestingly, even if first reports of non-aqueous synthesis investigations trace back to 1928 with the work of Dearing and Reid about alkyl orthosilicates (*i.e.* reactions between silicon tetrachloride and different alcohols under anhydrous conditions) [15], it was not until the

early 1990s that the first systematic works on the the synthesis of oxides and mixed oxides using non-hydrolytic condensations were published. At the same time, researchers from Montpellier, under the initiative of André Vioux, coined the term “non-hydrolytic sol-gel” [16-18]. Since then, the use of non-hydrolytic (or non-aqueous) sol-gel methodologies have proven highly successful for synthesizing oxides, mixed oxides and inorganic-organic hybrid materials, either as nanoparticles or porous materials.

The particularity of NHSG is the use of organic oxygen donors instead of water, in a non-aqueous medium. Typical oxygen donors are ethers, alcohols, and alkoxides; but ketones, carboxylic acids or acid anhydrides are also used [4]. Typical metal or silicon precursors are chlorides and alkoxides, but acetates, amides, acetylacetonates, etc. have also been used.

Two different classes of NHSG methods can be distinguished, depending on whether these methods imply the formation of hydroxyl groups (by non-hydrolytic hydroxylation) or not. Indeed, if hydroxyl groups are formed, the formation of oxo-bridges by elimination of water between two M-OH groups is a possibility. Nevertheless, reactions involving hydroxyl groups can be considered non-hydrolytic if the formation of water is prevented by reaction kinetics [19], that is if the hydroxyl groups are consumed rapidly by reaction with other groups (*e.g.* M-Cl, M-OR).

The major difference between HSG and NHSG processes lies in the reaction kinetics. Firstly, non-hydrolytic condensation reactions imply the cleavage of O-C bonds instead of M-O bonds. They are thus considerably slower than hydrolytic condensations and they are also more sensitive to the nature of the carbon group. Non-hydrolytic reactions around silicon are much slower than around metals (*e.g.* Ti, Zr, Al...), but they are very efficiently catalyzed by Lewis acid metal species. Those features supply thus better conditions for the production of metal oxide gels and of multicomponent oxide gels, including metastable multicomponent oxide gels and metal silicate gels (*e.g.* Si-Ti, Si-Zr, etc.) [20], avoiding the use of expensive modifiers that are needed for matching the reactivity of precursors in hydrolytic routes and obtain a homogeneous gel.

Another characteristic of the NHSG method is that the degree of condensation of gels can be very high, allowing them to withstand the capillary pressures developed during evaporative drying. Accordingly, NHSG is well suited to the preparation of mesoporous xerogels, avoiding the use of templating agents or sophisticated drying procedure (*e.g.* supercritical drying). Moreover, NHSG xerogels or nanoparticles usually show a higher degree of crystallization whereas hydrolytic processes often lead to amorphous oxo-hydroxyde gels [4, 9, 21, 22].

Before calcination, the surface chemistry of materials obtained by non-hydrolytic processes depends on the nature of the reactions involved, and can be very different from that of their hydrolytic counterparts (*i.e.* non-hydroxylated *vs.* hydroxylated surfaces). Furthermore, the presence of residual organic surface groups can influence crystal growth and morphology, and can act as a capping agent influencing the particle shape [4, 9, 21, 22].

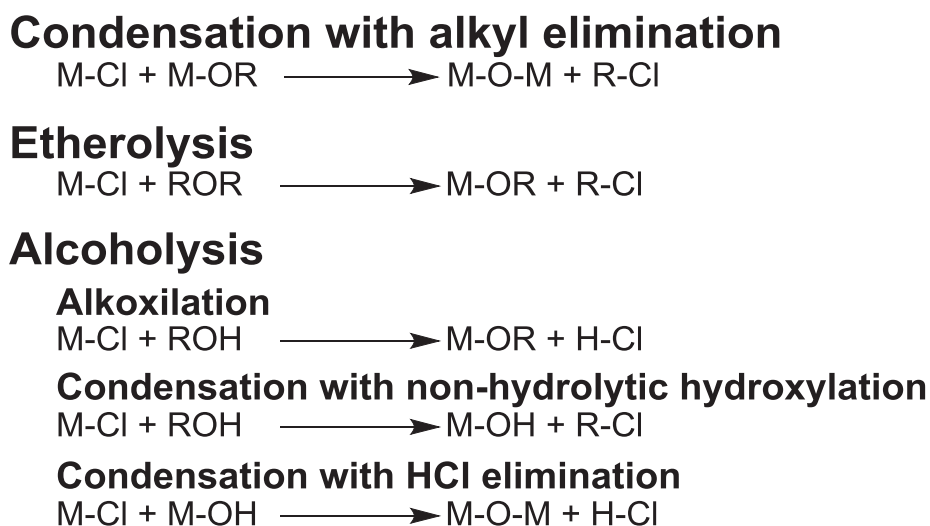
1.1.3 Non-hydrolytic sol-gel mechanisms

NHSG mechanisms differ from their hydrolytic counterpart; there is a wide variety of oxygen donors, precursors and condensation reactions involved in NHSG chemistry. Thus, NHSG routes are classified based on the nature of the predominant molecule eliminated during condensation, or on the nature of the oxygen donor [19].

1.1.3.1 Alkyl halide elimination

This non-hydrolytic synthesis method was among the first to be investigated, either for the synthesis of bulk oxides and mixed oxides or for the synthesis of nanoparticles.

It is based on the condensation between metal alkoxide and metal halide (usually chloride) groups leading to the elimination of an alkyl halide and the formation of oxo-bridges, at temperatures of *ca.* 100-150 °C. Thus oxides and mixed oxides can be prepared by reaction of metal or silicon chloride(s) with metal or silicon alkoxide(s) oxygen donor(s), by the so-called “alkoxide route”. In addition, metal alkoxide groups can be formed *in situ* by reaction of halide groups with an ether or an alcohol (“etherolysis” or “alcoholysis”); then, these alkoxide groups can further condensate with the remaining chloride groups. These options offer the possibility to prepare oxides by reaction of chloride precursors with ether (“ether route”) or alcohol (“alcohol route”) which is particularly attractive when alkoxide precursors are expensive or difficult to obtain [9, 19, 21]. In the case of the “alcohol route”, the mechanism can be more complicated due to the inevitable release of HCl, which may catalyze secondary reactions [9, 19, 21, 23]. It will depend on the nature of the alcohol: tertiary or benzylic alcohols can lead to the formation of hydroxyl groups (“non-hydrolytic hydroxylation”) with elimination of alkyl or benzyl chloride, and these hydroxyl groups can then condense with M-Cl groups to form oxo-bridges with (“HCl elimination”). The different reactions involved in alkyl elimination routes are displayed in Scheme 1.2.



Scheme 1.2 Different NHSG reactions involved in alkyl halide elimination routes.

Different oxides, mixed oxides and multi-compound metal oxides have been obtained by alkyl elimination routes. In order to show the scope of these NHSG routes, a list of different oxides (binary, tertiary and mixed oxides) obtained using alkyl halide elimination as reaction mechanism is presented in Table 1.1.

The most used oxygen donors are diisopropyl ether ($i\text{-Pr}_2\text{O}$) and benzyl alcohol. Diisopropyl ether has been widely explored for the synthesis of mesoporous mixed oxides catalyst. It offers a one-step route to non-ordered mesoporous materials with controlled composition and interesting textural properties, similar or higher than that of their ordered mesoporous counterparts [21, 22], while avoiding the use of templates or supercritical drying. The “benzyl alcohol route” has proven to be a highly efficient, surfactant-free way to prepare a wide range of oxide nanoparticles (*i.e.* binary, ternary and doped oxides) [24]. Its use has also been extended to reactions involving metal alkoxides, acetates or acetyl acetonate precursors [25]

and more recently to the synthesis of doped LiFePO₄ nanocrystals [26]. In this PhD thesis, the ether and to a lesser extent the alcohol route have been used to prepare TiO₂ based materials.

Table 1.1 Examples of oxides and mixed oxides obtained by alkyl halide elimination routes.

Metal oxide	Metal precursor(s)	Oxygen donor(s)	Reference
TiO ₂	TiCl ₄	Ti(O ⁱ Pr) ₄ ; ⁱ Pr ₂ O; ⁱ PrOH; THF; DME; Et ₂ O; EtOH; ^t BuOH; BnOH	[27-35]
SiO ₂	SiCl ₄	ⁱ Pr ₂ O; Et ₂ O; Si(O ⁱ Pr) ₄ ; Si(OEt) ₄	[36-38]
Al ₂ O ₃	AlBr ₃ ; AlCl ₃	Al(O ⁱ Pr) ₃ ; Al(O ^s Bu) ₃ ; Al(O ^t Bu) ₃ ; ⁱ Pr ₂ O	[39-43]
SnO ₂	SnCl ₄ ; SnCl ₂	ⁱ Pr ₂ O; Sn(O ⁱ Bu) ₄ ; Sn(OEt) ₂	[43, 44]
ZrO ₂	ZrCl ₄	ⁱ Pr ₂ O	[35, 45]
WO ₃	WCl ₆	ⁱ Pr ₂ O	[45]
Co ₃ O ₄	CoCl ₂	EtOH; BnOH	[46]
CoO	Co(ac) ₂	BnOH	[47]
Fe ₃ O ₄	Fe(acac) ₃ ; Fe(acac) ₂ ; Fe(ac) ₂	BnOH	[47, 48]
MnO, Mn ₃ O ₄	Mn(ac) ₂ ; Mn(acac) ₂	BnOH	[47]
ZnO	Zn(acac) ₂ ; Zn(ac) ₂	BnOH	[47]
(Ag, Nb, Fe, Eu, Co)/Al ₂ O ₃	AlCl ₃ ; AgCl; NbCl ₅ ; FeCl ₃ ; EuCl ₃ ; CoCl ₂	ⁱ Pr ₂ O	[49-53]
Sn/In ₂ O ₃	SnCl ₄ ; InCl ₃	EtOH	[54]
(La/Eu)/Nb ₂ O ₅	NbCl ₅ ; LaCl ₃ ; EuCl ₃	EtOH	[55]
Al ₂ O ₃ /SiO ₂	AlCl ₃ ; SiCl ₄	EtOH; ⁱ Pr ₂ O	[56]
SnO ₂ /Al ₂ O ₃	SnCl ₄ ; SnCl ₂ ; AlCl ₃	Al(O ^s Bu) ₃ ; Sn(OEt) ₂	[43]
SiO ₂ /ZrO ₂	SiCl ₄ ; ZrCl ₄	Si(O ⁱ Pr) ₄ ; ⁱ Pr ₂ O	[57, 58]
TiO ₂ /SiO ₂	TiCl ₄ ; SiCl ₄	Ti(O ⁱ Pr) ₄ ; Si(O ⁱ Pr) ₄ ; ⁱ Pr ₂ O	[36, 58-62]
TiO ₂ /ZrO ₂	TiCl ₄ ; ZrCl ₄	Ti(O ⁱ Pr) ₄ ; Zr(OEt) ₄ ; ⁱ Pr ₂ O; Pr ₂ O; Et ₂ O	[35, 63, 64]
TiO ₂ /Al ₂ O ₃	TiCl ₄ ; AlCl ₃	Ti(O ⁱ Pr) ₄ ; Al(O ⁱ Pr) ₃ ; ⁱ Pr ₂ O	[64-66]
TiO ₂ /V ₂ O ₅	TiCl ₄ ; VOCl ₃	ⁱ Pr ₂ O	[1, 67, 68]
SiO ₂ /NbVO ₅	SiCl ₄ ; NbCl ₅	VO(O ⁱ Pr) ₃ ; Si(OEt) ₄	[69]
Zr ₂ /WO ₃	WCl ₆	Zr(O ⁱ Pr) ₄ ; ⁱ PrOH; ⁱ Pr ₂ O	[45]
SiO ₂ /Al ₂ O ₃ /MoO ₃	SiCl ₄ ; AlCl ₃ ; MoCl ₅	ⁱ Pr ₂ O	[70, 71]
SiO ₂ /Al ₂ O ₃ /Re ₂ O ₇	SiCl ₄ ; AlCl ₃ ; ReCl ₅	ⁱ Pr ₂ O	[72]
Si-Al-Co oxide	AlCl ₃ ; CoCl ₂	Si(OEt) ₄ ; ⁱ Pr ₂ O	[73]
Y ₂ O ₃ (Eu ₂ O ₃)-V ₂ O ₅	VOCl ₂ ; YCl ₃ ; EuCl ₃	EtOH	[74]
TiO ₂ /V ₂ O ₅ /(MoO ₃ or WO ₃)	TiCl ₄ ; VOCl ₃ ; MOCl ₅ ; WCl ₆	ⁱ Pr ₂ O	[75]
(Tm/Tb/Eu)Y ₃ Al ₅ O ₁₂ , (Tm/Tb/Eu)Y ₄ Al ₂ O ₉	AlCl ₃ ; YCl ₃ ; TmCl ₃ ; TbCl ₃ ; EuCl ₃	EtOH	[76-80]
(Eu)SrWO ₄	WCl ₆ ; SrCl ₂ ; EuCl ₃	MeOH	[81, 82]
BaTiO ₃	Ba; Ti(O ⁱ Pr) ₄	BnOH	[47, 83]
(Ba,Sr)TiO ₃	Ba; Sr; Ti(O ⁱ Pr) ₄	BnOH	[83]
Na ₃ Zr ₂ Si ₂ PO ₁₂	SiCl ₄	OP(OBu) ₃ ; Zr(O ^t Bu) ₄ ; NaO ^t Bu	[84]

1.1.3.2 Ether, ester and acetamide elimination

Other typical non-hydrolytic condensations involve ether, ester or acetamide elimination, which are presented in Scheme 1.3. Ether elimination involves the formation of the oxo-bridges by the reaction between two metal alkoxide groups; it requires higher synthesis temperatures than the alkyl halide elimination. This reaction mechanism allows the direct obtention of inorganic molybdates or tungstates in the presence of pronounced basic alkoxides [9]. Concerning the ester elimination, it consists in the condensation between metal alkoxides and metal carboxylates (acetates); this route has commonly been used to obtain mixed metal oxides [9, 19, 21]. Another possibility is the reaction between metal alkoxides and acetic anhydride, which has been used to prepare TiO_2 [27]. Acetamide elimination has been recently developed by Pinkas and coworkers to prepare metasilicates ($\text{M} = \text{Ti, Zr, Al, Sn}$) [85-89]. This reaction mechanism involves the condensation between silicon acetates and metal amides.

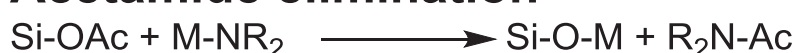
Ether elimination



Ester elimination



Acetamide elimination



Scheme 1.3 Non-hydrolytic condensation involving ether, ester and acetamide elimination.

1.2 Lithium-ion batteries (LIBs)

The battery concept is not a recent one, it started with the works of Alessandro Volta and Luigi Galvani in the beginning of the 19th century. Batteries are devices providing two main functions: supply and storage of energy. They are composed by two current collectors (positive/negative), two active materials (anode and cathode), a separator and an electrolyte [90].

Figure 1.2 shows the components in the particular case of a lithium-ion battery (LIB). The anode is traditionally composed of graphite (or a carbonaceous material), a lithium metal oxide is used as cathode (*e.g.* LiCoO_2 or LiFePO_4) and a solution of a lithium salt in a mixture of organic solvents as electrolyte (*e.g.* LiPF_6 in propylene carbonate, ethylene carbonate, and dimethyl carbonate –PC:EC:3DMC–). It is important to mention that a separator prevents short circuit in the battery [91].

In a battery, the external circuit provides the electron transfer and simultaneously there is an ion transfer via the electrolyte to ensure the electroneutrality of the system. Those transports correspond to redox reactions. Therefore, when a reaction finishes the electron transport also ceases. If the battery exhibits reversibility of the process by applying an external current (*i.e.* rechargeable battery) it is called a secondary battery; that is the case of Li-ion batteries that are also known as “rocking-chair” batteries [92, 93].

Li-ion batteries were not the first lithium batteries to be produced. The use of lithium in a battery system was firstly proposed in a 1949 patent [93]. However, the development of lithium battery investigations started in 1962 using MnO_2 and metal Li as electrodes (cathode

and anode respectively). One decade later, SANYO Inc. began their commercialization. Those batteries presented severe issues, principally explosions due to overcharging, overheating, short circuit due to the formation of Li dendrites (*i.e.* they pierce the separator) and poor Coulombic efficiency (*i.e.* short life cycle) [92, 94]. The solution to this problem arrived with the modification of electrodes, notably the abandon of metal Li anodes. Thus, lithium battery technology moved towards other anode materials that could allow the lithium intercalation/deintercalation processes, having lower production costs and higher capacities. Thus, in 1991, Sony Inc. gave birth to the first commercial Li-ion battery using LiCoO_2 and carbon as electrodes (*i.e.* cathode and anode respectively) [90, 92].

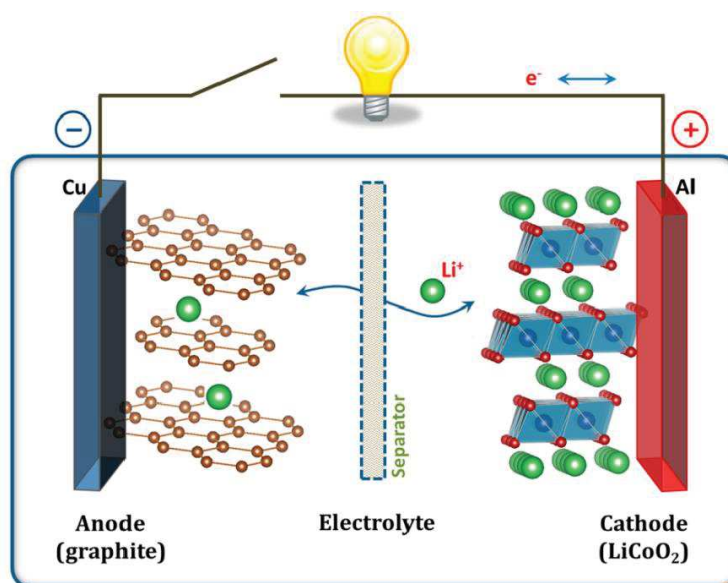


Figure 1.2 Scheme of components of Li-ion batteries. Figure taken from [95].

Materials used as electrodes in Li-ion batteries exhibit different work potentials as observed in Figure 1.3. The Li-ion potential of the battery corresponds to the difference between the potential of the electrodes (*i.e.* cathode and anode) *versus* Li^+/Li . It is noteworthy that anode materials exhibit a huge difference in capacity as compared with lithium metal. Besides, as graphite has been the classical anode material and it does not contain any lithium, cathodes needed to be also the lithium source. Thus, researches moved to the development of lithium based intercalation compounds to be employed as cathodes [96].

Concerning the electrolyte, Li-ion batteries broke the use of aqueous electrolytes due to the high reactivity of lithium with water, leading thus to the use of organic based electrolytes. This organic electrolyte contains from two to four carbonate based solvents because they are aprotic, polar and have a high dielectric constant allowing the formation of high concentration lithium salt solution. Regardless the nature of the other carbonate species, the presence of ethylene carbonate (EC) is necessary because it ensures the reversibility in the anode. EC decomposes at the anode forming a passivation layer; also known as surface electrolyte interface (SEI), during the first cycle. This layer prevents the co-intercalation of the other solvent molecules into the anode leading to exfoliation or disintegration of the electrode. Therefore, only Li^+ could intercalate into the active material. SEI is also responsible for capacity loss between the first and second cycle [92]. Those side reactions consume accessible lithium giving capacity fade during cycling [97].

It is worthy to mention that electrolyte also contains some additives that help to improve the electrochemical performance of Li-ion batteries. They usually do not exceed 5% of the

electrolyte (in either weight or volume). Additives possess different functions such SEI forming improver, cathode protection agent, salt thermal stabilizer, safety protection agent (*i.e.* overcharge protector and fire retardant agent) and ionic conductivity enhancer among others [98].

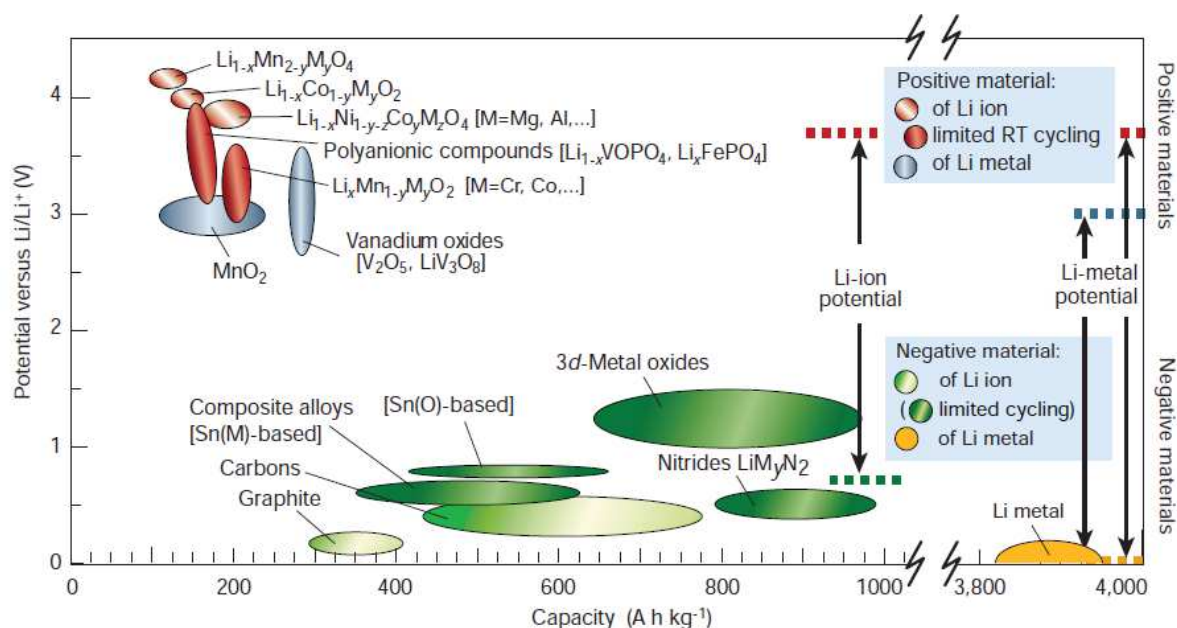


Figure 1.3 Voltage *versus* capacity for positive- and negative-electrode materials used in Li-based cells. The output voltage values for Li-ion cells and Li-metal cells are also represented. Figure taken from [96].

Li-ion batteries are characterized by having high specific energy and power density, a good efficiency and long life cycle. Moreover, Li-ion batteries will continue to dominate the portable storage market for the years to come. In fact, Li-ion batteries are considered as the best option to guarantee the supply of energy for the electric (EVs) and hybrid-electric vehicles (HEVs), even if for those practical applications, Li-ion batteries will need to provide at least twice the energy supplied by the actual technology [99]. The employment of Li-ion batteries in EVs and HEVs will limit CO₂ emissions and thus provide a better control of pollution emissions. Unfortunately, some issues may limit their applications. Two of them are: (1) the electrolyte solution which displays a narrow stability domain limiting the use of high voltage cathodes and (2) cost of production because of some cathodic compounds (*e.g.* cobalt) [91, 100]. Therefore, efforts need to be devoted to develop new cheaper and environmentally friendly electrode materials with good cyclability, high Li⁺ diffusion coefficient, good ionic and electronic conductivity and reversible capacity. Thus, progress in Li-ion batteries technology towards robust systems increasing energy and power density will be ensured and, also, the new market demands will be satisfied.

1.2.1 Negative electrode materials

Ideally, the perfect anode for Li-ion batteries must be composed of low weight compounds with low density that can intercept large amounts of Li per unit. Besides, it must be cheap, environmentally friendly, have good electronic and ionic conductivity, a good life cycle with stable and reversible capacity. Nevertheless, electrode materials should not be neither soluble nor reactive with the electrolyte compounds and they could operate at a potential as close as possible as the metal lithium one [101]. Unfortunately, this material does not exist yet.

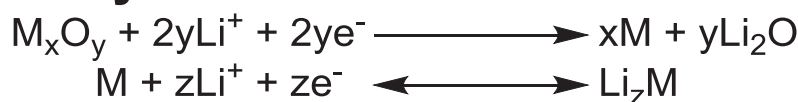
Historically, graphite has been used as anode material in Li-ion batteries and it continues to be used industrially because it fulfills most of the requirements for an ideal Li-ion battery anode. Graphite presented an abundant option to replace metal lithium anodes in early lithium battery technologies given that its laminar structure facilitates the lithiation/delithiation processes. Nevertheless, graphite capacity is based on the formation of LiC_6 which is relatively low ($372 \text{ mAh}\cdot\text{g}^{-1}$). Therefore, researches started looking for other materials that could improve the electrochemical performances of Li-ion batteries. Nowadays, there is a wide range of possibilities of active materials with potential applications as anodes for Li-ion batteries, as can be seen in Figure 1.3. Amongst this variety of choice, transition metal oxides have attracted scientific interest due to the higher capacities they could reach and low cost processes [102].

Not all anode materials for Li-ion batteries operate in the same way during the lithiation/delithiation processes; in fact, reactions involved in those processes are different depending on the nature of the active material. Therefore, anodes can be classified according to their reaction mechanisms into conversion, alloy or intercalation materials [99, 102]. All three mechanisms (shown in Scheme 1.4) have in common that Li^+ are the only ions involved in reactions.

Conversion



Alloy



Intercalation



Scheme 1.4 Reaction mechanisms observed in anodes for Li-ion batteries.

Lithiation/delithiation mechanisms also involve structural modifications as observed in Figure 1.4. A brief description of characteristics and common materials of the three anode categories will be detailed hereafter.

The first class, conversion reaction electrodes, corresponds to binary transition metal compounds (*i.e.* M_aX_b –M=transition metal, X= O, S, P, F, N–) which give metallic nanoparticles encrusted into Li_yX matrix after reacting with Li [92, 103]. One of the pioneer works in this field correspond to the research of Poizot *et al* [104] who started the use of transition metal oxides this way. They demonstrated the formation of metallic nanoparticles embedded into a lithia (Li_2O) matrix. One issue observed in this kind of electrodes is the presence of a large volume change during lithiation/delithiation processes. This strong structural modification leads to the pulverization of the electrode. Besides, this kind of materials evidences strong electrochemical hysteresis giving as a result poor cyclability. Strategies trying to enhance conversion materials consist in structuring materials at the nanoscale; the aim is to improve the strain relaxation and limit the expansion/shrinkage of the anode. Another option is the application of hollow materials where the void space can be advantageous towards volume changes [102, 105, 106].

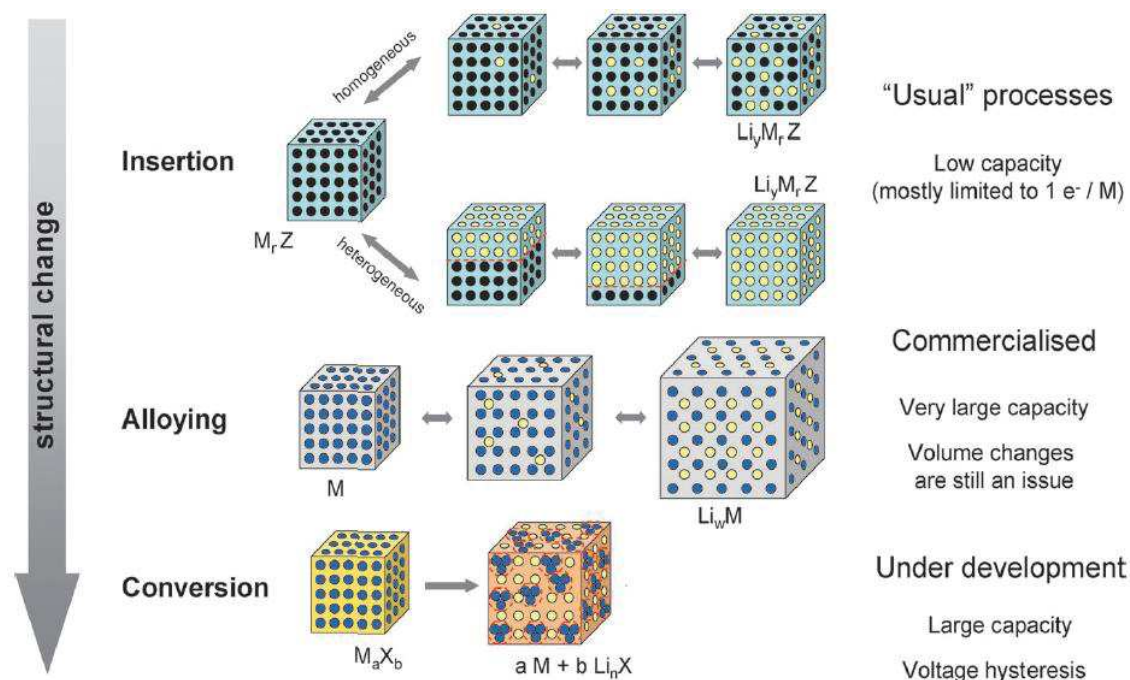


Figure 1.4 Structural changes observed during lithiation/delithiation processes in Li-ion batteries electrodes; black, blue and yellow circles correspond to voids in crystal structure, metal and lithium respectively. Figure taken from [92].

The second mechanism concerns alloy type materials. Elements of group IV and V such as Si, Ge, Sn, Pb, P, As, Sb and Bi have been studied as anodes for Li-ion batteries due to their capacity to form alloy phases with lithium, most of them at ambient temperature [107-111]. This category includes two processes. The first one concerns the reduction of the oxide to the respective metal to conform, in a second process, an intermetallic compound (*i.e.* Li alloy; Scheme 1.4). One must keep in mind that the first process is irreversible and leads, as a consequence, to capacity loss during the first cycle [101]. Those materials offer higher capacities than graphite (*e.g.* $4212 \text{ mAh} \cdot \text{g}^{-1}$ for a fully lithiated lithium-silicon alloy $\text{-Li}_{4.4}\text{Si}$ versus $372 \text{ mAh} \cdot \text{g}^{-1}$ for graphite [105]) and even higher than intercalation type materials [112-114]. However, they have several issues concerning life cycling. Apart from huge irreversible capacity during the first cycle; they also suffer a large volume expansion ($\sim 400\%$) during lithiation/delithiation processes [91, 107]. It has been proven SEI formation in alloy type anodes, agglomeration of alloy particles and lithium trapped in the host due to slow release kinetics. All these factors lead to a progressive decohesion and finally the disintegration of the electrode (*i.e.* capacity fade) [92, 97, 103, 113]. Although, efforts have been made to reduce volume change, it remains the biggest issue for alloys materials.

The last category, intercalation type materials includes principally carbonaceous materials, which were the first ones to be used in Li-ion batteries, and titanium oxides. Those materials are the most used in market today due to the simplicity and reversibility of reactions involved during lithiation/delithiation processes. They also exhibit the less structural and volume modification (*i.e.* major issue of the other mechanisms) because of the topotactic nature of the Li^+ insertion mechanism (*i.e.* Li^+ guest incorporates into the crystal host without involving severe crystal modifications). Thus, the active material must be crystalline and possess empty spaces (*i.e.* vacancies, channels or layers into the framework) in order to satisfy the requirements for topotactic reactions [101, 108, 115].

Carbonaceous materials are generally conformed by carbon more or less graphitized and their structure consists of graphene-based layers serving as host for Li^+ . Electrochemical performance of those materials will depend on the morphology, crystallinity degree and in some cases even on the electrolyte composition (*e.g.* promoting SEI formation). An increment of the distance between the graphene-based layers ($\sim 10\%$) can be observed during lithium intercalation. This volume change is negligible as compared with the alloy type electrodes [108]. Despite of abundance, low cost and good electrochemical performance of this electrode material; graphite presents, as mention before, some weakness (*e.g.* low power density) that need to be solved.

Table 1.2 Summary comparing common materials used as Li-ion batteries anodes according to their type classification; advantages and disadvantages are also presented. Table based on reference [99].

Anode Classification	Common Active Materials	Advantages	Issues
Conversion	Transition metal oxides (Fe_2O_3 , CoO , Mn_xO_y , etc)	High capacity High energy Low cost Environmentally friendly	Low Coulombic efficiency Unstable SEI formation Large potential hysteresis Poor cycling
	Metal phosphides/sulfides/nitrides (MX_y , $\text{M}=\text{Fe}$, Mn , Ni , Cu , Co and $\text{X}=\text{P}$, S , N)	High specific capacity Low operation potential Low polarization	Poor capacity retention Poor cycling High cost
Alloy	Si , Ge , Sn , Sb , SiO , SnO_2	High specific capacity High energy density	Large irreversible capacity Important capacity fading Poor cycling
Intercalation	Carbonaceous (hard carbon, carbon nanotubes and graphene)	Good working potential Low cost Good safety	Low Coulombic efficiency High voltage hysteresis High irreversible capacity
	Titanium oxides (LiTi_4O_5 and TiO_2)	Extreme safety Good life cycle Low cost High power capability	Low capacity Low energy density

Regarding titanium dioxides, there are two major candidates that work with the redox couple $\text{Ti}^{4+}/\text{Ti}^{3+}$: titanium dioxide (TiO_2) and lithium titanium oxide ($\text{Li}_4\text{Ti}_5\text{O}_{12}$), commonly called LTO. The case of TiO_2 will be discussed in detail in section 1.3. Briefly, 3D organization of TiO_6 octahedra, conforming TiO_2 , creates interstitial sites or channels where Li^+ can intercalate/deintercalate. TiO_2 exhibit a work potential between 1.5 and 1.8 V *versus* Li^+/Li and it presents only lesser modifications in its crystal structure [101, 116]. Concerning LTO, it exhibits a spinel structure, possesses a theoretical capacity of $175 \text{ mAh}\cdot\text{g}^{-1}$ and can intercalate up to 3 mol of Li per LTO unit (*i.e.* Li^+ occupies tetrahedral and octahedral sites of LTO

crystal structure). LTO exhibit a potential work at around 1.5 V *versus* Li⁺/Li with small hysteresis between charge/discharge processes and it is also consider the “zero-strain” material due to the almost null variation of its lattice parameters during such processes. Those characteristics bring it good stability and a long life cycle; however, it also suffers from low electronic conductivity [101, 117].

Finally, Table 1.2 summarizes the different categories of anodes materials for Li-ion batteries, with some examples, advantages and disadvantages.

1.2.2 Towards ideal anode mterials for lithium-ion batteries

Each of the three anode classes presented above exhibits different advantages that may cover the issues of the other two. Unfortunately, as mention before, nowadays it does not exit a perfect electrode material that fully satisfies the characteristics of safety and electrochemical performance for Li-ion batteries towards high energy applications. Thus, efforts must focus on the improvement of these two characteristics. Different general strategies have been commonly applied in designing more attractive active materials for anodes, regardless of their category (*e.g.* use of carbon –coatings or composites– for enhancing electronic conductivity).

The first common approach is the design of hollow, porous or hierarchical structure materials. These structures can provide high specific capacity, superior rate capability, and improved cycling performance. They possess low density and high surface area promoting more lithium storage sites and promoting a larger contact area between the electrode and the electrolyte. Thus, the Li⁺ flux is enhanced. This kind of structures has also been used to limit volume changes during lithiation/delithiation processes, notably for alloy and conversion anodes [118, 119]. In most cases, it is necessary to use sacrificial templates, which may be difficult to remove, in order to obtain this kind of structure materials [120]. For instance, Wang *et al* [119] and Shen *et al* [121], both teams prepared TiO₂ hollow spheres using carbon and cetyltrimethyl ammonium bromide –CTAB– as templates respectively. The use of templates is common but not mandatory as demonstrated by different template free synthesis methods (*e.g.* Ostwald ripening mechanism [106, 122]).

The nanostructuring approach consist in synthesizing materials at the nanoscale (*i.e.* nanoparticles, nanowires, etc.). This methodology offers the advantage of enabling some reactions that cannot take place in the bulk material. It also reduces the diffusion path enhancing the lithium and electron transport within the particles. In fact, decreasing the particle size results in an increment of surface area that boosts the formation of active sites for lithium ions. Another advantage lies in a quicker stress relaxation of particles making them more resistant to fracture than their bulky counterparts. Moreover, in some cases, nanoparticles chemical potential may differ from the bulk material; thus, the electrode potential will also change enhancing the specific capacity. However, nanoparticles may be more difficult to synthesize and the increment of surface area may introduce additional side reactions [99, 105, 123]. For instane, it has been reported the use of different oxide nanowires as electrodes for Li-ion batteries (*e.g.* TiO₂ [124, 125], SnO₂ [126], V₂O₅ [127], Co₃O₄ [128]).

Furthermore, the doping strategy may improve the electrochemical performance of the active material. Doping is preferred for materials that suffer from poor electronic conductivity such as LTO and TiO₂. It involves an alteration of the crystalline structure by adding other atom elements into the atomic framework by creating vacancies or modifying the oxidation state of the base material (*e.g.* mixture of Ti⁴⁺ and Ti³⁺ in LTO and TiO₂) in order to guarantee the charge balance. Doping approach usually uses, but not exclusive, transition metal cations.

Some examples of doping elements are: N [129]; Al [130]; S[131]; V [132]; Cr [133]; Fe [134]; Ni [135]; Cu [136]; Zn [137]; Br [138]; Zr [139]; Nb [140]; Sn [141]; Ta [142]. It is also feasible to use two or more elements as co-doping agents (*e.g.* one dopant creates vacancies while another promotes oxidation state modifications). In addition, it is important to keep in mind that, as there is a structural modification, Li⁺ intercalation process may also be affected (*i.e.* a slight reduction in capacity) [117, 143].

The last approach involves the use of carbon as electronic conductivity enhancer. This strategy is not limited to graphite coatings; it also includes carbon composites and hybrid materials using carbon of different nature (*i.e.* graphene, fullerenes, carbon nanotubes –CNT–, amorphous carbon and graphite). Carbonaceous coatings represent an easy option to follow this approach; it offers the possibility to improve the electronic conductivity of active materials without any internal structure modification (*i.e.* unlike doping). In the case of conversion anodes, C-coating also helps to adjust the strain of volume changes during lithiation/delithiation processes [102]. While, for alloy type materials, it has been proved to have a beneficial effect enhancing the electrode life cycle [144-148]. Coatings can also prevent agglomeration of particles during synthesis or inhibiting particle growth (*i.e.* keep nanosize) [149, 150]. Those coatings generally need an organic precursor than latter is transformed into carbon by pyrolysis under inert atmosphere and their thickness must be controlled in order to successfully achieve good electrochemical performances [102]. Carbon coating strategies have even been employed onto graphite spheres; those works aimed the formation of SEI over the coating instead over the graphite particle (*i.e.* inter-particle SEI) to have better yields [151-153]. On the other hand, concerning the other branch of this approach (*i.e.* hybrid and composite materials); carbon (graphene or CNT) may function as a template nuclei for growing metal oxides crystals [150, 154]. In addition, the carbon approach has been used to create hybrid capsule materials such carbon nanofibers encapsulated into carbon nanotubes [155] or carbon encapsulated into titania nanotubes [156]. It is worthy to mention that, as seen for the former examples, combination of different strategies is possible in order to optimize performances.

1.3 Titanium dioxide (TiO₂)

Titanium dioxide (TiO₂), also known as titania, has been an interesting material for applications in different areas. TiO₂ particles have been used as white pigments, ultraviolet (UV) light absorbers and/or thickeners in cosmetics, skin care products, food and paints [157]. One may search on the web and find more than 500 000 references containing at least one item related to this oxide (TiO₂, titania or titanium dioxide –research via Scifinder, April 24th 2017–). But, why has this material been so widely explored?

Firstly, in a world where the natural abundance of resources is limited, it becomes of utmost importance looking through the most available ones to benefit the most. Titanium (Ti) is the ninth most abundant element on Earth [158]; its oxide conforms approximately 0.65 wt% of the upper continental crust. That makes of it one amongst the ten major oxides presented on the Earth crust [159].

TiO₂ properties have made of it a versatile material. It presents a high refractive index ($n=2.49$ to 589 nm for TiO₂ anatase [160]) and it is known to be good degrading pollutants, due to its good chemical stability and excellent oxidative properties. However, its efficiency is limited to ultraviolet irradiation [161-163]. In order to enlarge it under natural sunlight (5% ultraviolet, 43% visible and 52% infrared [164]) efforts have been focused on narrowing its

band gap energy to extend the absorption range into the visible region [161]. Interestingly, TiO_2 has also been considered a promising substitute to replace graphite anodes in Li-ion batteries, mainly due to its competitive theoretical specific capacity ($335.6 \text{ mA.h.g}^{-1}$ corresponding to the insertion of 1 Li per $\text{TiO}_2 -x$ in the reaction of Scheme 1.5– and to the complete reduction of Ti^{4+} into Ti^{3+} [91]), low cost and good chemical stability [165, 166].



Scheme 1.5 Reaction of lithiation/delithiation processes of TiO_2 ; x taking values between 0 and 1.

Research-wise, considerable efforts have been devoted to controlling various parameters such as morphology, particle size, crystallinity and porosity. Such structural control opened new perspectives in terms of applications, ranging from photovoltaic cells and photocatalysis to biomedical applications and energy storage devices [157].

1.3.1 Polymorphs

Titanium dioxide crystals are composed by TiO_6 octahedra which could be organized in different arrays depending on the connections between them. Those different arrays are called polymorphs and all of them present the same chemical composition varying only in the crystal structure. Titania can be found in nature under three different forms (rutile, anatase and brookite); it is noteworthy to mention that rutile is the stable phase while the others are metastables ones. The other polymorphs are high synthetic metastable phases, they cannot be found in nature and require high pressure synthesis techniques in order to be obtained [167]. Interestingly, properties and applications of TiO_2 strongly depend on its crystal structure. Structure of most common TiO_2 polymorphs are presented in Figure 1.5, one may easily observe the differences between the different arrays.

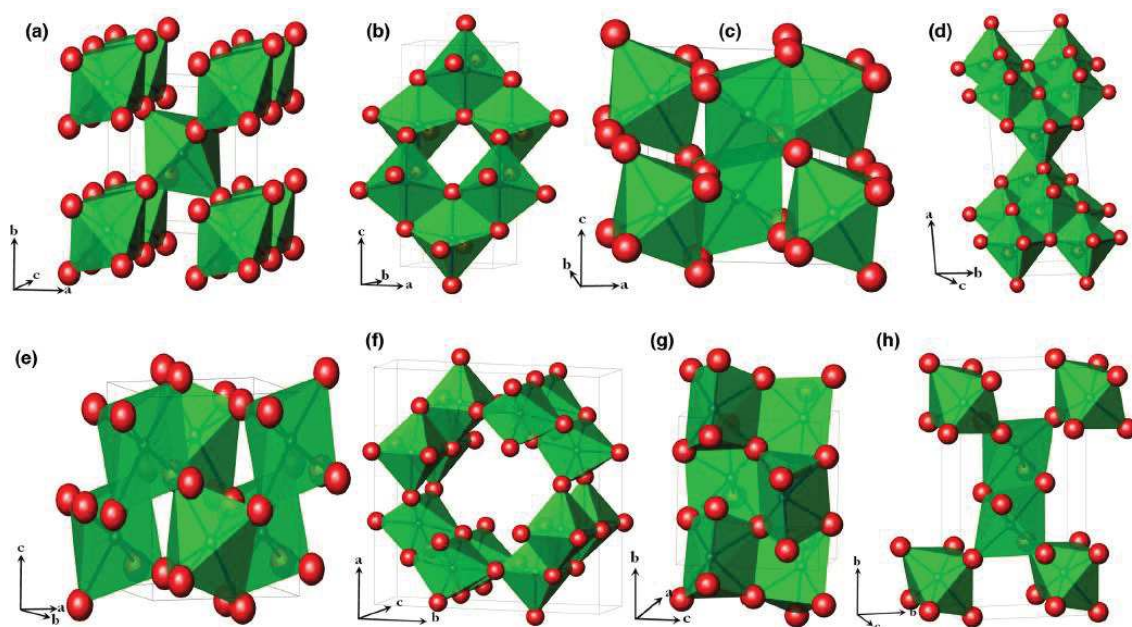


Figure 1.5 Crystal structures of (a) Rutile, (b) Anatase, (c) Bronze, (d) Brookite, (e) Columbite, (f) Hollandite, (g) Baddeleyite, and (h) Ramsdellite phases; red spheres correspond to oxygen, titanium is inside green octahedra. Figure taken from [168].

TiO₂ rutile, anatase and bronze crystal phases have been largely studied for Li-ion batteries applications (*i.e.* as anode material); brookite has also been investigated but in lesser measure. All TiO₂ polymorphs are active for the lithiation/delithiation processes following the reaction presented in Scheme 1.5. Their octahedra arrays have unoccupied sites that are available for Li⁺ insertion. However, as crystal structure differs among them, they display different host lattices for the insertion of lithium and different working potentials between 1.5-1.8 V *versus* Li⁺/Li [169-171].

Rutile is, as mention before, the most thermodynamically stable form of TiO₂. Its structure forms c-axis channels which favour Li⁺ diffusion; as a consequence, diffusion in the ab plane is slow and poor. This characteristic makes Li⁺ diffusion highly anisotropic, thus explaining the lower electrochemical performance *versus* Li⁺/Li of rutile comparing with the other two TiO₂ polymorphs (*i.e.* anatase and bronze) [168, 171, 172]. Nevertheless; rutile nanostructures have been proven to insert more Li⁺ than their micro-sized counterparts, thus improving the capacity [170, 173-176].

Anatase is a metastable phase of TiO₂ that transforms irreversibly to rutile at temperatures above 750 °C. There is a wide transformation range due to different parameters such as particle size, surface area, heat treatment atmosphere, impurities, doping and synthesis method. In addition, conversion into rutile is accompanied by shrinkage of around 8% due to the reconstructive nature of this transformation (*i.e.* breaking and reforming bonds) [177-180]. This polymorph has been used not only in the storage energy field; it has been claimed to be the most photoactive polymorph with a slightly bigger band gap of 3.2 eV comparing to the 3.0 eV of rutile phase [181, 182]. Coming back to electrochemistry, anatase is considered as one of the most promising candidates, among TiO₂ polymorphs, to be used as anode in Li-ion batteries. Besides, computer simulation studies have also confirmed the superiority of TiO₂ anatase over other polymorphs as the most stable host for lithium ions, due in particular to its high stability during lithiation process [183].

Lithium diffusion through anatase structure consists of a multi-step reaction; firstly there is a drop of potential from the open circuit to around 1.7 V *versus* Li⁺/Li corresponding to the formation of a solid solution between TiO₂ and lithium (Li_xTiO₂; x<0.5). Then, potential stabilizes forming a flat plateau characteristic of a two-phase reaction between the tetragonal solid solution compound and the orthorhombic lithium titanate (Li_{0.5}TiO₂) to finally lead to the formation of LiTiO₂ phase after another two step reaction (pseudoplateau at *ca.* 1.5 V *versus* Li⁺/Li) [184-186]. It is worthy to mention that nanostructures enhance more lithium insertion into TiO₂ as observed in the phase diagram presented in Figure 1.6(a). Wagemaker *et al* [184] also demonstrated that the coexistence or differentiation [(α+β) or (α)+(β) respectively] of both phases (*i.e.* TiO₂ and LiTiO₂) within one crystalline particle strongly depends on the particle size. In addition, Figure 1.6(b) illustrates the lithiation process for anatase TiO₂ described above.

The last polymorph discussed in this section correspond to the bronze phase –TiO₂(B)–; it was synthesized for the first time by Marchand *et al* [187] at 1980 and it is commonly obtained by hydrothermal methods. This synthetic metastable phase may transform into anatase phase, if heated enough [169]. TiO₂(B) exhibits lower density than anatase or rutile and a more open framework with a perovskite like layer structure offering an open channel along the b-axis. Presence of this axis promotes fast Li⁺ diffusion. TiO₂(B) exhibits a potential work at 1.5 V *versus* Li⁺/Li that is lower than anatase. This array possesses an unit cell with 8 Ti sites and 10 Li⁺ sites leading to a theoretical capacity of 1.25 Li⁺ per TiO₂(B) (instead of 1). However, due to Li⁺–Li⁺ repulsions only 8 Li⁺ sites are available leading to the same

theoretical capacity as anatase or rutile and its lithium insertion mechanism is not completely understood [188, 189].

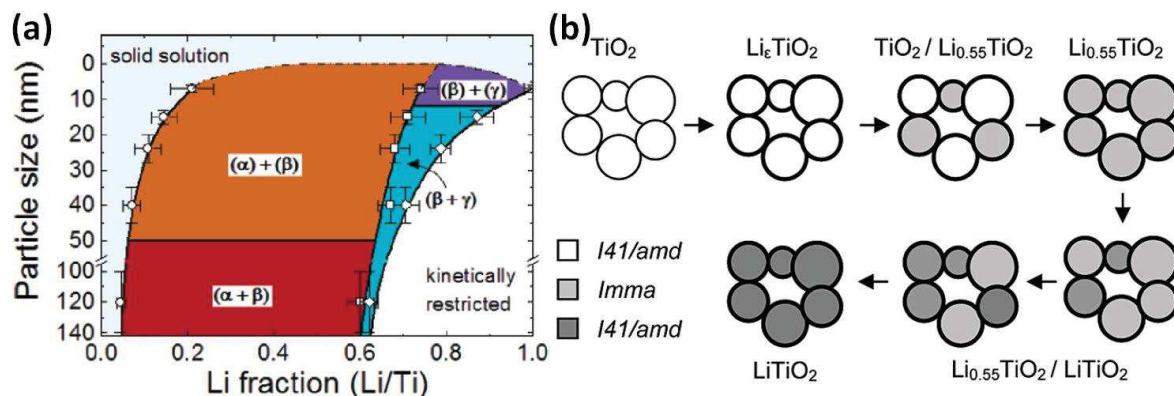


Figure 1.6 (a) Phase diagram of the Li composition in TiO_2 anatase as function of particle size (α , β and γ correspond to anatase, lithium titanate and LiTiO_2 respectively); and (b) scheme of phase transition upon Li insertion in anatase TiO_2 . Figures taken from [184] (a) and [185] (b).

Finally, a summary of structural and electrochemical properties of the different TiO_2 crystal phases is presented in Table 1.3. It also includes the other polymorphs not discussed in this section for comparison.

Table 1.3 Structural and lithiation properties of TiO_2 polymorphs. Table based on references [168, 190].

Polymorph	Space Group	Density ($\text{g} \cdot \text{cm}^{-3}$)	Lattice parameters	Lithiation for bulk material	Lithiation for nanomaterial
Anatase	Tetragonal $I4_1/amd$	3.79	$a=3.79$ $c=9.51$	0.5	1.0
Rutile	Tetragonal $P4_2/mnm$	4.13	$a=4.59$ $c=2.96$	0.1	0.85
Brookite	Orthorhombic $Pbca$	3.99	$a=9.17$ $b=5.46$ $c=5.14$	0.1	1.0
TiO_2 -B (Bronze)	Monoclinic $C2/m$	3.64	$a=12.17$ $b=3.74$ $c=6.51$ $\beta=107.29^\circ$	0.71	1.0
TiO_2 -II (Columbite)	Orthorhombic $Pbcn$	4.33	$a=4.52$ $b=5.5$ $c=4.94$	---	---
TiO_2 -H (Hollandite)	Tetragonal $I4/m$	3.46	$a=10.18$ $c=2.97$	---	---
TiO_2 -III (Baddeleyite)	Monoclinic $P2_1/c$	---	$a=4.64$ $b=4.76$ $c=4.81$ $\beta=99.2^\circ$	---	---
TiO_2 -R (Ramsdellite)	Orthorhombic $Pbmn$	3.87	$a=4.9$ $b=9.46$ $c=2.96$	---	---

1.3.2 State of art of TiO₂ as anode for Li-ion batteries

Despite plethora of reports, pure TiO₂ –either of its polymorphs– struggles with fulfilling the needs of emerging high energy applications. TiO₂ presents both poor electronic conductivity ($10^{-12} < \sigma < 10^{-7} \text{ s}\cdot\text{cm}^{-1}$ [191]) and low ion diffusion coefficient ($10^{-14} < D_c < 10^{-6} \text{ cm}^2\cdot\text{s}^{-1}$ [192-195]) [137, 140, 171]. In this context, doped TiO₂ and TiO₂-based nanocomposites have been of valuable interest in order to make it competitive for energy storage applications [102, 143, 196, 197].

As discussed before, doping aims to improve the electronic conductivity of the active material (*i.e.* TiO₂ anatase) by the creation either of vacancies or a mixture of Ti⁴⁺ and Ti³⁺ oxidation states. The electronic conductivity of TiO₂ depends on the oxygen vacancies and interstitial metal atoms in the framework. Thus, introducing higher valence elements like vanadium (V⁵⁺) should promote the reduction of Ti⁴⁺ to Ti³⁺, enhancing thus the electronic conductivity of TiO₂. During the last two decades, researches have used different atoms as doping agents (see section 1.2.2). Only few reports using vanadium have been found for this particular application (*i.e.* V-doped TiO₂ and TiO₂-V₂O₅ mixed oxides has commonly been used for catalyst applications). For instance Anh *et al* [132] and Reddy *et al* [143] added this element into the TiO₂ structure using solvothermal and molten salts synthesis methods respectively.

Alternatively, few groups proposed to use the non-hydrolytic sol-gel (NHSG) route to prepare TiO₂, TiO₂-based mixed oxides and nanocomposites. The special feature of NHSG routes lies in the fact that they allow the synthesis of metal oxides through the use of organic oxygen-donors (typically alcohols and ethers) instead of water. NHSG chemistry is rather versatile and has been seen as a simple surfactant-free route to obtain mesoporous metal oxides without any template; an interesting point since hollow and porous structures enhance lithium diffusion (see section 1.2.2). Besides, NHSG presents the main advantage of allowing the synthesis of mixed oxides in a one-step process, unlike its hydrolytic counterpart [4, 19, 20, 22].

When aiming at improving electrons transport, the coating of TiO₂ onto highly conductive carbons has been very favored. Particularly, with the emergence of nanocarbons, the coating of TiO₂ layers onto carbon nanotubes [198] and graphene-based [199-201] materials has been widely investigated. The other way round, *i.e.* the coating of carbonaceous layers onto TiO₂ particles, has been also largely studied. Such coatings should be homogenous and thin in order to allow Li ion diffusion through the carbon layer. It was demonstrated that the homogeneity of the carbon coating rather than the carbon/titania ratio plays a key role in tuning electrochemical performances [202-204]. Even though commercial TiO₂ particles are commonly used [205-208], the synthesis of original TiO₂ particles and the subsequent coating using various carbon precursors has been widely developed [209, 210]. A large variety of carbon precursors has been reported such as sucrose [211, 212], glucose [213, 214], poly(vinyl pyrrolidone) [215], dopamine [216], pyrrole [217], nanocellulose [218] and ethylene [219]. However, such multi-step strategies often involve a large excess of carbon precursors and suffer from rather inhomogeneous carbon coating. Besides carbon precursors, co-polymers and/or surfactants are usually necessary to generate mesoporous and/or nanostructured particles, involving extra costs.

Regarding the specific case of TiO₂-carbon composites, NHSG has been sporadically employed. For instance, Wang *et al* [220] used titanium (IV) chloride and anhydrous ethanol as oxygen-donor and carbon precursor. In this direct approach, neither extra surfactant nor solvent were necessary. Interestingly, the authors claimed the formation of C-doped TiO₂ as a result of the diffusion of the carbon atoms during calcination. More recently, Tahir *et al* [202]

reported on the *in situ* polymer functionalization of carbon-coated TiO₂ particles obtained via an alcohol NHSG route. Besides titanium (IV) chloride, benzylalcohol (oxygen-donor) and DMF (solvent), block copolymers were employed as carbon precursors. The presence of both chelating ligands (*i.e.* hydroxymate) to coordinate titanium cations and graphitizable blocks (*i.e.* polyacrylonitrile) allowed obtaining uniform and homogeneous carbon coating. In addition, in the last example, as-synthesized composites were tested as anode materials for sodium-ion batteries.

Inspired by those reports two different approaches have been explored aiming the improvement of the electronic conductivity of NHSG derived TiO₂, either by synthesizing TiO₂-V₂O₅ mixed oxides or by preparing TiO₂/carbon nanocomposites forming a *in situ* carbon coating.

2 Experimental part: Synthesis, characterizations and evaluation of performances

This chapter, composed by two sections, firstly focuses on the principles of the main characterization analyses used for the materials prepared during this PhD thesis. The second part is dedicated to the materials, the protocols for synthesis and preparation of TiO₂-V₂O₅ mixed oxides and TiO₂/C nanocomposites which results are discussed in the following chapters and the characteristics and parameters of the equipment.

2.1 Principle of the main characterizations techniques

Three techniques were widely explored during this PhD thesis on the basis of the main characteristics of materials in which this project was focused on: crystal phase, surface area and specific capacity. As discussed in section 1.3.1, lithium insertion into titania structure depends on the crystal phase; thus a key parameter to be controlled by X-ray diffraction was the polymorphism of the samples, specially the TiO₂ anatase and rutile crystal phases. In addition, as discussed before, porosity of materials enhance the lithium diffusion/insertion processes inside the structures; this was checked by molecular nitrogen physisorption. The last characterization technique, considering that the aimed application was Li-ion batteries anodes, concerns the analysis of the electrochemical performance of the synthesized materials via electrochemical cycling.

2.1.1 X-ray diffraction

For instrument and methods effectively used, see section 2.2.5-Devices characteristics.

The X-ray diffraction technique is a powerful tool to determine the crystal structure of materials, their particle size and even the orientation of a single crystal into a polycrystalline framework. The X-rays were discovered in 1895 and their wavelengths are included into the 0.5-2.5 Å range; however, it was not until 1912 that a crystal was used for the first time as diffraction network and one year later W.H. and W.L. Bragg determined the first crystalline structure [221, 222].

X-rays are generated for the fast deceleration of an electrically charged particle with enough kinetic energy. In practice, X-ray tubes contains an electron source and two metallic electrodes; when a high voltage is applied between them, electrons are thrown towards the anode striking the target at high speed. Thus, X-ray are the result of this impact and they radiate in all directions. This process may generate two different kind of spectrum: the continuous and the characteristic spectrum. The first one appears as a result of the process previously described; while the characteristic one, only appears above a certain high voltage value. The characteristic spectrum evidences new maxima over the continuous spectrum and they are dependent of the electron source (*i.e.* they do not depend from the electron

deceleration as continuous spectrum); this characteristic lines, notably $K\alpha$ line, have allowed the development of the X-ray diffraction technique [221].

Crystals are composed by periodic arrays of atoms along the three dimensions of a plane. The X-ray diffraction phenomena is closely linked to the fact that the interatomic distances, in crystals, are in the same range than the X-rays wavelength. The direction of the diffracted beam follows the Bragg's law (Equation 2.1)

$$n\lambda = 2d \sin \theta \quad \text{Equation 2.1}$$

where λ correspond to the wavelength of the diffracted X-ray; d is the distance between atomic planes; θ is the angle formed by the incident beam and the scattering plane and n , an integer, gives the reflection order. Bragg's law can be demonstrated geometrically by analogy to the reflection phenomenon as observed in Figure 2.1 [221, 222]. Briefly; Equation 2.2 and Equation 2.4 can be geometrically obtained; then, as segments AB and BC are equals, Equation 2.3 is determined. Finally, mixing Equation 2.3 and Equation 2.4, Bragg's law is obtained.

$$\sin \theta = \frac{AB}{d} = \frac{BC}{d} \quad \text{Equation 2.2}$$

$$AB + BC = 2d \sin \theta \quad \text{Equation 2.3}$$

$$AB + BC = n\lambda \quad \text{Equation 2.4}$$

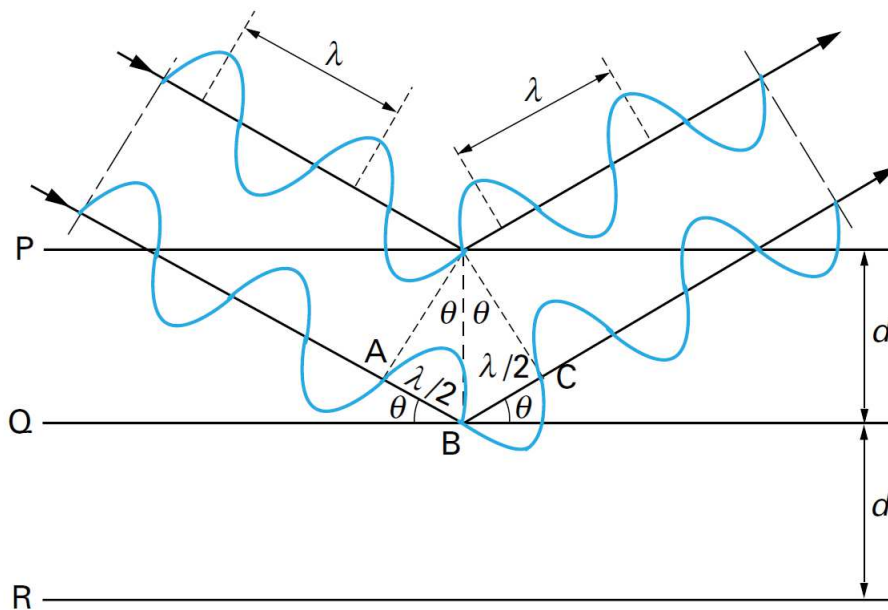


Figure 2.1 Scheme corresponding to Bragg's law. Figure taken from [222].

An easy method to determine crystallite size (L) was proposed by Scherrer as follows in Equation 2.5.

$$L = \frac{K\lambda}{\beta \cos \theta} \quad \text{Equation 2.5}$$

where K is a geometry factor which value is close to 1 (usually 0.9); β is full width at half maximum (FWHM); λ correspond to the X-ray wavelength and θ is the Bragg's angle [221, 222].

2.1.2 Molecular nitrogen physisorption

For instrument and methods effectively used, see section 2.2.5-Devices characteristics.

Pores can be defined as cavities or channels that appear inside materials (called porous materials). Their surface give part of the specific surface area of materials and they can be opened or closed (*i.e.* inaccessible for fluids). Aside from their shape, pores can be classified according to their width, assuming spherical or cylindrical shape: $\varnothing > 50$ nm pores are called macropores; $\varnothing < 2$ nm pores are known as micropores and $2 < \varnothing < 50$ pores are mesopores.

To measure this parameter, adsorption of molecules on the surface of the solid is the mostly used technique. This phenomenon can be described as the retention of atoms of a gas or liquid on the surface of a solid by physical or chemical interactions between the solid (*i.e.* adsorbent) and the fluid. However, only physisorption is used for textural characterization because it does not modify the properties of the solid. The opposite process, desorption, consist in the release of the adsorbed molecules. It is noteworthy that adsorption methods used for materials characterization only take into account the opened pores because they are the only accessible ones [223]. In the same idea, accessibility of a particular molecule will always depend of the pore size; this is why small molecules of chemically inert gas such as N_2 or Ar are generally used [223, 224].

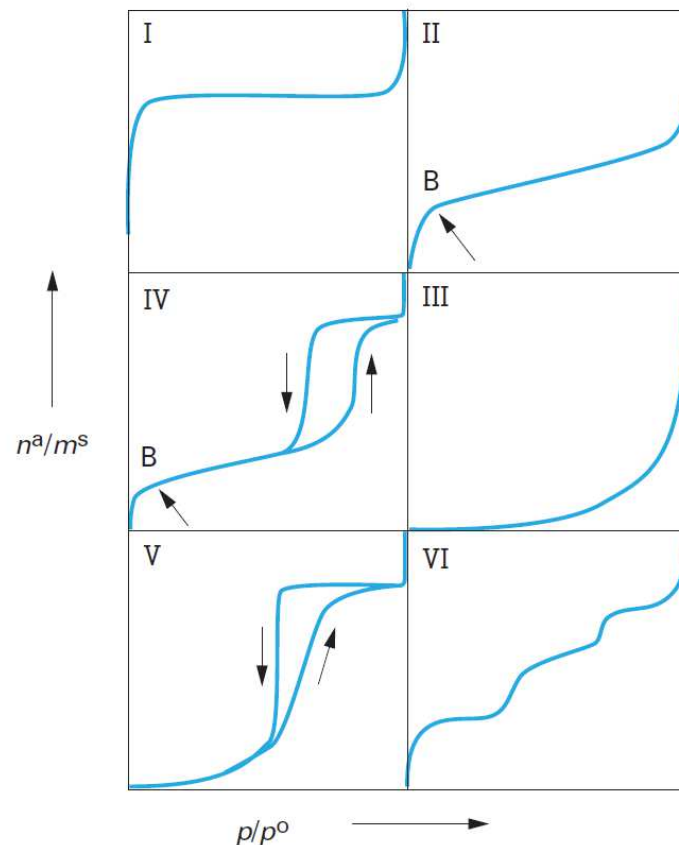


Figure 2.2 Classification of isotherms according to IUPAC. Figure taken from [223].

Physisorption isotherms classification, represented in Figure 2.2, was firstly used by Brunauer *et al* [225] in 1940 and then taken in by the IUPAC (International Union of Pure and Applied Chemistry) in 1985. Isotherms shapes give valuable information about textural characteristics of materials. Type I corresponds to strictly microporous compounds; they present an adsorbent saturation at low relative pressures. Type II is characteristic of non porous or

macroporous compounds and corresponds to a multimolecular adsorption. Type IV corresponds to mesoporous materials; this isotherm is characterized by a similar shape of isotherm of type II at low relative pressures ($P/P_0 < 0.42$ for molecular nitrogen) and saturation for higher relative pressures. Another feature of type IV is the presence of hysteresis due to the irreversible process of desorption of nitrogen condensed by capillarity into the mesopores. Shape, at low relative pressures, of type III and V isotherms evidences low interaction between the adsorbent and the fluid. The last isotherm (type VI) is characteristic of materials having homogenous surfaces forming adsorbing layers one after another [223, 224].

There are different adsorption theories; nevertheless, the Brunauer-Emmett-Teller (BET) one is the most widely used for textural characterization of porous materials. This theory is based on the formation of a monomolecular layer covering the whole surface of the adsorbent [226]. In brief, it states that multimolecular adsorption takes place on the basis of the Langmuir theory and takes into account that the surface may be represented as a set of superficies (S_N , $N=0, 1, 2$, etc.). In this set of superficies, N correspond to the number of layers of adsorbed molecules and those molecules may serve themselves as adsorbent sites for further ones, with no interaction between adsorbed molecules [227]. So, they established a relationship between the relative pressure ($x=P/P_0$) and the adsorbed amount of fluid (n^a) for a limited number of layers N (Equation 2.6).

$$\frac{n^a}{n_m^a} = \left(\frac{Cx}{1-x} \right) \left(\frac{1-(N+1)x^N + Nx^{N+1}}{1+(C-1)x - Cx^{N+1}} \right) \quad \text{Equation 2.6}$$

where n_m^a is the amount of fluid needed for covering the surface with a single molecular layer and C a constant linked to the adsorption energy for the first layer E_1 , the liquefaction energy of the adsorbable fluid E_L , the adsorption temperature T and the gas constant R (Equation 2.7).

$$C \approx \exp\left(\frac{E_1 - E_L}{RT}\right) \quad \text{Equation 2.7}$$

When the number of layers N tends to infinity, Equation 2.6 can be simplified in Equation 2.8.

$$\frac{n^a}{n_m^a} = \frac{Cx}{(1-x)(1-x+Cx)} \quad \text{Equation 2.8}$$

This equation is only valid for low relative pressures ($P/P_0 < 0.35$) and is more often used in its linear form (Equation 2.9) also named transformed BET equation where the only unknown values are C and n_m^a .

$$\frac{P/P_0}{n^a(1-P/P_0)} = \frac{1}{n_m^a C} + \left(\frac{C-1}{n_m^a C} \right) \left(\frac{P}{P_0} \right) \quad \text{Equation 2.9}$$

The specific surface area, S_{BET} , can be determined knowing the surface A of the adsorbent following Equation 2.10. Surface A , in turn, can be calculated once it is completely covered by a single layer of adsorbable fluid and also knowing the occupied surface by an adsorbed molecule σ_m ($\sigma_m = 0.162 \text{ nm}^2$ for the case of molecular nitrogen adsorbed at 77.4 K according to IUPAC).

$$S_{BET} = \frac{A}{m_a} = \left(\frac{n_m^a}{m_a} \right) N_A \sigma_m \quad \text{Equation 2.10}$$

with m_a being the adsorbent mass and N_A the Avogadro constant ($N_A = 6.023 \cdot 10^{23} \text{ mol}^{-1}$). Besides, n_m^a can be determined graphically using experimental data into the isotherm linear region (*i.e.* calculating the slope and the ordinate at the origin values with the transformed BET equation –Equation 2.9–).

The hysteresis shape, commonly observed in mesoporous materials, gives relevant information about the pores characteristics. For instance, Figure 2.3 shows the different hysteresis shapes according to IUPAC, H₁ and H₂ correspond to mesoporous compounds (*i.e.* type IV isotherms); H₁ is usually observed in materials with a narrow pore distribution; while H₂ evidences intercommunication amongst mesopores. H₃ appears in materials forming aggregates and H₄ is often correlated to laminar microporous materials; the two last shapes correspond to type II isotherms [223].

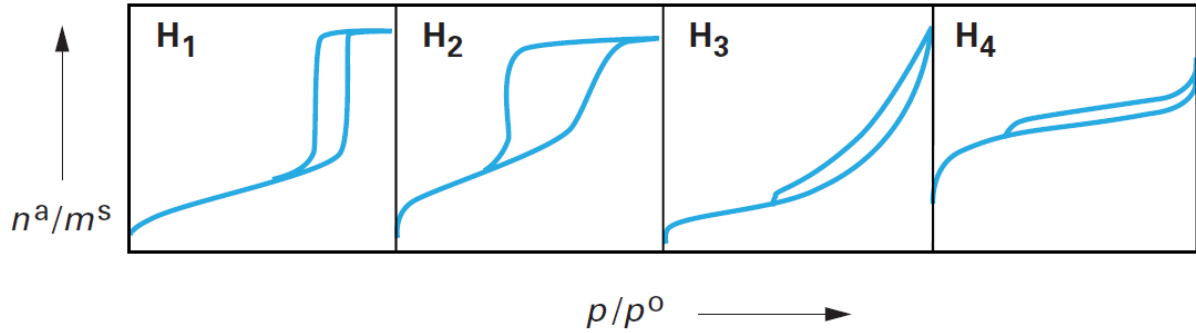


Figure 2.3 Hysteresis classification according to IUPAC. Figure taken from [223].

Finally, the molecular nitrogen physisorption technique also allows the determination of pore size. As seen for the adsorption theories, it also exists different methods to determine the pore size distribution; however, the Barret-Joyner-Halenda (BJH) method is the most widely used. It takes several assumptions such as porosity is constituted by independent, indeformable and well defined (*i.e.* cylinder) mesopores; multilayer adsorption in mesopores follows the same rules as adsorption over a plane surface; Kelvin's law for capillary condensation is valid for mesopores (this law brings the Kelvin radius r_K) and capillary condensation starts in pores already presenting a multi-molecular layer of thickness t which varies as a function of the relative pressure (e.g. Harkins and Jura method – Equation 2.11–). Moreover, it generally uses the desorption branch as it is considered more representative for the capillary condensation phenomenon. Equation 2.12 expresses the porous volume $\delta V_{p,n}$ for the n^{th} desorption step ($n > 2$)

$$t = \left(\frac{0.1399}{0.034 - \lg(P/P_0)} \right)^{0.5} \quad \text{Equation 2.11}$$

$$\delta V_{p,n} = \left(\frac{\bar{r}_{p,n}}{\bar{r}_{p,n} - t_n} \right)^2 \left(\delta V_n^l - \delta t_n \sum_{i=1}^{n-1} \delta a_{p,i} \left(1 - \frac{t_n}{\bar{r}_{p,i}} \right) \right) \quad \text{Equation 2.12}$$

where $\bar{r}_{p,n}$ is the average pore radius, t_n is the thickness of the multi-molecular layer, δV_n^l is the volume of evaporated liquid and $\delta a_{p,i}$ is the surface of mesopores desorbed previously (*i.e.* before n^{th} desorption step). Equations 2.13 to 2.16 define the unknown values of Equation 2.12.

$$\bar{r}_{p,n} = \frac{r_{p,n} + r_{p,n-1}}{2} \quad \text{Equation 2.13}$$

$$r_{p,n} = r_{K,n} + t_n \quad \text{Equation 2.14}$$

$$\delta a_{p,i} = \frac{2\delta V_{p,i}}{\bar{r}_{p,i}} \quad \text{Equation 2.15}$$

$$V_n^l = V_m^l \delta \left(\frac{n_n^a}{m_a} \right) \quad \text{Equation 2.16}$$

where V_m^l corresponds to the molar volume of molecular nitrogen at 77 K.

2.1.3 Electrochemical cycling

For instrument and methods effectively used, see section 2.2.5-Devices characteristics.

Two different techniques were used for electrochemical characterization of the TiO₂ based materials: galvanostatic cycling and potentiostatic electrochemical impedance spectroscopy (PEIS). As a reminder, it is important to differentiate the concepts of capacity and specific capacity. Capacity corresponds to the amount of electric charge stored in an electrode (Q expressed in mAh); while, the specific capacity corresponds to the former per mass unit (Q_m expressed in mAh·g⁻¹). Both can be calculated according to Equations 2.17 and 2.18 respectively.

$$Q = \frac{\Delta x \times F \times m_{ma}}{3.6 \times M_{ma}} \quad \text{Equation 2.17}$$

$$Q_m = \frac{Q}{m_{ma}} = \frac{\Delta x \times F}{3.6 \times M_{ma}} \quad \text{Equation 2.18}$$

where Δx corresponds to the number of exchanged electrons, F is the Faraday constant ($F=96485 \text{ A sec mol}^{electrons^{-1}}$), m_{ma} is the active material mass (g) and M_{ma} is the molar mass (g·mol⁻¹).

Galvanostatic cycling belongs to the controlled current techniques (chronopotentiometry); it consists of applying a constant current density to an electrode and recording the resulting potential between the working and reference electrodes as a function of time. As current density remains constant during measurements, electroactive species are oxidized or reduced at a constant rate. Moreover, this technique offers the option to switch between anodic and cathodic current densities (Figure 2.4). The determination of specific capacities during charge/discharge processes can be evaluated by selecting the boundary potentials. Profiles obtained using this technique brings information about multi-steps reactions during the lithiation/delithiation processes [228, 229].

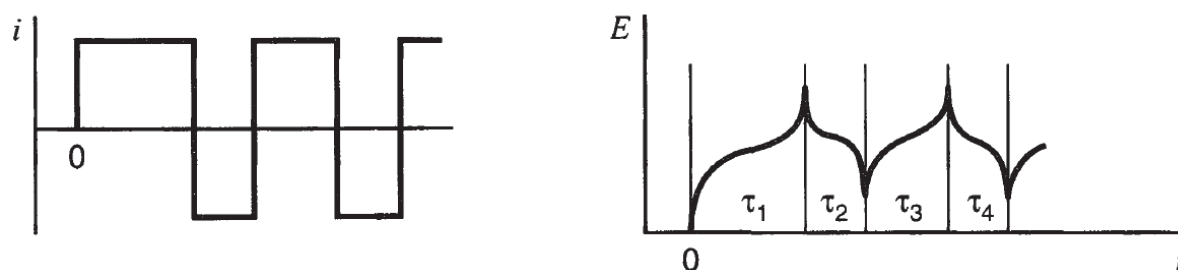


Figure 2.4 Scheme of excitation (left) and response (right) of galvanostatic cycling (cycling chronopotentiometry). Figure taken from [229].

In literature, results obtained by cycling chronopotentiometry are most often presented either as a function of the specific capacity or the amount of lithium inserted or extracted from the active material as presented in Figure 2.5(a) which shows a common galvanostatic profile for

a TiO_2 sample. Cycling chronopotentiometry data can be easily converted into specific capacities knowing the mass of the active material and the current applied.

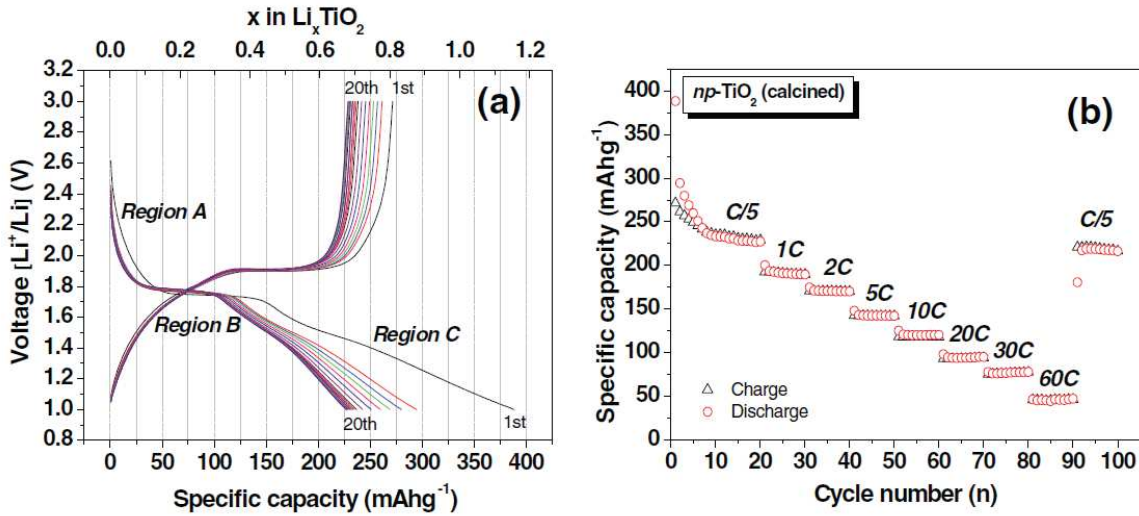


Figure 2.5 (a) Galvanostatic charge/discharge profile of a TiO_2 sample vs. Li^+/Li and (b) its rate performance at different current densities. Figure taken from [230].

It is also common the use of this kind of cycling for the evaluation of the cycling stability at a specific capacity value or at different capacities rates, as seen in Figure 2.5(b). In this case, the current density nC is determined in function of the active material in order to have a virtually fully charge or discharge battery in $1/n$ hours (e.g. $C=335.6 \text{ mA.g}^{-1}$ for a titania electrode) [228, 229].

On the other hand, PEIS consists in exciting the system with a sinusoidal signal (*i.e.* potential signal), small enough to not disturb the system, over a wide range of frequencies (from high to low frequencies). The excitation correspond to a time dependant signal according to Equation 2.19

$$E(t) = E_0 \sin(\omega t) \quad \text{Equation 2.19}$$

where $E(t)$ corresponds to the potential applied at a time t , E_0 is the amplitude and ω is the angular frequency. Therefore, analogously, the measured current response is also a sinusoidal signal shifted by a phase φ ruled by Equation 2.20

$$I(t) = I_0 \sin(\omega t - \varphi) \quad \text{Equation 2.20}$$

When plotting the potential signal on the x -axis and the current response on the y -axis, the shape of graph obtained is an ellipse corresponding to a Lissajous curve. Thus, the impedance, which is a kind of generalized resistance and can be determined using the Ohm's law, becomes a complex function and it becomes easier to use the Euler's formula (Equation 2.21) and works with complex notation.

$$\exp(jx) = \cos x + j \sin x \quad \text{Equation 2.21}$$

Using this notation, expressions for $E(t)$ and $I(t)$ becomes Equations 2.22 and 2.23 respectively.

$$E(t) = E_0 \exp(j\omega t) \quad \text{Equation 2.22}$$

$$I(t) = I_0 \exp[j(\omega t - \varphi)] \quad \text{Equation 2.23}$$

Thereby, impedance is defined by Equation 2.24

$$Z(\omega) = \frac{E_0 \exp(j\omega t)}{I_0 \exp[j(\omega t - \varphi)]} = \frac{E_0}{I_0} \exp(\varphi) = Z_0(\cos \varphi + j \sin \varphi) = Z_{Re} - jZ_{Im} \quad \text{Equation 2.24}$$

A common way to represent impedance is the Nyquist plot which displays Z_{Im} vs. Z_{Re} for different frequencies values (Figure 2.6). Here, a vector of length $|Z|$ corresponds to the impedance value and the angle formed between this vector and the real axis is correlated to the phase shift. This representation also evidences different regions due to the frequency sweeping (*i.e.* kinetic control region at high frequencies and mass transfer control at low frequencies) as observed in Figure 2.6.

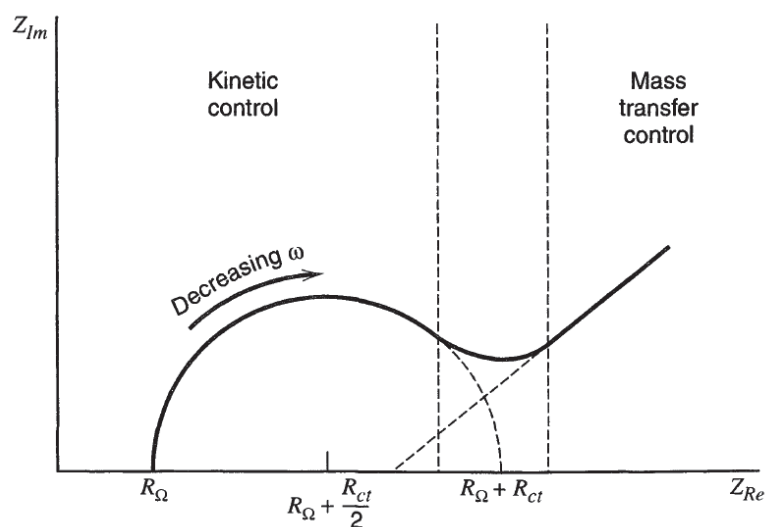


Figure 2.6 Nyquist plot for an electrochemical system evidencing the kinetic and mass transfer control regions at high and low frequencies respectively. Figure taken from [229].

2.2 Protocols of synthesis and analyses

2.2.1 Materials

A list of the reagents used during the different synthesis and during the preparation of samples for electrochemical cycling are listed below; details about their obtention are noted too:

- Titanium (IV) chloride (TiCl_4 , Sigma-Aldrich 99%).
- Vanadium oxychloride (VOCl_3 , Sigma-Aldrich 99 %).
- Diisopropyl ether (${}^i\text{Pr}_2\text{O}$, TCI chemicals 99.9 %). Dried by distillation over sodium (at least 8 h). $\text{H}_2\text{O} < 10$ ppm as verified by Karl Fischer coulometer.
- Tetrahydrofuran (THF, Fisher Scientific 99.8 %). Dried by a PureSolve MD5 solvent purification system from Innovative Technology. $\text{H}_2\text{O} < 5$ ppm as verified by Karl Fischer coulometer.
- Iso-propanol (anhydrous ${}^i\text{PrOH}$, Sigma-Aldrich 99.5 %).
- Tert-butanol (anhydrous ${}^t\text{BuOH}$, Alfa Aesar).
- Dichloromethane, for synthesis (CH_2Cl_2 for HPLC, unstabilised, Fisher Chemical) Dried by a PureSolve MD5 solvent purification system from Innovative Technology. $\text{H}_2\text{O} < 5$ ppm as verified by Karl Fischer coulometer.

- Dichloromethane, for washing step (CH₂Cl₂, Carlo Erba 99.8 %).
- Iron (III) chloride (FeCl₃, Reagent grade 97%, Sigma Aldrich)
- Acetylene black (Y50A, > 99.5 %, Société du Noir d'Acétylène de l'Aubette, France).
- Polyvinylidene difluoride (PVDF, Solef[®] 5130, Solvay).
- N-methyl-2-pyrrolidone (NMP, anhydrous, 99.5 %, Sigma Aldrich).
- Copper sheet (Goodfellow Cu sheet 99.9 %, with a thickness of 0.0175 mm).
- Lithium metal (Li ribbon, thickness × W 0.38 mm × 23 mm, 99.9% trace metals basis, Sigma Aldrich).
- Lithium hexafluorophosphate (LiPF₆, battery grade, ≥ 99.99 % trace metals basis).
- Propylene carbonate (PC, anhydrous, 99.7 %, Sigma Aldrich).
- Ethylene carbonate (EC, anhydrous, 99 %, Sigma Aldrich).
- Dimethyl carbonate (DMC, anhydrous, 99.9 %, Sigma Aldrich).
- Fluoroethylene carbonate (FEC, 99 %, Sigma Aldrich).
- Vinylene carbonate (VC, 99 %, Sigma Aldrich).
- Sodium metal (Na, ACS reagent, dry, Sigma Aldrich).
- Sodium perchlorate (NaClO₄, 98 %, Sigma Aldrich).
- Titanium (IV) oxide, anatase (nanopowder, <25nm particle size, 99.7%, Sigma Aldrich)

2.2.2 Synthesis

2.2.2.1 TiO₂ and TiO₂-V₂O₅ mixed oxides prepared by NHSG ¹Pr₂O route

All preparation of synthesis were carried out in a glovebox under argon atmosphere (amount of water and oxygen <10 ppm) using stainless steel digestion vessels (23 mL) with PTFE lining. Powders of TiO₂, V₂O₅ and TiO₂-V₂O₅ (with V content of 5, 10, 15 and 20 at %) were synthesized by the NHSG ¹Pr₂O route. The TiO₂-V₂O₅ samples were labeled TiV_x where *x* is the nominal vanadium atomic percentage.

Metallic precursors were introduced into the digestion vessel (23 mL); VOCl₃ in first place and then TiCl₄, followed by the addition of a stoichiometric amount of ¹Pr₂O (*i.e.* 1 ¹Pr₂O for 2 M-Cl bonds). Sealed digestion vessels were heated at 110 °C in an oven for 4 days under autogenous pressure. After cooling overnight, the resulting solid brown gel was washed 3 times with 50 mL of CH₂Cl₂, dried under vacuum at 120 °C for 5 hours and finally calcined in air at 500 °C for 5 hours (heating rate 10 °C min⁻¹), leading to light-brown to reddish brown powders depending of the amount of vanadium. Table 2.1 presents the quantities of reagents used for the materials synthesis; last column evidence the visual aspect of samples after calcination step.

Aside from these standard synthesis conditions, TiO₂ samples were kept for different aging times in autogenous pressure (1, 2, 4 and 8 days) at 110 °C in preliminary tests. Besides, all samples were also calcinated at 350 °C, 400 °C, 600 °C and 650 °C for 5 hours with a heating rate of 10 °C min⁻¹.

Table 2.1 Reagents used in the synthesis of TiO₂, V₂O₅ and TiO₂-V₂O₅ samples by NHSG ⁱPr₂O route.

Sample	TiCl ₄		VOCl ₃		ⁱ Pr ₂ O		Visual aspect
	(g)	(mmol)	(g)	(mmol)	(g)	(mmol)	
TiO ₂	2.374	12.52	---	---	2.558	25.03	
TiV5	2.240	11.81	0.108	0.62	2.508	24.55	
TiV10	2.108	11.11	0.214	1.23	2.460	24.07	
TiV15	1.977	10.42	0.319	1.84	2.412	23.60	
TiV20	1.848	9.74	0.422	2.44	2.365	23.14	
V ₂ O ₅	---	---	1.901	11.00	1.685	16.49	

2.2.2.2 TiO₂ prepared by NHSG ⁱPrOH and ^tBuOH routes and TiO₂-V₂O₅ mixed oxides prepared by NHSG ⁱPrOH route

TiO₂ samples were prepared by NHSG alcohol routes using ⁱPrOH and ^tBuOH as oxygen donors. Simultaneously, TiO₂-V₂O₅ mixed oxides (with V content of 5, 10, 15 and 20 at %) were also prepared by NHSG ⁱPrOH route. Samples were labeled TiV_x-OH where *x* is the nominal vanadium atomic percentage.

Synthesis were carried out in a glovebox under argon atmosphere (amount of water and oxygen <10 ppm) using stainless steel digestion vessels (45 mL) with PTFE lining. Metallic precursors were first introduced into the digestion vessel; starting by VOCl₃, followed by TiCl₄. Just before the addition of a stoichiometric amount of the corresponding alcohol, 10 mL of CH₂Cl₂ were added into the digestion vessel. Once sealed, they were heated at 110 °C in an oven for 4 days under autogenous pressure. After cooling overnight, the resulting solid xerogels were washed 3 times with 50 mL of CH₂Cl₂, dried under vacuum at 120 °C for 5 hours and finally calcined in air at 500 °C for 5 hours (heating rate 10 °C min⁻¹). Table 2.2 presents the reagents quantities used for the materials synthesis.

Table 2.2 Reagents used in the synthesis of TiO₂ and TiO₂-V₂O₅ samples by NHSH alcohol routes.

Sample	TiCl ₄		VOCl ₃		ⁱ PrOH		^t BuOH	
	(g)	(mmol)	(g)	(mmol)	(g)	(mmol)	(g)	(mmol)
TiO ₂ - ⁱ PrOH	2.374	12.52	---	---	1.504	25.03	---	---
TiO ₂ - ^t BuOH	2.374	12.52	---	---	---	---	1.855	25.03
TiV5-OH	2.240	11.81	0.108	0.62	1.475	24.55	---	---
TiV10-OH	2.108	11.11	0.214	1.23	1.447	24.07	---	---
TiV15-OH	1.977	10.42	0.319	1.84	1.419	23.60	---	---
TiV20-OH	1.848	9.74	0.422	2.44	1.391	23.14	---	---

2.2.2.3 TiO₂/C nanocomposites prepared by NHSH ⁱPr₂O or NHSG THF routes

In a digestion vessel (23 mL), TiCl₄ (12.52 mmol, 2.375 g) was first introduced and mixed with either ⁱPr₂O (25.04 mmol, 2.559 g) or THF (25.04 mmol, 1.806 g). Sealed digestion vessels were heated at 180 °C in an oven for 4 days under autogenous pressure. The as obtained xerogels (dark brown like powder for ⁱPr₂O and black small monoliths for THF) were dried under vacuum at 120 °C for 5 hours without any washing. Then, they were pyrolyzed under argon atmosphere at 750 °C for 4 hours (heating rate 10 °C min⁻¹) to obtain the TiO₂/C nanocomposites; or calcined in air at 500 °C for 5 hours (heating rate 10 °C min⁻¹) for their TiO₂ counterparts. Samples were labeled according to their nature (*i.e.* Xer- for xerogels; TiO₂- for calcinated samples and TiO₂/C- for pyrolyzed samples) and the oxygen donor (*i.e.* IPE for ⁱPr₂O or THF); Table 2.3 summarizes this nomenclature and Figure 2.7 shows the physical aspect of the same samples.

Preliminary tests were performed synthesizing TiO₂/C nanocomposites washing the xerogels before the drying step and, also, using phenol as oxygen donor. Different temperatures were explored too, either for the reaction (*i.e.* oven temperature, 110 °C and 150 °C) or for the heat treatment (*i.e.* pyrolysis temperature, 800 °C and 900 °C).

Figure 2.7 Picture of the IPE and THF derived TiO₂ xerogels and final products after heat treatment.

Table 2.3 Summary of samples nomenclature for TiO₂/C composites.

Sample	Oxygen donor	Heat treatment
Xer-IPE	ⁱ Pr ₂ O	---
TiO ₂ /C-IPE		750 °C, Ar
TiO ₂ -IPE		500 °C, air
Xer-THF	THF	---
TiO ₂ /C-THF		750 °C, Ar
TiO ₂ -THF		500 °C, air

2.2.3 Xerogels impregnation with a FeCl₃ solution

Xer-THF was ground; 583 mg of the resulting powder was placed in a Schlenk, and purged three times (*i.e.* vacuum-Ar). Then, 5.0 mL of anhydrous THF were added and 1.0 mL of FeCl₃ solution (0.10 M or 0.20 M FeCl₃ in anhydrous THF). That corresponds to 0.5 or 1.0 mmol metal per gramme of available organic byproducts (34.3 wt% for Xer-THF). Mixture was kept stirring for 12 h or 24 h; then, THF was evaporated at 50 °C under vacuum. Impregnated xerogels were collected and pyrolyzed at 750 °C (heating rate 10 °C·min⁻¹) for 4 h under inert atmosphere (*i.e.* Ar) or reducing atmosphere (*i.e.* Ar:H₂; 95:5 vol.).

2.2.4 Preparation of electrodes and assemblage of coin cells

TiO₂-V₂O₅ mixed oxides films preparation: All electrodes were composed of the active material (about 80 wt%), acetylene black (14 wt%) and polyvinylidene difluoride (6 wt%). Powders (about 200 mg total weight) were gently grinded on an agate mortar until obtaining a homogenous colored powder. This mixture was placed on agate jar and 700 μL of N-methyl-2-pyrrolidone (NMP) were added. After stirring for 30 minutes, the slurry was tape casted uniformly at 150 μm onto a copper current collector using a 3540 bird film applicator from Elcometer. Films were left drying at ambient temperature overnight. Figure 2.8 shows the appearance of films before and after drying step.

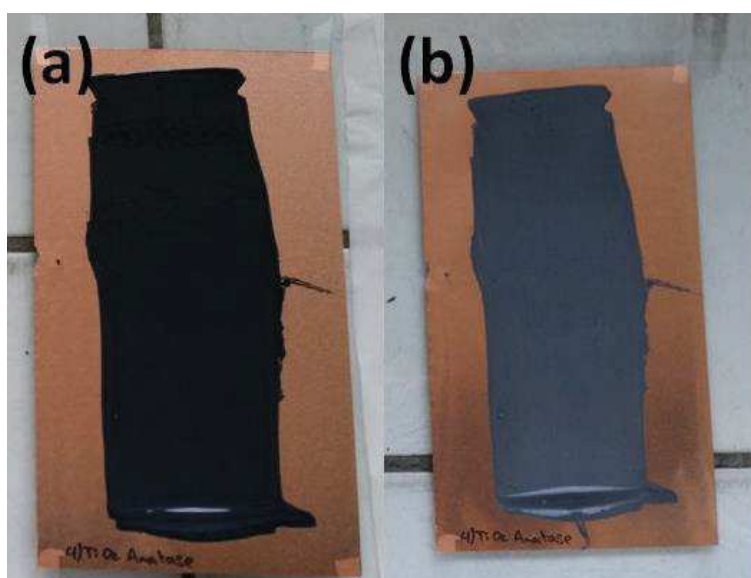


Figure 2.8 (a) As tape casted slurry visual aspect and (b) dried film visual aspect.

TiO₂/C nanocomposites films preparation: Electrodes were composed of the active material (*i.e.* either TiO₂/C nanocomposites or TiO₂ calcinated counterparts), acetylene black (unless otherwise indicated, Table 2.4) and polyvinylidene difluoride (6 wt%). Nomenclature and electrode compositions are summarized in Table 2.4. Briefly, powders mixtures (about 200 mg total weight) were gently grinded on an agate mortar until obtaining a homogenous colored powder. This mixture was placed on agate jar and 700 μ L of NMP were added. The whole was stirred for 30 minutes; then, the slurry was tape casted uniformly at 150 μ m onto a copper current collector using a 3540 bird film applicator from Elcometer. Films were left drying at ambient temperature overnight.

Table 2.4 Theoretical percentage values from electrodes films (TiO₂/C nanocomposite series).

Sample	TiO ₂ (wt%)	Extrinsic Carbon (wt%)	Intrinsic Carbon (wt%)	PVDF (wt%)
TiO ₂ -IPE-0CB	94	---	---	6
TiO ₂ -THF-0CB	94	---	---	6
TiO ₂ -IPE-18CB	76	18	---	6
TiO ₂ -THF-18CB	76	18	---	6
TiO ₂ /C-IPE-12CB	76	12	6	6
TiO ₂ /C-THF-0CB	76	---	18	6
TiO ₂ /C-IPE-0CB	88	---	6	6

When using TiO₂ as active material (*i.e.* calcinated samples) without addition of extrinsic carbon, the obtained slurry, and the electrode itself, were white (*e.g.* TiO₂-THF-0CB). However, slurry consistency and adherence over the copper sheet were not lost. An example of the electrodes obtained for this series are observed in Figure 2.9.



Figure 2.9 Visual aspect of TiO₂-THF electrodes with and without acetylene black.

Once the films were dried; electrodes, with a diameter of 12.7 mm (Figure 2.9), were cut with a disk cutter and later dried under vacuum at 80 °C overnight. Coin cells were assembled in a glove box under argon atmosphere (O₂<0.5 ppm, H₂O<0.5 ppm), using lithium metal both as reference and as counter-electrode (*i.e.* half-cell configuration). The electrolyte was 1 M LiPF₆ in PC:EC:3DMC (1:1:3 vol.) with 5% FEC and 1% VC as additives and it was deposited

over a Whatman glass fiber filters that served as the separator. Figure 2.10 schematizes all components that integrate a coin cell in order to give a better insight about the whole assemblage.

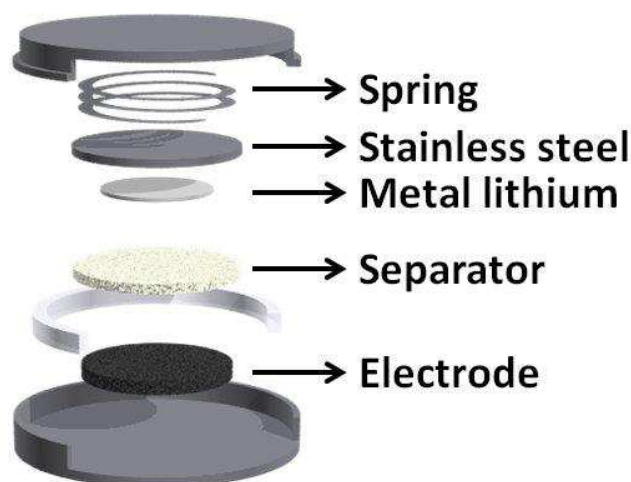


Figure 2.10 Scheme of coin cell assemblage.

For samples electrochemical cycled *versus* sodium, sodium metal was used both as reference and as counter-electrode. The electrolyte was 1 M NaClO₄ in PC with 5% FEC and it was deposited over a Whatman glass fiber filters that served as the separator.

2.2.5 Devices characteristics

A list of the divers equipments (enumerated by alphabetical order to facilitate locating) used for the materials characterization is presented below. This list describes the characteristics of the equipment and the parameters used during measurement.

- *Ammonia temperature programmed desorption*: Samples were calcinated in air at 350 °C or 500 °C for 7 h. Then, they were saturated in ammonia at 100 °C for 15 minutes, followed by a purge under nitrogen for 4 h to remove physisorbed ammonia. Samples were then heated to 550 °C with a heating rate of 10 °C min⁻¹, keeping a continuous nitrogen flow. Amount of desorbed ammonia, during the heating stage, was determined with a thermal conductivity detector (TCD).
- *Energy-dispersive X-ray spectroscopy*: EDX analysis was performed on a FEI Quanta FEG 200 scanning electron microscope.
- *Electrochemical galvanostatic cycling*: They were performed at room temperature on a BTS3000 (5 V, 1 mA) instrument from Neware Battery using CR2032-type coin cells. Electrodes and coin cells were prepared as detailed above. Measurements were principally done in the voltage range of 2.5-1.2 V *vs.* Li⁺/Li at different current densities (*e.g.* 16.8, 168, 336 mA g⁻¹). The latter densities have been selected as corresponding to specific capacities of C/20, C/2 and C, respectively (where C=335.6 mA g⁻¹) for pure titanium dioxide TiO₂. It is worthy to mention that another capacities and voltage windows were also used, those parameters will be specified in their corresponding sections. Experiments at higher current densities (C, 2C and 5C) were recorded on a BioLogic VSP instrument over the same voltage range (2.5-1.2 V *vs.*

Li⁺/Li). Specific capacities presented hereafter have been calculated from the content of active material of each electrode composition.

- *Electrochemical impedance spectroscopy*: Impedance measurements in powders were recorded in air-tight 4-electrode cells with the sample pressed between Au-plated brass plates in the frequency range 7 MHz to 100 mHz using a Biologic SP-300 impedance spectrometer. The powders were pressed into pellets with 0.946 cm diameter and then Au-plated by evaporation in inert atmosphere to reduce contact resistance. EIS studies in half-cells *versus* lithium were performed on a BioLogic VSP-300 instrument, from 100 kHz to 10 mHz, with a 10 mV amplitude. Plots were obtained in potentiostatic mode at different potentials *vs.* Li⁺/Li after 2 h relaxation time before and after the lithiation/delithiation processes.
- *Fourier transform infrared spectroscopy*: Infrared spectra were recorded using a PerkinElmer FTIR Spectrometer Spectrum Two on ATR mode.
- *Liquid nuclear magnetic resonance*: ¹³C and ¹H spectra were recorded on a Bruker 300 MHz spectrometer; NMR spectra were calibrated to TMS on the basis of the relative chemical shift of the solvent as an internal standard.
- *Nitrogen physisorption*: N₂-physisorption experiments were carried out at -196 °C on a Micromeritics TriStar 3000. Samples were out-gassed under vacuum at 110 °C overnight. Equivalent BET specific surface areas were determined in the relative pressure range P/P₀ from 0.08 to 0.25. The total pore volume was measured at P/P₀>0.985.
- *Raman spectroscopy*: Raman spectra were obtained on a Horiba Jobin Yvon LabRAM ARAMIS microspectrometer. The excitation wavelength used for TiO₂-V₂O₅ samples was 473 nm; spectra were recorded in the range of 50 to 1100 cm⁻¹ and later normalized. Otherwise, for TiO₂/C samples, a HeNe laser (λ=633 nm) was used as excitation source; spectra were recorded in a wider range also (50 to 2000 cm⁻¹) and then normalized.
- *Scanning electron microscopy*: Micrographs images were obtained with a Hitachi S-4800 electron microscope and a FEI Quanta FEG 200 scanning electron microscope. Samples were covered with platinum before analysis.
- *Solid state nuclear magnetic resonance*: ¹³C SSNMR spectra were recorded with a VARIAN VNMRs 300 at 75.44 MHz. It was used a T3 NMR probe with 3.2 mm ZrO₂ rotors. Experiments were performed using cross polarization magic angle spinning (CP-MAS) with the spun at 15 kHz, a contact time of 1.5 ms and 5 s for recycle delay. Plastic inset were removed from the rotor and short caps were used instead to minimize the ¹³C background.
- *Thermogravimetric analyses*: Experiments were performed on air on a Netzsch Simultaneous Thermal Analyzer STA 409 PC Luxx with a heating rate of 10 °C min⁻¹ in the 20-1200 °C range and a gas flow of 50 mL·min⁻¹.
- *Transmission electron microscopy*: TEM images were acquired with a high voltage 200 kV JEOL JEM ARM 200F transmission electron microscope equipped with a STEM level and a spherical aberration corrector. The STEM images were taken with high angle annular dark field (HAADF). EDX analysis used a JEOL CENTURIO detector and electron energy loss analyses were detected with a GATAN GIF QUANTUM.
- *UV/vis spectroscopy*: UV/vis absorption spectra were obtained with a JASCO V-760 UV–visible–NIR spectrophotometer in 10 mm quartz cells (Hellma). Spectra were recorder over the 900-200 nm range with a bandwidth of 1.0 nm at a rate of 200 nm·min⁻¹.

- *Wettability experiments:* Contact angle measurements were carried out on a GBX Digidrop Goniometer FAST/60 over as prepared electrode films using both water and the electrolyte (*i.e.* 1 M LiPF₆ in PC:EC:3DMC vol. with 5% FEC and 1% VC). Pictures were taken 100 ms after a 2 μ L drop was placed over the films.
- *X-ray diffraction:* XRD Patterns were obtained using a PANalytical X'Pert Pro MPD diffractometer, with the K α radiation of Cu ($\lambda=1.5418$ Å) and a step size of 0.033° (2 θ scale) into the 6-90° interval. Crystallite size of TiO₂ anatase particles was estimated using the Scherrer equation using the most intense reflection ($\approx 25.3^\circ 2\theta$) associated to the (101) crystal plane.

3 TiO₂-V₂O₅ Mixed Oxides

As mention in chapter 1-Bibliography, the NHSG methods easily lead to hierarchical mesoporous oxides, including TiO₂, and mixed oxides without the addition of expensive modifiers to match reactivity like their hydrolytic copunterparts. It has also been settled that titanium dioxide has attracted such more attention as a substitute of graphite as anode material in Li-ion batteries; notably for high-energy applications. TiO₂ is classified as an intercalation anode material, such as graphite, having a theoretical specific capacity of 335.6 mAh·g⁻¹; however, its poor conductivity and low ion diffusion coefficient are the major issues that need to be solved to completely fulfill this targeted application.

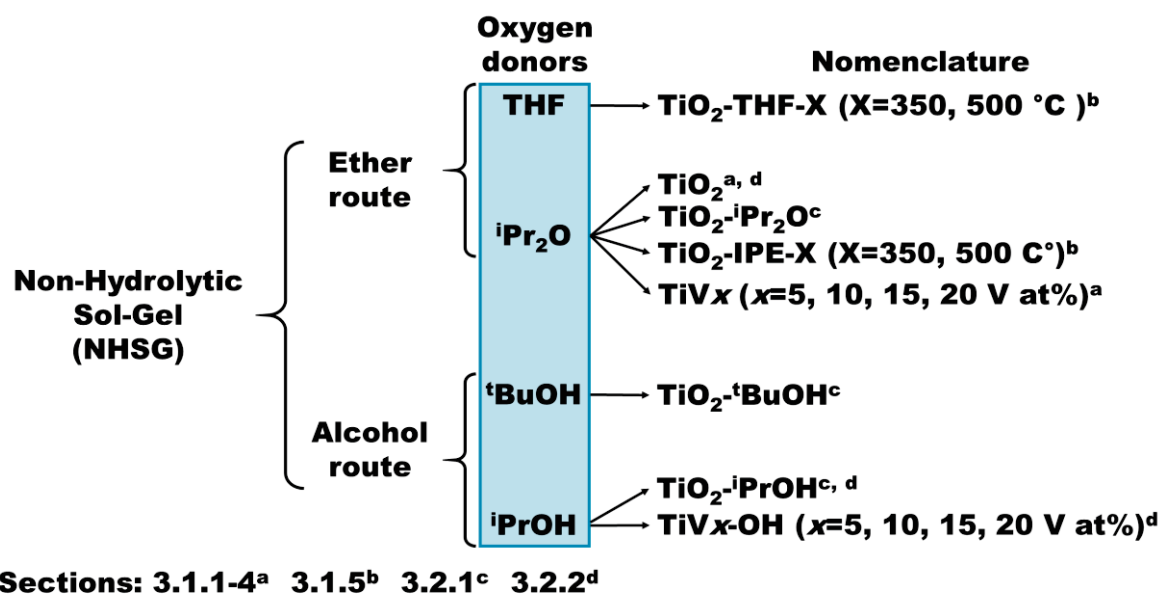
There are different general approaches to enhance the electrochemical performance of electrodes materials like nanostructuring and doping. Besides, NHSG chemistry has been largely used for the synthesis of catalyst but only few reports are found using this synthesis methodology targeting the Li-ion batteries electrode application. That being said, this chapter focuses on the doping strategy, in particular, the application of different vanadium loading during the NHSG synthesis of TiO₂ in order to modify its properties.

In the first part of this chapter, the elaboration of TiO₂-V₂O₅ mixed oxides using the NHSG ¹Pr₂O route is reported, as published in reference [1]. The texture, morphology and crystal phase of materials were determined and analyzed; moreover, their performances for lithium insertion are presented, for possible application as anode material in Li-ion battery. It has been emphasized the influence of the vanadium loading over the synthetic materials and correlated to the different characterizations to elucidate their electrochemical behavior. Then, discussion follows an analysis of the influence of the heat treatment and vanadium loading over the TiO₂ anatase-rutile phase transformation and the analysis is complemented with the electrochemical evaluation of these materials *versus* sodium, a new emerging technology that aims to substitute Li-ion batteries.

Then, the chapter aims the electrochemical analysis of two different TiO₂ obtained by non-hydrolytic ether routes (*i.e.* ¹Pr₂O and THF) and heat-treated at two differet temperatures (*i.e.* 350 °C and 500 °C) in air. Discussion of this section focuses in the electrochemical performance of these TiO₂ samples *versus* lithium at a constant current rate with a progressive increase of the voltage windows starting in the 1.2-2.5 V *versus* Li⁺/Li range to the 0.1-3.0 V *versus* Li⁺/Li during the same cycling.

The second part of this chapter focus on the alcohol NHSG routes. Synthesis using either ¹PrOH or ¹BuOH as oxygen donors were explored, as an alternative to the use of ether reported in the first part, for preparing TiO₂. These NHSG alcohol derived TiO₂ were structurally, texturally and electrochemically characterized. Then, a special focus on the use of ¹PrOH was taken into account for the elaboration of TiO₂-V₂O₅ mixed oxides and their comparison to the ones obtained by ether route. Discussion of this section focuses on the textural and morphology characterization of these materials; however, TiO₂-V₂O₅ mixed oxides prepared by this route were not further electrochemically characterized.

A global overview of samples prepared and discussed in this chapter is presented in Scheme 3.1.



Scheme 3.1 Global overview of samples prepared in chapter 3: TiO₂-V₂O₅ mixed oxides.

3.1 Evaluation of the influence of vanadium over the properties of TiO₂ prepared by the NESH ¹Pr₂O route

3.1.1 Published Article: *J. Sol-Gel Sci. Technol.*, 2016, 79, 270-278

Lithium insertion properties of mesoporous nanocrystalline TiO₂ and TiO₂-V₂O₅ microspheres prepared by nonhydrolytic sol-gel

A.M. Escamilla-Pérez¹, N. Louvain^{1,2*}, M. Kaschowitz³, S. Freunberger³, O. Fontaine^{1,2}, B. Boury¹, N. Brun¹, P.H. Mutin^{1*}

¹Institut Charles Gerhardt Montpellier, UMR 5253, Université Montpellier 2, CC 1701, Place Eugène Bataillon, 34095 Montpellier Cedex 5, France

²Réseau sur le Stockage Electrochimique de l'Energie (RS2E), FR CNRS 3459, France.

³Institute for Chemistry and Technology of Materials, Graz University of Technology, Stremayrgasse 9, 8010 Graz, Austria.

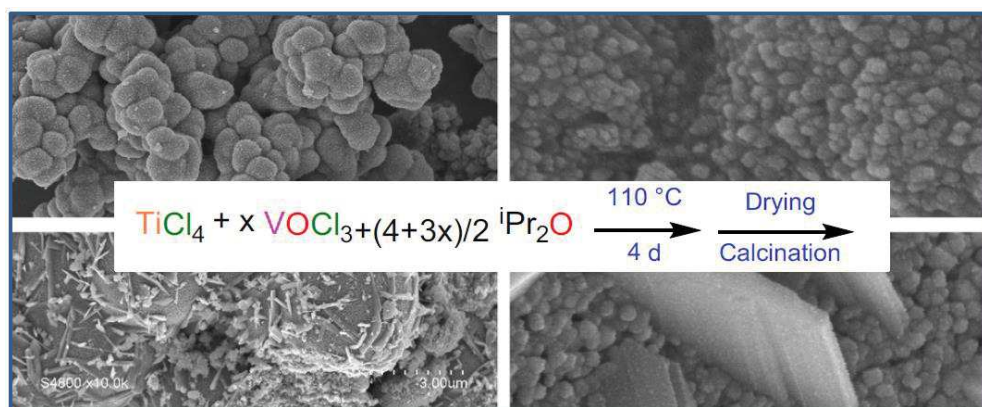
Corresponding authors e-mail:

nicolas.louvain@umontpellier.fr, hubert.mutin@umontpellier.fr

Abstract

Mesoporous nanocrystalline TiO₂ and TiO₂-V₂O₅ was prepared by non-hydrolytic sol-gel from TiCl₄, VOCl₃ and ¹Pr₂O at 110 °C without any solvent or additives. The samples were characterized by elemental analysis, X-ray diffraction, Raman spectroscopy, scanning electron microscopy, nitrogen physisorption, and impedance measurements. At low vanadium loadings, only TiO₂ anatase was detected, and V₂O₅ scherbinaite was also detected at high vanadium loadings. The texture of the samples depended on the V-loading, but all the samples appeared built of primary nanoparticles (≈10 to 20 nm in size) that aggregate to form mesoporous micron-sized spheres. The lithium insertion properties of these materials were evaluated by galvanostatic measurements performed using coin-type cells, in view of their application as electrode for rechargeable Li-ion batteries. The mesoporous TiO₂ microspheres showed good performances, with a specific reversible capacity of 145 mAh·g⁻¹ and 128 mAh·g⁻¹ at C/2 and C, respectively (C = 335.6 mA·g⁻¹), good coulombic efficiency, and a moderate capacity fade (6%) from the 2nd to the 20th cycle at C/20. Although the addition of V effectively increased the electronic conductivity of the powders, the specific reversible capacity and cycling performances of the TiO₂-V₂O₅ samples were only minimally improved for a 5 at% V loading, and were lower at higher V loading.

Graphical Abstract



Keywords

Non-hydrolytic sol-gel; Mesoporous xerogel; Titania; Vanadia; Lithium battery

1 Introduction

Over the last 25 years, several alternative non-hydrolytic sol-gel (NHS) routes have emerged, aiming at solving the issues met in conventional sol-gel chemistry by a drastic change of reactions and reaction medium [1-4].

The NHS route based on the reaction of chloride precursors with ether or alkoxide oxygen donors in anhydrous medium is now a well-established method for the preparation of mesoporous silica-based or metal oxide-based materials. Our group and others have successfully applied this route to the synthesis of mesoporous oxide and mixed oxide catalysts, as recently reviewed [5].

Other non-hydrolytic routes have recently been used for the synthesis of electrode materials for Li-ion batteries, notably the benzyl alcohol route. Bilecka *et al.* [6] prepared nanocrystalline LiFePO₄ and LiMnPO₄ cathode materials with excellent cycling stabilities by a microwave-assisted non-aqueous route in benzyl alcohol. Nanocrystalline Li₄Ti₅O₁₂ anode material obtained by the same route showed good lithium intercalation/deintercalation performances at high rates (up to 30C) and good cycling stabilities [7].

Owing to its high working voltage, good theoretical storage capability, low cost, and safe operation, TiO₂ is a promising anode material for lithium ion batteries [8]. Among the most common phases (rutile, anatase and brookite), anatase exhibits the best lithium insertion properties [9]. However, slow lithium-ion kinetics as well as intrinsic poor electronic conductivity of TiO₂ limits its applicability. The size of TiO₂ anatase particles plays a major part: Lowering the crystallite size increases specific surface area and improves the cyclability of these materials through better accommodation of the structural changes during the electrochemical process [9]. For instance, after 5 cycles at a current density of 1 C, ≈5 nm nanoparticles exhibited a capacity of ≈180-190 mAh·g⁻¹ [10, 11] compared to only ≈20 mAh·g⁻¹ for 300 nm particles [10]. Thus, much work aimed at developing nanostructured TiO₂ materials with high specific surface area and interconnected mesopores, readily accessible to electrolyte, which reduces the transport lengths of lithium ions and electrons and improves the performances of a Li-ion battery [12-19]. In addition, electronic conductivity can be improved by doping TiO₂ with aliovalent ions, such as vanadium, niobium, sulfur or nitrogen [8, 20, 21], or by deposition of a conductive metal oxide phase at the surface of the nanoparticles [10].

In previous works, we reported the NHS synthesis of TiO₂-V₂O₅ catalysts with a hierarchical structure, consisting of 10-25 nm nanoparticles that were aggregated to form mesoporous spherical micron sized particles. Calcination led to the migration of vanadium oxide species toward the anatase particle surface [22, 23].

In the present work, we wish to report the electrochemical properties of hierarchical mesoporous TiO₂ and TiO₂-V₂O₅ samples (5 to 20 at% V) prepared by the ether route in the absence of solvent or additives. The powders were characterized by elemental analysis, X-ray diffraction (XRD), Raman spectroscopy, scanning electron microscopy (SEM), nitrogen physisorption, and impedance measurements. The potential of the samples as Li-insertion materials was evaluated by galvanostatic cycling using coin-type cells. The TiO₂ sample showed promising performances, with a specific reversible capacity of 145 and 128 mAh·g⁻¹

at $C/2$ and C ($C = 335.6 \text{ mA} \cdot \text{g}^{-1}$), respectively, and a moderate capacity fade ($\approx 6\%$) from the 2nd to the 20th cycle at $C/20$. Although the addition of V effectively increased the electronic conductivity of all of the samples, the specific reversible capacity and cycling performances were only slightly improved for a 5 at% V loading, and were lower at higher V loadings.

2 Materials and methods

2.1 Synthesis

Powders of TiO₂ and TiO₂-V₂O₅ (with V content of 5, 10, 15 and 20 at%) were synthesized by the NHSG ether route (Table 1). The TiO₂-V₂O₅ samples were labeled TiV_x where x is the nominal vanadium atomic percentage. The samples were prepared under argon atmosphere in a glovebox using stainless steel digestion vessels (23 mL) with PTFE lining. Titanium chloride (TiCl₄, Sigma-Aldrich 99%) and vanadium oxychloride (VOCl₃, Sigma-Aldrich 99 %) were used as precursors; diisopropyl ether (ⁱPr₂O, TCI chemicals 99.9 %), dried by distillation over sodium, was used as oxygen donor. In a typical experiment (TiV5), TiCl₄ (11.81 mmol, 2.240 mg) and VOCl₃ (0.62 mmol, 0.108 mg) were introduced into the digestion vessel; then, a stoichiometric amount of ⁱPr₂O (24.55 mmol, 2.508 mg) was added (*i.e.*, 1 ⁱPr₂O for 2 M-Cl bonds). No solvent was used. The sealed digestion vessel was heated at 110 °C in an oven for 4 days under autogenous pressure. After cooling the resulting solid brown gel was washed 3 times with dichloromethane (CH₂Cl₂, Carlo Erba 99.8 %), dried under vacuum at 120 °C for 5 hours, then calcined in air at 500 °C for 5 hours (heating rate 10 °C·min⁻¹), leading to a light-brown powder.

Table 1 Reactants used in the synthesis of TiO₂ and TiO₂-V₂O₅ samples and experimental V content (derived from EDX analysis).

Sample	TiCl ₄ (g)	VOCl ₃ (g)	ⁱ Pr ₂ O (g)	V content (at%)
TiO ₂	2.374	0.000	2.558	0
TiV5	2.240	0.108	2.508	7.7
TiV10	2.108	0.214	2.460	8.4
TiV15	1.977	0.319	2.412	12.0
TiV20	1.848	0.422	2.365	17.0

2.2 Characterization

XRD patterns were obtained using a PANalytical X'Pert Pro MPD diffractometer, with the $K\alpha$ radiation of Cu ($\lambda=1.5418 \text{ \AA}$) and a step size of 0.033° (2θ scale) into the $6\text{-}90^\circ$ interval. Crystallite size was estimated using the Scherrer equation. N₂ physisorption experiments were carried out at $-196 \text{ }^\circ\text{C}$ on a Micromeritics TriStar 3000. Samples were out-gassed under vacuum at $120 \text{ }^\circ\text{C}$ overnight. Equivalent BET-specific surface areas were determined in the relative pressure range P/P_0 from 0.08 to 0.25. The total pore volume was measured at $P/P_0 > 0.985$. Scanning electron microscopy images were acquired with a Hitachi S-4800 electron microscope. Raman spectra were obtained on a Horiba Jobin-Yvon LabRAM ARAMIS microspectrometer. The excitation wavelength was 473 nm. Spectra were recorded in the range of 50 to 1100 cm^{-1} and then normalized. EDX analysis was performed on a FEI Quanta FEG 200 scanning electron microscope. Impedance measurements were recorded in air-tight 4-electrode cells with the sample pressed between Au-plated brass plates in the frequency range 7 MHz to 100 mHz using a Biologic SP-300 impedance spectrometer; the powders were pressed into pellets with 0.946 cm diameter and then Au-plated by evaporation in inert atmosphere to reduce contact resistance.

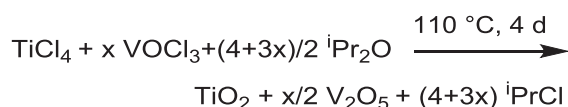
2.3 Electrochemical characterization

Galvanostatic electrochemical characterizations were performed at room temperature on a BTS3000 (5 V 1 mA) instrument from Neware Battery using CR2032-type coin cells. Electrochemical impedance spectroscopy (EIS) studies were done on a BioLogic VSP instrument, from 100 kHz to 10 mHz, with a 10 mV amplitude in potentiostatic mode. All electrodes were composed of the active material (about 80 wt%), acetylene black (14 wt%) and polyvinylidene difluoride (6 wt%). After stirring in *N*-methyl-2-pyrrolidone, the slurry was tape casted uniformly at 150 μm onto a copper current collector using a 3540 bird film applicator from Elcometer. Electrodes (diameter 12.7 mm) were cut with a disk cutter then dried under vacuum at 80 °C for 12 hours. Coin cells were assembled in a glove box under Ar atmosphere (O₂ < 0.5 ppm, H₂O < 0.5 ppm), using lithium metal both as reference and as counter electrode. The electrolyte was 1 M LiPF₆ in propylene carbonate, ethylene carbonate, and dimethyl carbonate (PC:EC:3DMC, 1:1:3 vol.) with 5% fluoroethylene carbonate and 1% vinyl carbonate. Whatman glass fiber filters were used as the separator. The electrochemical galvanostatic measurements were taken in the voltage range of 2.5-1.2 V versus Li⁺/Li at different current densities: 16.8, 33.6, 67.2, 168, 336 mA·g⁻¹. The latter densities have been selected as they correspond to specific capacities of *C*/20, *C*/10, *C*/5, *C*/2, and *C*, respectively (where *C* = 335.6 mA·g⁻¹), for pure titanium dioxide TiO₂. The specific capacities presented hereafter have been calculated from the content of active material (80 wt%).

3 Results and discussions

3.1 Synthesis and characterization of the mixed oxide

TiO₂ and TiO₂-V₂O₅ nanocrystalline powders with a nominal vanadium loading of 5, 10, 15, and 20 at% (Table 1) were prepared by the non-hydrolytic ether route, as shown in Scheme 1.



Scheme 1 ideal reaction scheme for the synthesis of TiO₂-V₂O₅ samples.

It is noteworthy that the synthesis was performed in the absence of solvent, surfactant, or any other additive. Elemental analysis performed by EDX indicated that the V content of the powders was close to the expected one (Table 1).

The X-ray diffraction (XRD) patterns of all the different samples (Fig. 1) indicate the formation of anatase phase TiO₂ (JCPDS 00-21-1272). No significant shift of XRD peaks was observed, confirming that the solubility of V in TiO₂ is low. In previous work, we reported that even for a V content of ≈3 at%, most of the vanadium species were located close to the surface of the anatase grains after the calcination step [23]. No reflection arising from rutile was found. Crystalline V₂O₅ (scherbinaite, JCPDS 00-041-1426) was detected for the samples with the highest V loadings. The approximate amount of crystalline V₂O₅ estimated from the XRD pattern was 11 wt% (≈10 at%) for TiV15 and 17 wt% (≈15 at%) for TiV20, suggesting that in these samples only about 5 at% of vanadium was accommodated in the bulk (doping) and at the surface of the anatase crystallites.

Raman spectroscopy (Fig. S1 in supplementary material) confirmed these findings. The only TiO₂ crystalline phase detected is anatase, as shown by the intense band at 144 cm⁻¹ and weaker bands at 638, 515, and 395 cm⁻¹ [24]. The weaker bands are slightly shifted probably due to the incorporation of V atoms into the anatase crystallites. Bands arising from V₂O₅

(994, 285, and 405 cm⁻¹) and not overlapping with anatase bands are detected in the spectra of TiV15 and TiV20 [25].

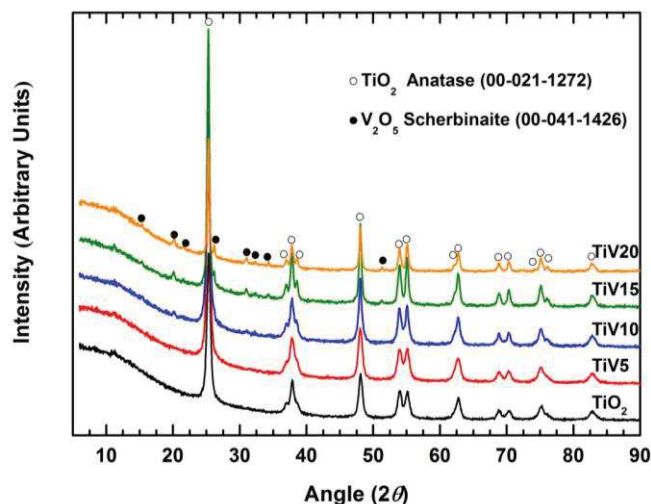


Fig. 1 Powder X-ray diffraction patterns of the TiO₂ and TiO₂-V₂O₅ samples.

The anatase crystallite size was determined using the Scherrer equation (Table 2). It can be noticed that the addition of vanadium above 5 at% leads to larger anatase crystallites.

Table 2 Crystallite size and textural data for the TiO₂ and TiO₂-V₂O₅ samples.

Sample	Crystallite size ^a (nm)	S _{BET} ^b (m ² /g)	V _p ^c (cm ³ /g)	D _p ^d (nm)
TiO ₂	13	68	0.17	5.7
TiV5	12	64	0.15	6.5
TiV10	17	58	0.16	7.9
TiV15	25	27	0.13	16.2
TiV20	25	15	0.09	20.2

^a Derived from XRD data using Scherrer equation; ^b specific surface area; ^c total pore volume; ^d BJH average pore diameter calculated from the desorption branch D_p.

Typical SEM micrographs of the NHSG samples are given in Fig. 2. In all cases, the sample showed an interesting hierarchical texture, resulting from the aggregation of primary nanoparticles around 15-20 nm in size (in good agreement with XRD results), to form spherical micron-sized particles, themselves aggregated. Interestingly, the secondary particles are significantly smaller in the TiO₂ sample (0.6-1.2 μm) than in the TiV_x samples (3-6 μm). At high vanadium loading (TiV15 and TiV20), scherbinaite crystals with a plank-like morphology are found interspersed with the anatase nanocrystals.

The nitrogen adsorption-desorption isotherms of the different samples are presented in Fig. 3, and the characteristic textural data are reported in Table 2. All isotherms are of type IV according to the IUPAC classification, typical of mesoporous solids. The BJH pore size distribution shows the presence of well-defined mesopores in the 3 to 10 nm range for TiO₂ and TiV5, and of larger mesopores (10-40 nm) for the TiV15 and TiV20 samples. A bimodal distribution is clearly observed for TiV10, which shows both types of pores. The specific surface area decreases with the V loading, ranging from 68 m²·g⁻¹ for TiO₂ to 15 m²·g⁻¹ for TiV20 (Table 2). This decrease can be accounted for by the increase of the anatase crystallite size found by XRD and by the large size of V₂O₅ crystallites. Interestingly, the presence of the broad pores is correlated with the formation of crystalline V₂O₅. A possible explanation would be that V₂O₅ crystallites prevent a close contact between the anatase nanocrystals.

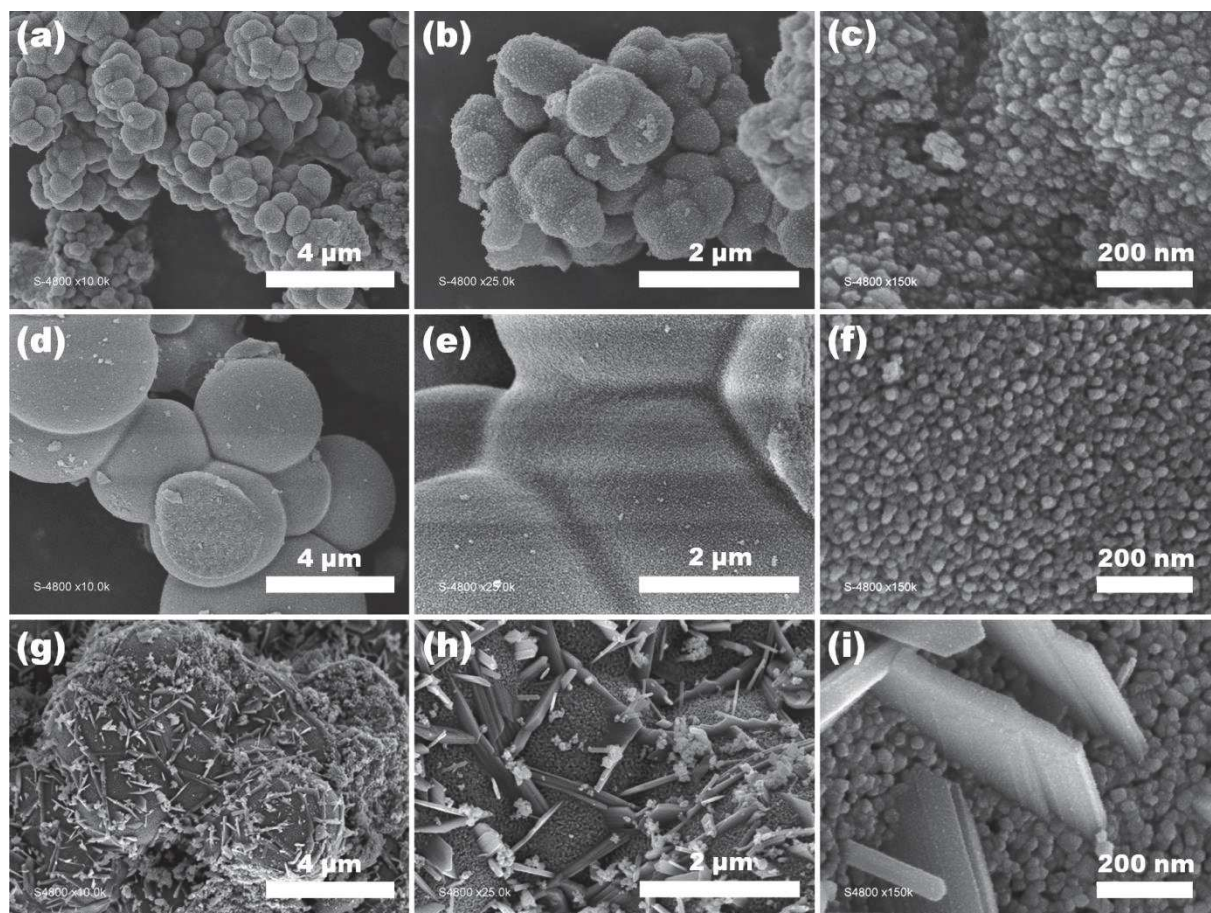


Fig. 2 SEM images of TiO₂ (a-c), TiV₅ (d-f), and TiV₂₀ (g-i) at different magnifications.

Conductivity spectra of the samples pressed in pellets are given in Fig. 4. $\sigma'(\nu)$ is shown as a function of frequency ν with σ' being the real part of the complex conductivity $\hat{\sigma}$. These spectra lump together the mobility of all mobile charges. At high frequencies, a dispersive regime is seen, which is associated with short range motion. At the low frequency end, electrode polarization is seen. Over a wide frequency domain, the samples reveal distinct plateaus referring to the dc conductivity σ_{dc} . The addition of V results in significant increase of conductivity versus the pure TiO₂ sample by a factor of around 6-11. However, there is no correlation between the V content and the conductivity, the differences observed between the TiV_x samples may be attributed to variations in sample compressibility during the uniaxial sample compression. The complex plane plots of the complex impedance Z (insert in Fig. 4) show depressed semicircles with their origin lying in the positive imaginary part. This is indicative of charge transport resistance being composed of bulk and grain boundary contributions as expected for these pressed powder samples [26].

The interpretation of this behavior is not simple, as the addition of vanadium influences the morphology and texture of the samples, and as the vanadium is distributed between the bulk of the anatase nanocrystals (doping), amorphous vanadate surface species and V₂O₅ crystallites for the high V loadings. The similar conductivity observed for all the TiV_x samples suggests that only the V doping (<2 at%) increases significantly the electronic conductivity, as expected [20], and that the remaining vanadium in surface vanadates and in scherbinait crystal play only a minor part.

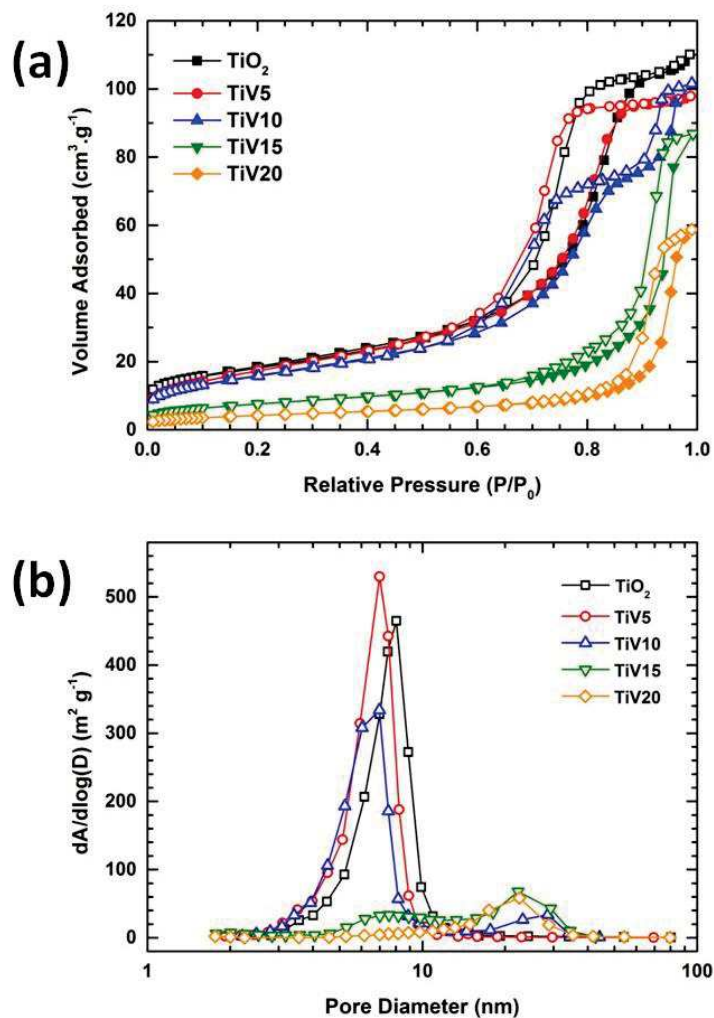


Fig. 3 (a) N₂ physisorption isotherms and (b) BJH pore size distribution (desorption branch) of TiO₂ and TiO₂-V₂O₅ samples. Filled and open symbols refer to adsorption and desorption, respectively.

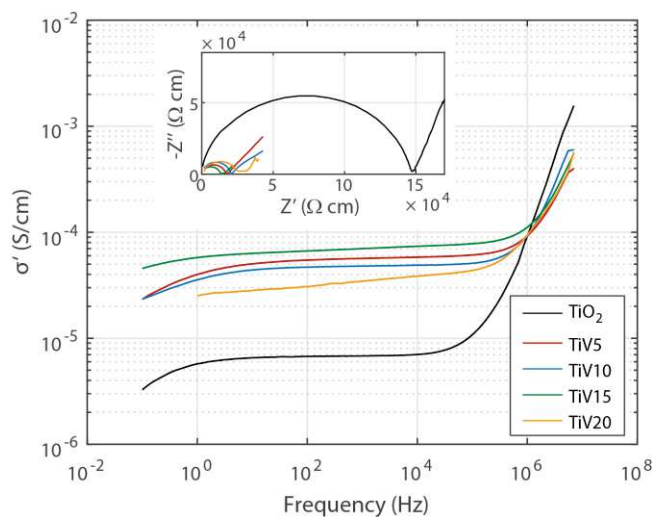


Fig. 4 Conductivity spectra of the as-synthesized TiO₂ and TiO₂-V₂O₅ samples at 293 K. The insert shows the complex plane (Nyquist) plot.

3.2 Electrochemical Performance

The galvanostatic charge-discharge voltage profiles of the different samples for the first cycle are shown in Fig. 5. Firstly, all materials display clear characteristics of the anatase phase of titanium dioxide cycled versus lithium [27]. Both discharge and charge curves show a constant voltage plateau, typical of the two-phase region where anatase and lithium titanate phases coexist during the lithium insertion. As a reminder, lithium insertion into TiO₂ shows three major storage mechanisms: (1) a rapid potential drop to ca. 1.7 V versus Li⁺/Li characteristic of the formation of a solid-solution Li_εTiO₂, where ε depends on particle size [28]; (2) a two-phase reaction between the tetragonal Li_εTiO₂ and the orthorhombic lithium titanate Li_{0.5±δ}TiO₂ inducing a constant-voltage plateau around 1.7 V followed by (3) another two-phase reaction up to 1 V toward rock-salt-type tetragonal LiTiO₂ [29]. The irreversibility of the latter mechanism is usually overcome through nanostructuring of the electrode material, which induces a monophasic reversible pseudo-capacitive interfacial storage [27].

The influence of addition of vanadium oxide can be identified on the first part of the discharge curve, from the open-circuit voltage to approximately 1.8 V versus Li⁺/Li. Around 2.0 V and 2.3 V versus Li⁺/Li, shoulders accounting for 50-100 mAh·g⁻¹ (from TiV5 to TiV20, respectively), indicate the electrochemical activity of a redox couple; these features are in good agreement with the electrochemical behavior of vanadium oxide versus lithium [30]. They are observed only on the first discharge curve and may correspond to the formation of lithiated vanadium oxide particles in the electrode. The absence of these features in the first charge curve indicates that the lithium insertion into vanadates is not reversible within the voltage range used in the present study (2.5-1.2 V vs Li⁺/Li). The presence of vanadium also influences the average voltage of the plateau during the first reduction. From ≈1.73 V versus Li⁺/Li for TiO₂, the voltage is increased by ≈0.04 V versus Li⁺/Li for TiV5 and TiV10, and by ≈0.1 V versus Li⁺/Li for TiV15 and TiV20 (Fig. 5a), while the charge voltage is identical for all materials, thus leading to an improved polarization when the vanadium content increases. As a consequence, the specific capacity of the biphasic plateau associated with the formation of Li_{0.5}TiO₂ is enhanced for TiV5 compared with TiO₂. It is close to the theoretical value (167.5 mAh·g⁻¹) for TiV5 (170 mAh·g⁻¹), while lower for TiO₂ (150 mAh·g⁻¹). The plateau length is lower than 150 mAh·g⁻¹ for TiV10, TiV15, and TiV20, thus indicating that a vanadium content of 5 at% is the best one among the samples prepared. Finally, the last part of the discharge curves, between ca. 1.7 and 1.2 V versus Li⁺/Li, requires a short discussion, as the shape of the curve may evidence the difference of texture, morphology, and surface area between all the samples, from TiO₂ to TiV20. As stated above, monophasic reversible pseudo-capacitive interfacial storage preferentially occurs below 1.7 V versus Li⁺/Li for nanostructured anatase TiO₂ (*vide infra*), while LiTiO₂ irreversibly forms for larger particles. TiO₂ and TiV5 display well-defined mesopores and BET surface areas close to 65 m²·g⁻¹, thus showing significant interfacial lithium storage with associated specific capacities of nearly 100 mAh·g⁻¹. The other materials, TiV10, TiV15, and TiV20, exhibit curve shapes in accordance with larger particle size and smaller surface areas. As a conclusion, the presence of 5 at% of vanadium significantly increases the first discharge specific capacity for TiO₂, from 326 to 375 mAh·g⁻¹. Such an improvement may originate from the moderate textural modification combined with the significant increase in electronic conductivity brought about by the addition of a low vanadium content. This is further confirmed by impedance measurements at the inception of lithiation (Fig. S2 in supplementary material), where TiV5 exhibits an improved global conductivity (Table S1). TiVx materials display lower interfacial and charge transfer resistances, the global resistance increasing with the vanadium content (Table S1).

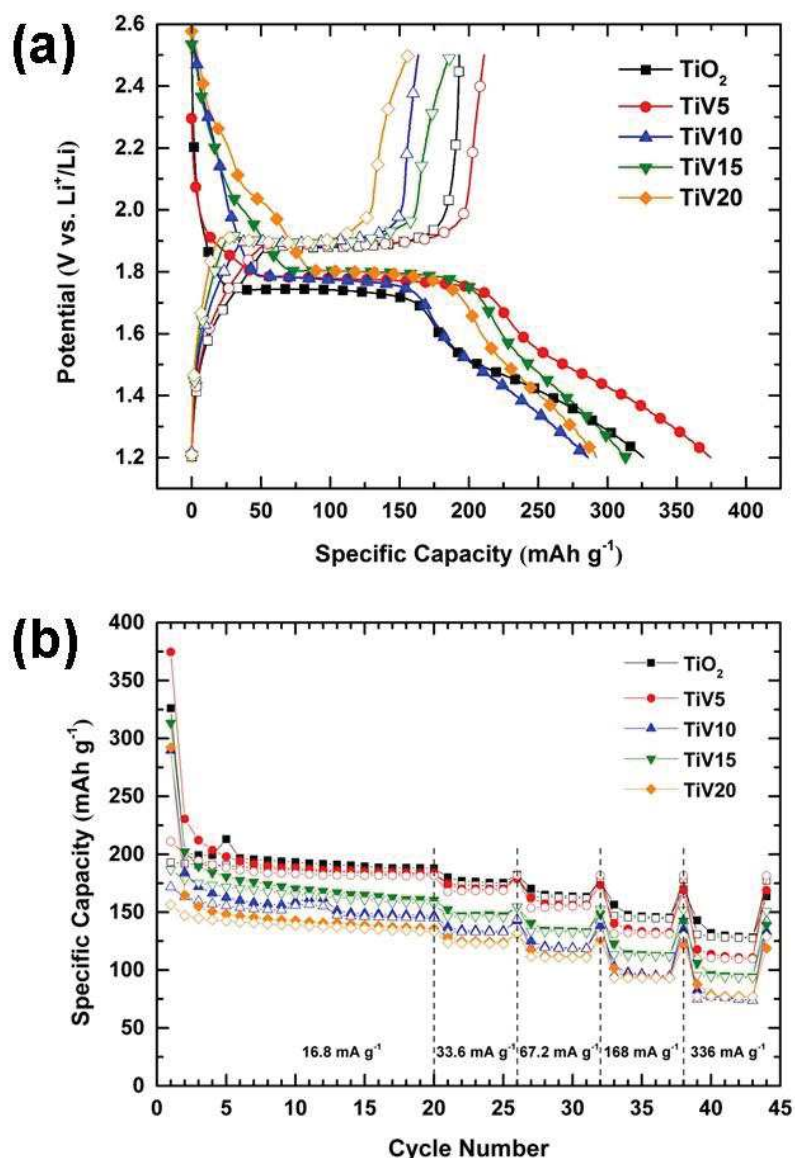


Fig. 5 (a) Initial (first cycle) charge/discharge profiles at a current rate of $16.8 \text{ mA} \cdot \text{g}^{-1}$ ($C/20$) of TiO₂ and TiO₂-V₂O₅ electrodes versus Li; (b) cycling performances at different C rates ($C = 335.6 \text{ mA} \cdot \text{g}^{-1}$) for a voltage window of 1.2-2.6 V versus Li^{+/}Li (filled and open symbols refer to reduction (discharge) and oxidation (charge), respectively).

The cyclability study of all materials is presented in Fig. 5b. It is important to keep in mind that the capacities provided have not been corrected from their vanadium oxide content, as the electrode material is a composite. All samples display moderate capacity retention upon cycling at gradually increasing current rates. TiO₂ and TiV5 display reversible capacities of approximately $185 \text{ mAh} \cdot \text{g}^{-1}$ at $16.8 \text{ mA} \cdot \text{g}^{-1}$, and these values decrease to 125 and $115 \text{ mAh} \cdot \text{g}^{-1}$ at $336 \text{ mA} \cdot \text{g}^{-1}$ for TiO₂ and TiV5, respectively. When the electrodes are cycled back to $16.8 \text{ mA} \cdot \text{g}^{-1}$, the initial value of $185 \text{ mAh} \cdot \text{g}^{-1}$ is recovered for TiV5, while the reversible capacity for TiO₂ remains lower. The improvements in terms of electronic conductivity brought by the addition of a small amount of vanadium are not transposed to the galvanostatic results. At higher V loading, the specific capacity is lower, suggesting that the scherbinaita crystals do not contribute to the lithium insertion under this conditions and that the vanadate surface species do not improve significantly the ionic diffusion at the solide-electrolyte interface.

Interestingly, comparison to the literature shows that the undoped TiO₂ prepared by NHSG is a promising material, considering the simplicity and low cost of the synthesis. As shown in

Fig. 5b, our mesoporous hierarchical TiO₂ showed a specific reversible capacity of 145 and 128 mAh·g⁻¹ after 5 cycles at a current density of $C/2$ and C , respectively ($C = 336 \text{ mA}\cdot\text{g}^{-1}$), with good coulombic efficiency (99.3 % after 5 cycles at C). In addition, the capacity fade was moderate, from 200 to 187 mAh·g⁻¹ for the 2nd and 20th cycle (at $C/20$), respectively. As detailed in Table 3, these values are comparable to those reported for various nanostructured anatase TiO₂ (mesoporous microspheres, hollow spheres, nanosheets, nanorods, or nanospindles), but significantly lower than the values reported for TiO₂ nanotubes.

It must be noted that comparison for such high surface area materials is difficult, as the cycling "history" can have a major influence on the capacity measured, due to the large contribution of pseudo-capacitive interfacial storage (in addition to bulk insertion). Thus, cycling directly at high rates emphasizes interfacial storage [27], leading to significantly higher capacity. For instance, the specific capacity of high surface area hierarchical nanoporous TiO₂ anatase measured after 10 cycles at a rate of $1 C$ but after 20 cycles at $C/5$ reached $\approx 180 \text{ mAh}\cdot\text{g}^{-1}$, compared to $\approx 320 \text{ mAh}\cdot\text{g}^{-1}$ when cycled 30 times directly at $1 C$ [27].

Table 3 Performances of selected nanostructured anatase TiO₂ materials as anode in lithium batteries.

Type of material	Synthetic method	S _{BET} (m ² ·g ⁻¹)	Capacity (mAh·g ⁻¹)	Conditions	Ref.
Mesoporous microspheres	Template-free hydrolytic sol-gel	117	≈ 145	5 th cycle at $0.6C$	[31]
Mesoporous microspheres	TiO ₂ -CdSO ₄ composite intermediate	130	≈ 165	5 th cycle at C	[10]
Microspheres built of nanosheets	Solvothermal	170	≈ 185 ≈ 145	5 th cycle at $0.5C$ 5 th cycle at $2.5C$	[32]
Hollow spheres	Hard-templated sol-gel process	/	≈ 160	20 th cycle at $0.18C$	[33]
Spindle-shaped mesocrystals	Non-aqueous solvothermal	114	≈ 160 ≈ 140	5 th cycle at $0.5C$ 5 th cycle at C	[34]
Nanospindles	Hydrothermal process from tubular titanates	/	≈ 145	5 th cycle at C	[35]
Nanorods	Reaction in NaOH/KOH of a TiO ₂ nanopowder	99	≈ 180	5 th cycle at $0.36C$	[36]
Nanotubes	Hydrothermal process	/	≈ 220	5 th cycle at $0.11C$	[37]
Vertically aligned amorphous nanotubes	Anodization of Ti foils	/	≈ 250	10 th cycle at $C/3$	[38]

4 Conclusions

In summary, mesoporous TiO₂ anatase with a hierarchical structure, consisting of 10-25 nm nanoparticles that aggregate to form spherical submicronic particles, was obtained by a straightforward non-hydrolytic sol-gel route (ether route) in the absence of additives or solvent. These mesoporous TiO₂ microspheres showed fairly good electrochemical

performances. TiO₂-V₂O₅ samples were prepared with the aim of improving these performances. Although the electrical conductivity of the TiO₂-V₂O₅ samples was significantly increased compared to TiO₂, the reversible capacity beyond the first cycle was not improved. Increasing the V loading above *ca.* 5 at% simply resulted in the growth of V₂O₅ crystals, decreasing the specific surface area of the electrode material and its specific capacity.

Several directions should be explored to further improve the electrochemical performances of non-hydrolytic TiO₂, such as decreasing the nanoparticles size by playing on the synthesis and/or calcination temperatures (to increase Li-ion insertion), doping with other elements, or coating with carbon (to improve electron and ion transfer).

Acknowledgments This work was supported by the “Centre National de la Recherche Scientifique” and the University of Montpellier, and through a PhD grant of the “Consejo Nacional de Ciencia y Tecnología” in Mexico.

References

- Mutin PH, Vioux A (2009) Nonhydrolytic processing of oxide-based materials: simple routes to control homogeneity, morphology, and nanostructure. *Chem Mater* 21:582-596
- Mutin PH, Vioux A (2013) Recent advances in the synthesis of inorganic materials via non-hydrolytic condensation and related low-temperature routes. *Journal of Materials Chemistry A* 1:11504-11512
- Pinna N, Niederberger M (2008) Surfactant-free nonaqueous synthesis of metal oxide nanostructures. *Angew Chem, Int Ed* 47:5292-5304
- Bilecka I, Niederberger M (2010) New developments in the nonaqueous and/or non-hydrolytic sol-gel synthesis of inorganic nanoparticles. *Electrochim Acta* 55:7717-7725
- Debecker DP, Hulea V, Mutin PH (2013) Mesoporous mixed oxide catalysts via non-hydrolytic sol-gel: A review. *Applied Catalysis A* 451:192-206
- Bilecka I, Hintennach A, Rossell MD, Xie D, Novak P, Niederberger M (2011) Microwave-assisted solution synthesis of doped LiFePO₄ with high specific charge and outstanding cycling performance. *J Mater Chem* 21:5881-5890
- Yu S-H, Pucci A, Hertrich T, Willinger M-G, Baek S-H, Sung Y-E, Pinna N (2011) Surfactant-free nonaqueous synthesis of lithium titanium oxide (LTO) nanostructures for lithium ion battery applications. *J Mater Chem* 21:806-810
- Song T, Paik U (2016) TiO₂ as an active or supplemental material for lithium batteries. *J Mater Chem A* 4:14-31
- Sudant G, Baudrin E, Larcher D, Tarascon J-M (2005) Electrochemical lithium reactivity with nanotextured anatase-type TiO₂. *J Mater Chem* 15:1263-1269
- Guo YG, Hu YS, Sigle W, Maier J (2007) Superior electrode performance of nanostructured mesoporous TiO₂ (Anatase) through efficient hierarchical mixed conducting networks. *Adv Mater (Weinheim, Ger)* 19:2087-2091
- Sondergaard M, Shen Y, Mamakhel A, Marinaro M, Wohlfahrt-Mehrens M, Wonsyld K, Dahl S, Iversen BB (2015) TiO₂ nanoparticles for Li-ion battery anodes: mitigation of growth and irreversible capacity using LiOH and NaOH. *Chem Mater* 27:119-126
- Maier J (2005) Nanoionics: ion transport and electrochemical storage in confined systems. *Nat Mater* 4:805-815
- Arico AS, Bruce P, Scrosati B, Tarascon J-M, van Schalkwijk W (2005) Nanostructured materials for advanced energy conversion and storage devices. *Nat Mater* 4:366-377
- Guo Y-G, Hu Y-S, Maier J (2006) Synthesis of hierarchically mesoporous anatase spheres and their application in lithium batteries. *Chem Commun (Cambridge, U K)* 2006:2783-2785
- Deng D, Kim MG, Lee JY, Cho J (2009) Green energy storage materials: Nanostructured TiO₂ and Sn-based anodes for lithium-ion batteries. *Energy & Environmental Science* 2:818-837
- Ge M, Cao C, Huang J, Li S, Chen Z, Zhang K-Q, Al-Deyab SS, Lai Y (2016) A review of one-dimensional TiO₂ nanostructured materials for environmental and energy applications. *Journal of Materials Chemistry A*. doi:10.1039/C5TA09323F
- Yan X, Wang Z, He M, Hou Z, Xia T, Liu G, Chen X (2015) Titania nanomaterial as anode for lithium-ion rechargeable batteries. *Energy Technol (Weinheim, Ger)* 3:801-814
- Zhang Y, Jiang Z, Huang J, Lim LY, Li W, Deng J, Gong D, Tang Y, Lai Y, Chen Z (2015) Titanate and titania nanostructured materials for environmental and energy applications: a review. *RSC Adv* 5:79479-79510
- Chen JS, Archer LA, Wen Lou X (2011) SnO₂ hollow structures and TiO₂ nanosheets for lithium-ion batteries. *J Mater Chem* 21:9912-9924
- Anh LT, Rai AK, Thi TV, Gim J, Kim S, Shin E-C, Lee J-S, Kim J (2013) Improving the electrochemical performance of anatase titanium dioxide by vanadium doping as an anode material for lithium-ion batteries. *J Power Sources* 243:891-898
- Fehse M, Cavaliere S, Lippens PE, Savych I, Iadecola A, Monconduit L, Jones DJ, Roziere J, Fischer F, Tessier C, Stievano L (2013) Nb-Doped TiO₂ nanofibers for lithium ion batteries. *J Phys Chem C* 117:13827-13835

22. Popa AF, Mutin PH, Vioux A, Delahay G, Coq B (2004) Novel non-hydrolytic synthesis of a V₂O₅-TiO₂ xerogel for the selective catalytic reduction of NO_x by ammonia. *Chem Commun*:2214-2215
23. Debecker DP, Bouchmella K, Delaigle R, Eloy P, Poleunis C, Bertrand P, Gaigneaux EM, Mutin PH (2010) One-step non-hydrolytic sol-gel preparation of efficient V₂O₅-TiO₂ catalysts for VOC total oxidation. *Appl Catal, B* 94:38-45
24. Ohsaka T, Izum F, Fujiki Y (1978) Raman Spectrum of Anatase, TiO₂. *J Raman Spectrosc* 7:321-324
25. Santangelo S, Messina G, Faggio G, Willinger MG, Pinna N, Donato A, Arena A, Donato N, Neri G (2010) Micro-Raman investigation of vanadium-oxide coated tubular carbon nanofibers for gas-sensing applications. *Diamond Relat Mater* 19:590-594
26. Sidebottom DL (2009) Colloquium: Understanding ion motion in disordered solids from impedance spectroscopy scaling. *Rev Modern Phys* 81:999-1014
27. Shin J-Y, Samuelis D, Maier J (2011) Sustained lithium-storage performance of hierarchical, nanoporous anatase TiO₂ at high rates: emphasis on interfacial storage phenomena. *Adv Funct Mater* 21:3464-3472
28. Wagemaker M, Borghols WJH, Mulder FM (2007) Large impact of particle size on insertion reactions. A case for anatase Li_xTiO₂. *J Am Chem Soc* 129:4323-4327
29. Lafont U, Carta D, Mountjoy G, Chadwick AV, Kelder EM (2009) In situ structural changes upon electrochemical lithium insertion in nanosized anatase TiO₂. *Journal of Physical Chemistry C* 114:1372-1378
30. Reddy MV, Sharma N, Adams S, Rao RP, Peterson VK, Chowdari BVR (2015) Evaluation of undoped and M-doped TiO₂, where M = Sn, Fe, Ni/Nb, Zr, V, and Mn, for lithium-ion battery applications prepared by the molten-salt method. *RSC Adv* 5:29535-29544
31. Wang J, Zhou Y, Hu Y, O'Hayre R, Shao Z (2011) Facile synthesis of nanocrystalline TiO₂ mesoporous microspheres for lithium-ion batteries. *J Phys Chem C* 115:2529-2536
32. Chen JS, Tan YL, Li CM, Cheah YL, Luan D, Madhavi S, Boey FYC, Archer LA, Lou XW (2010) Constructing hierarchical spheres from large ultrathin anatase TiO₂ nanosheets with nearly 100% exposed (001) facets for fast reversible lithium storage. *J Am Chem Soc* 132:6124-6130
33. Wang J, Bai Y, Wu M, Yin J, Zhang WF (2009) Preparation and electrochemical properties of TiO₂ hollow spheres as an anode material for lithium-ion batteries. *J Power Sources* 191:614-618
34. Ye J, Liu W, Cai J, Chen S, Zhao X, Zhou H, Qi L (2011) Nanoporous anatase TiO₂ mesocrystals: additive-free synthesis, remarkable crystalline-phase stability, and improved lithium insertion behavior. *J Am Chem Soc* 133:933-940
35. Qiu Y, Yan K, Yang S, Jin L, Deng H, Li W (2010) Synthesis of size-tunable anatase TiO₂ nanospindles and their assembly into anatase@titanium oxynitride/titanium nitride-graphene nanocomposites for rechargeable lithium ion batteries with high cycling performance. *ACS Nano* 4:6515-6526
36. Bao S-J, Bao Q-L, Li C-M, Zhi-Li D (2007) Novel porous anatase TiO₂ nanorods and their high lithium electroactivity. *Electrochem Commun* 9:1233-1238
37. Xu J, Jia C, Cao B, Zhang WF (2007) Electrochemical properties of anatase TiO₂ nanotubes as an anode material for lithium-ion batteries. *Electrochim Acta* 52:8044-8047
38. Wu QL, Li J, Deshpande RD, Subramanian N, Rankin SE, Yang F, Cheng Y-T (2012) Aligned TiO₂ nanotube arrays as durable lithium-ion battery negative electrodes. *J Phys Chem C* 116:18669-18677

Supplementary material

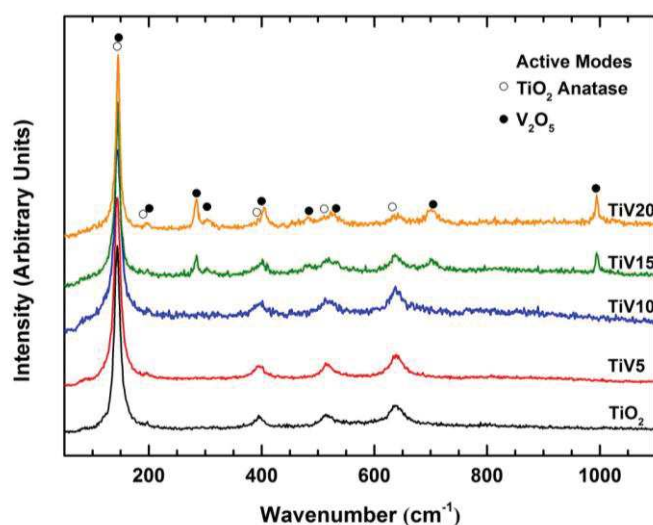


Fig. S1 Raman spectra of the TiO₂ and TiO₂-V₂O₅ samples.

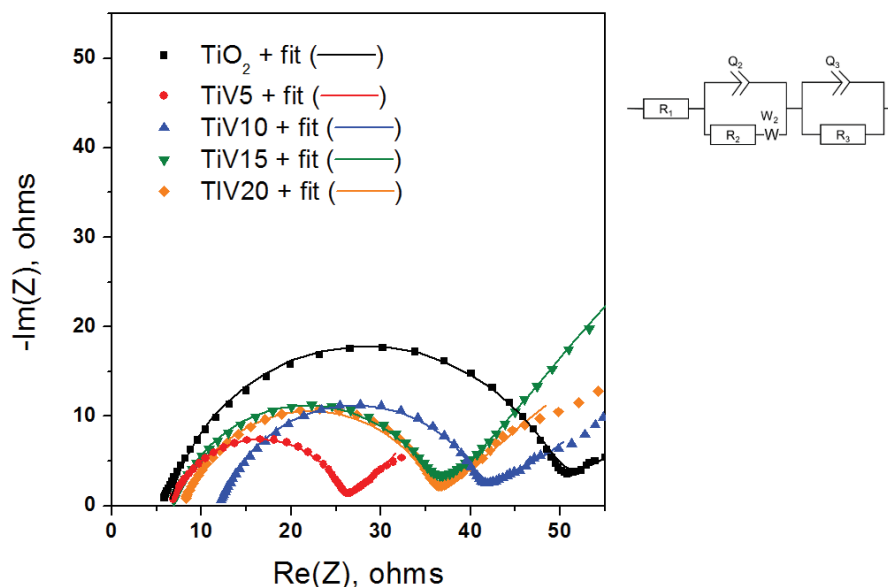


Fig. S2 Complex impedance plots of TiO₂, TiV5, TiV10, TiV15, and TiV20 electrodes in half-cells versus lithium. Plots were obtained in potentiostatic mode at 1.8 V vs Li⁺/Li after 2 h relaxation time before the lithiation. The equivalent circuit used for the analysis of the complex impedance plots is shown on the top right hand corner.

Table S1. Fitted resistance values from impedance plots of TiO₂, TiV5, TiV10, TiV15, and TiV20 electrodes in half-cell versus lithium.

Resistances (Ω)	TiO ₂	TiV5	TiV10	TiV15	TiV20
R1	6.32	6.28	12.23	7.003	7.982
R2	52.17	0.43	4.193	28.75	41.43
R3	42.7	19.14	29.87	15.94	27.34
Total R	101.188	25.845	46.293	51.693	76.752

3.1.2 Complementary characterizations of the samples from the published article: *J. Sol-Gel Sci. Technol.*, 2016, 79, 270-278

3.1.2.1 Thermogravimetric analysis of TiO₂-V₂O₅ xerogels

It was interesting to follow the evolution of the TiO₂-V₂O₅ system by thermogravimetric analysis in order to see if the VOCl₃, used as vanadium precursor, have an influence over the reaction. Therefore, TGA of TiO₂-V₂O₅ mixed oxides xerogels was performed and are presented in Figure 3.1. Considering the melting point of V₂O₅ (690 °C), analyses were recorded until 650 °C in order to avoid its fusion. One may observe that the increase in the amount of vanadium promotes a larger weight loss in mixed oxides by comparison to the pure TiO₂ sample. To understand this behavior, one must first keep in mind that VOCl₃, used as vanadium source during synthesis, is a Lewis acid that may catalyse side reactions.

Arnal *et al* [28] studied the NHSG etherolysis/condensation system of TiCl₄-ⁱPr₂O and also the direct condensation between TiCl₄ and Ti(OⁱPr)₄. That work showed the presence of two alkoxylation steps, having a faster rate than the first one due to dilution of chloroisopropoxide species by the ⁱPrCl formed. They evidenced the autocatalytic character of the condensation because of the formation of oxochloroisopropoxides intermediates. Authors also confirmed that the true molecular precursors of this NHSG process are in fact a mixture of titanium

chloroisopropoxides in equilibrium. Besides, Acosta *et al* [39] prepared alumina gels in a similar way (*i.e.* NHSG reaction between aluminium alkoxides and aluminium halides) and discussed the complexity of the reaction suggesting the alkene elimination as a side reaction.

That said, here, VOCl₃ is added into the system thus giving a mixture of titanium and vanadium chloroisopropoxides precursors more complex, than the one exposed by Arnal *et al* [28]. Keeping in mind that VOCl₃ is commonly used as a catalyst in industry for the ethylene-propylene copolymerization [231-233] and that the alkene elimination mechanism is present [39], a possible hypothesis of the effect of VOCl₃ is the polymerization of any alkene resulting from some dehydrochlorination of the by-products of the NHSG reaction. It is also observed that the weight loss becomes constant after 500 °C showing that all organic compounds are eliminated, guaranteeing that the final product only correspond to the mixed oxides. The organic compound percentage increases from *ca.* 10% for TiO₂ and TiV5 to 13% for TiV20.

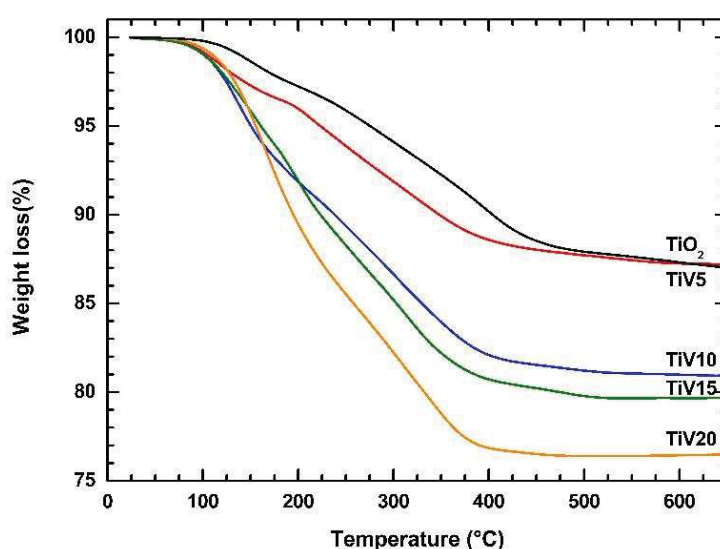


Figure 3.1 Thermogravimetric analysis of xerogels of TiO₂ and TiO₂-V₂O₅ mixed oxides.

3.1.2.2 Wettability analysis of electrodes by contact angle measurements

An important feature to consider during the electrode preparation is that electrodes need a good wettability towards the electrolyte for a well electrochemical performance. Keeping in mind that the specific surface area of TiO₂-V₂O₅ mixed oxides decreases with the vanadium loading, it may also modify the wettability of the electrodes due to capillarity effects. Therefore, contact angle measurements were performed using both water and the electrolyte (*i.e.* 1 M LiPF₆ in PC:EC:3DMC vol. with 5% FEC and 1% VC), results are given in Figure 3.2. Tests were performed over glass and copper sheet (*i.e.* the same used as current collector for the electrodes) for comparison. All electrodes formulations exhibit good wettability towards the electrolyte, contact angle measured was around 10° for all electrodes; there are not significant differences among the different vanadium loadings. Regarding the references, glass and copper sheet exhibit average contact angles of 42° and 52° respectively towards the electrolyte.

On the other hand, contact angles measured after the deposition of the water droplet were always higher, even for the references. Here, vanadium loading seems to have an impact towards the contact angle. All TiO₂-V₂O₅ mixed oxides possess average contact angles above

100°; while pure TiO₂ electrode films present a similar behavior than the copper sheet of *ca.* 89°. The best wettability towards water corresponds to glass (74°). Considering that all electrode films were prepared by the same way (*i.e.* active material: acetylene black: PVDF; 80:14:6 wt% in NMP), the different behavior may be linked to the surface area of samples. TiO₂ sample exhibit higher specific surface area and pore volume than the TiO₂-V₂O₅ mixed oxides. Thus, water may be easily adsorbed by capillarity in the TiO₂ electrode film.

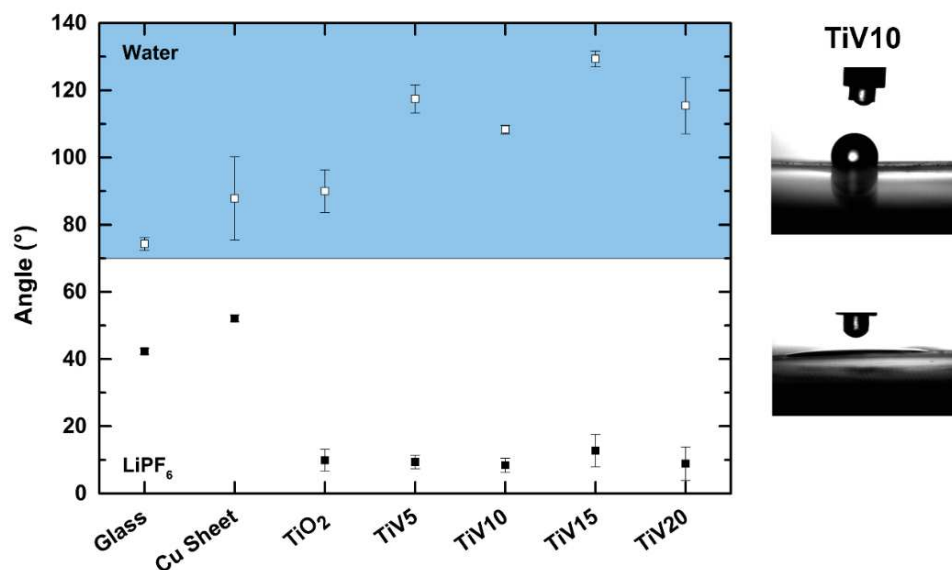


Figure 3.2 Contact angle measured after deposition of a water drop (bleu section) or an electrolyte drop (white section) over glass, copper sheet (current collector) and electrode films; two images corresponding to the droplet deposition (water up and electrolyte down) over TiV10 electrode film are presented on the right side.

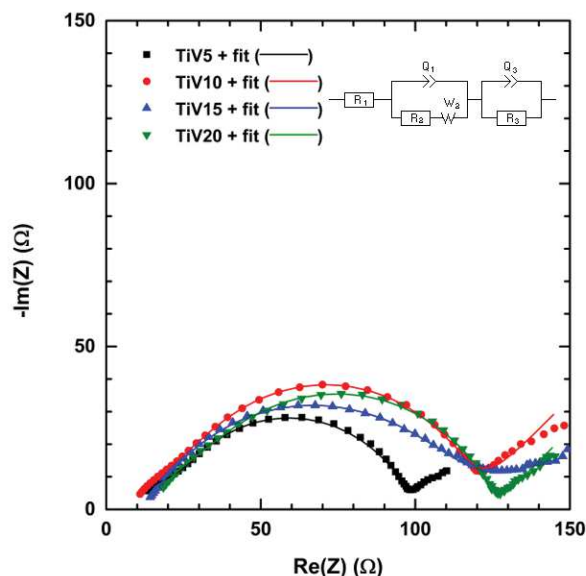
3.1.2.3 PEIS evaluation of mechanically prepared TiO₂-V₂O₅ mixed oxides and galvanostatic cycling of a commercial TiO₂

For comparison, mechanically prepared TiO₂-V₂O₅ mixed oxides were formulated by adding the corresponding amount of TiO₂ and V₂O₅, each prepared by the NHSG ¹Pr₂O route. Corresponding electrodes films were prepared and coin cells assembled using these mechanically oxides as active materials. Experiences were carried out under the same conditions used for the NHSG TiO₂-V₂O₅ mixed oxides (measures at 1.8 V *versus* Li⁺/Li after 2 h relaxation time before lithiation).

Complex impedance plots are presented in Figure 3.3 and values corresponding to the fitting plot are shown in Table 3.1. Those mechanically prepared mixed oxides display global resistance similar, even higher, to TiO₂ electrode (*ca.* 101 Ω) showing no improvement at all compared to the mixed oxides prepared by NHSG. These values also suggest a certain doping degree of vanadates species into the TiO₂ framework, enhancing conductivity as described by Reddy *et al* [143], effect that is not observed for materials obtained by simple mechanically mixing of the two oxides. It also reinforces the fact that the TiV5 exhibits the best electrochemical performances among the four TiV_x formulations.

Table 3.1 Fitted resistance values from impedance plots of TiO₂-V₂O₅ mechanically mixed electrodes in half-cell versus lithium.

Resistances (Ω)	TiV5	TiV10	TiV15	TiV20
R1	11.3	7.98	10.29	15.69
R2	8.95	18.83	57.46	8.97
R3	76.89	89.64	74.29	100.9
Total R	97.14	116.45	142.04	125.56

**Figure 3.3** Complex impedance plots of TiO₂-V₂O₅ mechanically mixed electrodes in half-cells versus lithium. Plots were obtained in potentiostatic mode at 1.8 V vs Li⁺/Li after 2 h relaxation time before the lithiation. The equivalent circuit used for the analysis of the complex impedance plots is shown on the top right hand corner.

In the published article (section 3.1.1), discussion is focused essentially on the comparison between different nanostructured TiO₂. It has been showed the difficulties for a direct comparison between samples due to the cycling “history” and the different current densities used in literature. Thus, a direct comparison of the electrochemical stability between a commercial TiO₂ anatase (*i.e.* Sigma Aldrich) and the nanostructured NHSG TiO₂ is presented in this section. Both samples were galvanostatic cycled under the same conditions (*i.e.* current rates going from 16.8 to 336 mA·g⁻¹ between 1.2-2.5 V versus Li⁺/Li). This commercial TiO₂ sample have a comparable particle size (<25 nm) to the NHSG mixed oxides and a slightly smaller specific surface area (55 m²·g⁻¹) than the pure NHSG TiO₂ anatase.

The cycling performance of both TiO₂ samples is presented in Figure 3.4. It is clearly observed that, even if for the few first cycles TiO₂ from Sigma Aldrich displays higher capacities, the NHSG TiO₂ posses a better stability all along the cycling at different current rates. In addition, at a constant rate of 336 mA·g⁻¹ (corresponding to 1C), capacity is practically lost for the commercial sample. This comparison brings out the fact that not all nanosized TiO₂ particles are optimized for Li-ion battery applications.

These results evidenced that the nanostructured TiO₂ and TiO₂-V₂O₅ mixed oxides and the close interaction of the former, bring appropriated conditions for lithiation/delithiation processes.

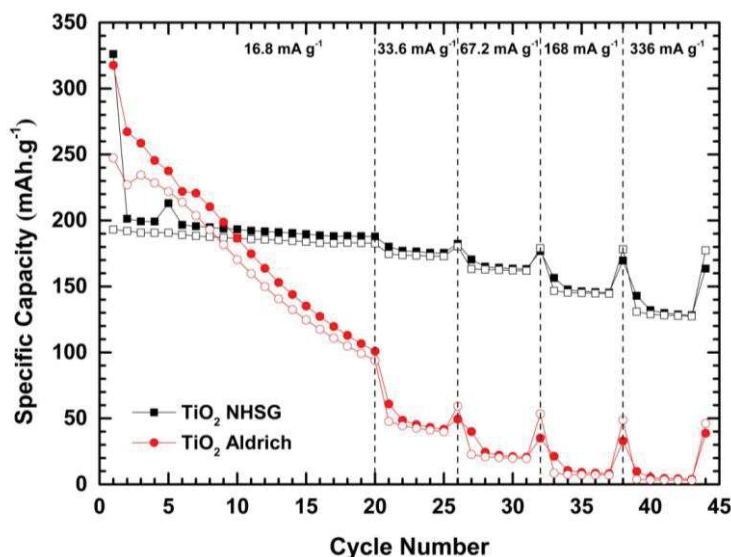


Figure 3.4 NHSG and commercial TiO₂ cycling performances at different C rates ($C=335.6 \text{ mA}\cdot\text{g}^{-1}$) for a voltage window of 1.2-2.6 V versus Li⁺/Li (filled and open symbols refer to reduction (discharge) and oxidation (charge), respectively).

3.1.3 Optimization of synthesis conditions and influence of the heat treatment temperature over the anatase-rutile TiO₂ phase transformation

3.1.3.1 Influence of the synthesis time over the preparation of TiO₂

Preliminary works synthesizing TiO₂ using NHSG chemistry were performed in order to determine the best conditions for the elaboration of the TiO₂-V₂O₅ mixed oxides. TiO₂ was prepared by the NHSG ¹Pr₂O route and samples were kept for different periods of time (1 to 8 days) under autogenous pressure. Xerogels and 500 °C heat-treated TiO₂ samples were then analyzed. Starting with the X-ray diffraction, patterns were obtained for both xerogels and calcinated TiO₂ samples (Figure 3.5). One can distinguish the formation of anatase crystal phase of TiO₂ in all samples; it is interesting to see well defined reflection corresponding to the formation of anatase TiO₂ after only 1 day of reaction. Calcinated samples exhibit, as expected, most well defined reflections after the heat treatment.

Crystallite size was determined using the Scherrer equation and values are presented in Table 3.2. Crystallite size of xerogels do not vary a lot when increasing the time of reaction, all of them exhibit sizes of ≈ 6 nm. These results suggest that TiO₂ crystals in the xerogel can be considered as nuclei for further growth of TiO₂ particles during the calcination step. Therefore, the calcination will have a major impact over the crystals growth, this point in particular is discussed in section 3.1.3.2. Regarding the crystallite size for calcinated samples, they vary between 13-15 nm and this slight difference can be considered as not significant.

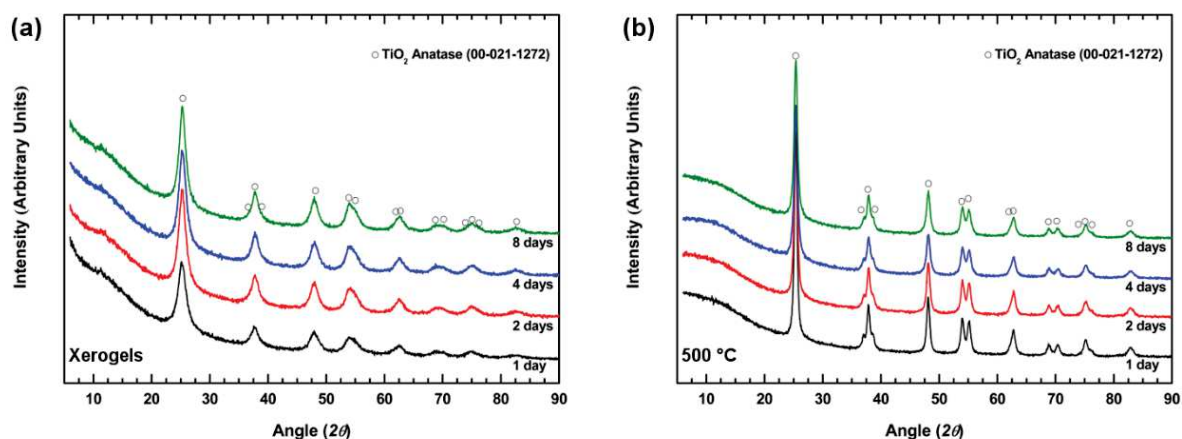


Figure 3.5 Powder X-ray diffraction patterns of TiO₂ xerogels (a) and calcinated TiO₂ (b) for different reaction times.

Table 3.2 Organic content present in xerogels, crystallite size of both xerogels and calcinated TiO₂ and textural data of TiO₂ from different synthesis periods.

Sample	Xerogel		Calcination at 500 °C			
	Crystallite size ^a (nm)	Organic ^b (%)	Crystallite size ^a (nm)	S _{BET} ^c (m ² ·g ⁻¹)	V _p ^d (cm ³ ·g ⁻¹)	D _p ^e (nm)
1 day	6	15.0	15	63	0.14	6.4
2 days	6	11.3	14	65	0.15	6.6
4 days	6	10.8	13	68	0.17	5.7
8 days	6	9.8	13	56	0.10	4.9

^aderived from XRD data using Scherrer equation, ^bderived from TGA analysis between the 200-900 °C range, ^cspecific surface area, ^dtotal pore volume, ^eBJH average pore diameter calculated from desorption branch.

Xerogels were analyzed by TGA in Figure 3.6 and weight loss percentage corresponding to organic compounds are summarized in Table 3.2. The former was determined in the 200-900 °C range and it decreases with increasing the time of reaction. As mentioned before, NHSG reaction between ⁱPr₂O and TiCl₄ gives different oxochloroisopropoxides intermediates which are, in fact, the precursors for TiO₂. Therefore, the following of the weight loss evolution by TGA of this binary system brings some insights about the kinetics of the reaction.

It has been settled by Arnal *et al* [28] that this system exhibits two alkoxydation steps, the first one ending at around 3h after reaction begins and the second one is a hundred of times slower. Besides, condensation was not detected at 28 h at room temperature. Thus, considering that oxochloroisopropoxides intermediates are formed at earlier steps of the reaction and that condensation step starts much later, the main lost observed in the TGA graphs (Figure 3.6) may be associated to the elimination of the first ones. Therefore, weight loss will decrease along with the time as these reaction intermediates will be consumed for the formation of TiO₂. Results are consistent with this observation, giving weight loss from 15.0 to 9.8 %, corresponding to day 1 and day 8 respectively with a yield of almost 90 % at the end of the 4th day.

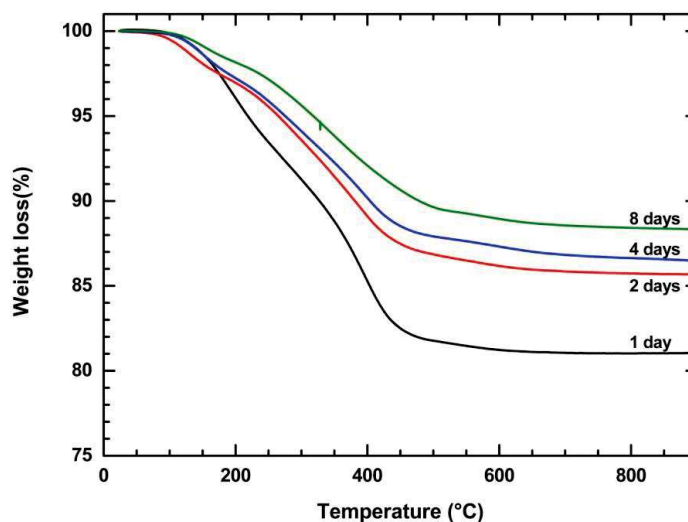


Figure 3.6 Thermogravimetric analysis of TiO₂ xerogels for different reaction times.

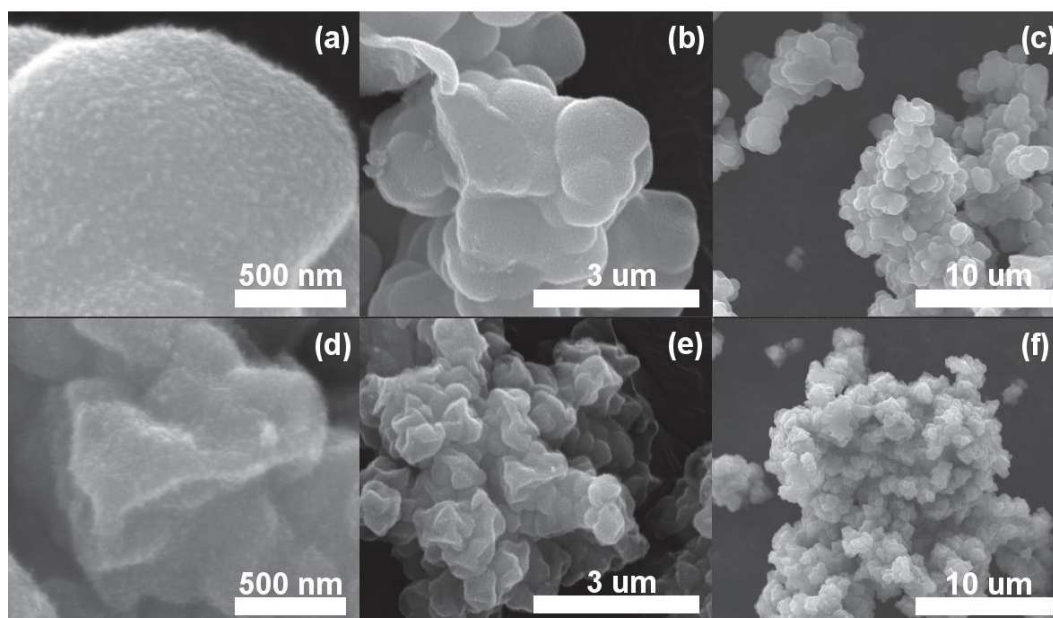


Figure 3.7 SEM micrographs at different magnifications of NHSG ¹Pr₂O derived TiO₂ after 1 day (a-c) and 8 days (d-f) of synthesis.

Scanning electron micrographs of TiO₂ corresponding to day 1 and day 8 are displayed in Figure 3.7. After 1 day, TiO₂ already exhibit the hierarchical texture described before for the mixed oxides after 4 days of reaction (Fig. 2 in section 3.1.1). It corresponds to aggregated primary nanoparticles forming spherical clusters. This morphology is slightly modified at day 8, the spherical shape of aggregates observed until day 4 (Fig. 2 in section 3.1.1) becomes less spherical (Figure 3.7). One can see that the surface of clusters starts to flatten. Unfortunately, microscope resolution does not allow to determine the size of the primary particles in order to verify the crystallite sizes determined by DRX.

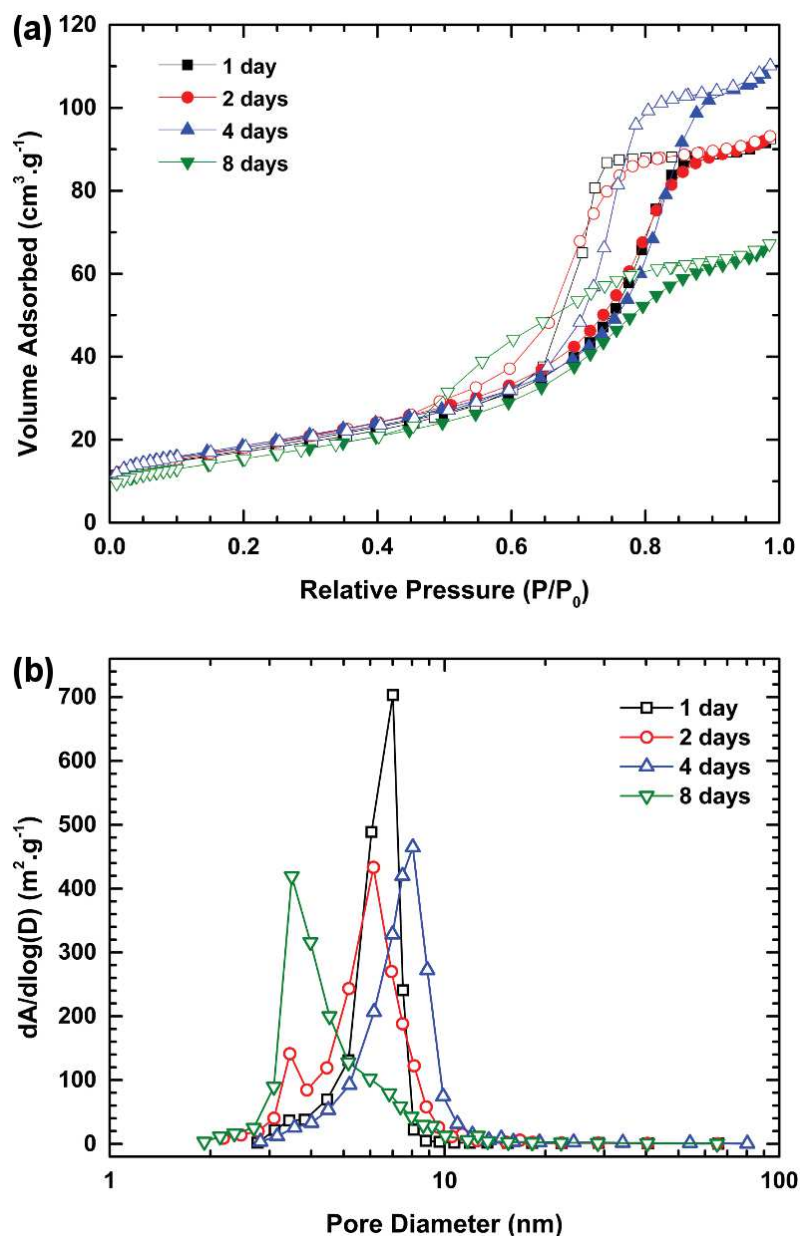


Figure 3.8 (a) Molecular nitrogen physisorption isotherms and (b) BJH pore size distribution (desorption branch) of TiO₂ prepared at different reaction times. Filled and open symbols refer to adsorption and desorption, respectively.

Porosimetry data of samples at different time of reaction are presented in Figure 3.8. They all exhibit type IV isotherms according to the IUPAC classification, corresponding to mesoporous materials. Pore size distributions confirm the presence of well defined mesopores with diameters around 7 nm, except for the 8 days sample in which pore size distribution goes towards smaller values. Textural data in Table 3.2 evidence a slight increment in the specific surface area from day 1 to day 4, then it decreases as observed for the day 8 TiO₂, going from 68 m²·g⁻¹ to 56 m²·g⁻¹. This evolution in the specific surface area can be correlated to the change in the morphology of the aggregates between days 4 and 8, as presented by SEM images (Figure 3.7), given that edges of this sample start to be flattened instead of rounded as observed until day 4 (Fig. 2 in section 3.1.1).

In summary, 4 days of reaction seems to be the best choice for the preparation of the mixed oxides. The time of reaction does not have any effect for the crystallite growth; however, morphology and surface area evidence some sensitivity to the reaction time. Four days

synthesis leads to the higher specific surface area with good mesoporosity. Additionally, weight loss does not drastically change during the period between 2 and 8 days and the morphology of micronsize aggregated spheres formed by primary nanoparticles is conserved.

3.1.3.2 Influence of calcination temperature over crystallinity and texture of TiO₂ and TiO₂-V₂O₅ mixed oxides

Once synthesis conditions were chosen, the heat treatment temperature needed to be determined. Therefore, TiO₂-V₂O₅ mixed oxides were synthesized by the NHSG ¹Pr₂O route and the evolution of their properties against calcination temperature was studied. Xerogels of TiO₂ and TiO₂-V₂O₅ were calcinated at different temperatures from 350 °C to 650 °C. Temperature was not further increased because of TiO₂ anatase to rutile transformation and the V₂O₅ melting point.

The verification of the crystal phase was determined at first by XRD analysis. Diffractograms of representative samples (TiO₂, TiV10 and TiV20), presented in Figure 3.9, show the TiO₂ anatase crystal phase (JCPDS 00-021-1272). Moreover, for the TiO₂-V₂O₅ mixed oxides at 600 °C, one can distinguish some traces of V₂O₅ scherbinaite (JCPDS 00-041-1426) even in samples which does not present it at 500 °C (*e.g.* TiV10). Then, at 650 °C all TiO₂-V₂O₅ mixed oxides present the characteristic reflections of the TiO₂ rutile crystal phase (JCPDS 00-021-1276). The formation of TiO₂ rutile is a clear evidence of a certain amount of vanadium doping. Indeed, it has been reported that vanadium doping promotes the anatase to rutile transformation at lower temperatures. The vanadium valence creates oxygen vacancies into the TiO₂ crystal structure which serve as nucleation centers and, polymorphe transition becomes easier [167, 180, 234].

Values of crystallite sizes for TiO₂-V₂O₅ (Table 3.3) are between 4-6 nm, the slight difference among the samples cannot be considered significant. However, samples containing higher vanadium loading express the smallest sizes: 4 nm for TiV15 and TiV20; while 6 nm for pure TiO₂. Crystallite size of TiV_x samples increases exponentially along with the calcination temperature until 600°C; in the case of pure TiO₂ sample, it continues increasing at 650 °C. Mixed oxides samples exhibit bigger crystallites sizes compared to the pure TiO₂ sample, this observation is consistent with literature. It has been reported that vanadium promotes sintering of TiO₂ anatase leading to bigger TiO₂ anatase and also rutile particles than pure TiO₂ prepared under the same synthesis conditions [235, 236].

By contrast to pure TiO₂ sample, all four TiV_x mixed oxides expose a slight decrease in the crystallite size at 650 °C. As a reminder, all these samples exhibit reflections corresponding to TiO₂ rutile crystal phase; moreover, the anatase to rutile transformation is followed by a shrinkage of around 8% (*i.e.* breaking and rearrangement of Ti-O bonds) [167, 178, 237]. Therefore, this reduction of the crystallite size of the TiO₂ anatase nanoparticles is the result of its transformation into rutile.

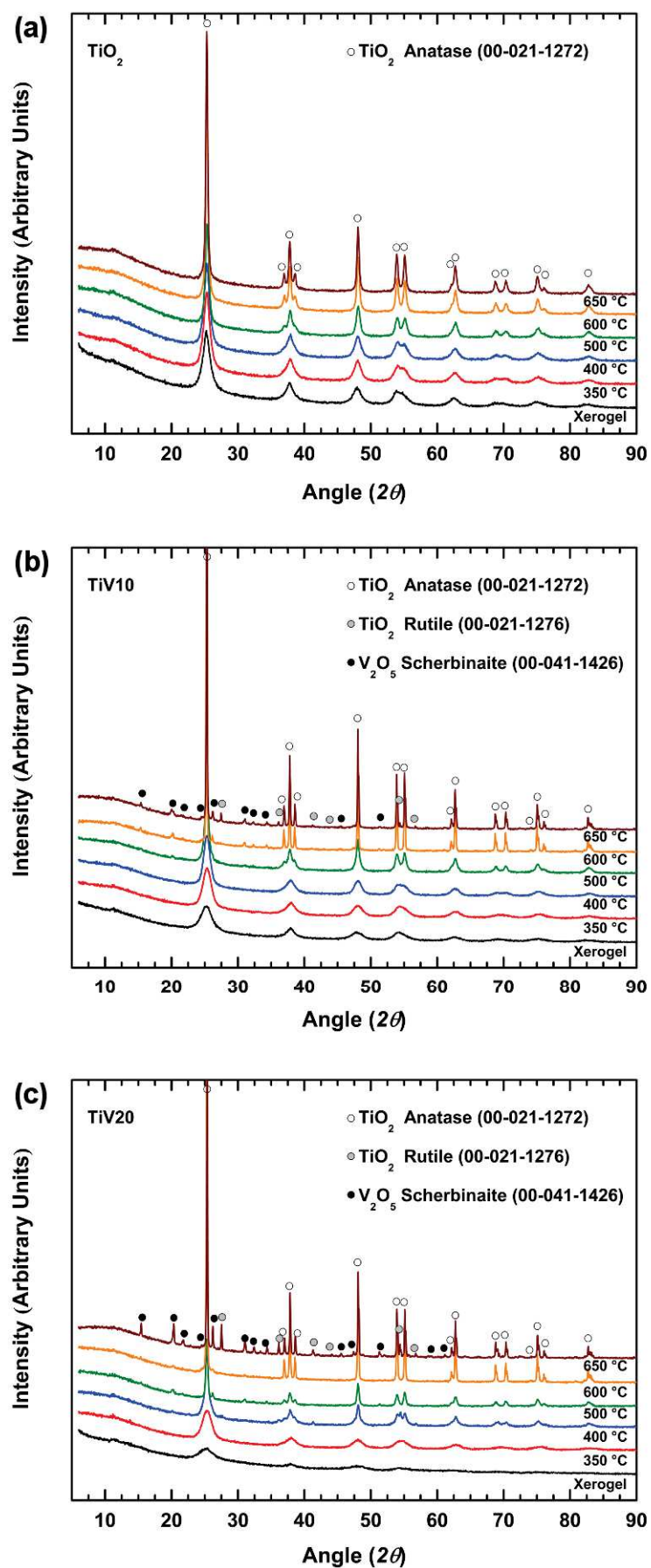
Figure 3.9 Powder X-ray diffraction patterns of TiO₂ (a), TiV10 (b) and TiV20 (c) xerogels and calcinated samples.

Table 3.3 Crystallite size and textural data for TiO₂ and TiO₂-V₂O₅ samples after different heat treatments.

Sample	Crystallite size ^a (nm)	S _{BET} ^b (m ² ·g ⁻¹)	V _p ^c (cm ³ ·g ⁻¹)	D _p ^d (nm)
TiO ₂	Xerogel	6	---	---
	350 °C	8	139	0.23
	400 °C	8	104	0.18
	500 °C	13	68	0.17
	600 °C	22	42	0.13
	650 °C	27	28	0.09
TiV5	Xerogel	5	---	---
	350 °C	6	153	0.24
	400 °C	9	134	0.22
	500 °C	12	64	0.15
	600 °C	55	---	---
	650 °C	60	---	---
TiV10	Xerogel	5	---	---
	350 °C	6	164	0.26
	400 °C	7	138	0.24
	500 °C	17	58	0.16
	600 °C	60	---	---
	650 °C	58	---	---
TiV15	Xerogel	4	---	---
	350 °C	6	210	0.23
	400 °C	7	133	0.20
	500 °C	25	27	0.13
	600 °C	67	---	---
	650 °C	61	---	---
TiV20	Xerogel	4	---	---
	350 °C	5	172	0.13
	400 °C	15	83	0.11
	500 °C	25	15	0.09
	600 °C	64	---	---
	650 °C	60	---	---

^aderived from XRD data using Scherrer equation, ^bspecific surface area, ^ctotal pore volume, ^dBJH average pore diameter calculated from desorption branch.

Besides, Gouma *et al* [237] propose three different scenarios for the anatase to rutile transformation, one of them consisting in the formation of rutile on the surface of the coarser anatase particles followed by the attachment of boundary particles. The attached particles rotate in order to find a good crystallographic match (*i.e.* (200) rutile planes grow parallel to (112) anatase planes) promoting the rutile crystal growth. This scenario actually match with the present discussion, bigger TiO₂ anatase particles transform first into rutile; at that stage, only smaller anatase particles remain, waiting to be absorbed and transformed into rutile, thus explaining the reduction of crystallite sizes in TiO₂-V₂O₅ mixed oxides calcinated at 650 °C.

Another possible mechanism at the origin of this phenomenon is proposed by Gallardo-Amores *et al* [236]. Briefly, TiO₂ anatase particles with high defects density merge forming bigger particles. Then, the boundary between these particles serve as a nuclei center for TiO₂

rutile which, in an exothermic process, disperse across the original anatase particles. Therefore, the original size of anatase particles is reduced and thus the merged particles are converted in rutile. This mechanism is illustrated in Figure 3.10.

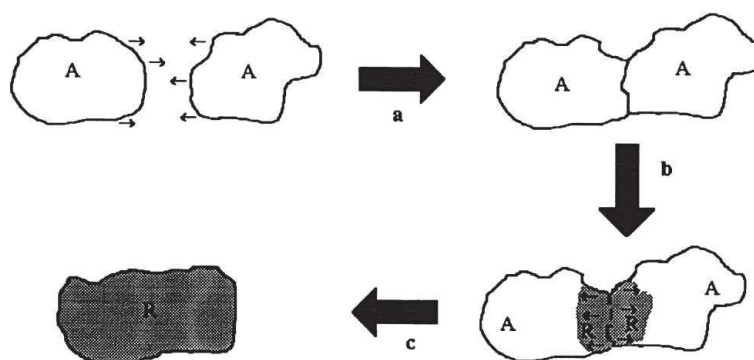


Figure 3.10 Mechanism proposed for the TiO₂ anatase (A) to rutile (R) transformation. Figure taken from [236].

At that point, it is difficult to conclude with certitude about the nature of this transformation. Further analyses need to be performed in order to elucidate the real mechanism involved in the TiO₂ anatase to rutile transformation for these materials.

Furthermore, molecular nitrogen physisorption isotherms and BJH pore size distribution of heat-treated TiO₂ at different temperatures are presented in Figure 3.11. All isotherms correspond to type IV according to the IUPAC, typical for mesoporous materials. Samples calcinated at lower temperatures (*i.e.* 350 °C and 400 °C) exhibit kind of bimodal and wider pore size distributions comparing to samples that underwent higher heat treatments. The temperature of calcination also impacts the size of pores: for instance pore size distributions of TiO₂ calcinated at 500 °C, 600 °C and 650 °C are centered 8 nm, 9 nm and 10 nm respectively; while the other two samples (*i.e.* 350 °C and 400 °C) evidences a vaste mesoporosity between 2-10 nm range.

By the same technique, TiO₂-V₂O₅ samples, heat-treated at 600 °C and above, prove to loose all their porosity bringing no exploitable data. This is principally due to the formation of the V₂O₅ and TiO₂ rutile as observed by XRD (Figure 3.9) and an increment of the particle size (Table 3.3).

Textural data of the whole series of TiO₂ and of TiO₂-V₂O₅ mixed oxides (350-500 °C heat-treated samples) are presented in Table 3.3. In general, the specific surface area decreases with the increment of the calcination temperature and this effect becomes critical in mixed oxides samples. For instance, specific surface area of TiV20 decreases by half between 350 °C and 400 °C calcinations; this may be correlated to the fact that this sample contains the highest amount of vanadium among the TiV_x samples, surpassing the doping level of vanadium into the TiO₂ framework and promoting the formation of V₂O₅ and other vanadate species. Then, between 400 °C and 500 °C, TiV15 and TiV20 exhibit similar behavior; specific surface area in both cases is divided by five, while for TiV5 and TiV10 samples it is only divided by two. This difference of behaviors is clearly associated with the vanadium content; one may note that TiV5 and TiV10 does not evidence any reflection associated to V₂O₅ at 500 °C, while TiV15 and TiV20 do (XRD patterns, Fig. 1 in section 3.1.1). In the case of pure TiO₂ sample, it is also evidenced a decrease of the specific surface area with the increment of calcination temperature; nevertheless, it is more gradual and, as the only crystal phase observed is TiO₂ anatase, it is associated to the natural growth of particles promoted by the heat treatment.

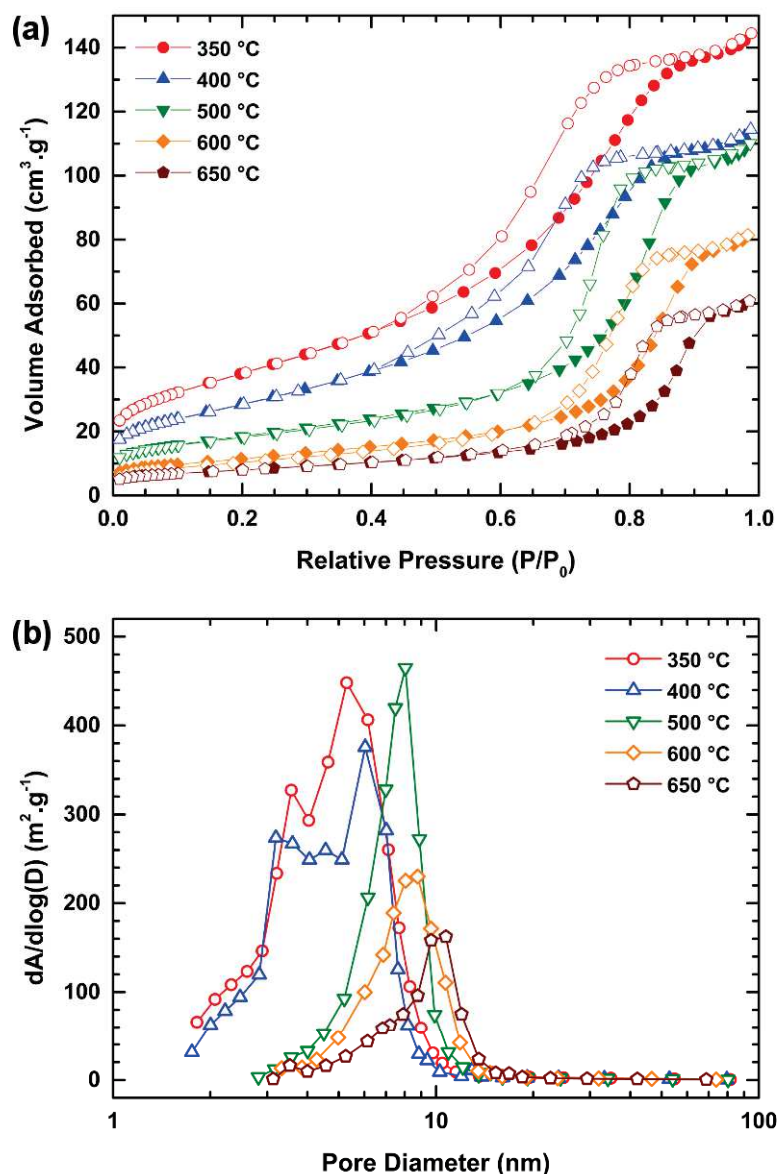


Figure 3.11 (a) Molecular nitrogen physisorption isotherms and (b) BJH pore size distribution (desorption branch) of TiO₂ after different heat treatments. Filled and open symbols refer to adsorption and desorption, respectively.

3.1.3.3 Electrochemical performance of TiO₂ calcinated at different temperatures (*i.e.* 350-650 °C)

TiO₂ samples calcinated at different temperatures were electrochemically tested *versus* lithium. It was interesting to determine the long-term stability of these samples and also verify a possible effect due to the surface area and crystallite size which differs in the different heat-treated TiO₂ samples.

Therefore, electrodes using the TiO₂ xerogel and the 350-650 °C heat-treated TiO₂ samples, as active material, were prepared. It is worthy to mention that during the electrode preparation, TiO₂ xerogel sample was the only ink presenting a slight deficiency of adhesion to the copper sheet used as current collector. This phenomenon may be the consequence of the organic by-products kept into the xerogel network as they will have a bigger affinity with the

organic binder (*i.e.* PVDF). It is important to keep in mind that for this reaction conditions the amount of organic compounds in xerogel was of 10.8 % (determined by TGA, Figure 3.6). All electrodes were cycled at a current rate of 16.8 mA·g⁻¹ and kept it for 75 cycles. Besides the NHSG derived TiO₂, a commercial TiO₂ (anatase Sigma Aldrich) electrode was also tested under the same conditions. Cycling performances of these materials are presented in Figure 3.12. Xerogel sample is the only one, amongst the NHSG ones, which specific capacity drastically decays from the first cycles, stabilizing it at around 50 mAh·g⁻¹. In a similar way, Liu *et al* [238] show an as-grown amorphous TiO₂, prepared by anodic oxidation, with poor stability compare with a 400 °C heat-treated TiO₂. Besides, the electrode may have suffered from disintegration due to the poor adhesion of the ink onto the current collector. For its part, anatase Aldrich sample loses gradually its capacity since the beginning of the cycling as observed before during the cycling at different current rates (Figure 3.4).

Interestingly, TiO₂ samples that underwent heat treatments at 600 °C and above start the cycling proving good stability. However, at some point both samples start losing gradually their specific capacity. This behavior can be correlated with the reduction of specific surface area and an increment of particle size; both samples also exhibit the smallest pore volumes of the series, letting less available spaces for the lithium insertion and thus giving less capacity (Table 3.3). Moreover, 350 °C heat-treated TiO₂ exhibits the best performances; it displays a specific capacity of 199 mAh·g⁻¹ at the end of the cycling (*i.e.* cycle 75) *versus* 176 mAh·g⁻¹ from the 500 °C heat-treated counterpart. For its part, the 400 °C heat-treated TiO₂ only presents a specific capacity of 137 mAh·g⁻¹. The fact that 350 °C TiO₂ possesses better performances can be explained because it presents the highest specific surface area (139 m²·g⁻¹) area and the highest pore volume (0.23 cm³·g⁻¹) among the TiO₂ calcinated samples; thus, having more free spaces to allow lithiation of TiO₂. Besides, its smaller crystallite size may reduce the Li⁺ diffusion path inside the electrode.

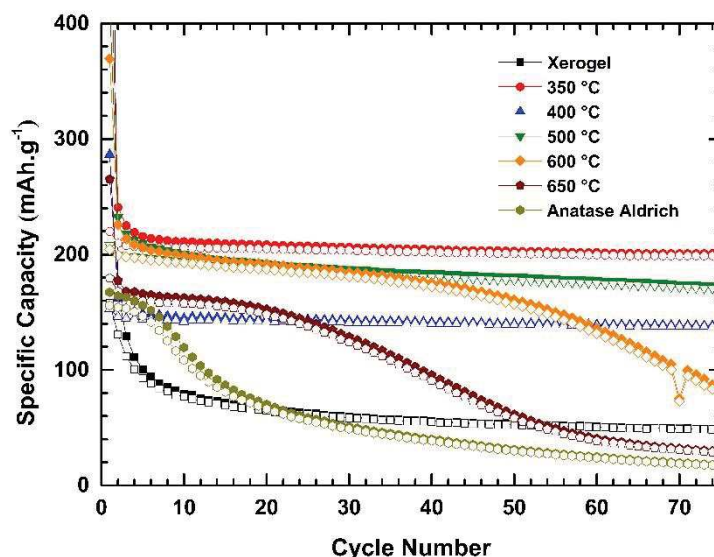


Figure 3.12 Cycling performances at a current rate of 16.8 mA·g⁻¹ ($C/20$; $C=335.6$ mA·g⁻¹) of TiO₂ calcinated at different temperatures (xerogel and commercial TiO₂ also included) for a voltage window of 1.2-2.5 V *versus* Li⁺/Li (filled and open symbols refer to reduction (discharge) and oxidation (charge), respectively).

Initial galvanostatic charge/discharge profiles of TiO₂ calcinated at different temperatures are displayed in Figure 3.13. All samples exhibits the typical behavior of lithium insertion into the anatase crystal phase of TiO₂ showing a constant plateau at 1.75 V *versus* Li⁺/Li, associated to the coexistence of the lithium-poor and the lithium-rich titanates phases [184, 185]. Then, a pseudoplateau appears at *ca.* 1.5 V *versus* Li⁺/Li corresponding to the beginning of the

formation of the LiTiO₂ phase. The extension of this section strongly depends of the surface area of the material [186]; so, it is not surprising that 350 °C TiO₂ sample, having the highest surface area, presents a larger lithiation process compare to the other samples of the series.

It is worthy remarkable that the fast drop of potential from the open circuit, associated to the formation of a solid solution Li_xTiO₂ ($x < 0.5$), differs for the 350 °C sample. It decreases with a slower rate than the rest of the series and it also exhibits a small plateau at 1.86 V *versus* Li⁺/Li. This phenomenon may be associated to the presence of residual organic compounds that still remains trapped into the TiO₂ framework, as all organic byproducts are eliminated after 500 °C (TGA Figure 3.1 and Figure 3.6). At this stage, it is a little precipitate to make conclusions about the origin of this behavior, mainly because reduction of the electrolyte compounds and other organic compounds appears at lower potentials [239-241]. This electrochemical behavior only appears in the first reduction, it is not observed during the oxidation step, indicating that this phenomenon correspond to an irreversible process during the first lithiation.

In order to provide a better understanding of this phenomenon and to clarify if it is originated for the reduction of either the electrode or the electrolyte, further analyses need to be performed such as *in situ* XRD or *in situ* FTIR. These analyses will bring information about the crystal structure modification or the electrolyte composition, respectively, along the galvanostatic cycling.

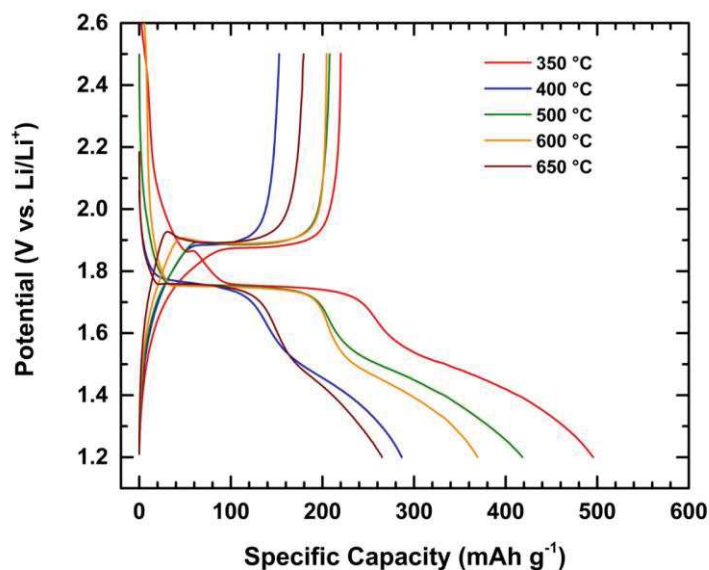


Figure 3.13 Initial galvanostatic charge/discharge profiles at a current rate of 16.8 mA·g⁻¹ ($C/20$; $C=335.6$ mA·g⁻¹) of different temperature heat-treated TiO₂ electrodes for a voltage window of 1.2-2.5 V versus Li⁺/Li.

3.1.4 Electrochemical performance of NHSG TiO₂ and TiO₂-V₂O₅ mixed oxides *versus* sodium

Recently, French researches from CNRS and CEA belonging to the Réseau sur le stockage électrochimique de l'énergie (RS2E) have developed a sodium battery prototype based on the industry standard format "18650". This prototype has proven to be attractive for industry mainly due to its electrochemical competitive performances as compared with its lithium counterparts (lifespan exceeding 2000 charge/discharge cycles). Besides, sodium is an abundant resource unlike lithium [242].

Thus, inspired by this prototype, the TiO₂ and TiO₂-V₂O₅ based electrodes, previously analyzed *versus* lithium (section 3.1.1), were galvanostatic cycled *versus* sodium. The cycling performances, efficiency and galvanostatic charge/discharge profiles from the 1st and 20th cycles are shown in Figure 3.14. Current rates chosen were the same as those used before for the lithium cycling, *i.e.* 16.8, 33.6, 67.2, 168 and 336 mAh·g⁻¹, for comparison.

It is important to keep in mind that lithium and sodium insertion mechanisms differ, even if they show some similarities. As a reminder, standard reduction potentials (E^0 at 25 °C and 1 atm) for the redox couples Li⁺/Li and Na⁺/Na are -3.04 V and -2.71 V, respectively to the standard hydrogen electrode [243]. Thus, lithium is a stronger reducing agent.

Moreover, electrolyte employed is not the same in both cases. For instance, non-aqueous liquid electrolytes used in Na-ion batteries (SIBs) usually present an electrochemical stability range between around 0-5 V *versus* Na⁺/Na [244]; while for its lithium counterparts, organic carbonates in electrolyte get reduced at potentials around 1.0 V *versus* Li⁺/Li [239-241]. TiO₂ is also considered an intercalation material in Na-ion batteries, as for the Li-ion batteries case, and is considered a zero-strain material too [245]. Calculations suggest that diffusion barriers for Li⁺ and Na⁺ are similar in TiO₂ anatase, even if Na⁺ radius is larger; however, micron-sized TiO₂ anatase has been proven electrochemically inactive in sodium cells [246-248].

Unlike the well known insertion/desinsertion mechanism of into TiO₂, the sodiation/desodiation process of TiO₂ remains still unclear. The lithiation mechanisms cannot be simple extrapolated to sodium processes. Some characteristics of TiO₂ based electrodes towards sodiation are that the first discharge exhibits major differences as compared with the following ones, and Na⁺ may only interact with the particle surface. The former suggest that the surface area is a key parameter to keep in mind in order to optimize performances [249].

Wu *et al* [250] proposes a three section mechanism consisting in a fast potential drop until 1.0 V *versus* Na⁺/Na corresponding to pseudocapacitive events without any structural modification. Then, it is followed by the sodium insertion into the TiO₂ with a structural rearrangement (*i.e.* distortion of the anatase lattice) forming a sodium titanate intermediate phase (Na_{0.25}TiO₂) at 0.3 V *versus* Na⁺/Na. At the same time, TiO₂ is reduced to metallic titanium producing also sodium oxide and oxygen. This reaction continues until reach the potential of 0.1 V *versus* Na⁺/Na. Then, the sodium titanate, previously formed, disproportionates into another metastable sodium titanate (a rhombohedral Na_xTiO₂ phase with high degree of disorder), which can reversibly desodiate *ca.* 0.41 Na⁺ per TiO₂. Besides Li *et al* [251] deduced by refinement the formula of the former: (Na_{0.43}Ti_{0.57})_{3a}(□_{0.22}Na_{0.39}Ti_{0.39})_{3b}O₂ where □ corresponds to vacancies.

Initial galvanostatic charges/discharge profiles for the TiO₂-V₂O₅ mixed oxides (Figure 3.14a) are consistent with the mechanism detailed above with some differences. All samples exhibit a fast potential drop from the open circuit to 1.3 V *versus* Na⁺/Na, followed by the formation of a pseudoplateau in the 1.1-1.3 V *versus* Na⁺/Na region. Then, a constant slope is maintained until 0.2 V *versus* Na⁺/Na where a second pseudoplateau appears. Mao *et al* [252] also observe the presence of the first pseudoplateau over the same potential range; unfortunately, they doped its TiO₂ with Sn and discussion was not deeper about that point. This second plateau at around 0.2 V *versus* Na⁺/Na has already been reported in literature and is associated to irreversible two-phase reactions [249, 251].

As for the lithiation case discussed before (section 3.1.1), the influence of vanadium is observed at the beginning of the discharge profile. Shoulders, indicating electrochemical activity, appear at potentials above 1.3 V *versus* Na⁺/Na and are in accordance with the

activity of vanadate compounds [253]. Absence of this features in subsequent cycling indicates the irreversibility of this process.

The shape of the charge profile indicates that not all the sodium inserted is desodiated in a reversible process. Initial coulombic efficiency is low, *ca.* 39% for TiO₂ and TiV5 samples and *ca.* 47% for the rest. As indicated by the mechanism of this process, a considerable amount of Na⁺ is not recuperated after the first cycle; nevertheless, once the formation of the metastable sodium titanate is done, the reversibility of the system is improved and coulombic efficiency reaches values around 98 % after 20 cycles.

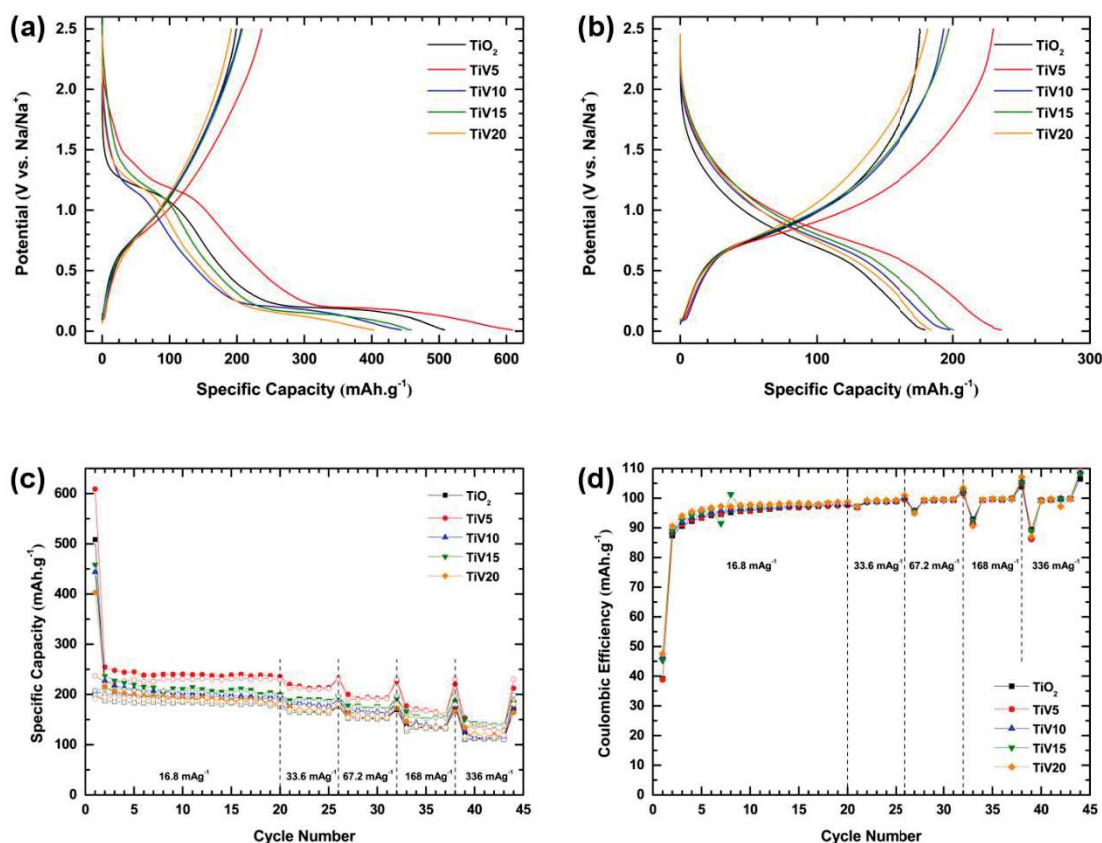


Figure 3.14 Galvanostatic charge/discharge profiles at a current rate of 16.8 mA·g⁻¹ (*C*/20) of TiO₂ and TiO₂-V₂O₅ electrodes *versus* Na, (a) 1st cycle and (b) 20th cycle; (c) cycling performances and (d) coulombic efficiency at different *C* rates (*C* = 335.6 mA·g⁻¹) for a voltage window of 0.0-2.5 V *versus* Na⁺/Na (filled and open symbols refer to reduction –discharge– and oxidation –charge–, respectively).

Figure 3.14b shows the charge/discharge profile of the 20th cycle. Shapes of both profiles indicate the good reversibility of the sodiation/desodiation process and the discharge profile, in particular, evidences the irreversibility of the first sodiation cycle (*i.e.* absence of the two pseudoplateaus). Results are in agreement with the TiO₂ cycling behavior reported in literature [251, 254-256]. Influence of vanadium continues to be observed as mixed oxides samples evidence a shift in the slope starting from *ca.* 1.9 V *versus* Na⁺/Na during the discharge profile, proving some reversibility of the sodiation process into the vanadate species.

Moreover, all samples present good stability. Electrodes were subjected to different current rates and the coulombic efficiency was not drastically affected by the current rate modifications. Contrary to the lithium case, specific capacity of TiO₂ was considerably improved by the addition of 5 % of vanadium. The TiO₂ sample present the lowest capacities

along the cycling as compared with all mixed oxides, and TiV5 sample exhibits the best performances amongst this material series as observed in Figure 3.14c. Lower specific capacities obtained for the other mixed oxides will be the consequence of a bigger amount of vanadium and the presence of V₂O₅ preventing the sodiation of TiO₂, similar to the behavior observed during the lithiation process (section 3.1.1). It is noteworthy that TiV10, TiV15 and TiV20 samples exhibit lower initial specific capacities than TiO₂ sample, this “blocking” phenomenon may limit the SEI formation improving the latter cycling performances (*i.e.* better initial coulombic efficiency).

A summary comparing the performances of TiO₂ and the TiO₂-V₂O₅ mixed oxides against the lithiation and sodiation processes is presented in Table 3.4. Briefly, all samples exhibit higher capacities for the first reduction *versus* sodium; however, due to the complexity of the sodiation mechanism and the formation of different irreversible processes the capacity fade is more important for this samples after 20 cycles. It is also remarkable that all mixed oxides exhibit higher specific capacities *versus* sodium than *versus* lithium; the only exception being the pure TiO₂ sample which performances are below those obtained *versus* lithium.

As a conclusion, contrary to the lithiation process, the addition of different vanadium loading in the TiO₂-V₂O₅ mixed oxides improves the electrochemical performances of TiO₂ *versus* sodium. A vanadium loading equal to 5 % seems to be the optimal amount for the best results, considerably improving the specific capacity due to the small vanadium content. Besides, this vanadium loading is not high enough to form the V₂O₅ scherbinaite crystal phase that seems to block the initial sodiation process.

Table 3.4 Comparison of TiO₂ and mixed oxides reduction specific capacities of galvanostatic cycling versus Li and Na.

Sample	1 st cycle (mAh·g ⁻¹)		20 th cycle (mAh·g ⁻¹)		43 rd cycle (mAh·g ⁻¹)	
	vs. Li	vs. Na	vs. Li	vs. Na	vs. Li	vs. Na
TiO ₂	326	508	188	180	128	110
TiV5	375	609	184	235	110	128
TiV10	290	444	147	197	74	116
TiV15	313	458	160	200	94	138
TiV20	292	403	135	184	77	119

3.1.5 Electrochemical performance of TiO₂ over different potential ranges

As discussed before, pure TiO₂ prepared by the NHSG ¹Pr₂O route and calcinated at 350 °C shows the best galvanostatic cycling performances and good stability of the different calcination temperature series (section 3.1.3.3). Therefore, it was tested under unusual voltage window conditions; for instance, decreasing the potential to 0.3 V *versus* Li⁺/Li, below the reduction potential of the electrolyte compounds. It has been reported that organic carbonates, commonly used as components in Li-ion batteries electrolytes (*e.g.* PC, EC, DMC), present a reduction potential around 1.0 V *versus* Li⁺/Li [239-241]; thus, one may expect a fast drop of capacity during the cycling of TiO₂ based electrodes in this range, as already reported in literature [170].

Preliminary tests consisted in cycling the 350 °C heat-treated TiO₂ at a constant current rate of 67.2 mA·g⁻¹ (C/5). Cycling performances are presented in Figure 3.15. The first five charges/discharge cycles were recorded between the common potential window used before (*i.e.* 1.2-2.5 V *versus* Li⁺/Li); then, cycles were carried out in the 0.3-2.5 V *versus* Li⁺/Li

range. It is observed that, after the modification of the potential range, TiO₂ remains stable. There is a slight decrement in capacity; however, a fast or drastical drop is not evidenced after 50 cycles under the new voltage window. A coulombic efficiency above 97 % is reached in 10 cycles after the voltage window chagement (*i.e.* 97.1 % for cycle 15 of the whole cycling) and it continues to increase till the end (99.2 %). Specific capacity at the end of the cycling reaches 196 mAh·g⁻¹ and is comparable to the capacity obtained after the long cycling described above (section 3.1.3.3).

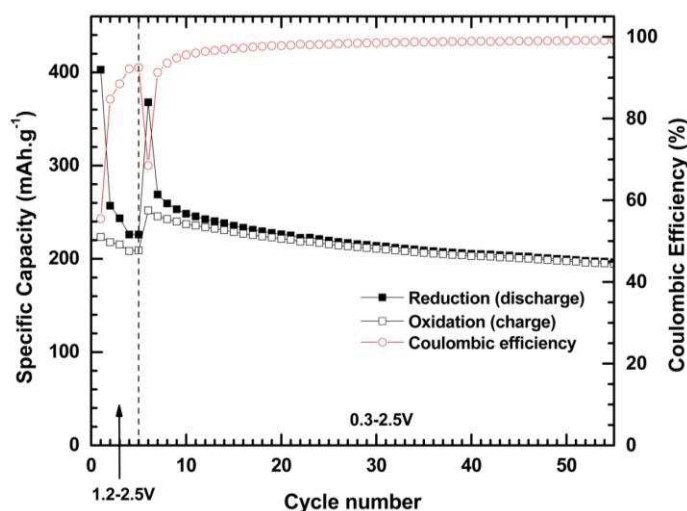


Figure 3.15 Cycling performances at a current rate of 67.2 mA·g⁻¹ (C/5) of TiO₂ from NHSG ¹Pr₂O ether route calcinated at 350 °C for different voltage windows versus Li⁺/Li.

Stability of this NHSG TiO₂ may also be derivated of the synthesis method. There are some side reactions linked to the presence of adsorbed water into the active material, leading to the formation of LiOH and H₂ [257]. Thus, as water is avoided by the own synthesis method, those reactions are also avoided and possible catalytic degradation of the electrolyte is prevented.

In order to evaluate if this characteristic was dependant of these particular synthesis conditions or rather a intrinsic property coming from the synthesis method, a series of diferent ether derived TiO₂ (*i.e.* ¹Pr₂O and THF) calcinated at 350 °C and 500 °C was prepared for galvanostatic cycling. Crystal structures of these samples were analyzed by XRD and diffractograms are presented in Figure 3.16.

All samples only exhibit reflections associated to the TiO₂ anatase crystal phase (JCPDS 00-021-1272). The 500 °C heat-treated samples evidence narrow and better defined reflections (*e.g.* reflections *ca.* 70 ° 2θ) as an indication of an improvement in crystallinity and also suggesting the presence of bigger particles. The crystallite size values, determined by the the Scherrer equation, are summarized in Table 3.5. Samples calcinated at the same temperature evidence similar crystallite size, regardless the oxygen donor. Samples calcinated at 350 °C shows crystallite sizes that are just slightly bigger in comparison with values obtained for the xerogels (Table 3.3). Thus, one may consider that at this temperature, there are not major modification in the crystalline structure of the TiO₂ and only organic byproducts are eliminated. A clear increment of the crystallite size is observed at 500 °C.

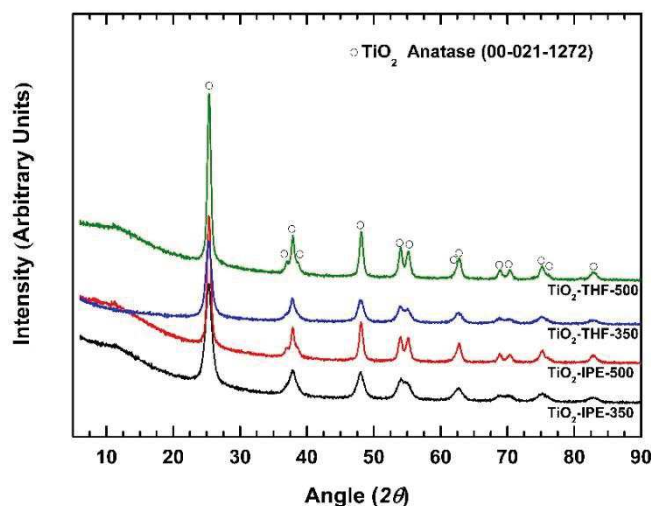


Figure 3.16 Powder X-ray diffractograms of ¹Pr₂O and THF derived TiO₂ calcinated at different temperatures (*i.e.* 350 °C and 500 °C).

Table 3.5 Crystallite size, textural data and NH₃ uptake for TiO₂ from different oxygen donors (*i.e.* ¹Pr₂O and THF) and different calcination temperatures (*i.e.* 350 °C and 500 °C).

Sample	Crystallite size ^a (nm)	S _{BET} ^b (m ² ·g ⁻¹)	V _p ^c (cm ³ ·g ⁻¹)	D _p ^e (nm)	NH ₃ desorbed (μmol NH ₃ ·g ⁻¹)	NH ₃ desorbed (μmol NH ₃ ·m ⁻²)
TiO ₂ -IPE-350	8	139	0.23	5.2	620	4.46
TiO ₂ -IPE-500	13	68	0.17	5.7	310	4.56
TiO ₂ -THF-350	8	163	0.33	6.0	850	5.21
TiO ₂ -THF-500	14	75	0.24	9.8	290	3.87

^aderived from XRD data using Scherrer equation, ^bspecific surface area, ^ctotal pore volume, ^dBJH average pore diameter calculated from desorption branch.

Molecular physisorption isotherms and pore size distributions are presented in Figure 3.17. One may note that all isotherms correspond to type IV according to the IUPAC classification. This shape is characteristic of mesoporous materials. The BJH pore size distributions confirm the presence of mesopores in the 2-11 nm range. All samples exhibit broad distributions with the exception of TiO₂-IPE-500, which shows a narrow distribution centered at 8 nm. Interestingly, heat treatments at 500 °C lead to larger pore sizes than the 350 °C heat-treated counterparts. Textural data, summarized in Table 3.5, evidences a decrease of the surface area with the increment of calcination temperature; this behavior is also correlated with the crystal growth as determined by XRD. One also notices an augmentation in the average pore size with the increment of temperature and, in general terms, THF derived samples exhibit higher surface areas than their ¹Pr₂O counterparts. Thus, the oxygen donor used during the synthesis step have a major effect over the textural properties of these materials, as also observed for the case of alcohols as oxygen donors (section 3.2).

The acidic properties of these samples were evaluated by ammonia temperature programmed desorption (NH₃-TPD). This test was performed with the idea to bring some insights about the acidic sites present in these samples susceptible to promote electrolyte degradation and to determine a possible influence of the calcination temperature over the acidity of samples. NH₃-TPD profiles of the different NHSG TiO₂ are presented in Figure 3.18 and NH₃ uptake in Table 3.5. The area under the curve of the samples calcinated at 350 °C double the the area of the 500 °C counterparts, indicating the presence of more acidic sites. These results are in agreement to the surface area of these materials (*i.e.* S_{BET} at 350 °C ≈ 2 S_{BET} at 500 °C). Both TiO₂ samples prepared with ¹Pr₂O have practically the same density of acidic sites and is

comparable to TiO₂ Degussa P25 [258]. However, TiO₂-THF-350 is more dense than its 500 °C counterpart. Profile shape is similar for all samples with maxima around 260-320 °C range, in agreement with literature [258, 259]. Besides, the 350 °C heat-treated samples need higher temperatures to completely desorb ammonia showing that the strength of acidic sites slightly decreases when the calcination temperature increases.

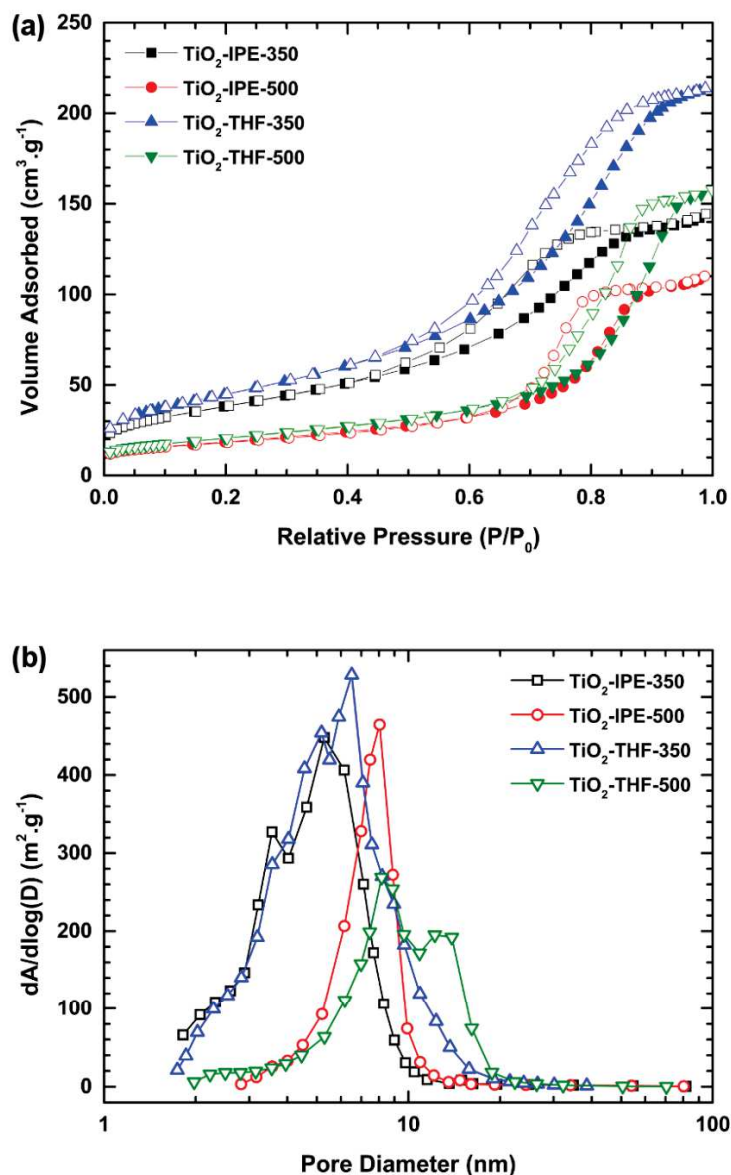


Figure 3.17 (a) Molecular nitrogen physisorption isotherms and (b) BJH pore size distribution (desorption branch) of *i*Pr₂O and THF derived TiO₂ calcinated at 350 °C and 500 °C. Filled and open symbols refer to adsorption and desorption, respectively.

In summary, acidity is similar in both materials regardless of the heat treatment. The main difference is the amount of acidic sites that depends of the surface area. This, the electrochemical performances, notably specific capacity, may probably be more affected by the surface area (*i.e.* more sites for Li⁺) than from the acidity of these materials.

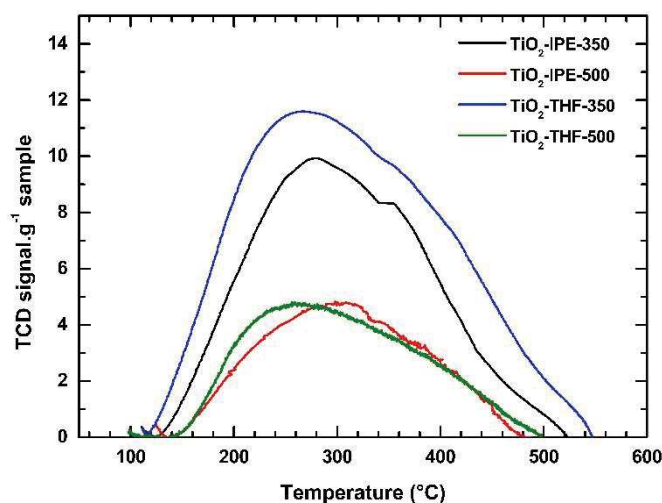


Figure 3.18 NH₃-TPD profiles of the TiO₂ samples prepared by NHSG ether routes.

Regarding the electrochemical performances of TiO₂, it is quite remarkable the fact that there are only a few reports using wider potential windows in literature. Some authors have worked with slightly larger voltage windows between 0.8-3.0 V *versus* Li⁺/Li without any particular remarks [185, 230, 260, 261]. The only reports found working with enlarged potential window going down to 0.01 V *versus* Li⁺/Li correspond to studies of TiO₂ rutile [262, 263] and TiO₂/C composites, using graphene [264], amorphous carbon [265] and carbon nanofibers [266].

In the case of TiO₂ rutile, authors settled that their electrodes evidence good reversibility working with this enlarged potential window due to an increment in the amount of lithium inserted during the lithiation process. Besides, Hong *et al* [262] also associated this electrochemical storage behavior to the hierarchical structure of their mesoporous TiO₂ rutile, providing more active sites allowing thus easy access to the electrolyte. Regarding the TiO₂-graphene composite, authors choose this voltage window (*i.e.* 0.01-3.0 V *versus* Li⁺/Li) because it correspond to the graphene work potential; thus, as the authors agreed, the electrochemical performance is improved by the coexistence of both lithium insertion mechanisms into the TiO₂ and into the graphene.

Taking inspiration of the literature discussed above; the four NHSG ether derived TiO₂ samples were used as active material in assemblage of coin cells. Then, they were cycled at a constant current rate of 67.2 mA·g⁻¹ (C/5) starting in the 1.2-2.5 V *versus* Li⁺/Li range followed by a succession of broader potential windows (each ten cycles) until reaching the 0.1-2.9 V *versus* Li⁺/Li range. Cycling performances of this cycling are shown in Figure 3.19 and a commercial sample (*i.e.* TiO₂ anatase Aldrich) was also added for comparison. The four NHSG derived TiO₂ samples evidence a quite good stability through the different voltage windows, opposite to the commercial one, which capacity significantly drops after the first voltage window changement (*i.e.* 1.2-2.5 to 0.3-2.5 V *versus* Li⁺/Li). Interestingly, specific capacities of the 350 °C heat-treated samples always surpass capacities of their 500 °C heat-treated counterparts after the first regime modification (*i.e.* 11th cycle). However, at the end of the cycling, TiO₂-THF-350 seems to drop faster, probably due to a higher acidic sites density. Besides, it is noteworthy that the stability is only provided by the TiO₂ anatase, without any influence of carbon sources (*e.g.* carbon coatings or carbon composites) compare to reported works [264-266]. Electrochemical stability of these materials can be associated to the mesoporosity and the hierarchical structure of the NHSG derived TiO₂, as suggested by Hong *et al* [262]; in addition, the absence of water may also be a key parameter in stability.

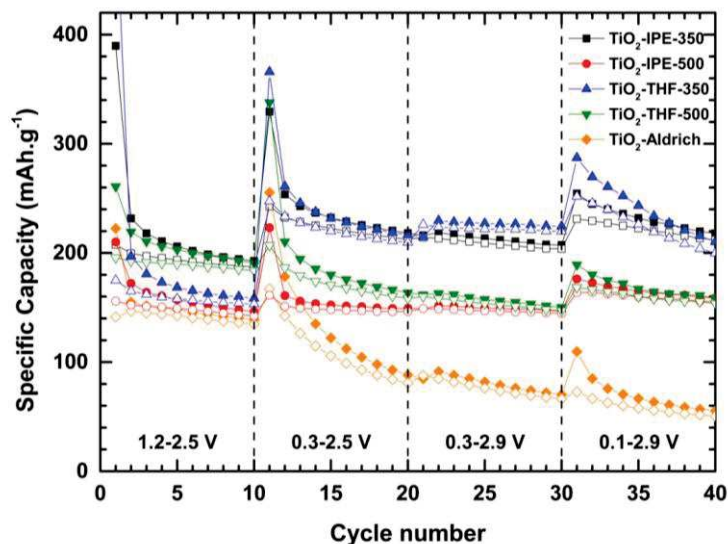


Figure 3.19 Cycling performances at a current rate of $67.2 \text{ mA}\cdot\text{g}^{-1}$ ($C/5$) of TiO₂ from NHSG ether route (*i.e.* ¹Pr₂O and THF; both heat treatments 350 and 500 °C in air) for different voltage windows *versus* Li⁺/Li (filled and open symbols refer to reduction (discharge) and oxidation (charge), respectively).

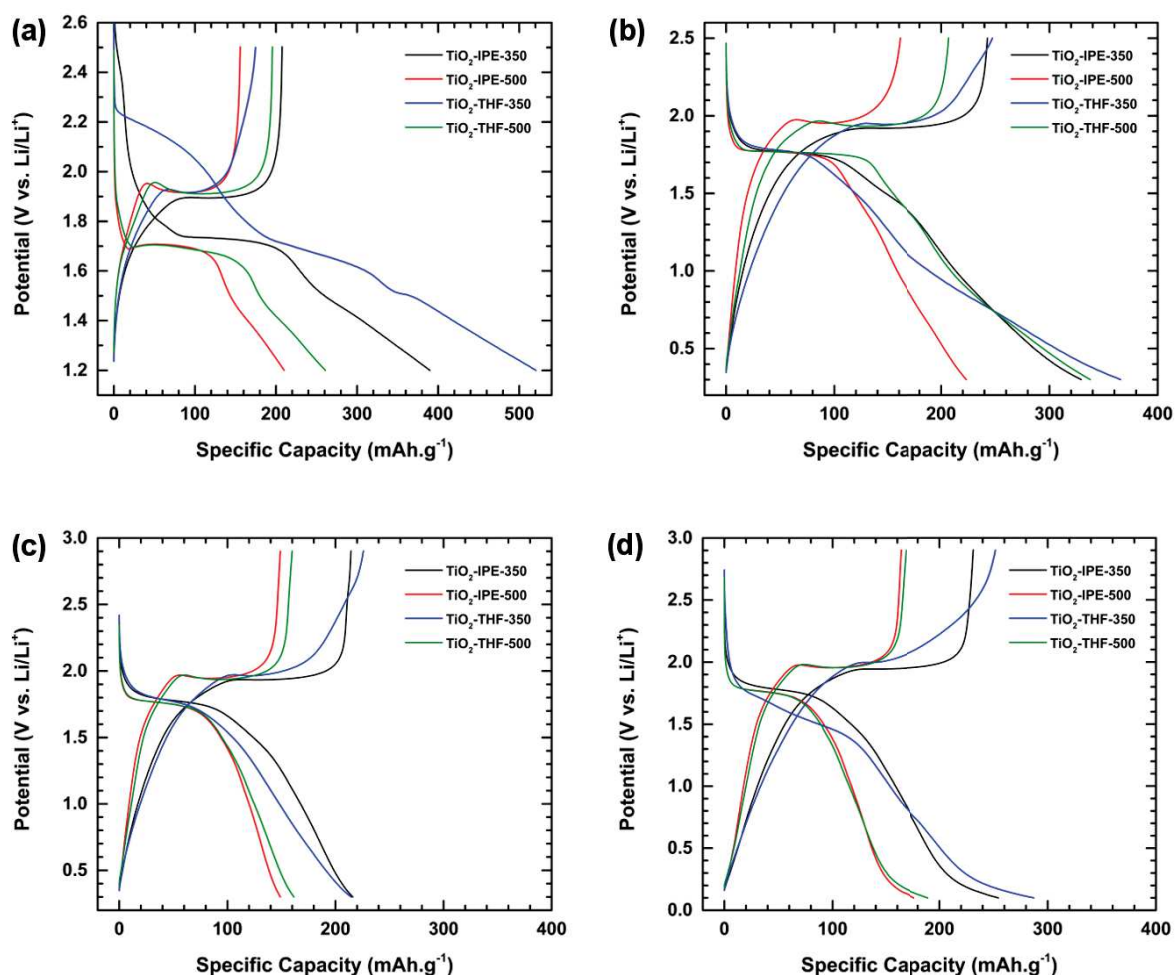


Figure 3.20 Galvanostatic charge/discharge profiles at a current density rate of $67.2 \text{ mA}\cdot\text{g}^{-1}$ ($C/5$) of TiO₂ from NHSG ether route (*i.e.* ¹Pr₂O and THF; both heat treatments 350 and 500 °C in air) for different voltage windows *versus* Li⁺/Li (a) 1st cycle; (b) 11th cycle; (c) 21st cycle and (d) 31st cycle (*i.e.* 1st cycles after changing the potential window; Figure 3.19).

Charge/discharge profile of the first cycles after modification of the voltage window (*i.e.* 1st, 11th, 21st and 31st cycles) are presented in Figure 3.20. The initial profiles of 500 °C treated samples (Figure 3.20a) exhibit the characteristics of lithium insertion into TiO₂ anatase framework. Both 500 °C heat-treated TiO₂ samples show a potential drop from the open circuit corresponding to the formation of a solid solution of Li_xTiO₂ ($x < 0.5$). When the potential reaches *ca.* 1.70 V *versus* Li⁺/Li, the characteristic constant plateau associated to the coexistence of the as formed Li_xTiO₂ and the lithium rich Li_{0.5}TiO₂ appears and it is followed by another two-phase reaction, evidenced by the pseudoplateau at *ca.* 1.5 V *versus* Li⁺/Li, towards the formation of LiTiO₂.

On the other hand, TiO₂-IPE-350 sample presents the same characteristics described for the two precedent samples. However, it also exhibits a shoulder evidencing an electrochemical activity besides TiO₂, and the average voltage of the constant plateau is increased by *ca.* 0.03 V *versus* Li⁺/Li. Interestingly, the plateau observed before for this samples at *ca.* 1.9 V *versus* Li⁺/Li (section 3.1.3.3) is not observed at the present current rate. As a reminder, cycling detailed in that section correspond to a current rate of C/20; while here, current rate employed correspond to C/5; in other words, the lithiation process is faster in this cycling. The presence of the shoulders joined to the absence of this plateau suggests that a fast lithiation process mitigates this particular electrochemical activity which seems to need a slow lithium flux in order to be activated. In addition, TiO₂-IPE-350 sample also presents a slight difference for the first oxidation (charge). Its average voltage plateau during oxidation is decreased by *ca.* 0.02 V *versus* Li⁺/Li as compared with the other three samples that exhibit identical potential. Thus, polarization is also minimized for this sample.

Redarging the TiO₂-THF-350 sample, it exhibits a more marked shoulder, starting from *ca.* 2.2 V *versus* Li⁺/Li until 1.72 V *versus* Li⁺/Li. This sample also presents a pseudoplateau instead of a well defined constant one in the biphasic Li_xTiO₂-TiO₂ region and is also increased by 0.02 V *versus* Li⁺/Li (at the beginning of the pseudoplateau). Differences in the first lithiation process of this sample are contrasting; therefore, the amount of residual organic compounds was determined by TGA trying to elucidate if the origin of this behavior may be caused by the presence of remaining byproducts. Results evidence a 3 wt% of residual organic compounds; however, as mention before further analyses need to be performed in order to successfully conclude about this behavior.

When changing the voltage window to the 0.3-2.5 V *versus* Li⁺/Li region, Figure 3.20(b), all samples continue to exhibit the characteristics of TiO₂ anatase lithiation process. Here, the four samples present identical average voltage plateau (1.77 V *versus* Li⁺/Li). TiO₂-IPE-350 sample presents, also here, less polarization compare with the other samples. Its average oxidation voltage plateau is decreased by *ca.* 0.03 V *versus* Li⁺/Li (1.92 V *versus* Li⁺/Li against 1.95 V *versus* Li⁺/Li of its 500 °C heat-treated counterpart). This behavior continue to be observed within the last two voltage windows. On the contrary, its THF TiO₂ analogue increases its polarization throughout the cycling along with the increment of the voltage window, losing faster its specific capacity through the end of the cycling (*i.e.* last section of Figure 3.19). Concerning the 500 °C heat-treated TiO₂ samples, both of them exhibit practically identical behavior throughout the last two sections (*i.e.* 0.3-2.9 and 0.1-2.9 V *versus* Li⁺/Li). The main difference between both of them is that the THF derived TiO₂ loses capacity during the second section (*i.e.* 0.3-2.5 V *versus* Li⁺/Li) and then stabilizes passing to the next voltage window.

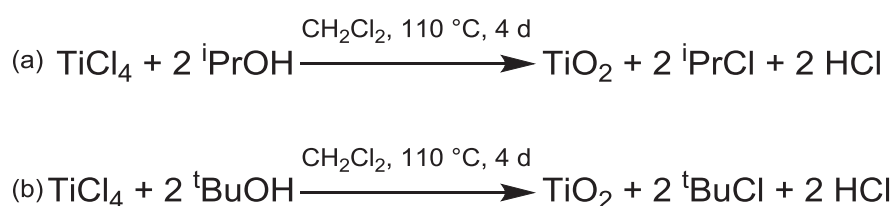
In summary, these samples exhibit a stable behavior trough this particular cycling (*i.e.* voltage window modification). Acidity does not affect the stability and surface area of samples seems

to promote higher capacities. Longer cycling should be performed to determine the long-term stability, as 350 °C heat-treated samples seem to lose their capacity faster than their 500 °C calcinated counterparts in the voltage window between 0.1-2.9 V *versus* Li⁺/Li.

3.2 TiO₂ and TiO₂-V₂O₅ mixed oxides prepared by NHSG alcohol routes

3.2.1 Influence of the oxygen donor, alcohol *versus* ether, over the TiO₂ properties

Aside from the NHSG ⁱPr₂O route, two NHSG alcohol routes were tested. Preliminary works were performed to synthesize pure TiO₂ and the results were used to setup the experimental conditions for the preparation of TiO₂-V₂O₅ mixed oxides. The two alcohols used as oxygen donors were isopropanol (ⁱPrOH) and tert-butanol (^tBuOH) and global balance for ideal reactions is presented in Scheme 3.2.



Scheme 3.2 Global balance for ideal reaction synthesis of TiO₂ by NHSG alcohol routes.

These syntheses were performed using TiCl₄, as titanium precursor, and one of the two alcohols mentioned above, as oxygen donor. Besides, 10 mL of anhydrous CH₂Cl₂ were added to slow reaction kinetics; thus, decelerating the initial formation of HCl. After 4 days of reaction, xerogels were washed and calcinated. Both alcohols lead only to anatase TiO₂ crystal phase (JCPDS 00-21-1272) after calcination at 500 °C, as determined by XRD (Figure 3.21). Crystallite size values, determined by the Scherrer equation (Table 3.6), are similar with values in the 12-14 nm range.

Table 3.6 Crystallite size and textural data for TiO₂ prepared by NHSG using different oxygen donors.

Sample	Crystallite size ^a (nm)	S _{BET} ^b (m ² ·g ⁻¹)	V _p ^c (cm ³ ·g ⁻¹)	D _p ^e (nm)
TiO ₂ - ⁱ Pr ₂ O	13	68	0.17	5.7
TiO ₂ - ⁱ PrOH	14	62	0.13	5.9
TiO ₂ - ^t BuOH	12	88	0.35	12.8

^aderived from XRD data using Scherrer equation, ^bspecific surface area, ^ctotal pore volume, ^dBJH average pore diameter calculated from desorption branch.

Textural characteristics of these samples by molecular nitrogen physisorption are reported in Table 3.6, isotherms and pore size distributions being shown in Figure 3.22. Isotherm for TiO₂-ⁱPrOH corresponds to type IV, similarly to the one of TiO₂-ⁱPr₂O prepared by the ether route. This kind of isotherm is characteristic of mesoporous materials. However, isotherm of TiO₂-^tBuOH sample correspond to type II with hysteresis associated to mesoporous materials. Its hysteresis corresponds to a H₃ type according to the IUPAC classification [223]. This kind of hysteresis shape is characteristic of materials that tend to create agglomerates suggesting that this TiO₂ does not present intrinsic porosity, or only in small amount. TiO₂-ⁱPrOH, presents well defined mesopores in the range of 3-10 nm, similarly to the TiO₂-ⁱPr₂O prepared by the ether route, while TiO₂-^tBuOH exhibits a wider distribution going up to 50 nm pores.

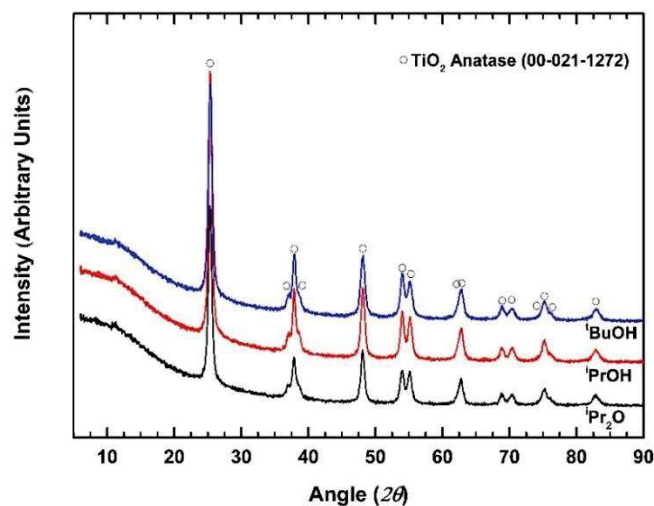


Figure 3.21 Powder X-ray diffraction patterns of TiO₂ from different oxygen donors.

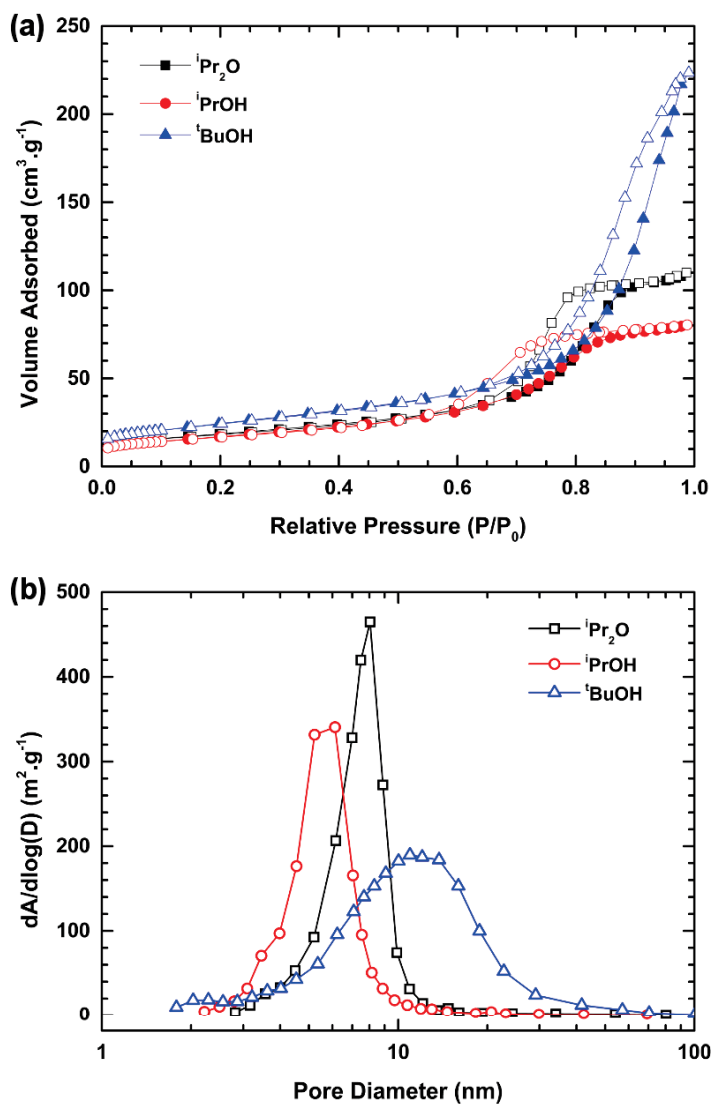


Figure 3.22 (a) Molecular nitrogen physisorption isotherms and (b) BJH pore size distribution (desorption branch) of TiO₂ from ⁱPr₂O, ⁱPrOH and ^tBuOH route. Filled and open symbols refer to adsorption and desorption, respectively.

Initial galvanostatic charge/discharge profiles of the two alcohol derived and the ether derived TiO₂ are shown in Figure 3.23. All of them present the typical characteristics of anatase TiO₂ towards lithium insertion. One may observe a fast potential decay from the open circuit, followed by the plateau corresponding to solid solution Li_xTiO₂ ($x < 0.5$) and Li_{0.5}TiO₂ coexistence and ending with a pseudoplateau at *ca.* 1.5 V *versus* Li⁺/Li to the formation of LiTiO₂. Interestingly, TiO₂-ⁱPrOH and TiO₂-^tBuOH evidence, during the first reduction, an increment in the average voltage of the plateau of *ca.* 0.04 V *versus* Li⁺/Li (*i.e.* 1.78 V *versus* Li⁺/Li against 1.74 V *versus* Li⁺/Li for TiO₂-ⁱPr₂O). Concerning the first oxidation, all samples display the same potential; thus, electrodes polarization seems to be enhanced by using alcohols as oxygen donors during the synthesis step.

Additionally, TiO₂-ⁱPrOH displays the biggest initial specific capacity (256 mA·h·g⁻¹) while TiO₂-^tBuOH exhibits the lowest one (238 mA·h·g⁻¹). As mentioned before, the last section of the galvanostatic charge/discharge profiles is highly dependent of the nature and surface area of the active material [186]. However, even if TiO₂-^tBuOH exhibits the highest specific surface area, it does not improve the specific capacity at the end of the lithiation process. This phenomenon can be correlated with the porosity nature of this sample. As observed by the N₂ physisorption isotherm (Figure 3.22), mesoporosity of this sample can be originated by the formation of aggregates (according to the hysteresis and isotherm shape) that may be weakly bounded and easily disaggregated throughout the preparation of the electrodes films (30 minutes stirring); thus, reducing the accessible sites for lithium storage.

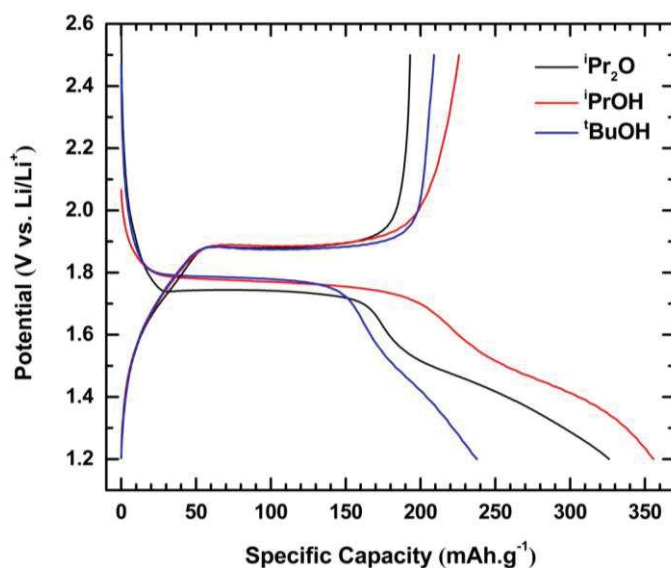


Figure 3.23 Initial galvanostatic charge/discharge profiles at a current rate of 16.8 mA·g⁻¹ ($C/20$; $C=335.6$ mA·g⁻¹) of different oxygen donors TiO₂ electrodes for a voltage window of 1.2-2.5 V *versus* Li⁺/Li.

To summarize, NHSG ⁱPrOH route was selected for the preparation of TiO₂-V₂O₅ mixed oxides given that it offers similar specific surface area that those obtained by the NHSG ⁱPr₂O route and it also displays better initial electrochemical performances *versus* lithium (*i.e.* 256 mA·h·g⁻¹ for TiO₂-ⁱPrOH against 238 or 326 mA·h·g⁻¹ for TiO₂-^tBuOH and TiO₂-ⁱPr₂O respectively). Additionally, it also presents intrinsic mesoporosity opposite to the ^tBuOH derived TiO₂.

3.2.2 Structural and textural characterization of TiO₂-V₂O₅ mixed oxides prepared by NHSG ⁱPrOH route

Based on the synthesis reported above, TiO₂-V₂O₅ mixed oxides were prepared using the NHSG ⁱPrOH route in the same conditions and using the same vanadium loading used for the ⁱPr₂O case (*i.e.* 4 days reaction at 110 °C, calcination at 500 °C, section 3.1.1). In order to avoid confusion, samples from NHSG ⁱPrOH route are labeled as their ⁱPr₂O counterparts by adding “-OH” at the end of the name (*i.e.* TiV_x-OH, *x* corresponding to the nominal vanadium atomic percentage).

Diffraction patterns of these samples are presented in Figure 3.24. All samples exhibit reflections of TiO₂ anatase crystal phase (JCPDS 00-021-1272) and not significant shift of anatase reflections was detected. Samples with higher vanadium loading, *i.e.* TiV15-OH and TiV20-OH, also exhibit traces of V₂O₅ scherbinaite crystal phase (JCPDS 00-041-1426). Scherbinaite reflections are more intense in TiV20-OH than TiV15-OH evidencing a more important presence of V₂O₅ crystals (≈ 17 wt% and ≈ 9 wt% respectively). Estimations of the crystalline amount of V₂O₅ are similar as those obtained for the ⁱPr₂O route (section 3.1.1) suggesting that TiO₂-V₂O₅ mixed oxides prepared by this NHSG route also accept a maximum doping of vanadium of about 5 at%.

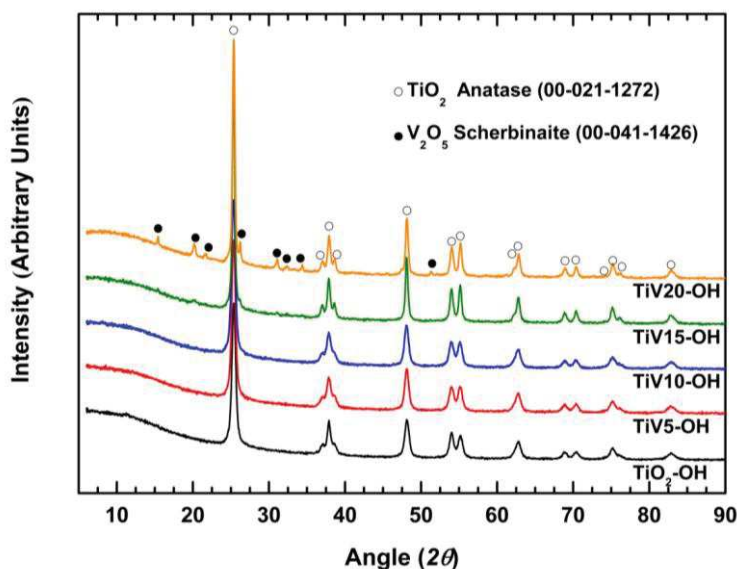


Figure 3.24 Powder X-ray diffraction patterns of ⁱPrOH derived mixed oxides.

Crystallite size, reported in Table 3.7, show that low vanadium loadings (*i.e.* 5 and 10 V%) does not have any impact on the crystallite size of TiO₂ anatase. However, for the 15 and 20 V% loadings, crystallite size becomes bigger for both samples. For the latter, this is apparently correlated with the formation of V₂O₅ crystals as observed in their diffraction patterns (Figure 3.24). A possible interpretation is that the formation of the V₂O₅ scherbinaite phase consume V atoms that are less disponible for inclusion into the TiO₂-V₂O₅ solid solution and consequently does not limit crystal growth of the TiO₂ particles. Thus, the anatase to rutile transformation is accelerated, as discussed above (section 3.1.3.2). A similar behavior has been observed for the ⁱPr₂O TiV_x series (section 3.1.1).

Table 3.7 Crystallite size and textural data for TiO₂ and TiO₂-V₂O₅ samples from the ⁱPrOH NHSG route.

Sample	Crystallite size ^a (nm)	S _{BET} ^b (m ² ·g ⁻¹)	V _p ^c (cm ³ ·g ⁻¹)	D _p ^e (nm)
TiO ₂ -OH	14	62	0.13	5.9
TiV5-OH	15	52	0.15	8.4
TiV10-OH	14	48	0.14	8.7
TiV15-OH	25	20	0.09	18.0
TiV20-OH	24	8	0.06	27.9

^aderived from XRD data using Scherrer equation, ^bspecific surface area, ^ctotal pore volume, ^dBJH average pore diameter calculated from desorption branch.

One may observe in scanning electron micrographs of Figure 3.25 that all samples exhibit similar hierarchical structures as those presented before for the ⁱPr₂O derived samples (section 3.1.1). TiV15-OH and TiV20-OH mixed oxides are principally composed by nanoparticles of *ca.* 30 nm which seem slightly bigger than predicted by XRD. All samples are powders of micron-sized rounded-shape particles. Samples containing higher vanadium loading, exhibit also long and flate needles typical of V₂O₅ scherbinaite crystals. This morphology is different from the one observed for TiV20 obtained with ⁱPr₂O as oxygen donor (Fig.2 in section 3.1.1). In the former case, V₂O₅ crystals exhibit a plate-like morphology and are homogeneously dispersed throughout the compound. Besides, their size does not exceed the nanometer scale. By contrast, V₂O₅ crystals in TiV20-OH are of few microns length.

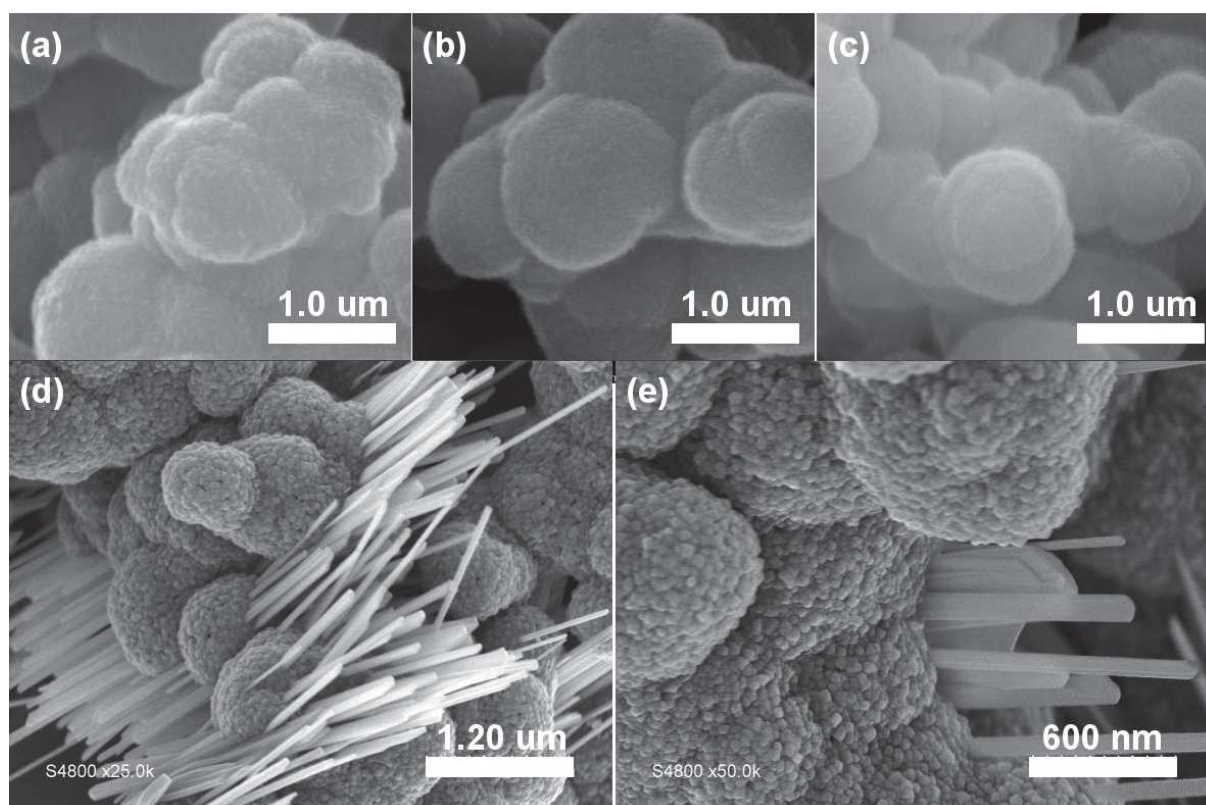


Figure 3.25 SEM micrographs of TiV5-OH (a), TiV10-OH (b), TiV15-OH (c) and TiV20-OH (d-e) from the NHSG ⁱPrOH route.

The difference in the morphology of the V₂O₅ crystals can also be originated from the solvent used during synthesis, indeed the TiV_x mixed oxides prepared with ⁱPr₂O were synthesized without any addition of solvent or additives. On the other hand, CH₂Cl₂ was used as solvent in the ⁱPrOH route. A third difference is the presence of HCl that is inevitably released as

byproduct in the latter case while it is absent in the ether route. Although, it is possible to establish these differences between the two NHSG routes, a clear and definitive understanding and interpretation of them is impossible at that point of the study.

Molecular nitrogen physisorption isotherms, pore size distribution and textural characteristics of the ⁱPrOH derived mixed oxides are summarized in Figure 3.26 and Table 3.7. Isotherms of pure TiO₂, TiV5-OH and TiV10-OH samples correspond to the type IV according to the IUPAC classification and are associated with mesoporous materials. Regarding the TiV15-OH and TiV20-OH isotherms shape, both of them are more like type II, with a sketch of saturation at the end, they exhibit hysteresis behavior evidencing some mesoporosity.

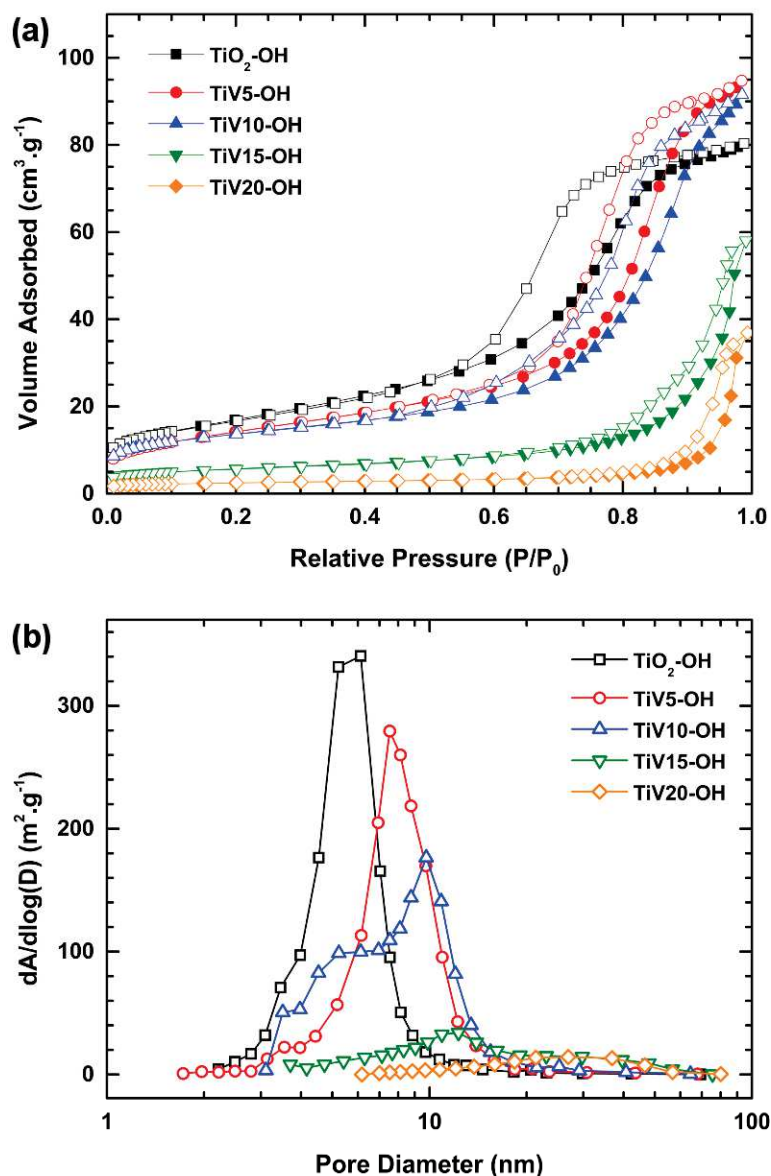


Figure 3.26 (a) Molecular nitrogen physisorption isotherms and (b) BJH pore size distribution (desorption branch) of TiO₂ and TiO₂-V₂O₅ from the NHSG ⁱPrOH route. Filled and open symbols refer to adsorption and desorption, respectively.

As a general trend, specific surface area decreases when the vanadium loading increases, which is consistent with the increase of crystallite size found by XRD and the formation of V₂O₅ crystals. This phenomenon has already been observed in literature [67].

The evolution of the pore size distributions according to the vanadium loading is quite interesting; pure TiO₂ and samples with amount of vanadium below 10 % exhibit well defined mesopores in the 2-11 nm range. As for the ¹Pr₂O case, TiV10-OH sample exhibits an intermediate texture, showing a kind of bimodal distribution. Nevertheless, samples with higher vanadium loading, present wider distributions reaching pores within the limit size range of mesoporosity (*i.e.* 50 nm) at it is agreement to their isotherm shape. Pore volume also drastically decreases, caused principally by the filling of pores with vanadates species.

As previously seen, the electrochemical performances of the TiO₂-V₂O₅ mixed oxides prepared by the NHSG ¹Pr₂O route where somewhat disappointing. Therefore, these materials that present globally similar physico-chemical characteristics were not further electrochemically characterized.

3.3 Chapter Conclusion

In summary, this chapter proposed an original application for TiO₂ based mixed oxides obtained by non-hydrolytic sol-gel chemistry. Inspired by the application of the well kown NHSG methods, commonly used in the synthesis of oxides in the catalyst field, we have revisited these synthesis methods by targeting materials with potential application as electrodes in Li-ion batteries. Therefore, TiO₂ and TiO₂ based mixed oxides were prepared following different NHSG routes.

The simplicity of the NHSG ¹Pr₂O route allowed the easy formation of TiO₂-V₂O₅ mixed oxides with vanadium loadings from 5 to 20 at%. These oxides were characterized in detail by XRD, SEM and N₂ physisorption. NHSG ¹Pr₂O derived samples exhibit interesting mesoporous hierarchical structure. The TiO₂ parts are composed by primary nanoparticles with average sizes between 10-15 nm forming micronsized spherical agglomerates.

The only TiO₂ crystal phase observed at mid calcination temperatures (up to 500 °C) was the anatase phase. Interestingly, xerogels already evidenced their crystal nature as they exhibit reflections associated to this phase. Their crystallite size suggests that those particles are in fact the crystal nuclei, formed during the synthesis and they grows during calcination. High vanadium loading results in the formation of V₂O₅ scherbinaite. Besides, the presence of vanadium promotes the TiO₂ anatase to rutile transformation at lower temperatures (*i.e.* 650 °C) and particle growth. Thus, it leads as consequence, the detrimental of the porosity. The V₂O₅ crystals were also observed by electron microscopy, and the particle size was correlated to the XRD calculated one.

Vanadium loading successfully improved the electronic conductivity in the case of TiO₂-V₂O₅ samples. Surprisingly this behavior was not transposed to the electrochemical cycling *versus* lithium, evidencing only fairly good electrochemical performances. Mixed oxides samples were also electrochemical cycled *versus* sodium and they exhibited interesting behavior. Contrary to the lithium cycling, mixed oxides shows good improvement of the specific capacity obtained during the sodium cycling. NHSG TiO₂ with a 5% vanadium loading resulted to be the most promising material of the series with the highest capacities *versus* sodium and good lithiation process. Vanadium, in this sample, is mostly like a doping agent that improves the conductivity without sacrificing the porosity of the material and does not introduce other crystal phases detrimental for the electrochemical performances.

Interestingly, the 350 °C heat-treated TiO₂ coming from the NHSG ¹Pr₂O route exhibit good long term electrochemical stability and higher specific capacities than its 500 °C calcinated

counterpart. Both samples, and additionally another ether derived TiO₂ (*i.e.* THF employed as oxygen donor), were subjected to a series of gradually wider potential windows evidencing good stability. The samples heat-treated at 350 °C show irreversible electrochemical activities during the first lithiation process aside the characteristic TiO₂ behavior. Further analyses need to be performed to clarify the nature of this phenomena.

TiO₂ and TiO₂-V₂O₅ mixed oxides were also synthesized using ⁱPrOH and ^tBuOH as oxygen donors for the NHSG alcohol routes. Samples with higher vanadium content evidence traces of V₂O₅ scherbinaite like those prepared using the ⁱPr₂O ether route. Besides, alcohol derived samples possess a similar hierarchical structure. The differences between samples of different routes are observed only for the highest vanadium loading. The V₂O₅ crystals were heterogeneously dispersed in the ⁱPrOH samples while V₂O₅ were more homogeneously dispersed in ⁱPr₂O mixed oxides. This behavior was associated to the use of CH₂Cl₂ as solvent during the synthesis and the inevitable release of HCl in the alcohol route. Vanadium content also affects the porosity of the mixed oxides, the specific surface area of mixed oxides decreased with the increase of vanadium content. This behavior was observed for both, ⁱPr₂O and ⁱPrOH, routes.

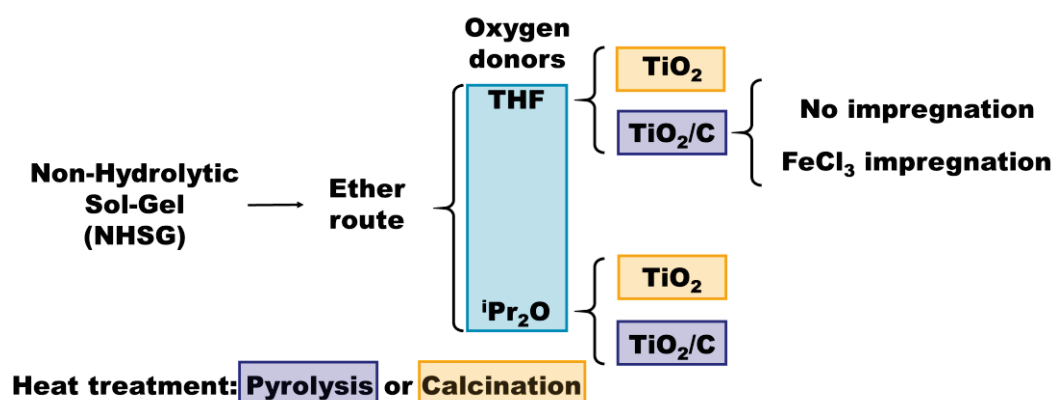
4 TiO₂/C Nanocomposites

Always targeting the anode materials for Li-ion batteries as final application and benefiting of the already implemented NHSG route to prepare TiO₂, it was decided to explore the use of carbon as electronic conductivity enhancer instead of the doping approach described in the previous chapter. Accordingly, materials prepared in this section underwent a heat treatment under Ar atmosphere in order to promote the formation of carbonaceous materials using the organic byproducts obtained during the synthesis step as carbon precursors.

It has been settled in chapter 1-Bibliography the common use of carbonaceous materials, either coatings or hybrids composites, as conductivity enhancers for electrode applications in the battery field. It also describes the reactions (particularly condensations) involved in NHSG chemistry. They set up the different byproducts that can be obtained during the synthesis step apart from the aimed oxides (*i.e.* TiO₂ in this case). As the oxygen donors possess an organic nature, the byproducts also do. They are partially removed by washing steps and totally taken off after calcination. Nevertheless, they may be used as an intrinsic carbon source for the formation of carbon composites instead of the addition of external carbon sources (the common way nowadays).

Main discussion of this chapter is based on the formation of carbonaceous TiO₂ nanocomposites following two NHSG ether routes (*i.e.* ⁱPr₂O and THF). Simultaneously, calcinated samples were also prepared under the same synthesis conditions for comparison. Major results are presented in the submitted article emphasizing the formation of the carbon coating that is dependent on the oxygen donor and how it modifies the characteristics of the synthetic TiO₂ by a direct comparison with their calcinated TiO₂ counterparts. Besides, discussion highlights the analysis of the electrochemical role played by this intrinsic carbon against the invariable application of extrinsic carbon sources during the electrode preparation and how it affects the overall electrochemical performances at low and at high current rates.

In the last section of the chapter, discussion centers on the formation of TiO₂/C nanocomposites after the addition of a reducing agent into the xerogel (*i.e.* Fe metal impregnation). The objective of this treatment was to improve the graphitization degree of the carbon coating onto NHSG derived TiO₂ nanoparticles. A global overview of samples prepared and discussed in this chapter is presented in Scheme 4.1



Scheme 4.1 Global overview of samples prepared in chapter 4: TiO₂/C nanocomposites.

4.1 Evaluation of oxygen donors over the carbon formation

4.1.1 Submitted article: *J. Mater. Chem. A*, 2017

Non-hydrolytic sol-gel route to carbon-coated mesoporous TiO₂ and evaluation of lithium insertion-deinsertion performances

A.M. Escamilla-Pérez¹, N. Louvain^{1,2*}, O. Fontaine^{1,2}, B. Boury¹, N. Brun¹, P.H. Mutin^{1*}

¹Institut Charles Gerhardt Montpellier, UMR 5253, Université Montpellier 2, CC 1701, Place Eugène Bataillon, 34095 Montpellier Cedex 5, France

²Réseau sur le Stockage Electrochimique de l'Energie (RS2E), FR CNRS 3459, France.

Corresponding authors e-mail:

nicolas.louvain@umontpellier.fr, hubert.mutin@umontpellier.fr

Abstract

Mesoporous carbon-coated TiO₂ nanocomposites were synthesized using an original, solvent-free NHSG route, based on the reaction of simple ethers (diisopropyl ether or tetrahydrofuran) with titanium tetrachloride at 180 °C. In this method, the ethers were used not only as oxygen donors but also as carbon sources. After pyrolysis at 750 °C, mesoporous TiO₂/carbon nanocomposites built of anatase nanocrystals coated by an amorphous carbon film were obtained. The nanocomposites and their TiO₂ counterparts (obtained by calcination) were characterized by XRD, Raman spectroscopy, ¹³C solid state NMR spectroscopy, and electron microscopy. The carbon content can be easily controlled by the reaction temperature. The nature of the ether impacted the carbon content and the carbon coating thickness, as well as the texture of the nanocomposite and TiO₂ crystallite size. To further characterize the carbon coatings, the electrochemical behavior of TiO₂/C nanocomposites and their TiO₂ counterparts towards lithium insertion-deinsertion was investigated in half-cells. The influence of the carbon coating on the electrochemical performance was evidenced and compared to that of a conventional carbon-black additive. This simple NHSG approach should provide a general method to synthesize a wide range of carbon-metal oxide nanocomposites.

Keywords

Non-hydrolytic sol-gel; TiO₂-C nanocomposites; Anatase; Mesoporous materials; Carbon coating ; Li-ion batteries

Introduction

Mesoporous oxides and mixed oxides are of paramount importance in the areas of heterogeneous catalysis, separation, adsorption, or energy.¹⁻³ The sol-gel process is the most common method used to synthesize mesoporous oxides, as this low temperature process offers the possibility to obtain metastable phases, with control over composition, homogeneity, and texture. The conventional, hydrolytic methods naturally predominate.^{4, 5} However, over the last 25 years, several alternative nonhydrolytic sol-gel (NHSG) routes have been developed⁶⁻⁹. In particular, the NHSG route based on the reaction of chloride precursors with an ether (*e.g.* diisopropyl ether) has proven highly successful for the synthesis

of mesoporous oxides and mixed oxides with well-controlled compositions and non-ordered mesoporous textures, avoiding the use of supercritical drying or templates.^{10, 11}

Owing to its outstanding electronic and optical properties, high chemical stability and low cost, mesoporous titanium dioxide has been the focus of intense research¹² for applications such as photovoltaic conversion^{13, 14}, sensing¹⁵, or lithium batteries^{16, 17}. However, pure TiO₂ struggles with fulfilling all the needs of those emerging applications, because of its low electronic conductivity ($10^{-12} < Ec < 10^{-7} \text{ s cm}^{-1}$ ¹⁸), low ion diffusion coefficient ($10^{-14} < Dc < 10^{-6} \text{ cm}^2 \text{ s}^{-1}$ ¹⁹⁻²²) and fast electron-hole recombination. Accordingly, a wide variety of TiO₂-based nanocomposites has been developed to make titanium dioxide more competitive²³. In particular, TiO₂-carbon composite nanomaterials have been elaborated to improve performances for instance in photovoltaic conversion, photocatalysis, or lithium batteries.²⁴⁻²⁸ In lithium batteries, TiO₂ is considered a promising substitute to replace graphite anodes for high-power Li-ion batteries, but its electronic conductivity is too low. Accordingly, the coating of TiO₂ onto highly conductive carbons has been favored. With the emergence of nanocarbons, the coating of TiO₂ layers onto carbon nanotubes²⁹ and graphene-based^{30, 31} materials has been widely investigated. The other way around, the coating of carbonaceous layers onto TiO₂ particles has been also largely studied and proved more advantageous effects³². Such carbon coatings should be homogenous and thin in order to allow Li ion diffusion through the carbon layer. It was demonstrated that the homogeneity of the carbon coating rather than the carbon:TiO₂ ratio plays a key role in tuning electrochemical performances^{28, 33, 34}. Two-step approaches involving the synthesis of TiO₂ nanomaterials by hydrolytic sol-gel routes and their subsequent coating using various carbon precursors has been widely developed^{35, 36}. A large variety of carbon precursors has been reported such as sucrose^{37, 38}, glucose³⁹⁻⁴¹, poly(vinyl pyrrolidone)⁴², dopamine⁴³, pyrrole⁴⁴, and ethylene⁴⁵. In these multi-step strategies, controlling the homogeneity of the carbon coating is not straightforward; in addition, besides carbon precursors, co-polymers or surfactants are usually necessary to generate mesoporous or nanostructured materials, involving extra costs.

Very few groups proposed to use NHSG routes to prepare carbon-coated TiO₂. Recently, Tahir *et al*³³ reported on the synthesis of carbon-coated TiO₂ nanoparticles *via* an alcohol NHSG route. Besides TiCl₄ (precursor), benzylalcohol (oxygen-donor) and DMF (solvent), a block copolymer was used as a carbon precursor. The presence in the copolymer of hydroxamic acid groups able to coordinate titanium cations and of graphitizable polyacrylonitrile blocks led after pyrolysis at 650 °C to small TiO₂ nanoparticles covered with a uniform and homogeneous carbon coating. The nanocomposites were tested as anode materials for sodium-ion batteries. These studies revealed a beneficial impact on the electrochemical performance of both the small particle size and the carbon coating, but acetylene black was added during electrode formulation, making the contribution of the carbon coating hard to evaluate.³³ Recently we showed that mesoporous nanocrystalline TiO₂ with good performances in lithium insertion could be prepared by NHSG from TiCl₄ and iPr₂O at 110 °C.⁴⁶

Drawing our inspiration from those recent works, we developed an original way to obtain mesoporous carbon-coated TiO₂ (TiO₂/C) through a solvent-free NHSG route. In this simple approach, we used a conventional ether (IPE, THF) not only as oxygen donor but also as sole carbon source. After pyrolysis at 750 °C, mesoporous TiO₂/carbon nanocomposites built of anatase nanocrystals coated by an amorphous carbon film were obtained. The carbon content and carbon coating thickness could be controlled by playing on the nature of the ether and the reaction temperature. Both nanocomposites and the corresponding oxides (obtained by calcination in air of the xerogels) were thoroughly characterized by X-ray diffraction, Raman

and infrared spectroscopies, ¹³C solid state nuclear magnetic resonance, N₂-physisorption and scanning and transmission electron microscopy. The electrochemical behavior and performance of TiO₂/C nanocomposites toward lithium (de-)insertion were investigated through galvanostatic cycling in half coin cells. The effect of texture, carbon coating and carbon-black additive was investigated. This simple NHSG approach provides a general way to mesoporous carbon-metal oxide nanocomposites that could be of great interest for catalysis and photocatalysis.

Experimental section

Samples synthesis

TiO₂/C nanocomposites were synthesized by reaction of TiCl₄ with an ether (2 equivalents). To avoid water, all manipulations were done in a glovebox under argon atmosphere (<10 ppm of water and O₂). Titanium (IV) chloride, (Sigma-Aldrich 99%) was used as received; diisopropyl ether, IPE, (TCI chemicals 99.9 %) was dried by distillation over sodium; tetrahydrofuran (THF, Fisher Scientific 99.8 %) was dried over a PureSolve MD5 solvent purification system from Innovative Technology. The amount of water in the ethers was controlled with a Karl Fischer coulometer before reaction (H₂O < 10 ppm for IPE and H₂O < 5 ppm for THF). TiCl₄ (12.52 mmol) then the ether (25.04 mmol) were added in a stainless steel digestion vessel (23 mL) with PTFE lining. The sealed digestion vessel was heated in an oven at 180 °C (unless mentioned otherwise) for 4 days under autogenous pressure. The gels were dried under vacuum at 120 °C for 5 hours, then the resulting xerogels were pyrolyzed under argon atmosphere (50 mL/min) at 750 °C for 4 hours (heating rate 10 °C min⁻¹) to obtain the TiO₂/C nanocomposites.

For comparison, the corresponding TiO₂ samples were obtained by calcination in air (50 mL min⁻¹) of the xerogels at 500 °C for 5 hours (heating rate 10 °C min⁻¹).

The samples were labeled according to their composition (TiO₂ or TiO₂/C) and to the ether used (IPE or THF). For instance, the nanocomposite obtained using THF as an O-donor and C source is labeled TiO₂/C-THF, and the corresponding oxide is labeled TiO₂-THF.

Characterization

X-Ray diffraction (XRD) patterns were obtained using a PANalytical X'Pert Pro MPD diffractometer, with the K α radiation of Cu ($\lambda=1.5418$ Å) and a step size of 0.033° (2 θ scale) into the 6-90° interval. Crystallite size was estimated using the Scherrer equation from the most intense reflection (25.28 ° 2 θ). Scanning electron microscopy images were acquired with a Hitachi S-4800 electron microscope. Transmission electron microscopy images were acquired with a high voltage 200 kV JEOL JEM ARM 200F transmission electron microscope equipped with a STEM level and a spherical aberration corrector; STEM images were taken with high angle annular dark field (HAADF). EDX analyses were acquired with a JEOL CENTURIO detector and electron energy loss analyses were detected with a GATAN GIF QUANTUM. N₂-physisorption experiments were carried out at -196 °C on a Micromeritics TriStar 3000. Samples were out-gassed under vacuum at 110 °C overnight. Equivalent BET specific surface areas were determined in the relative pressure range P/P₀ from 0.08 to 0.25. The total pore volume was measured at P/P₀>0.985. Thermogravimetric analyses (TGA) were performed on a Netzsch Simultaneous Thermal Analyzer STA 409 PC Luxx with a heating rate of 10 °C min⁻¹ in the 20-1200 °C range, under a dry air atmosphere (50 mL min⁻¹).

Raman spectra were obtained on a Horiba Jobin Yvon LabRAM ARAMIS microspectrometer excited by a HeNe laser ($\lambda=633$ nm). Spectra were recorded in the range of 50 to 2000 cm⁻¹ and then normalized. Solid-state ¹³C NMR spectra were recorded with a VARIAN VNMRS 300 at 75.44 MHz, using a T3 NMR probe with 3.2 mm ZrO₂ rotors. Experiments were performed using cross polarization and magic angle spinning (CP-MAS) with a spinning frequency of 15 kHz, a contact time of 1.5 ms and a 5 s recycle delay. Polymer insets were removed from the rotor and short caps were used instead to minimize the ¹³C background. Xerogels were not washed before analyses.

Electrochemical characterization

In order to evaluate their electrochemical performance as negative electrodes in lithium batteries, films containing TiO₂/C or TiO₂ samples were prepared adding polyvinylidene fluoride (PVDF, Solef[®] 5130, Solvay) as a binder and eventually carbon black (NY50A from SN2A). The amount of PVDF in the films was kept constant for all samples (6 wt%). A summary of films composition can be found in Table 1.

Table 1. Nominal active material, carbon black, and PVDF content of the electrode films, and TiO₂ and intrinsic C content calculated from the films composition and from the pyrolytic C content of the TiO₂/C nanocomposites (6.6 wt% C for TiO₂/C-IPE and 18.9 wt% C TiO₂/C-THF).

Electrode	Active material (wt%)	Carbon black (wt%)	PVDF (wt%)	TiO ₂ (wt%)	Intrinsic C (wt%)
TiO₂-IPE-0CB	94.0	0	6.0	94.0	0
TiO₂-THF-0CB	94.0	0	6.0	94.0	0
TiO₂-IPE-18CB	76.0	18.0	6.0	76.0	0
TiO₂-THF-18CB	76.0	18.0	6.0	76.0	0
TiO₂/C-IPE-0CB	94.0	0	6.0	87.8	6.2
TiO₂/C-IPE-12CB	82.0	12.0	6.0	76.6	5.4
TiO₂/C-THF-0CB	94.0	0	6.0	76.2	17.8

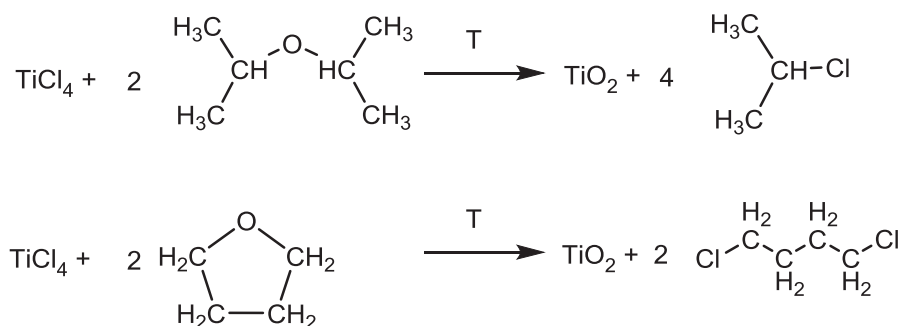
Galvanostatic electrochemical characterizations were performed at room temperature on a BTS3000 (5 V, 1 mA) instrument from Neware Battery using CR2032-type coin cells. Electrodes were composed of the active material, carbon black (unless otherwise indicated) and polyvinylidene difluoride. After stirring in N-methyl-2-pyrrolidone, the slurry was tape casted uniformly at 150 μ m onto a copper current collector using a 3540 bird film applicator from Elcometer. Electrodes (diameter 12.7 mm) were cut with a disk cutter then dried under vacuum at 80 °C overnight. Coin cells were assembled in a glove box under Ar atmosphere (O₂<0.5 ppm, H₂O<0.5 ppm), using lithium metal both as reference and as counter-electrode. The electrolyte was 1 M LiPF₆ in propylene carbonate, ethylene carbonate, and dimethyl carbonate (PC:EC:3DMC, 1:1:3 vol.) with 5% fluoroethylene carbonate and 1% vinylene carbonate as additives. Whatman glass fiber filters were used as the separator. The electrochemical galvanostatic measurements were done in the voltage range of 2.5-1.2 V vs. Li⁺/Li at different current densities: 16.8, 168, 336 mA·g⁻¹. The latter densities have been selected as corresponding to specific capacities of C/20, C/2 and C, respectively (where C=335.6 mA·g⁻¹) for pure titanium dioxide. The specific capacities presented hereafter have been calculated based on the TiO₂ content of the electrodes.

Results and discussion

Herein, we propose a very simple and original NHSG route to synthesize mesoporous carbon-coated nanocrystalline TiO₂. This route is based on the reaction of TiCl₄ with 2 equivalents of a simple ether, either diisopropyl ether (IPE) or THF tetrahydrofuran (Scheme 1), followed by a pyrolysis treatment under an inert atmosphere to convert the residual organics into carbon. It is important to note that the synthesis was carried out without any solvent, surfactant, or other additive. The ether is thus the sole oxygen and carbon source.

Choice of reaction temperature and pyrolysis temperature

NHSG syntheses of TiO₂ are generally performed at 110 °C under autogenous pressure. Under these conditions, the major organic by-products detected are isopropyl chloride in the case of IPE and 1,4-dichlorobutane in the case of THF,^{47, 48} as depicted in Scheme 1. These products are volatile, and the carbon content in the TiO₂/C nanocomposites after pyrolysis is quite low (3 wt%).



Scheme 1. Ideal reaction scheme for the NHSG synthesis of TiO₂ from IPE and THF.

Preliminary experiments indicated that the final C content in TiO₂/C nanocomposites could be increased by increasing the reaction temperature (Table 2). A higher reaction temperature obviously favors secondary reactions such as elimination of HCl and polymerization of the resulting alkenes, leading to less volatile by-products. Interestingly, the carbon content is higher with THF than with IPE, although THF contains only 4 carbon atoms, compared to 6 C atoms for IPE. This can be explained by the fact that dehydrochlorination of 1,4-dichlorobutane would lead to 1,3-butadiene, which can form highly crosslinked polymers. In the following sections, all the samples were prepared by reaction at 180 °C.

Table 2. Carbon content for TiO₂/C composites prepared by reaction at different temperature, then pyrolyzed at 750 °C under argon. The C content was determined by TGA from the weight loss between 300 and 1000 °C (Figure S11).

Sample	Oxygen donor	T reaction °C	C content wt%
TiO ₂ /C-IPE	IPE	110	3.3
		150	6.6
		180	6.6
		260	15.2
TiO ₂ /C-THF	THF	110	3.4
		150	13.7
		180	18.9
		260	21.5

The pyrolysis temperature is an important parameter, which directly impacts the nature of the carbon formed, the texture of the material, and the crystallinity of the TiO₂ phase. To find the optimal pyrolysis temperature, xerogels prepared from IPE and THF at 180 °C were pyrolyzed at 3 different temperatures (750, 800, and 900 °C), then analyzed by X-ray diffraction and nitrogen physisorption.

X-ray diffraction showed the formation of a nearly pure anatase phase for pyrolysis temperatures of 750 °C or 800 °C, whereas a significant amount of rutile was detected in the samples pyrolyzed at 900 °C (Figure SI2). Nitrogen physisorption showed a significant decrease of the specific surface area between 750 °C and 800 °C (Table SI1). Accordingly, we chose a pyrolysis temperature of 750 °C, ensuring the formation of virtually pure anatase phase and a satisfactory mesoporous texture.

Structural and textural characterization of TiO₂/C composites and the corresponding TiO₂

The nitrogen adsorption-desorption isotherms of TiO₂/C and TiO₂ samples (Figure 1a) and the associated textural data (Table 3) showed that the four samples were mesoporous. According to the IUPAC classification⁴⁹, the isotherms are intermediate between Type II (interparticle porosity) and type IV (mesoporous solids). BJH pore size distributions (Figure 1b) show the presence in all cases of mesopores in the 3 to 11 nm range. The sharp component at *ca.* 3-4 nm is an artefact related to the unstability of the meniscus at P/P₀ lower than 0.42,⁵⁰ and simply shows the presence of small mesopores (<4 nm). The TiO₂/C samples have a significantly higher specific surface areas than their TiO₂ counterparts, which could be attributed to the presence of pores within the carbonaceous phase.

Table 3. Textural data and TiO₂ crystallite size for the composite and oxide samples; ^aspecific surface area, ^btotal pore volume; ^cBJH average pore diameter calculated from the desorption branch; ^dcrystallite size determined by the Scherrer equation.

Sample	S _{BET} ^a (m ² g ⁻¹)	V _p ^b (cm ³ g ⁻¹)	D _p ^c (nm)	TiO ₂ crystallite size ^d (nm)
TiO ₂ /C-IPE	70	0.18	9.3	20
TiO ₂ -IPE	50	0.17	9.3	16
TiO ₂ /C-THF	75	0.21	10.2	13
TiO ₂ -THF	63	0.23	10.3	14

The powder X-ray diffraction (XRD) patterns of the xerogels, TiO₂/C composites obtained by pyrolysis at 750 °C, and TiO₂ samples obtained by calcination at 500 °C in air are shown in Figure 2. All of the patterns present a single crystalline phase – *i.e.* anatase TiO₂ (JCPDS 00-21-1272) – except in the case of TiO₂/C-IPE where a very weak reflection associated with the rutile phase (JCPDS 00-021-1276) is detected in addition to the anatase phase. XRD reflections for the xerogels are less intense and broader than for the composite or the oxide samples, indicating the presence of smaller or possibly less organized anatase crystallites. The anatase crystallite size in the TiO₂/C and TiO₂ samples, estimated from the main reflection using the Scherrer equation, are close, ranging from 13 to 20 nm (Table 3). The anatase crystallites are slightly larger in the materials derived from IPE than in those derived from THF.

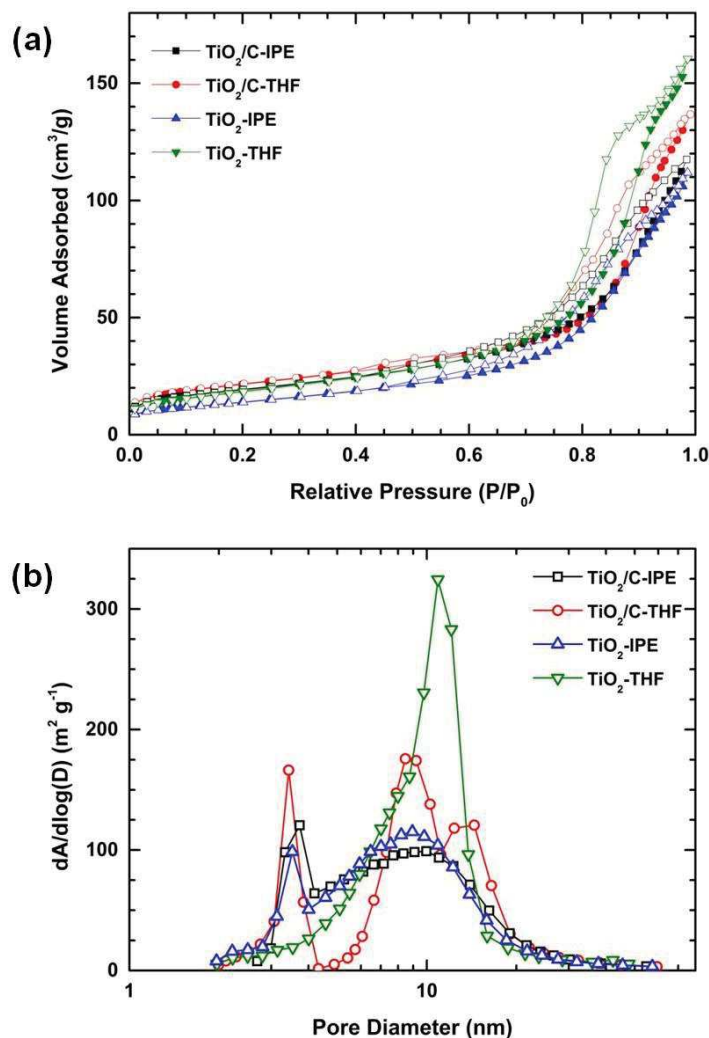


Figure 1. (a) N₂ physisorption isotherms of TiO₂ and TiO₂/C samples (filled and open symbols refer to adsorption and desorption, respectively); (b) BJH pore size distributions (desorption branch).

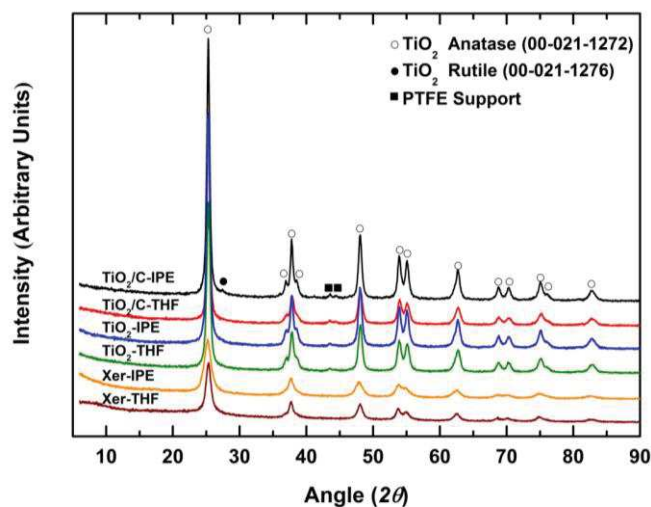


Figure 2. Powder X-ray diffraction patterns of TiO₂ and TiO₂/C samples. Additionally to typical TiO₂ reflections; XRD patterns show the presence of two weak reflections around 45° 2θ. Both of them have been correlated to the PTFE of the support used during analysis.

Although the TiO₂/C-IPE and TiO₂/C-THF nanocomposites contain 6.6 and 18.9 wt% of carbonaceous phase, respectively, no reflection related to graphitic carbon (JCPDS 01-075-2078) was detected, suggesting that the carbon phase is largely amorphous.

The Raman spectra of TiO₂ and TiO₂/C samples in the 100 to 800 cm⁻¹ range (Figure SI3) confirmed the presence of anatase as shown by the intense peak at *ca.* 144 cm⁻¹, while no band related to the rutile phase was detected^{51, 52}. It is important to mention that the Raman active vibrations related to anatase TiO₂ are much less intense in TiO₂/C samples, as shown by the lower signal to noise ratio. This observation suggests the presence of carbon surrounding the TiO₂ particles. In order to verify this assumption, the Raman spectrum of TiO₂/C-THF was compared with the spectrum of a physical mixture of TiO₂-THF (82 wt%) and carbon black (18 wt%) (sample labeled TiO₂-THF+CB in Figure SI4). This mixture was milled until a homogenous powder was obtained. As shown in Figure SI4, the anatase vibration modes were clearly observed in the spectrum of the physical mixture, while for the TiO₂/C-THF sample these bands were much weaker, which supports the formation of a carbon coating around the TiO₂ nanoparticles.

Raman spectroscopy is also a valuable technique to investigate carbonaceous materials, especially graphitic carbons. The Raman spectra in the graphitic region (900-2000 cm⁻¹) of TiO₂/C nanocomposites is displayed in Figure 3. For comparison, the spectrum of a carbon black sample (the acetylene black used in electrodes preparation) is also shown. Both carbon black and TiO₂/C samples displayed G and D bands, characteristic of graphitic and partially graphitic carbons, respectively. While the G band is usually centered at *ca.* 1580 cm⁻¹, the disorder-induced band (D band) appears at around 1350 cm⁻¹. The former is related to the presence of impurities or defects into the graphitic crystal framework⁵³⁻⁵⁵. Nevertheless, the quantification of the crystallinity of graphitic carbons by Raman spectroscopy is difficult. The intensity ratio I_D/I_G can give precious information on the graphitized crystallite coherence length using the Knight formula.⁵⁵ However, in our case, G band is centered at 1597 cm⁻¹ (instead of 1580 cm⁻¹ as expected for graphitic carbons) while the D band is very broad with a noticeable shoulder at around 1200 cm⁻¹. Thus, the Knight formula is hardly applicable. Such feature was also observed by Sadezky *et al*⁵⁶ when studying soot and amorphous carbonaceous materials. Previous reports demonstrated that the D band could be decomposed into four components⁵⁶⁻⁵⁸: D1, D2, D3 and D4 which appear at 1350; 1620; 1500 and 1200 cm⁻¹ respectively. D3 corresponds to amorphous carbon while the three other bands are related to disordered graphitic layers (A_{1g} and E_{2g}- symmetry). The presence of these four bands could explain the shift and the shape of both D and G bands in TiO₂/C samples in comparison with theoretical values.^{59, 60} These results are in good agreement with XRD patterns and support the amorphous character of the carbon phase in TiO₂/C nanocomposites.

The nature of the carbon species in the xerogels and in the TiO₂/C samples was further investigated using ¹³C solid state NMR (Figure 4). The spectra of the two xerogels were similar, and showed the presence of both *sp*³ (0-40 ppm) and *sp*² (110-140 ppm) carbon atoms. The signal corresponding to the *sp*³ carbons suggests the formation of a cross-linked polyolefin network, with no evidence for aliphatic C-OH or C-O-C groups (55–75 ppm).⁶¹ The *sp*² signal shows the presence of significant amounts of vinylic or aromatic carbons. At least in the case of IPE, this suggests the occurrence of significant dehydrogenation during the synthesis of the gel. The spectra of the two TiO₂/C samples are also quite similar, showing very broad resonances indicating the presence of both *sp*³ (0-90 ppm) and *sp*² (90-150 ppm) carbon atoms. For comparison, carbon black mainly shows resonances at 10 and 170 ppm.⁶² The large *sp*³ contribution in our sample is consistent with the Raman results pointing to the formation of an amorphous carbon phase.

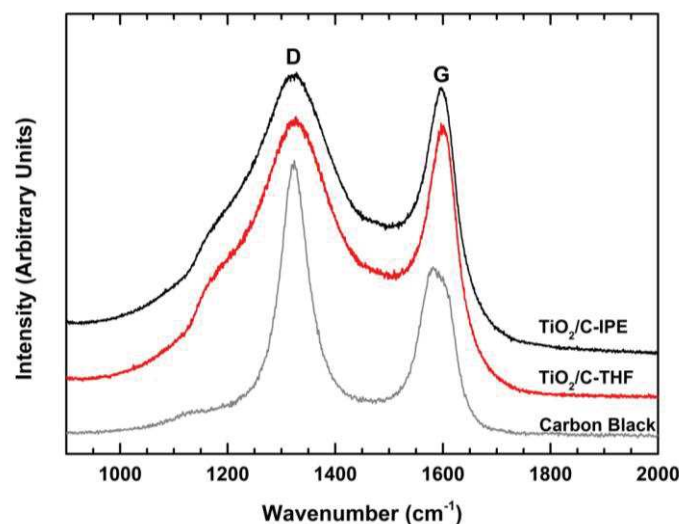


Figure 3. Raman spectra of TiO₂/C samples (graphite region).

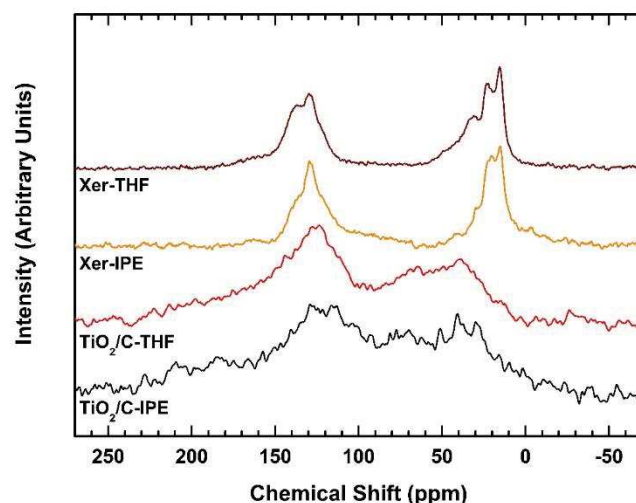


Figure 4. Solid-state ¹³C CP-MAS NMR spectra of dried xerogels and TiO₂/C nanocomposites. Spectra were normalized. The background signal was removed by subtracting the spectrum obtained without the sample.

Typical scanning electron micrographs of TiO₂ and TiO₂/C samples are given in Figure 5. In all cases, the samples are composed of primary nanoparticles, *ca.* 15 to 25 nm for IPE-derived samples, 10 to 15 nm for THF-derived samples. These particle size are in good agreement with the crystallite size derived from XRD (Table 3), indicating that the particles are monocrystalline. The packing of these dense primary particles accounts for the mesoporosity of TiO₂ and TiO₂/C samples. In addition, the samples derived from IPE show an interesting hierarchical texture, the primary particles forming micron-sized spherical secondary particles (Figure 5 a-b), as previously reported for IPE-derived TiO₂.⁴⁶ Such texture was not observed for the THF-derived samples, in which primary nanoparticles simply form large agglomerates. It is noteworthy that the morphology depends on the oxygen donor (IPE or THF) but not on the heat treatment (calcination or pyrolysis), again suggesting that the carbon phase forms a coating around the anatase nanocrystals.

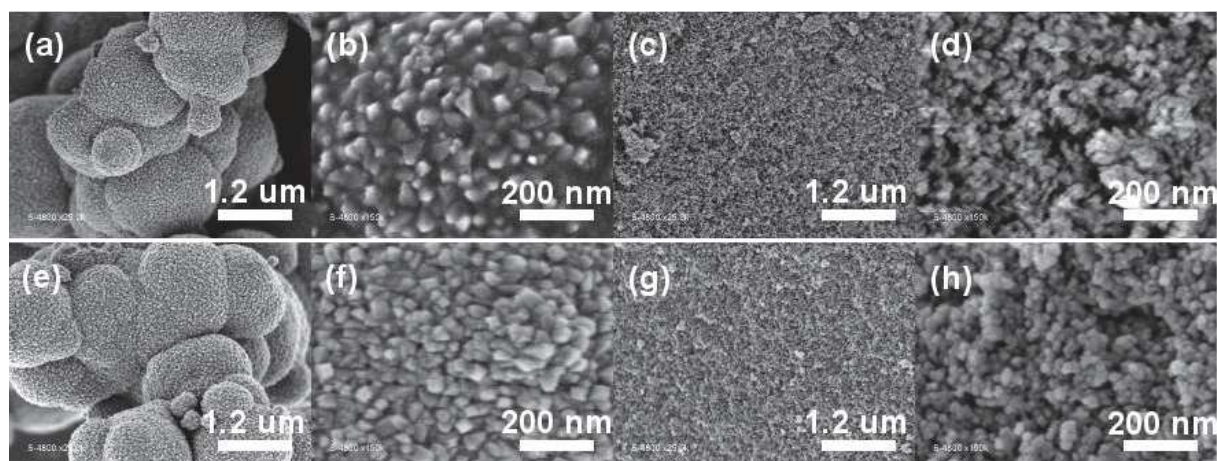


Figure 5. Scanning electron micrographs of TiO₂-IPE (a,b), TiO₂-THF (c,d), TiO₂/C-IPE (e,f), TiO₂/C-THF (g,h) at different magnifications.

Transmission electron microscopy of the TiO₂/C nanocomposites (Figure 6) allow distinguishing the crystalline TiO₂ nanoparticles from the amorphous carbon phase, which forms a coating around TiO₂ nanocrystals. The crystal planes of anatase TiO₂ particles can be clearly observed, while the carbon coating appears in light gray on the HAADF images, as shown by EDX analyses (in supporting information, Figures SI5 and SI6), support this statement. The particle size (average over 100 particles) obtained by analysis of TEM micrographs was 16.2 ± 5.7 nm for TiO₂/C-IPE and 12.5 ± 3.3 nm for TiO₂/C-THF, confirming the smaller size of THF-derived anatase particles. The thickness of the coatings (average over 50 different areas) was 1.5 ± 0.9 nm for TiO₂/C-IPE and 3 ± 1.5 nm for TiO₂/C-THF. The thicker coating in TiO₂/C-THF is consistent with the higher C content in this sample.

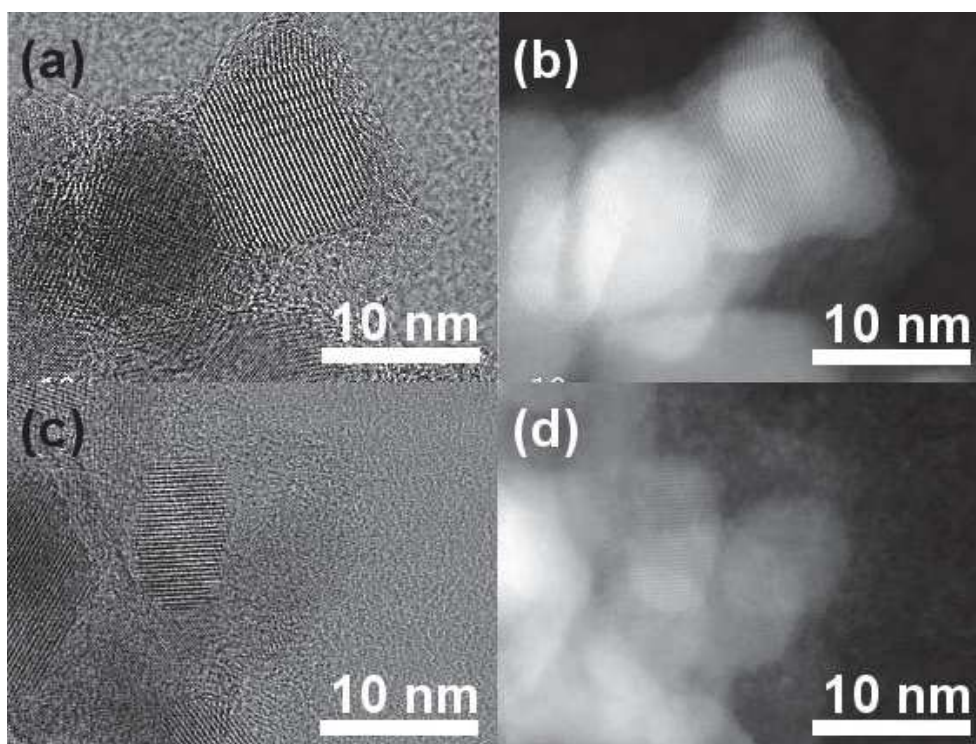


Figure 6. Transmission electron micrographs and HAADF images of TiO₂/C-IPE (a,b) and TiO₂/C-THF (c,d) samples.

Electrochemical characterization

Thus far, we demonstrated that NHSG provided a simple and original method to synthesize carbon-coated TiO₂ nanocrystals. One potential application of TiO₂/C nanocomposites is their use as negative electrodes in lithium batteries. In order to evaluate their electrochemical performance for this application, the electrochemical performances of both TiO₂ and TiO₂/C composites were investigated.

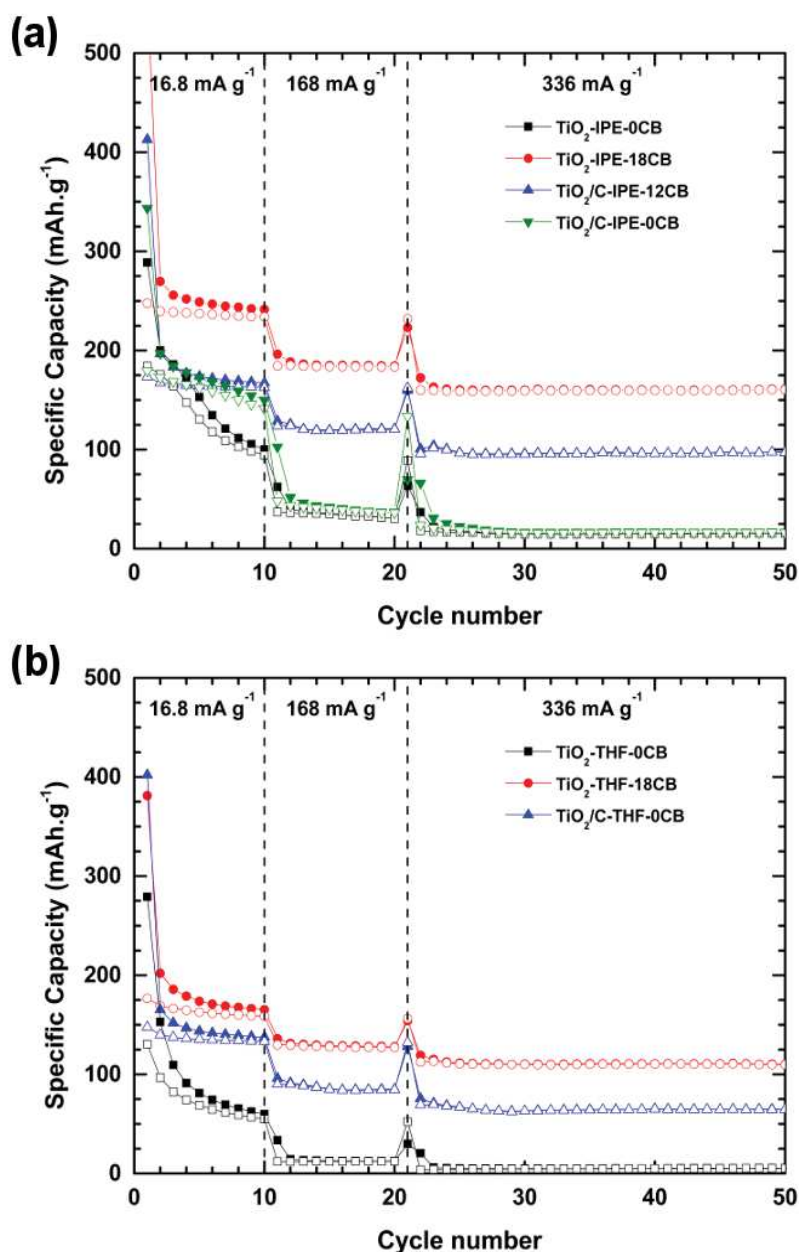


Figure 7. Cycling performance at different C rates ($C=335.6 \text{ mAh}\cdot\text{g}^{-1}$) of (a) electrodes prepared with IPE-based samples and (b) electrodes prepared with THF-based samples. Voltage window of 1.2-2.5 V *versus* Li⁺/Li. Filled and open symbols refer to reduction (discharge) and oxidation (charge) respectively. The intrinsic and/or extrinsic carbon content of the electrodes is given in Table 1.

The cyclability of all electrodes is presented in Figure 7. Columbic efficiency and initial (1st cycle) galvanostatic charge/discharge profiles are presented in Figures SI7 and SI8. It is important to keep in mind that all seven electrodes did not contain the same amount of active

material (TiO₂), and that the specific capacities were calculated based on the TiO₂ present in electrodes.

Galvanostatic profiles (Figure SI8) evidence the characteristics of anatase TiO₂ cycled versus lithium. All electrodes present a constant plateau at a potential of *ca.* 1.7 V *vs.* Li⁺/Li, characteristic of a two-phase reaction between the tetragonal solid solution compound (*i.e.* Li_xTiO₂; x<0.5 formed during the drop of potential from the open circuit) and the orthorhombic lithium titanate (Li_{0.5}TiO₂). Then, the formation of LiTiO₂ phase is evidenced by the presence of a pseudoplateau at *ca.* 1.5 V *vs.* Li⁺/Li, corresponding also to a two-step reaction.⁶³⁻⁶⁵

As expected, TiO₂-IPE-0CB and TiO₂-THF-0CB “white electrodes” which contain no carbon (neither carbon black nor intrinsic carbon) exhibited low capacity even at low current densities (*e.g.* 16.8 mA g⁻¹, C/20). After 10 cycles at 16.8 mA g⁻¹ these electrodes displayed specific capacities below 100 mAh g⁻¹ (Figure 7) and columbic efficiencies below 95% (Figure SI7).

TiO₂/C-IPE-0CB and TiO₂/C-THF-0CB electrodes prepared with the TiO₂-C nanocomposites but without carbon black exhibited significantly better specific capacities of 150 and 137 mAh g⁻¹ after 10 cycles at C/20, respectively, showing that the C coating was beneficial. However, while columbic efficiency was significantly improved from TiO₂-THF-0CB to TiO₂/C-THF-0CB (91.6% to 96.8% for cycle 10), no improvement was observed for IPE-derived electrodes (94.3% for both). This feature is most probably related to the presence of a higher amount of intrinsic carbon into TiO₂/C-THF-0CB (18 wt%) as compared to TiO₂/C-IPE-0CB (6 wt%). This trend was further confirmed at higher current density (336 mA g⁻¹, cycles 21-50). While both “white electrodes” and TiO₂/C-IPE-0CB showed negligible specific capacities below 15 mAh g⁻¹, TiO₂/C-THF-0CB displayed a reasonable specific capacity of 65 mAh g⁻¹ at cycle 50, with an efficiency above 99.7% from cycle 25 to 50 (Figure SI7). At this stage, the presence of intrinsic carbon clearly improves the electrochemical performances of the electrodes. Moreover, a higher amount of intrinsic carbon significantly increases the cycling performances at high current densities.

To provide further insights into the role and efficiency of the intrinsic carbon, electrodes with a total carbon content of *ca.* 18 wt% were prepared by adding carbon black. Thus, the TiO₂/C-THF-0CB electrode (18 wt% of intrinsic carbon) was compared with TiO₂-THF-18CB and TiO₂-IPE-18CB (18wt% of carbon black), as well as with TiO₂/C-IPE-12CB (6 wt% of intrinsic carbon and 12 wt% of carbon black). These four electrodes displayed similar columbic efficiency profiles with an efficiency of *ca.* 97% after 10 cycles at a current density of 16.8 mA g⁻¹ and above 99% after only three cycles at 336 mA g⁻¹ (Figure SI7). This feature proves the excellent capacity reversibility of those materials. These four electrodes exhibit the same moderate capacity fade, losing around 30 mA g⁻¹ between the 2nd and the 10th cycle, and around 100 mA g⁻¹ between the 2nd and the 50th cycle (Figure 7). This behavior clearly evidences the importance of carbon in electrode formulation, either intrinsic carbon or carbon black. However, regarding specific capacities, significant differences can be observed. For a given oxygen donor and a 18 wt% total carbon amount, electrodes that contain a higher carbon black content display higher specific capacity (Figure 7). This feature shows that as far as electrochemical performances are concerned, carbon black is more effective than intrinsic carbon. Several hypotheses can be suggested to explain this situation. First, the intrinsic carbon formed at 750 °C is amorphous, whereas the carbon black presents a more graphitic nature; accordingly, both electronic conductivity and lithium diffusion should be more favorable for the carbon black additive than for the intrinsic carbon. Secondly, the intrinsic

carbon forms a homogeneous coating around the anatase nanocrystals, which could hinder lithium ion diffusion toward the TiO₂, thus limiting specific capacity. On the contrary, the carbon black particles, simply bridge the TiO₂ nanocrystals, allowing for improved electronic conductivity while preserving the accessibility of TiO₂ to lithium ions.

Recent studies on carbon-coated TiO₂ electrodes reported in the literature showed clear improvement of the electrochemical performances of for lithium-ion and sodium-ion batteries.^{39, 40, 44, 66-71} It is noteworthy that those studies always used carbon black additive in electrode formulation. Moreover, the total carbon amount was not kept constant, making comparisons between coating and additive carbons difficult. Recently, Tahir *et al.*³³ proposed a comparison at constant carbon content in electrodes for sodium-ion batteries. However, as lithium-ion and sodium-ion batteries are two different devices and involve different mechanisms, we cannot properly compare our results with this study.

Apart from carbon coating, it is noteworthy that IPE-derived TiO₂ displays a better electrochemical behavior than THF-derived TiO₂ (at constant carbon content). This feature is particularly noticeable for TiO₂-THF-18CB and TiO₂-IPE-18CB electrodes, which showed a specific capacity in the 50th cycle of 110 mA g⁻¹ and 160 mA g⁻¹, respectively (Figure 7), whereas the particle size in TiO₂-THF is smaller than in TiO₂-IPE. Accordingly, this behavior could be ascribed the hierarchical texture of the TiO₂-IPE sample, which could facilitate accessibility of lithium ions to the surface of anatase nanocrystals.

Conclusion

In conclusion, mesoporous carbon-coated TiO₂ nanocomposites were successfully synthesized using an original, solvent-free NHSG route. We proposed to use simple ethers in a stoichiometric amount not only as oxygen donors but also as carbon sources. After pyrolysis at 750 °C, mesoporous TiO₂/carbon nanocomposites built of anatase nanocrystals coated by an amorphous carbon film were obtained, as shown by XRD, Raman and ¹³C CPMAS-NMR spectroscopies, and electron microscopy. The carbon content can be controlled by playing on the reaction temperature. The nature of the ether impacted the carbon content and the carbon coating thickness, as well as the texture of the nanocomposite and TiO₂ crystallite size. To further characterize the carbon coatings, the electrochemical behavior of TiO₂/C nanocomposites and their TiO₂ counterparts (obtained by calcination in air) toward lithium insertion was investigated. The influence of the carbon coating on the electrochemical performances was evidenced and compared to that of a conventional carbon-black additive. This simple NHSG approach should provide a general method to synthesize mesoporous metal oxide-carbon nanocomposites, and much remains to be done to explore different oxide and mixed oxide-carbon systems, different oxygen/carbon donors, and to investigate the potential applications of these nanocomposites.

Acknowledgments

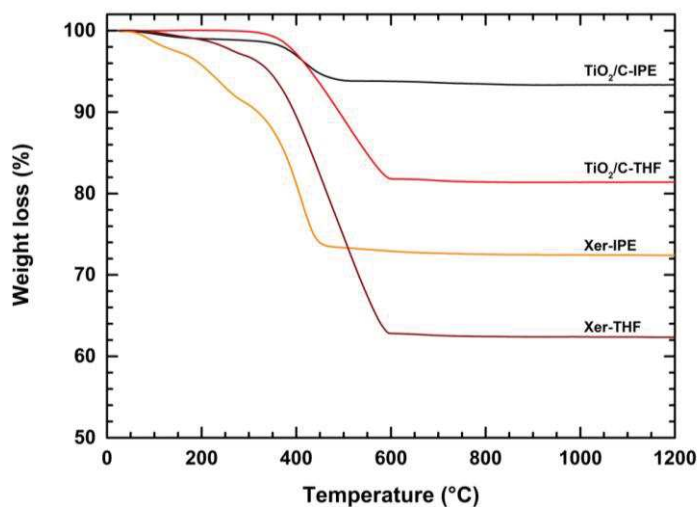
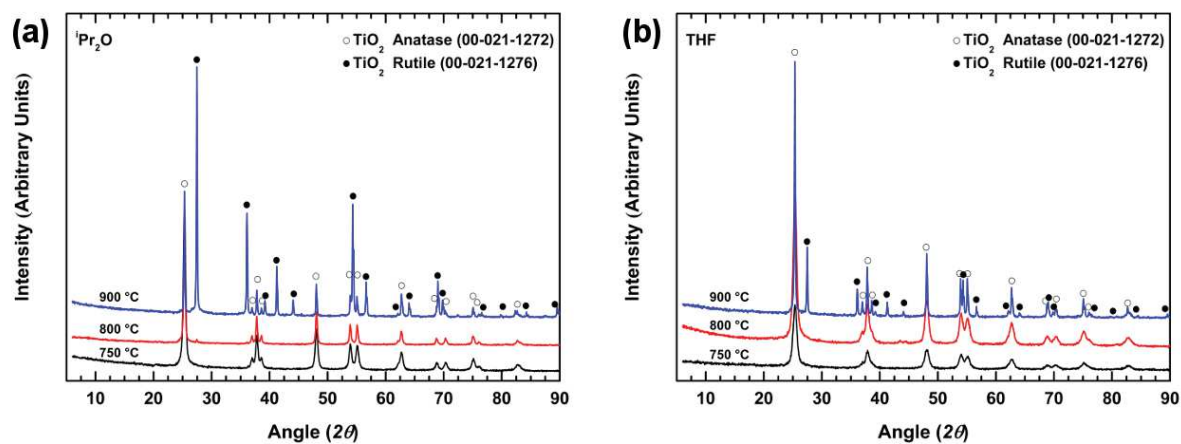
This work was supported by the “Centre National de la Recherche Scientifique” and the University of Montpellier, and through a PhD grant of the “Consejo Nacional de Ciencia y Tecnología” in Mexico.

References

1. G. Q. Lu and X. S. Zhao, eds., *Nanoporous Materials: Science and Engineering* World Scientific, Singapore, 2011.
2. Y. Ren, Z. Ma and P. G. Bruce, *Chem. Soc. Rev.*, 2012, **41**, 4909-4927.
3. A. Corma, *Chem. Rev.*, 1997, **97**, 2373-2419.
4. L. L. Hench and J. K. West, *Chem. Rev.*, 1990, **90**, 33-72.
5. C. J. Brinker and G. W. Scherer, *Sol-gel Science: the physics and chemistry of sol-gel processing*, Academic Press, Boston, MA, 1990.
6. A. Vioux, *Chem. Mater.*, 1997, **9**, 2292-2299.
7. N. Pinna and M. Niederberger, *Angew. Chem., Int. Ed.*, 2008, **47**, 5292-5304.
8. P. H. Mutin and A. Vioux, *Chem. Mater.*, 2009, **21**, 582-596.
9. A. Styskalik, D. Skoda, C. Barnes and J. Pinkas, *Catalysts*, 2017, **7**, 168.
10. D. P. Debecker, V. Hulea and P. H. Mutin, *Appl. Catal., A*, 2013, **451**, 192-206.
11. P. H. Mutin and A. Vioux, *J. Mater. Chem. A*, 2013, **1**, 11504-11512.
12. W. Li, Z. Wu, J. Wang, A. A. Elzatahry and D. Zhao, *Chem. Mater.*, 2014, **26**, 287-298.
13. Y. Bai, I. Mora-Seró, F. De Angelis, J. Bisquert and P. Wang, *Chem. Rev.*, 2014, **114**, 10095-10130.
14. U. Bach, D. Lupo, P. Comte, J. E. Moser, F. Weissortel, J. Salbeck, H. Spreitzer and M. Gratzel, *Nature*, 1998, **395**, 583-585.
15. J. Bai and B. Zhou, *Chem. Rev.*, 2014, **114**, 10131-10176.
16. T. Song and U. Paik, *J. Mater. Chem. A*, 2016, **4**, 14-31.
17. J. Jin, S.-Z. Huang, J. Liu, Y. Li, D.-S. Chen, H.-E. Wang, Y. Yu, L.-H. Chen and B.-L. Su, *J. Mater. Chem. A*, 2014, **2**, 9699-9708.
18. Y. Liu and Y. Yang, *J. Nanomater.*, 2016, **2016**, 8123652/8123651-8123652/8123615.
19. L. H. Nguyen, V. Aravindan, S. A. Kulkarni, F. Yanan, R. R. Prabhakar, S. K. Batabyal and S. Madhavi, *ChemElectroChem*, 2014, **1**, 539-543.
20. F. Gligor and S. W. de Leeuw, *Solid State Ionics*, 2006, **177**, 2741-2746.
21. S. Bach, J. P. Pereira-Ramos and P. Willman, *Electrochim. Acta*, 2010, **55**, 4952-4959.
22. M. V. Koudriachova, N. M. Harrison and S. W. de Leeuw, *Phys. Rev. Lett.*, 2001, **86**, 1275-1278.
23. M. Dahl, Y. Liu and Y. Yin, *Chem. Rev.*, 2014, **114**, 9853-9889.
24. L. Zhao, X. Chen, X. Wang, Y. Zhang, W. Wei, Y. Sun, M. Antonietti and M.-M. Titirici, *Adv. Mater.*, 2010, **22**, 3317-3321.
25. G. Qin, X. Wu and H. Zhang, *RSC Adv.*, 2014, **4**, 52438-52450.
26. F.-F. Cao, Y.-G. Guo, S.-F. Zheng, X.-L. Wu, L.-Y. Jiang, R.-R. Bi, L.-J. Wan and J. Maier, *Chem. Mater.*, 2010, **22**, 1908-1914.
27. K.-T. Kim, C.-Y. Yu, S.-J. Kim, Y.-K. Sun and S.-T. Myung, *J. Power Sources*, 2015, **281**, 362-369.
28. B. Oschmann, D. Bresser, M. N. Tahir, K. Fischer, W. Tremel, S. Passerini and R. Zentel, *Macromol. Rapid Commun.*, 2013, **34**, 1693-1700.
29. F. F. Cao, Y. G. Guo, S. F. Zheng, X. L. Wu, L. Y. Jiang, R. R. Bi, L. J. Wan and J. Maier, *Chem. Mater.*, 2010, **22**, 1908-1914.
30. C. J. Chen, Y. W. Wen, X. L. Hu, X. L. Ji, M. Y. Yan, L. Q. Mai, P. Hu, B. Shan and Y. H. Huang, *Nat. Commun.*, 2015, **6**.
31. G. H. Qin, X. Y. Zhang and C. Y. Wang, *J. Mater. Chem. A*, 2014, **2**, 12449-12458.
32. B. Wang, H. Xin, X. Li, J. Cheng, G. Yang and F. Nie, *Sci. Rep.*, 2014, **4**, 3729.
33. M. N. Tahir, B. Oschmann, D. Buchholz, X. Dou, I. Lieberwirth, M. Panthoefler, W. Tremel, R. Zentel and S. Passerini, *Adv. Energy Mater.*, 2016, **6**, 1501489.
34. F. Mueller, D. Bresser, E. Paillard, M. Winter and S. Passerini, *J. Power Sources*, 2013, **236**, 87-94.
35. L. Mai, C. Huang, D. Wang, Z. Zhang and Y. Wang, *Appl. Surf. Sci.*, 2009, **255**, 9285-9289.
36. Q. Xiao, J. Zhang, C. Xiao, Z. Si and X. Tan, *Sol. Energy*, 2008, **82**, 706-713.
37. J.-J. Zhang, Z. Wei, T. Huang, Z.-L. Liu and A.-S. Yu, *J. Mater. Chem. A*, 2013, **1**, 7360-7369.
38. S.-M. Oh, J.-Y. Hwang, C. S. Yoon, J. Lu, K. Amine, I. Belharouak and Y.-K. Sun, *ACS Appl. Mater. Interfaces*, 2014, **6**, 11295-11301.
39. D. Pham-Cong, J.-H. Kim, S.-Y. Jeong, J. H. Choi, J. Kim and C.-R. Cho, *Electrochem. Commun.*, 2015, **60**, 204-207.
40. X. Bai, T. Li, Y.-X. Qi, X.-P. Gao, L.-W. Yin, H. Li, H.-L. Zhu, N. Lun and Y.-J. Bai, *Electrochim. Acta*, 2015, **169**, 241-247.
41. L.-Y. Wang, Y. Wu, J.-P. Han, B. Zhang, X. Bai, Y.-X. Qi, N. Lun, Y.-M. Cao and Y.-J. Bai, *Electrochim. Acta*, 2017, **245**, 186-192.
42. Y. Ge, H. Jiang, J. Zhu, Y. Lu, C. Chen, Y. Hu, Y. Qiu and X. Zhang, *Electrochim. Acta*, 2015, **157**, 142-148.

43. L. Tan, L. Pan, C. Cao, B. Wang and L. Li, *J. Power Sources*, 2014, **253**, 193-200.
44. S. Guo, J. Liu, S. Qiu, W. Liu, Y. Wang, N. Wu, J. Guo and Z. Guo, *J. Mater. Chem. A*, 2015, **3**, 23895-23904.
45. N. K. Memon, D. H. Anjum and S. H. Chung, *Combust. Flame*, 2013, **160**, 1848-1856.
46. A. M. Escamilla-Perez, N. Louvain, M. Kaschowitz, S. Freunberger, O. Fontaine, B. Boury, N. Brun and P. H. Mutin, *J. Sol-Gel Sci. Technol.*, 2016, **79**, 270-278.
47. P. Arnal, R. J. P. Corriu, D. Leclercq, P. H. Mutin and A. Vioux, *Chem. Mater.*, 1997, **9**, 694-698.
48. P. Arnal, R. J. P. Corriu, D. Leclercq, P. H. Mutin and A. Vioux, *J. Mater. Chem.*, 1996, **6**, 1925-1932.
49. M. Thommes, K. Kaneko, A. V. Neimark, J. P. Olivier, F. Rodriguez-Reinoso, J. Rouquerol and K. S. W. Sing, *Pure Appl. Chem.*, 2015, **87**, 1051-1069.
50. M. Thommes, *Chem. Ing. Tech.*, 2010, **82**, 1059-1073.
51. T. Ohsaka, F. Izum and Y. Fujiki, *J. Raman Spectrosc.*, 1978, **7**, 321-324.
52. R. M. Kadam, B. Rajeswari, A. Sengupta, S. N. Achary, R. J. Kshirsagar and V. Natarajan, *Spectrochim. Acta, Part A*, 2015, **137**, 363-370.
53. A. C. Ferrari and J. Robertson, *Phys. Rev. B: Condens. Matter Mater. Phys.*, 2000, **61**, 14095-14107.
54. F. Tuinstra and J. L. Koenig, *J. Chem. Phys.*, 1970, **53**, 1126-1130.
55. M. J. Matthews, M. A. Pimenta, G. Dresselhaus, M. S. Dresselhaus and M. Endo, *Phys. Rev. B: Condens. Matter Mater. Phys.*, 1999, **59**, R6585-R6588.
56. A. Sadezky, H. Muckenhuber, H. Grothe, R. Niessner and U. Poschl, *Carbon*, 2005, **43**, 1731-1742.
57. N. P. Ivleva, U. McKeon, R. Niessner and U. Poschl, *Aerosol Sci. Technol.*, 2007, **41**, 655-671.
58. B. Dippel, H. Jander and J. Heintzenberg, *Phys. Chem. Chem. Phys.*, 1999, **1**, 4707-4712.
59. D. R. Tallant, T. A. Friedmann, N. A. Missert, M. P. Siegal and J. P. Sullivan, *Mater. Res. Soc. Symp. Proc.*, 1998, **498**, 37-48.
60. H. J. Scheibe, D. Drescher and P. Alers, *Fresenius' J. Anal. Chem.*, 1995, **353**, 695-697.
61. W. Cai, R. D. Piner, F. J. Stadermann, S. Park, M. A. Shaibat, Y. Ishii, D. Yang, A. Velamakanni, S. J. An, M. Stoller, J. An, D. Chen and R. S. Ruoff, *Science (Washington, DC, U. S.)*, 2008, **321**, 1815-1817.
62. H. Darmstadt, C. Roy, S. Kaliaguine, G. Xu, M. Auger, A. Tuel and V. Ramaswamy, *Carbon*, 2000, **38**, 1279-1287.
63. M. Wagemaker, W. J. H. Borghols and F. M. Mulder, *J. Am. Chem. Soc.*, 2007, **129**, 4323-4327.
64. U. Lafont, D. Carta, G. Mountjoy, A. V. Chadwick and E. M. Kelder, *J. Phys. Chem. C*, 2010, **114**, 1372-1378.
65. T. Froeschl, U. Hoermann, P. Kubiak, G. Kucerova, M. Pfanzelt, C. K. Weiss, R. J. Behm, N. Huesing, U. Kaiser, K. Landfester and M. Wohlfahrt-Mehrens, *Chem. Soc. Rev.*, 2012, **41**, 5313-5360.
66. U. Ulissi, J. Zimmermann, S. Brutti and J. Hassoun, *Electrochim. Acta*, 2016, **201**, 158-164.
67. L. Ding, J. Chen, B. Dong, Y. Xi, L. Shi, W. Liu and L. Cao, *Electrochim. Acta*, 2016, **200**, 97-105.
68. W. Yang, X. Bai, T. Li, Y.-Y. Ma, Y.-X. Qi, L.-W. Yin, H. Li, N. Lun and Y.-J. Bai, *RSC Adv.*, 2015, **5**, 93155-93161.
69. S. Jiang, R. Wang, M. Pang, H. Wang, S. Zeng, X. Yue, L. Ni, Y. Yu, J. Dai, S. Qiu and Z. Zhang, *Electrochim. Acta*, 2015, **182**, 406-415.
70. S. Qiu, L. Xiao, X. Ai, H. Yang and Y. Cao, *ACS Appl. Mater. Interfaces*, 2017, **9**, 345-353.
71. W. Zhu, H. Yang, K. Nakanishi, K. Kanamori and X. Guo, *RSC Adv.*, 2015, **5**, 24803-24813.

Supplementary material

Figure S11. Thermogravimetric analysis in air of xerogels and TiO₂/C composites.Figure S12. Powder X-ray diffraction patterns of TiO₂/C nanocomposites pyrolyzed at different temperatures: IPE derived samples (a) and THF derived ones (b).Table S11. Textural data for TiO₂/C composites prepared at 180 °C and pyrolyzed at 750 or 800 °C, ^atemperature of pyrolysis, ^bspecific surface area, ^ctotal pore volume.

Sample	T _{pvr} ^a (°C)	S _{BET} ^b (m ² g ⁻¹)	V _p ^c (cm ³ g ⁻¹)
TiO ₂ /C-IPE	750	70	0.18
	800	15	0.05
TiO ₂ /C-THF	750	75	0.21
	800	38	0.09

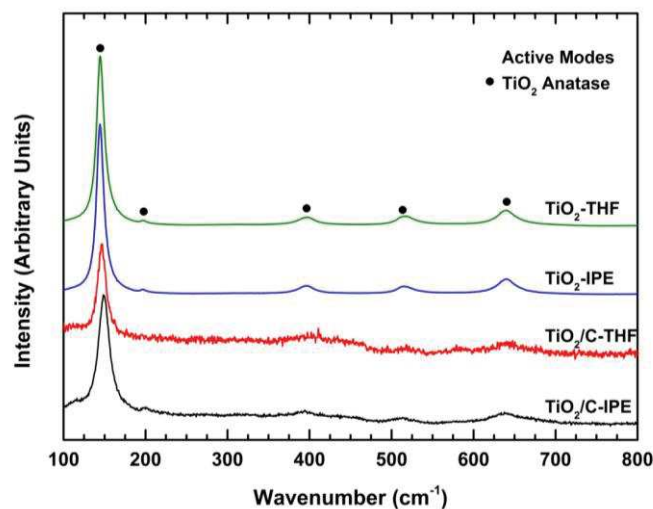


Figure SI3. Raman spectra of TiO₂ and TiO₂/C composites in the 100-800 cm⁻¹ range.

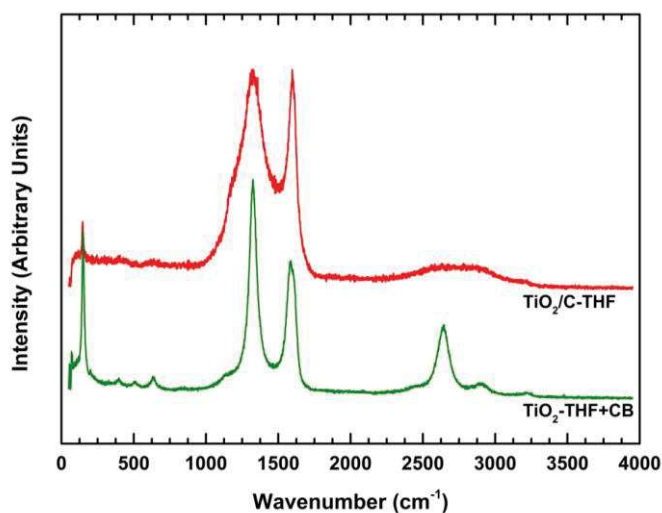


Figure SI4. Comparison of Raman spectra of TiO₂/C-THF and of a mixture of TiO₂-THF with carbon black. The amount of carbon for each sample was 18 wt%.

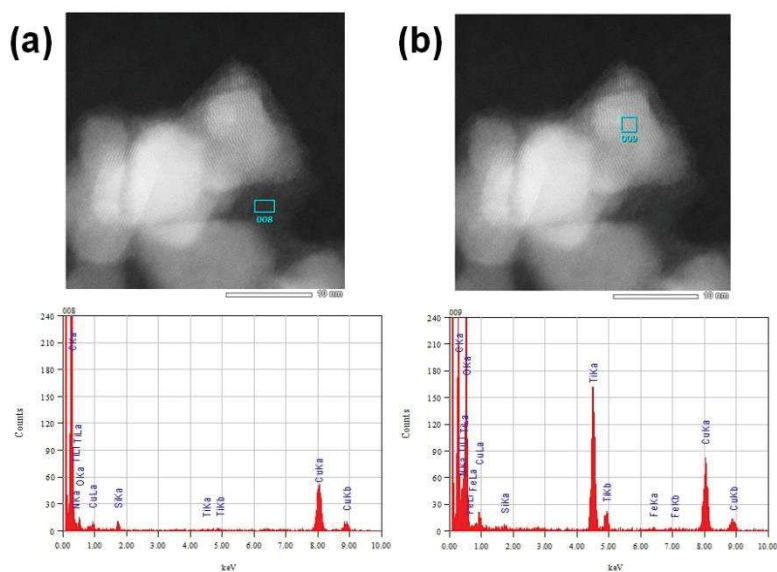


Figure SI5. EDX analysis over different sections of the TiO₂/C-IPE sample: (a) carbon coating; (b) TiO₂ nanoparticle.

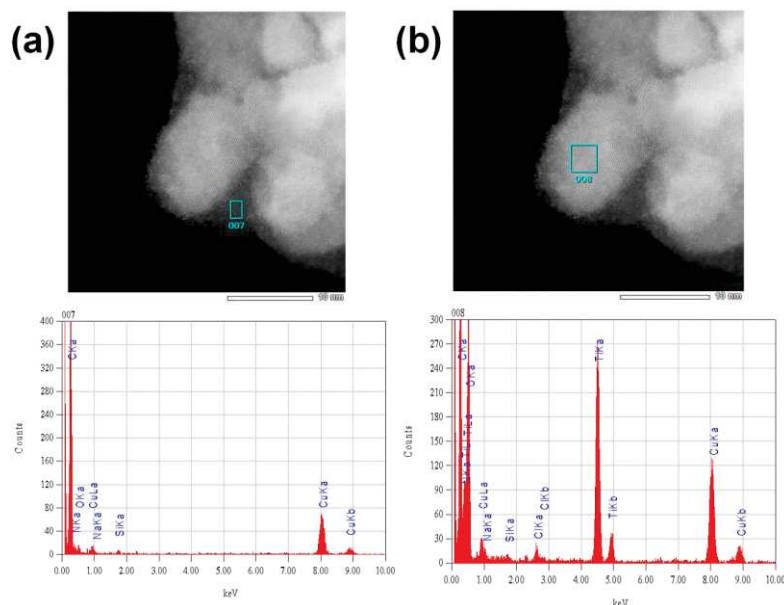


Figure SI6. EDX analysis over different areas of the TiO₂/C-THF sample: (a) carbon coating; (b) TiO₂ nanoparticle.

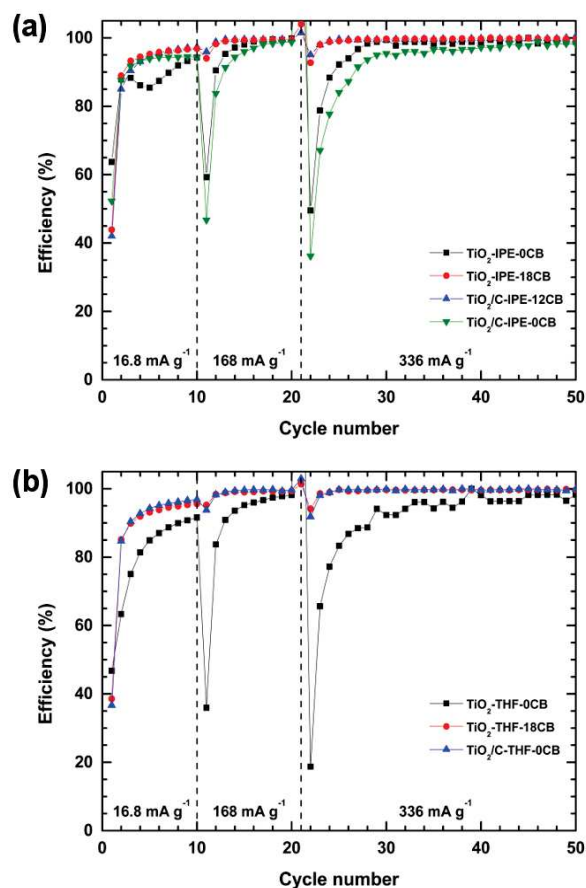


Figure SI7. Columbic efficiency of electrodes cycled at different C rates ($C=335.6 \text{ mAh g}^{-1}$) for a voltage window of 1.2-2.5 V versus Li⁺/Li; (a) electrodes prepared with IPE-based samples and (b) electrodes prepared with THF-based samples. It is worth reminding that electrodes contain different carbon amounts (*i.e.* intrinsic and/or extrinsic carbon; Table 1).

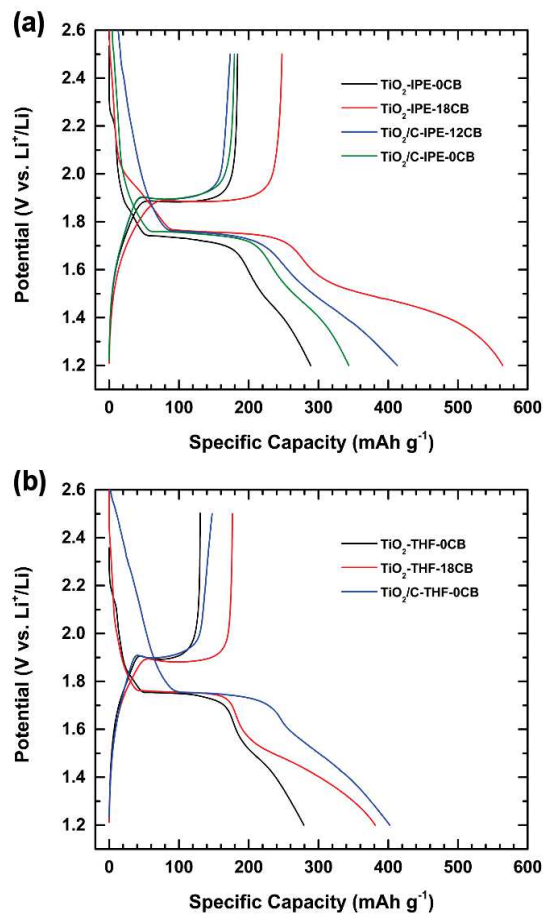


Figure SI8. Initial (first cycle) charge/discharge profiles at a current rate of 16.8 mA g^{-1} ($C/20$) of IPE (a) and THF (b) based electrodes versus Li.

4.1.2 Electrochemical performances at higher current densities (above C)

Aside from the electrochemical evaluation described above, THF derived TiO₂ and TiO₂/C nanocomposite were tested at higher current rates to determine their stability for faster energy demanding applications. Electrochemical stability *versus* lithium is presented in Figure 4.1a. An activation cycle (cycle 0) at C/20 was recorded in order to have a slow initial lithiation/delithiation process before increasing the current rate. This cycle serves to observe the secondary and irreversible processes, commonly present in TiO₂ samples, that are at the origin of the initial capacity fade between the first and second cycles. This cycle also served to perform PEIS measurements at 1.8 and 1.2 V *versus* Li⁺/Li. These potentials were selected because they correspond at the potential just before the emergence of the constant plateau, characteristic of TiO₂ lithiation process and at the end of the first lithiation process. As a reminder, the constant plateau is associated to the two phase reaction between the solid solution compound Li_xTiO₂ ($x < 0.5$) and the orthorhombic lithium titanate Li_{0.5}TiO₂. Complex impedance plots are presented in Figure 4.2, discussed later.

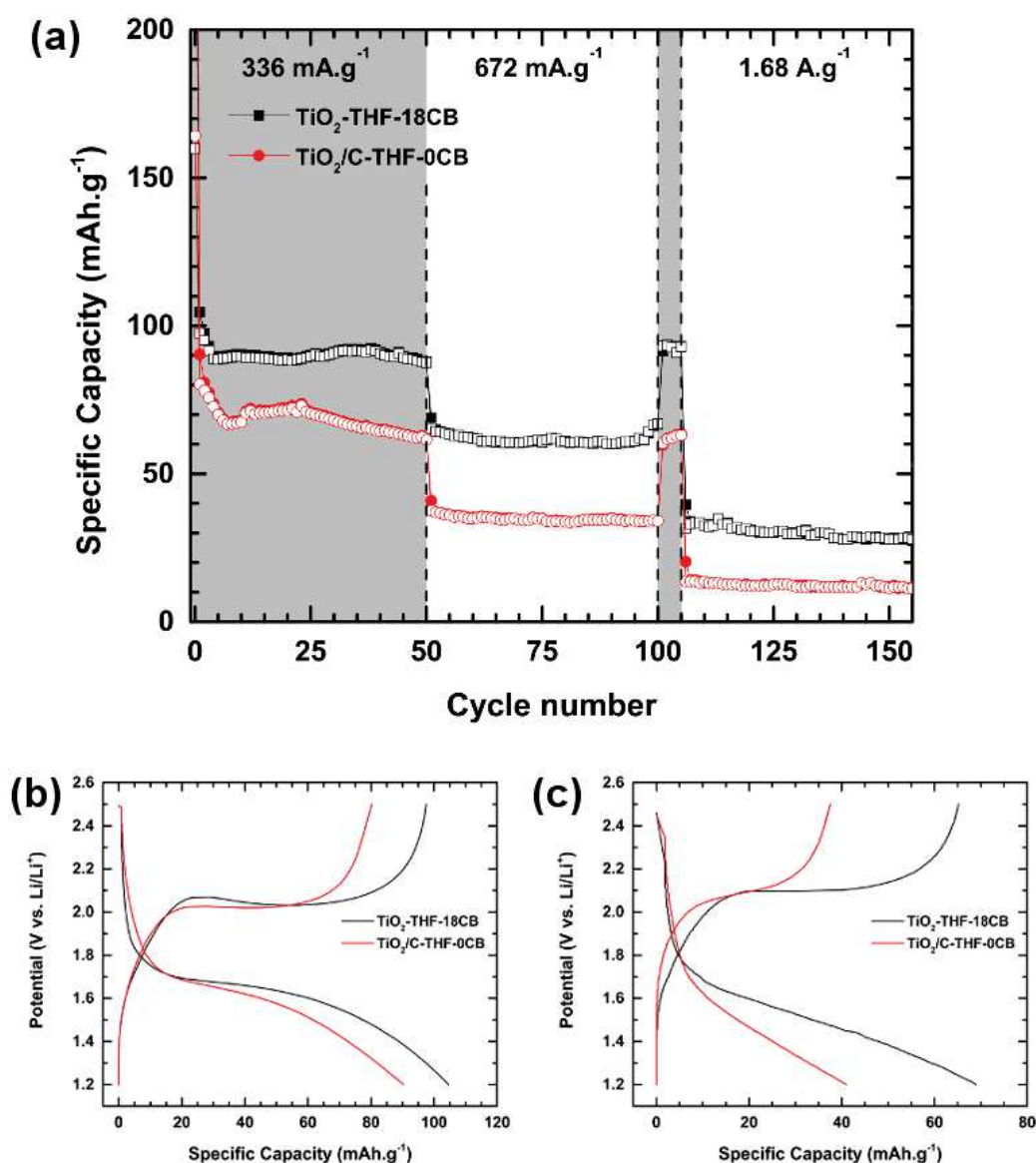


Figure 4.1 Cycling performances of THF derived TiO₂ at different C rates (C; 2C and 5C; C=335.6 mA·g⁻¹) for a voltage window of 1.2-2.5 V *versus* Li⁺/Li (filled and open symbols refer to reduction –discharge– and oxidation –charge–, respectively) (a); galvanostatic charge/discharge profiles after varying the C rate at a current rate of 336 mA·g⁻¹, *i.e.* cycle 1 (b) and at a current rate of 672 mA·g⁻¹, *i.e.* cycle 51 (c).

Galvanostatic cycling presented in Figure 4.1a evidences the stability of both samples after 50 charge/discharge cycles at 336, 672 and 1680 mA·g⁻¹ corresponding to *C*, 2*C* and 5*C* respectively ($C=335.6 \text{ mA}\cdot\text{g}^{-1}$). One may also observe that specific capacity does not decay after the 2*C* cycling as shown in the grey section between 2*C* and 5*C*. This small section correspond to 5 cycles at a current rate equal to *C* and the specific capacity obtained for these cycles reaches the same values as those obtained during the initial *C* cycling (93 and 63 mA·g⁻¹ for TiO₂-THF-18CB and TiO₂/C-THF-0CB respectively).

Samples display similar performances, as those described above (section 4.1.1), at a current rate of 336 mA·g⁻¹. TiO₂ containing extrinsic carbon continues to exhibit higher capacities than their TiO₂/C nanocomposite counterpart; however, intrinsic carbon improves the cycling stability of TiO₂. In fact, capacity falls down to zero for THF derived TiO₂ without any carbon (neither intrinsic nor extrinsic) as observed in Figure 7 (section 4.1.1), at a current rate equal to *C*. Here, current rate was set up to 5*C* and TiO₂/C-THF-0CB, only containing intrinsic carbon (*i.e.* carbon from pyrolysis), exhibits capacities of *ca.* 12 mA·g⁻¹.

Galvanostatic charge/discharge profiles of cycles 1 and 51 corresponding to current rates of *C* and 2*C* respectively are presented in Figure 4.1(b-c). At a current rate of *C*, both samples exhibit a fast drop of potential until *ca.* 1.7 V *vs.* Li⁺/Li; evidencing a typical behavior of lithiation of TiO₂. Then, slope decreases slowly and the characteristic constant voltage plateau of the two-phase reaction at 1.7 V is not well defined; nevertheless, the whole shape of the discharge profile evidences the three steps during the lithium insertion into TiO₂ anatase. It is noteworthy that potential of TiO₂/C nanocomposite decreases faster than the one of its calcinated counterpart; however, polarization is the same for both samples (0.37 V *versus* Li⁺/Li). In the last part of the discharge profile, potential drops faster towards the formation of LiTiO₂.

When passing to a current rate of 2*C* (Figure 4.1c), the formation of the solid solution at the beginning of the lithiation is always present with the rapid drop of potential. Then, the constant voltage plateau is practically absent meaning a fast transition towards the orthorhombic Li_{0.5}TiO₂ phase. At that point, both samples evidences a quasi-linear decrement of potential from *ca.* 1.7 V *versus* Li⁺/Li until the end of the reduction. Polarization becomes more important and a clear difference between the behavior of the two samples is observed. Among the two samples, TiO₂/C-THF-0CB exhibits the higher polarization, *i.e.* 0.65 V against 0.59 V from TiO₂-THF-18CB.

As mention before, complex impedance plots taken before the biphasic region and at the end of the first lithiation are presented in Figure 4.2. Aside the electrodes discussed above, PEIS was performed over the TiO₂/C-IPE-12CB sample. The former was selected as it contains both intrinsic and extrinsic carbon and the total amount of carbon is the same in all three electrodes. One may observe that there are no significant differences in the shape of their Nyquist plots. Fitting plots were obtained using the equivalent circuit shown in the top right hand corner in Figure 4.2 and resistance values are summarized in Table 4.1. Interestingly, one may observe the impact of the intrinsic carbon at the beginning of the lithiation process (*i.e.* 1.8 V *versus* Li⁺/Li) analyzing the global resistances in the half cells.

At the beginning of the lithiation process, both electrodes containing intrinsic carbon (*i.e.* TiO₂/C-THF-0CB and TiO₂/C-IPE-12CB) exhibit lower global resistances than TiO₂-THF-18CB, which only contains extrinsic carbon. Those values suggest that conductivity is enhanced in TiO₂/C nanocomposites by the close interaction of the pyrolytic carbon and the TiO₂ nanoparticles (*i.e.* carbon coating) against the only physical interaction of the extrinsic

carbon due to the mechanical grinding. These results are analogous to the mechanically prepared TiO₂-V₂O₅ mixed oxides discussed before (section 3.1.2.3). In brief, it has been settled that a close interaction among the particles, as a result from the synthesis, becomes beneficial for conductivity than the one obtained by physically grinding.

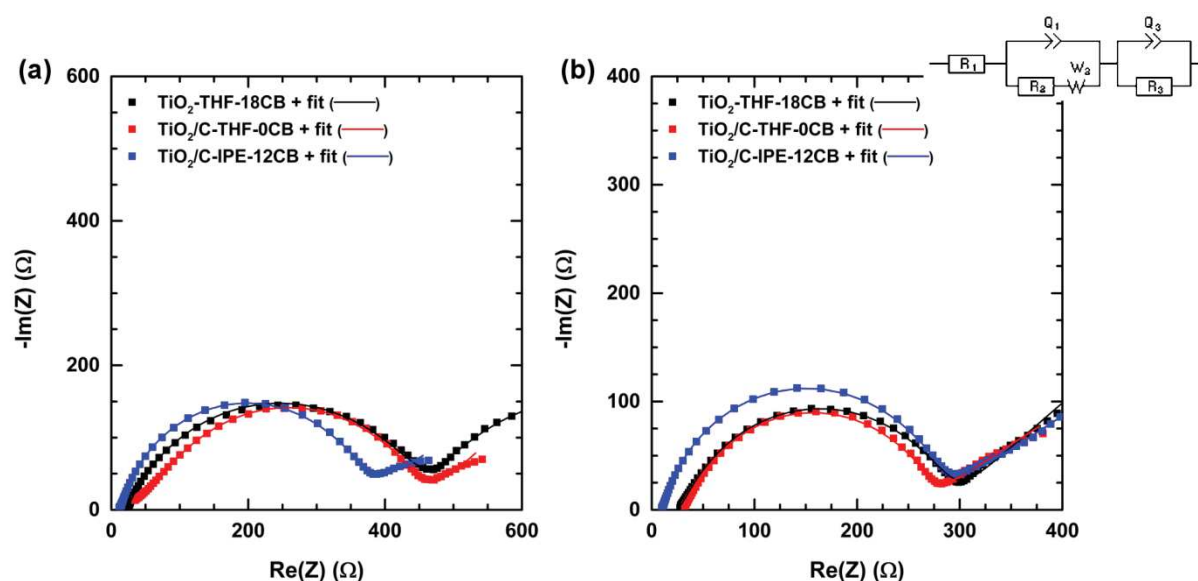


Figure 4.2 Complex impedance plots of TiO₂-THF and TiO₂/C-THF(IPE) electrodes with a total amount of 18 wt% of C in half-cells versus lithium. Plots were obtained in potentiostatic mode at 1.8 V versus Li⁺/Li (a) and 1.2 V versus Li⁺/Li (b) after 2 h relaxation time before the lithiation. The equivalent circuit used for the analysis of the complex impedance plots is shown on the top right hand corner.

Interestingly, the sample containing both types of carbon exhibits an intermediated behavior. Admittedly, its global resistance is lower than the one from TiO₂-THF-18CB, but it is also higher compare with TiO₂/C-THF-0CB. This behavior is certainly due to the presence of less intrinsic carbon in TiO₂/C-IPE-12CB (≈ 6 wt%). Regarding the plot values at the end of the first lithiation, all samples present similar global resistances regardless the carbon nature (*i.e.* intrinsic, extrinsic or both). They are also lower than those obtained at the beginning of the lithiation, probably due to the formation of an ionic conducting phase.

Table 4.1 Fitted resistance values from impedance plots of TiO₂-THF and TiO₂/C-THF(IPE) electrodes in half-cell versus lithium.

Resistances (Ω)	TiO ₂ - THF- 18CB	TiO ₂ /C- THF-0CB	TiO ₂ /C- IPE-12CB	TiO ₂ - THF- 18CB	TiO ₂ /C- THF-0CB	TiO ₂ /C- IPE-12CB
	1.8 V vs Li ⁺ /Li			1.2 V vs Li ⁺ /Li		
R1	23.01	15.16	19.64	23.49	26.55	20.94
R2	496.60	320.80	422.2	29.25	36.93	20.33
R3	435.80	131.50	156.1	245.40	224.00	236.3
Total R	955.41	467.46	597.94	298.14	287.48	277.57

In summary, pyrolytic carbon has proven to enhance conductivity of the electrodes before lithiation. Nevertheless, at the end of the lithiation process, contribution of carbon is similar, regardless its nature, principally due to the formation of an ionic conducting phase. Besides,

intrinsic carbon demonstrated to enhance the long-term stability of pure TiO₂ (*i.e.* as compared with the white THF derived electrode) at higher current densities, interesting for high-power energy applications.

4.1.3 Spectroscopic analyses for further insights to the carbon coating formation mechanism.

Different spectroscopy techniques were used trying to elucidate the mechanisms involved in the formation of the carbon coating. Xerogels were analyzed by Raman spectroscopy (Figure 4.3). Both samples present a lot of fluorescence which hides anatase bands, even if this phase was identified by X-ray diffraction (Figure 2 in section 4.1.1). Concerning the graphitic region, Xer-THF displays both D and G bands proving the formation of poorly graphitic domains even before pyrolysis. On the contrary, neither D nor G bands were identified for Xer-IPE. While this feature suggests differences between IPE and THF towards carbon intermediates, clear conclusion cannot be drawn. One may assume that the cyclic structure of THF could not only promote carbon yield, as shown earlier, but also low-temperature graphitization. However, Xer-IPE has threefold less carbon than Xer-THF (12.4 wt.% against 31.3 wt.%) and fluorescence may hide the bands. At this stage, a qualitative study of ether-derived intrinsic carbon coatings appears to be extremely delicate and would deserve further characterizations.

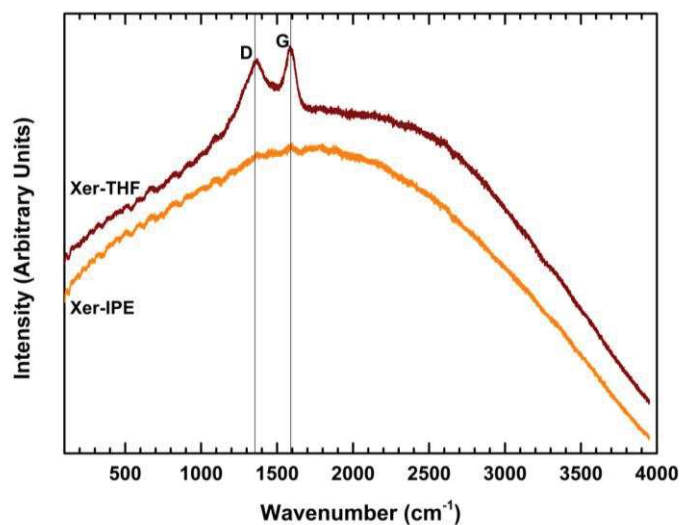


Figure 4.3 Raman spectra of Xer-THF and Xer-IPE.

To provide further insights into mechanisms involved in carbon formation and elucidate possible differences between THF and IPE, organic intermediate by-products were investigated. Xerogels were washed with different solvents (*i.e.* CHCl₃, CH₂Cl₂ or THF). Washing solvents were evaporated and residual by-products were analyzed using ¹H and ¹³C NMR. Ideal reaction products, as seen in Scheme 1 (section 4.1.1), are TiO₂ and a chloride compound correlated with the nature of the oxygen donor. NMR spectra elucidated the presence of 1,4-dichlorobutane as the main by-product for the THF route (Figure 4.4). However, presence of expected isopropyl chloride for the IPE route was not determined by this technique. Considering the low boiling point (36 °C) of this compound, it is very likely that evaporation occurred before analyses. In addition to 1,4-dichlorobutane, few bands in the region of *sp*³ carbons were observed but any unsaturated carbon was detected. It is worth

mentioning that gels keep their color after this washing step, so it is likely that vinylic compounds, probable carbon precursors, stayed entrapped into the gel matrix.

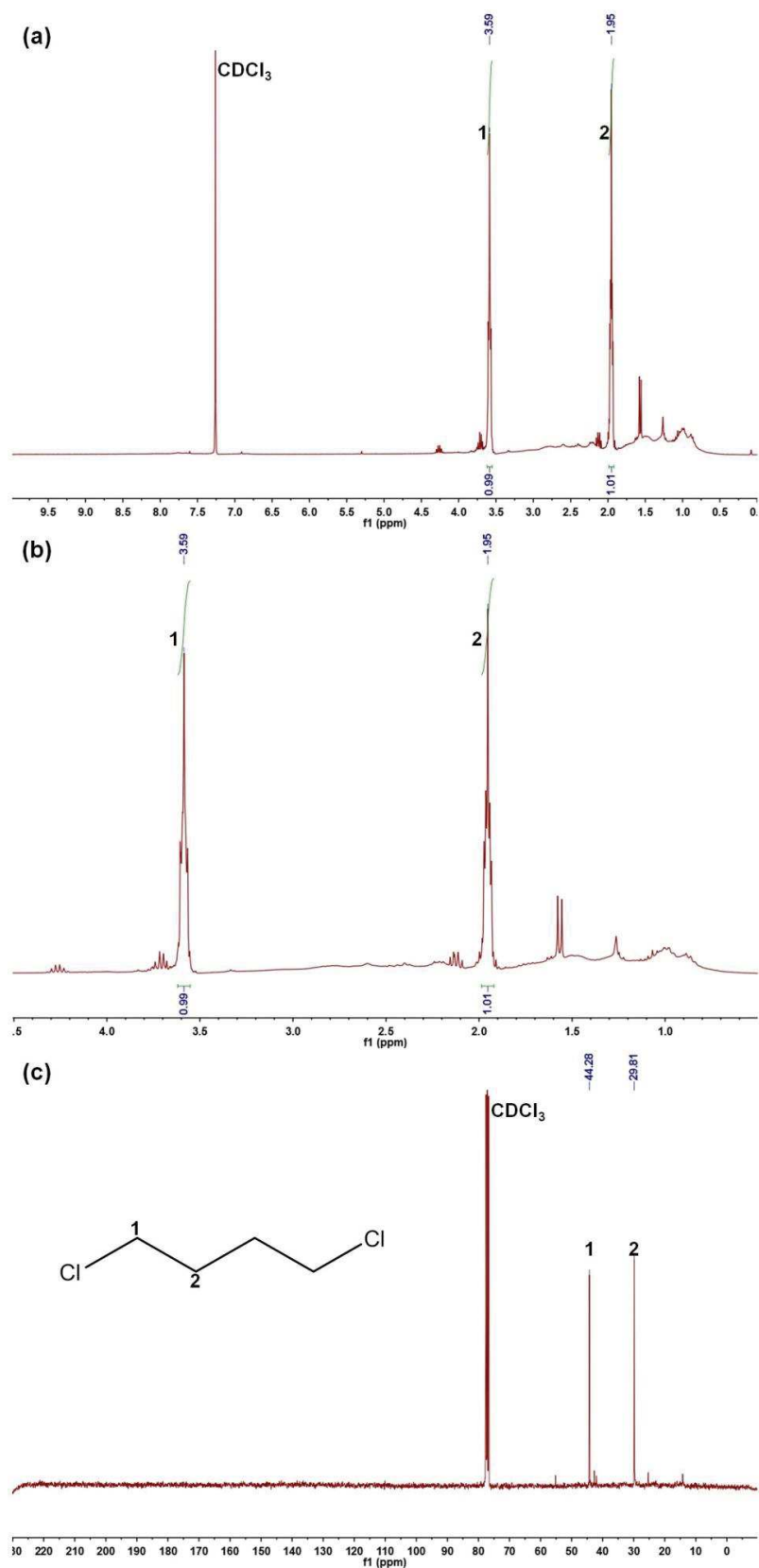


Figure 4.4 ¹H NMR spectrum in CDCl₃, 300 MHz of byproducts of Xer-THF after washing with CHCl₃, full range (a) and aliphatic region (b). ¹³C NMR spectrum of the same sample (c).

In addition to NMR analyses, UV-visible spectra of the washing solvents were recorded (Figure 4.5). Most of the washing solvents were dark (Figure 4.6). Briefly, for the same dilutions, solvents used for washing Xer-THF were always darker and absorbance intensities were bigger than for Xer-IPE. These results are in good agreement with the fact that Xer-THF presents a higher amount of organic matter (as determined by TGA). Moreover, IPE-derived soluble by-products absorb below 360 nm while THF-derived ones absorb in a broader range, up to ca. 600 nm.

FTIR spectra (Figure 4.7) confirmed the presence of aliphatic *sp*² carbons in xerogels. Bands in the 2950-2850 cm⁻¹ and 1500-1375 cm⁻¹ ranges can be assigned to aliphatic C-H bonds, while signals below 1300 cm⁻¹ correspond to C-O vibrations of residual ether. Surprisingly, no characteristic double bond signals could be observed, except for the one at around 1600 cm⁻¹. Besides carbonaceous framework, a continuous absorption below 1000 cm⁻¹ [267], and a band appearing at around 1340 cm⁻¹ can be assigned to Ti-O-Ti bonds [268]. Even though a qualitative study remains difficult, no significant differences could be noticed between IPE-derived and THF-derived carbon precursors.

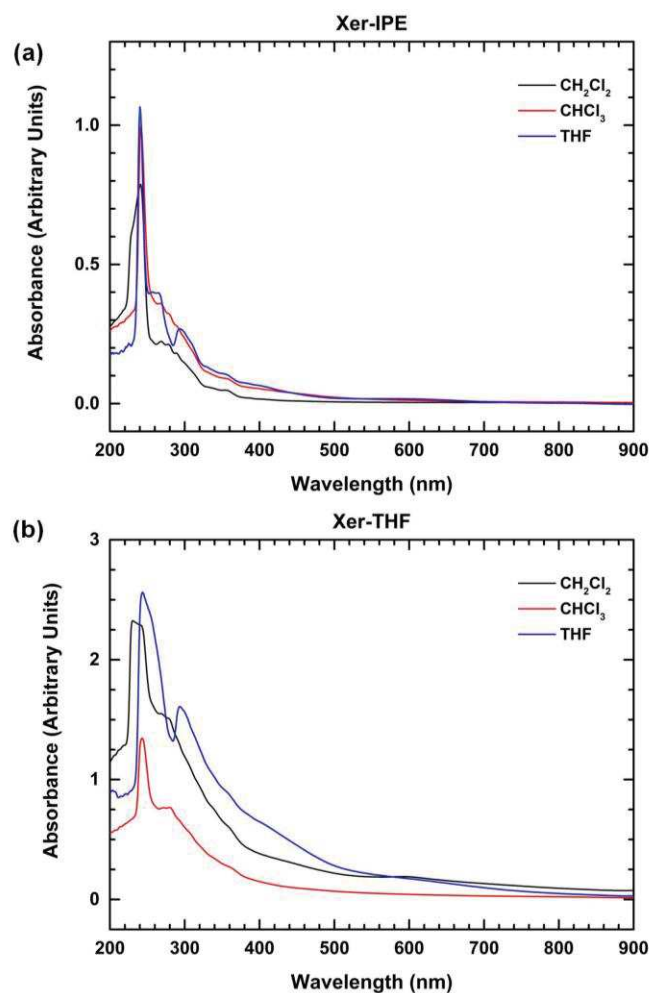


Figure 4.5 UV-vis spectra of solvents used for washing Xer-IPE (a) and Xer-THF (b); solutions diluted 600 times before analysis.

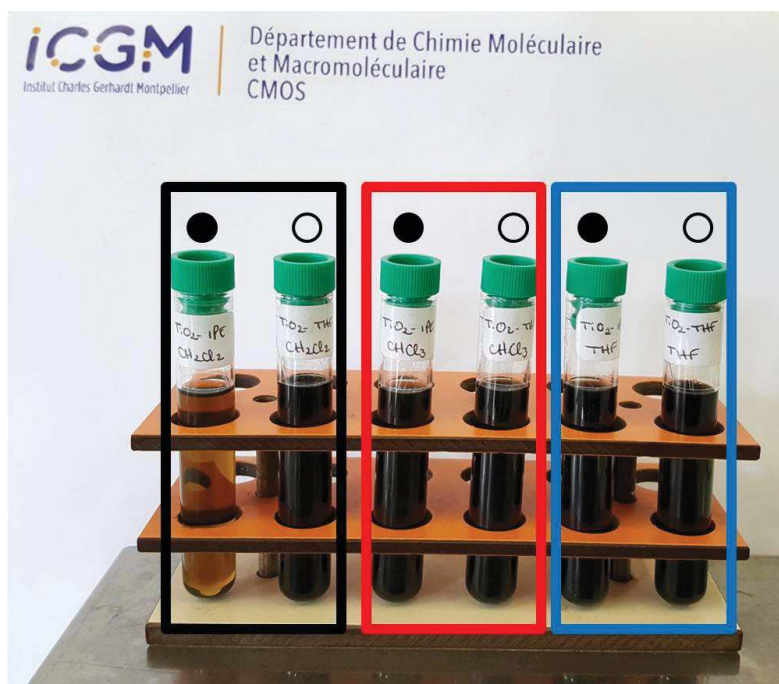


Figure 4.6 Solvents after washing Xer-IPE (filled symbols) and Xer-THF (open symbols); each box correspond to the same solvent: CH₂Cl₂ (black), CHCl₃ (red) and THF (blue).

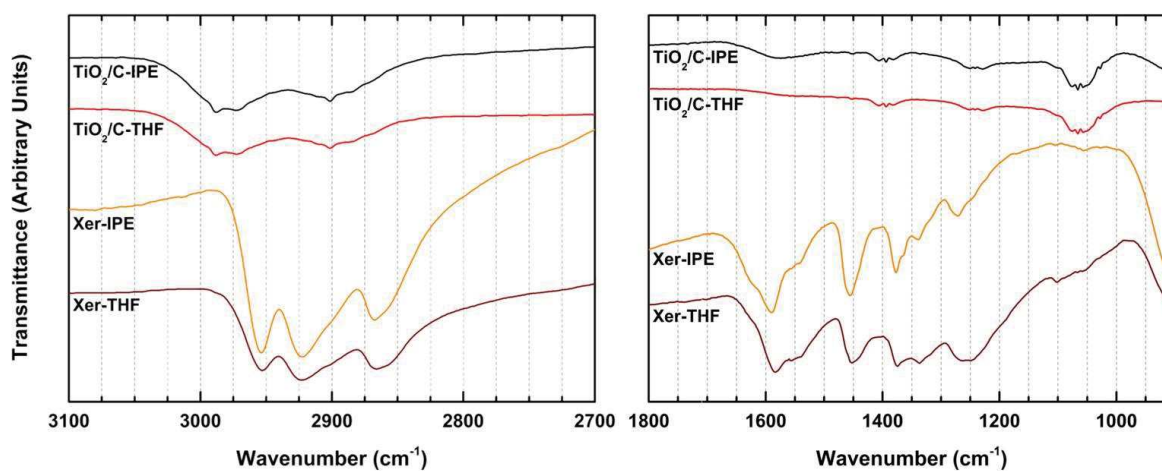


Figure 4.7 FTIR spectra of dried xerogels and pyrolysed samples in the 900-1800 and 2700-3100 cm⁻¹ ranges.

As a summary, Raman spectrum of THF derived xerogel exhibited some graphitic domains and fluorescence may hide them in the IPE derived one. The absence of bands associated to unsaturated carbons in NMR spectra confirms that byproducts leading to the formation of the carbon coating mostly stay trapped in xerogels. It is possible that some unsaturated carbons get away with the washing solvents given the strong coloration of solutions, but in small amounts, making them difficult to determine. Moreover, not significant differences between the two ether (*i.e.* oxygen/carbon donors) could be determined.

4.2 Catalytic graphitization of the NHSG organic byproducts by FeCl₃ impregnation

Considering that an increment of the pyrolysis temperature promotes the formation of rutile TiO₂ crystal phase, it was desirable to investigate other directions in order to increase the graphitization of the carbon coating of the TiO₂/C nanocomposites. One interesting approach is the obtention of graphitic carbon at moderated temperatures in presence of transition metals which act as graphitization catalysts. It is important to keep in mind that graphite has historically been used as anode material in Li-ion batteries technology and that the carbon coating obtained after the pyrolysis of xerogels is amorphous. Thus, inspired by the fact that some authors benefit from a dual insertion process (*e.g.* lithiation of TiO₂ and graphene [264]) and considering that the impregnation of carbon precursors with different metallic salts could improve graphitization [269-273], we decided to explore the catalytic graphitization of the remaining organic byproducts in our xerogels in presence of an iron salt, *i.e.* FeCl₃.

The THF derived xerogel was chosen for this procedure as it presents a larger amount of organic byproducts (34.3 wt%). Besides, preliminary tests evidenced a better solubility of FeCl₃ in THF. Impregnated xerogels were prepared using two different concentrations (*i.e.* 0.5 and 1.0 mmol of FeCl₃ per gramme of byproduct) and two different impregnation times (*i.e.* 12 and 24 h). Two different atmospheres (*i.e.* Ar and Ar-H₂, 95:5 vol.) were also tested during pyrolysis. Aside from a potential influence over graphitization, it has been reported that the pyrolysis atmosphere could impact on the lithium storage properties of carbonaceous materials [274]. Samples are named hereafter by the Fe concentration (*i.e.* 0.5 or 1.0 mmol) and impregnation time (12h or 24h). A direct comparison between the two pyrolysis atmospheres will be presented.

At first, crystal phases were evidenced by XRD and the obtained diffractograms are displayed in Figure 4.8. All samples pyrolyzed under argon atmosphere only exhibit the TiO₂ anatase crystal phase (JCPDS 00-021-1272); nevertheless, it was not the same case for the samples pyrolyzed under reducing atmosphere (*i.e.* Ar-H₂). The TiO₂ sample treated for 24 h at a concentration of 1.0 mmol of FeCl₃ per gram of carbon source not only exhibit reflections associated to the anatase phase, but also reflections corresponding to the TiO₂ rutile crystal phase (JCPDS 00-021-1276). More surprisingly, a reflection corresponding to iron oxide (*i.e.* Fe₂O₃ maghemite crystal; JCPDS 00-039-1346) was observed. The presence of rutile is certainly due to the formation of Fe₂O₃, as it has been reported that Fe₂O₃ could act as a promoter for the anatase to rutile transformation and could also enhance particle growth [167, 275].

Apart from these differences, no significant shift was observed for the anatase reflections and neither graphite (JCPDS 01-075-2078) nor metallic iron (JCPDS 01-085-1410) were detected. The absence of those reflections suggests that either the xerogels were not successfully impregnated, despite the formation of Fe₂O₃ in one sample, or that pyrolysis temperature is not high enough to enhance the catalytic graphitization of the xerogel byproducts. For instance, works of Sevilla *et al* [269, 270] and Han *et al* [272] evidenced catalytic graphitization using higher pyrolysis temperatures (*i.e.* 900 °C and 1000 °C). All of them used XRD as a demonstration of the graphite formation. Interestingly, reflections related to metal iron were also observed in their diffractograms. Nevertheless, such high pyrolysis temperatures are not suitable for this work given that, as noticed before, the formation of TiO₂ rutile can be observed above 800 °C. Furthermore, Hoekstra *et al* [276] obtained reflections related to graphite at rather low temperature, *i.e.* 725 °C; however, they also observe the formation of cementite (Fe₃C) at the same temperature.

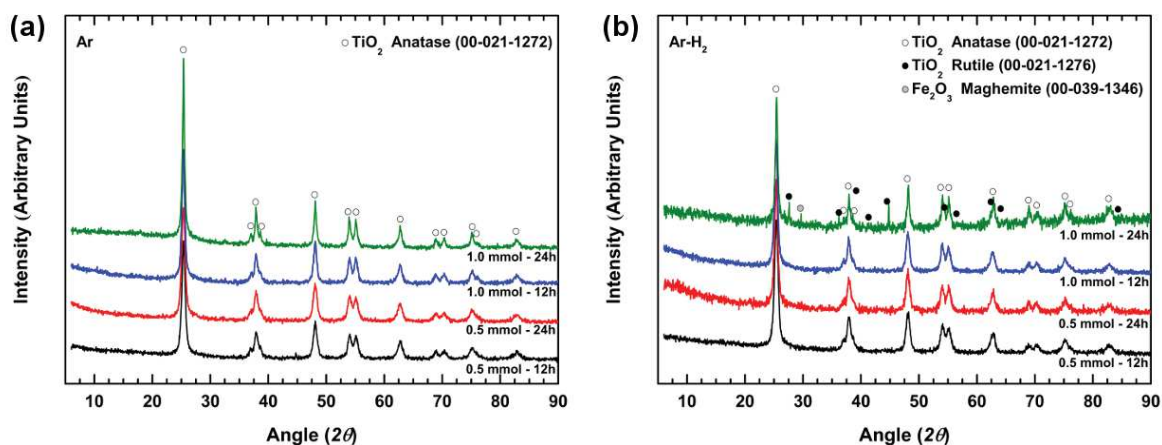


Figure 4.8 Powder X-ray patterns of TiO₂/C nanocomposites after Fe impregnation (different concentrations and time) under Ar (a) and Ar-H₂ (b) atmospheres.

Further analyses by Raman spectroscopy (Figure 4.9a-b) confirm the presence of TiO₂ anatase; though, a band appearing at 447 cm⁻¹ is attributed to a Raman active fundamental of rutile [277] and it is recurrent in all samples. Thus, traces of some rutile domains must be present in small amounts that are not detected by XRD.

Crystallite size was determined with the Scherrer formula and values are reported in Table 4.2. All samples present similar crystallite size values (\approx 13-14 nm) and are in agreement with the sizes previously observed for TiO₂/C nanocomposites, without iron chloride impregnation (section 4.1.1). The sample with the largest crystallites (*i.e.* 18 nm) also corresponds to the one that exhibits reflections of TiO₂ rutile. This slightly bigger size can be explained by the formation of Fe₂O₃ as discussed above.

Table 4.2 Crystallite size and textural data for TiO₂ after impregnation treatment and pyrolysis under Ar or Ar-H₂.

	Sample	Crystallite size ^a (nm)	S _{BET} ^b (m ² ·g ⁻¹)	V _p ^c (cm ³ ·g ⁻¹)	D _p ^e (nm)
Ar	0.5 mmol – 12h	12	67	0.20	11.8
	0.5 mmol – 24h	12	69	0.19	10.6
	1.0 mmol – 12h	15	67	0.14	7.3
	1.0 mmol – 24h	16	84	0.20	7.7
Ar-H ₂	0.5 mmol – 12h	14	68	0.24	14.1
	0.5 mmol – 24h	13	51	0.15	13.2
	1.0 mmol – 12h	13	68	0.21	12.0
	1.0 mmol – 24h	18	71	0.18	8.4

^aderived from XRD data using Scherrer equation, ^bspecific surface area, ^ctotal pore volume, ^dBJH average pore diameter calculated from desorption branch.

Raman spectra of the pyrolyzed samples under different atmospheres are presented in Figure 4.9. Spectra was divided in two sections for an individual analysis of TiO₂ and graphite. As mention before, Raman spectra confirms the presence of TiO₂ anatase (Figure 4.9a-b), but also evidences traces of TiO₂ rutile. No significant differences were detected among the different samples; however, spectra of samples subjected to the argon atmosphere exhibit higher intensity/noise ratio than their counterparts treated under reducing atmosphere. This feature may suggest a modification over the carbon coating.

Raman spectra region where graphite is active is presented in Figure 4.9c-d; all samples exhibit similar behavior as the one described earlier (section section 4.1.1) for the TiO₂/C

nanocomposites. Briefly, partial graphitic carbonaceous materials display two bands in the Raman spectrum centered at *ca.* 1580 cm⁻¹ and 1350 cm⁻¹. These bands are associated to graphitic carbon (G band) and disorder-induced carbon (D band) respectively; the former indicates the presence of impurities or defects into the graphitic framework [278-280]. However, in the present case, both bands are shifted; G band is shifted at around 1600 cm⁻¹ and D band at around to 1325 cm⁻¹, such as in the previous TiO₂/C nanocomposites without being subjected to the iron chloride impregnation. D band is broader and it exhibits a shoulder at around 1200 cm⁻¹. Due to this characteristic, the application of the Knight formula for the evaluation of the graphitization degree in these materials becomes arduous.

As for the materials discussed in the previous section 4.1.1, the shape of the Raman spectra and the observed shifts, compare with the theoretical values, are explained by the presence of the four components of the D band (*i.e.* D1, D2, D3 and D4 centered at 1350, 1620, 1500 and 1200 cm⁻¹ respectively) [281-283]. It is important to keep in mind that these materials are based upon the TiO₂/C-THF nanocomposite presented above, thus this behavior is not completely astonishing. However, one may have expected narrow and well defined G bands as observed in literature for materials subjected to catalytic graphitization [270-272].

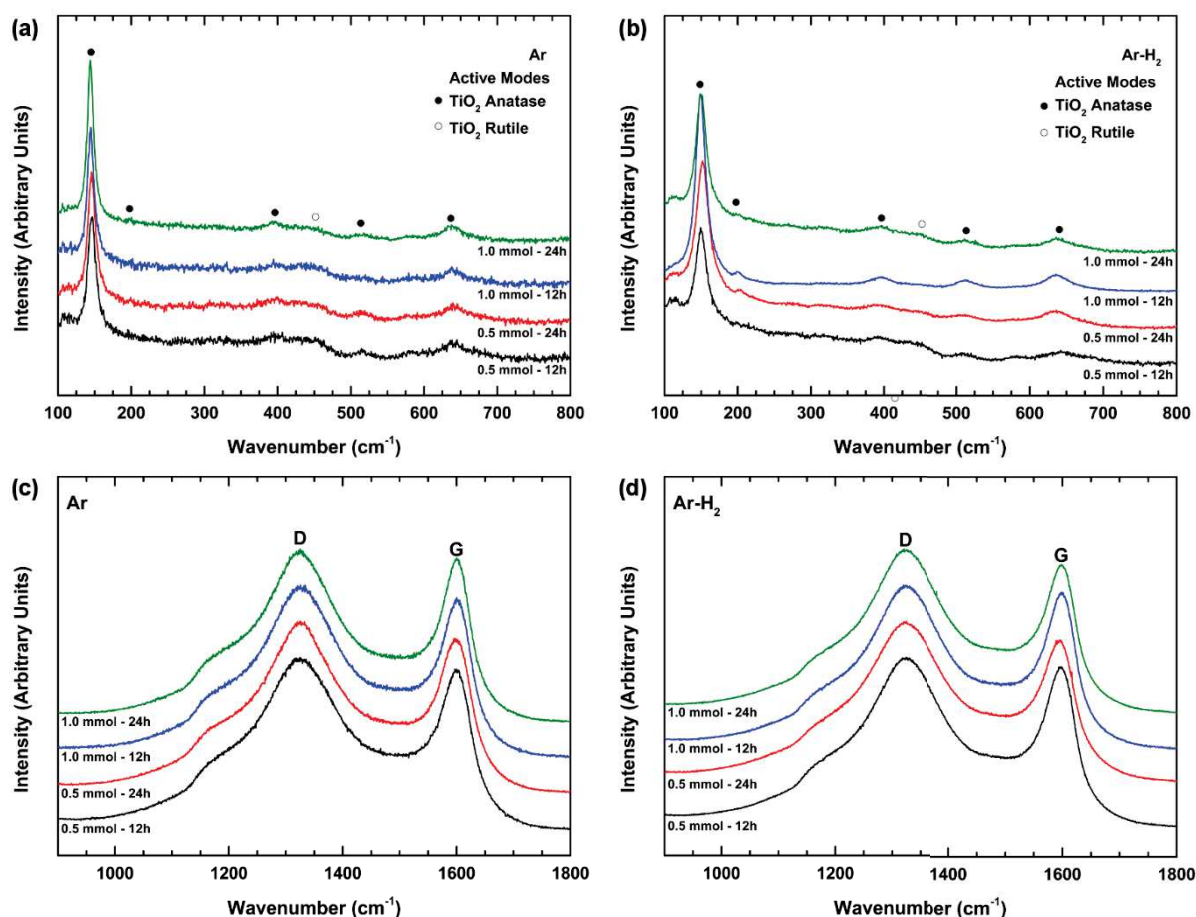


Figure 4.9 Raman spectra of TiO₂/C nanocomposites (a-b) TiO₂ region and (c-d) graphite region. Samples pyrolyzed under Ar atmosphere are presented in (a, c), while under Ar-H₂ atmosphere are presented in (b, d).

Presence of this behavior indicates that the graphitization of the C-coating was not significantly improved. Actually, D3 band is associated to amorphous carbon and its contribution is clearly observed by an increment of the intensity, as compared with the linear background, at around 1500 cm⁻¹. In order to provide further insights about the real

contribution of the Fe impregnation in those materials, a deeper analysis needs to be performed including the deconvolution of the spectra into the five bands (*i.e.* G and D1-D4 bands). This analysis will allow the determination of the intensities for each band and the Knight formula would be properly applied for the evaluation of the graphitized-crystallite coherence length (L_a).

Although the graphitization degree of the carbon coating has not been significantly improved a priori, extra textural characterizations of those materials were performed. Molecular physisorption isotherms and BJH pore size distribution of the pyrolyzed samples are shown in Figure 4.10. All samples present hysteresis behavior and the isotherm shape is similar for samples treated under the same atmosphere. Isotherms of impregnated xerogels pyrolyzed under argon atmosphere present an intermediated type II – type IV shape according to the IUPAC classification. Isotherms evidence a progressive adsorption of N₂ until a relative pressure of *ca.* 0.6; then adsorption increases at higher relative pressures. This behavior can be associated to multimolecular adsorption; however, saturation, a characteristic feature of type IV isotherms, is not clearly reached (even though inflection points can be observed). Concerning the xerogels pyrolyzed under reducing atmosphere, they also present a similar intermediate type II – type IV shape isotherm with hysteresis behavior. The main difference against the Ar-pyrolyzed samples is that adsorption increases at even higher relative pressures, but faster and a saturation plateau is vaguely sketched. It is noteworthy that hysteresis in Ar-H₂-pyrolyzed samples is less pronounced than in those pyrolyzed under argon atmosphere. The hysteresis shape matches with an H₃ type attributed to capillary condensation in non-rigid textures.

Regarding the pore size distributions, all samples exhibit similar behavior regardless of the pyrolysis atmosphere. The narrow “distribution” centered at *ca.* 3.5 nm is associated to cavitation phenomenon. Samples exhibit broad distributions centered between 9-10 nm for samples pyrolyzed under Ar and in the 10-11 nm range for samples pyrolyzed under Ar-H₂ atmosphere. The only exception in both cases corresponds to the sample treated with a bigger amount of iron salt solution for a longer period of time (*i.e.* 1.0 mmol Fe per gramme of carbon source for 24 h, green plotted line). This sample also presents pores around 7 nm when pyrolyzed under Ar and in the 4-10 range when pyrolyzed under Ar-H₂.

Textural data are summarized in Table 4.2. Samples treated for 12 h present surface areas around 68 m²·g⁻¹ regardless of the pyrolysis atmosphere, slightly inferior than the surface area obtained for TiO₂/C-THF (75 m²·g⁻¹, section 4.1.1) may be due to the presence of iron particles at the surface of materials. By contrast, samples treated for longer periods of time exhibit a heterogeneous behavior; xerogels containing 1.0 mmol Fe per gram of carbon source display higher surface areas (*i.e.* same samples of the previous discussion about the pore size distribution, green plots in Figure 4.10). Ar-0.5mmol-24h sample present similar surface area as those obtained for the 12 h treated samples and finally, Ar-H₂-0.5mmol-24h sample exhibits lower surface (51 m²·g⁻¹). Interestingly, the molecular physisorption was the only characterization evidencing a more remarkable difference between the two atmospheres used in the pyrolysis step, notably concerning the isotherm shape.

Selected samples were electrochemically evaluated using galvanostatic cycling *versus* lithium. Given that pyrolyzed samples under reducing atmosphere do not evidence significant differences from those pyrolyzed under Ar, it was determined to test just the last ones. Besides, only the two samples impregnated for 12 h were analyzed. The carbon amount was determined by TGA and no significant differences were observed as compared with the carbon content previously determined for the TiO₂/C-THF sample obtained without iron

chloride (*ca.* 19 wt%). Electrodes were prepared without any addition of extrinsic carbon, then cycled at the same current rates as the TiO₂/C nanocomposites discussed in section 4.1.1 (*i.e.* 16.8, 168, 336 mA·g⁻¹).

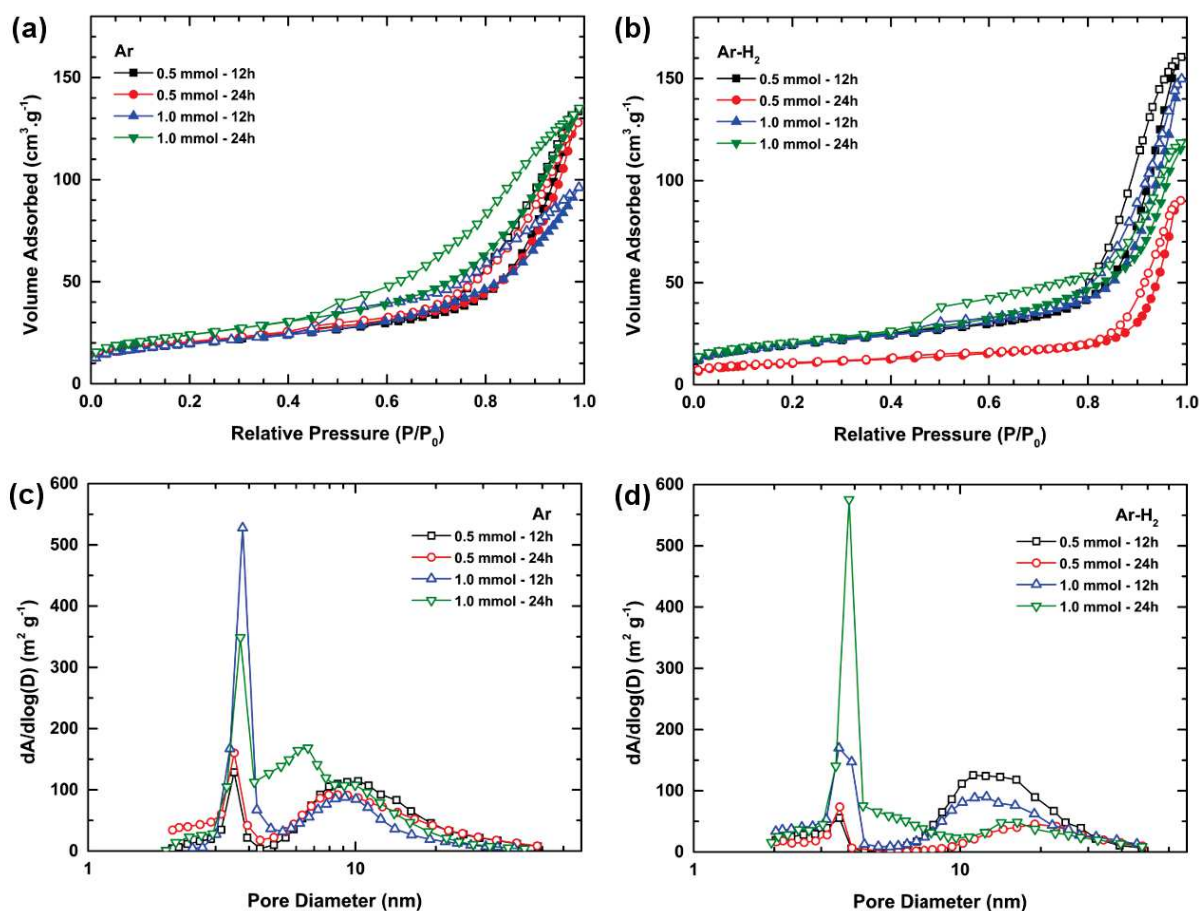


Figure 4.10 (a-b) Molecular nitrogen physisorption isotherms and (c-d) BJH pore size distribution (desorption branch) of TiO₂/C nanocomposites after impregnation treatment. Filled and open symbols refer to adsorption and desorption, respectively. Samples pyrolyzed under Ar atmosphere (a, c) and samples pyrolyzed under Ar-H₂ atmosphere (b, d).

Cycling performance and initial charge/discharge profiles of the two impregnated samples (noted thereafter TiO₂/C-THF-0CB-XFe, where X correspond of the theoretical concentration of Fe) and the original TiO₂/C-THF-0CB electrode are displayed in Figure 4.11. Specific capacities were calculated according to the amount of TiO₂ present in each electrode. All three samples present good stability towards the whole cycling.

Initial galvanostatic charge/discharge profiles of the three samples evidence the characteristics of lithium insertion into TiO₂ anatase framework. A initial relatively fast drop of potential can be observed from the open circuit to *ca.* 1.75 V *versus* Li⁺/Li leading to specific capacities of around 100 mAh·g⁻¹. This drop of potential is associated to the formation of a solid solution compound (Li_xTiO₂ with *x*<0.5) and is followed by a constant voltage plateau. The former correspond to a biphasic region where the as formed tetragonal lithium titanate coexists with the orthorrombic Li_{10.5}TiO₂ lithium titanate. It is noteworthy that this region is larger for the TiO₂/C-THF-0CB-0.5Fe electrode; the other two samples show quasi identical behaviors. Besides, the average reduction voltage plateau of this sample is increased by 0.01V *versus* Li⁺/Li; in parallel, its average oxidation voltage plateau is decreased by 0.02V *versus* Li⁺/Li in comparison with the other two electrodes. Thus, the polarization of this sample has been

enhanced. The last section of the profiles evidences another two-phase reaction towards the formation of the tetragonal LiTiO₂.

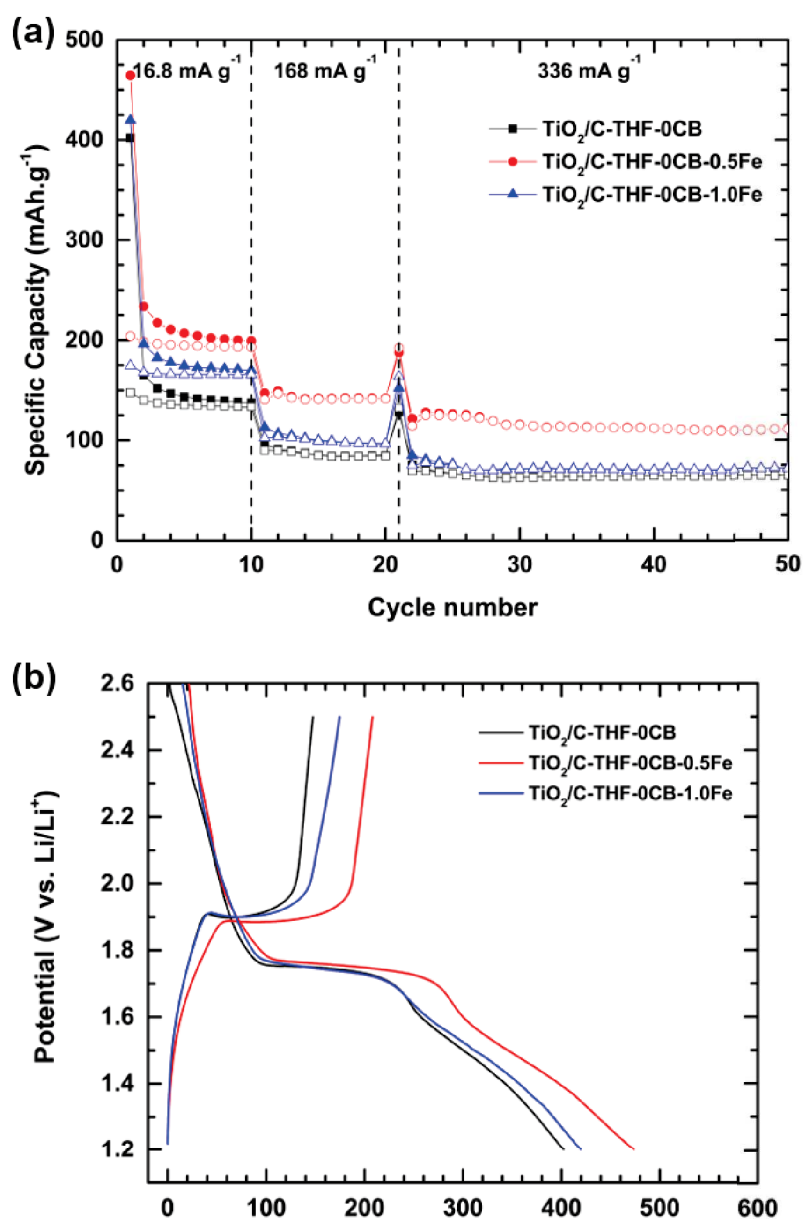


Figure 4.11 Cycling performances of THF derived TiO₂/C nanocomposites at different current densities for a voltage window of 1.2-2.5 V versus Li⁺/Li (filled and open symbols refer to reduction –discharge– and oxidation –charge–, respectively) (a); initial galvanostatic charge/discharge profiles at a current rate of 16.8 mA·g⁻¹ versus lithium. (12h impregnation).

TiO₂/C-THF-0CB and TiO₂/C-THF-0CB-1.0Fe samples, as observed for the first cycle (*i.e.* initial galvanostatic profiles, Figure 4.11b), exhibit similar cycling performances along the different current rates. At the beginning, at lower current densities (*i.e.* 16.8 mA·g⁻¹), the impregnated sample presents higher specific capacities. However, as current rate becomes more important, specific capacities decrease until they reach similar values as those obtained for the TiO₂/C nanocomposite without any Fe impregnation treatment (72 and 65 mAh·g⁻¹ respectively) at a current rate of C (*i.e.* 336 mA·g⁻¹).

Regarding the performances of the other impregnated sample, TiO₂/C-THF-0CB-0.5Fe shows its superiority all along the cycling. One may observe that this sample possesses a larger

reduction voltage plateau than the two other samples. This behavior is transposed to the oxidation process leading to higher specific capacities at the end of the lithiation/delithiation processes and thus, enhancing the reversible capacity. Interestingly, the difference between the capacities obtained with this sample and those from the original TiO₂/C nanocomposite is almost constant along the whole cycling ($\approx 60 \text{ mAh}\cdot\text{g}^{-1}$). That said, a clear improvement is observed and this performance is comparable to the one from the ¹Pr₂O derived nanocomposite mixing intrinsic and extrinsic carbon (TiO₂/C-IPE-12CB from section 4.1.1). Nevertheless, capacities are far from those corresponding to the TiO₂-IPE-18CB sample. This enhanced behavior may be originated by a certain doping degree of iron into the TiO₂ framework during the pyrolysis step, as it has been reported in literature that Fe doping improves the electrochemical performances of TiO₂ [143].

In summary, impregnation treatment does not significantly improve the graphitization degree of these samples. Materials heat-treated under two different atmospheres exhibit similar characteristics. The temperature chosen seems not to be high enough to promote the catalytic graphitization of xerogel byproducts. However, increasing it will result in the formation of TiO₂ rutile instead of TiO₂ anatase. Despite this, electrochemical performances were improved with similar capacities as those obtained for the IPE derived electrode containing both kind of carbon (*i.e.* intrinsic and extrinsic).

4.3 Chapter conclusion

This chapter propose an interesting approach to the preparation of TiO₂/C nanocomposites. Mesoporous TiO₂ and TiO₂/C nanocomposites were successfully synthesized using solvent-free NHSG ether routes. Two conventional ethers, *i.e.* diisopropyl ether and tetrahydrofuran, has been employed in a stoichiometric ratio not only as oxygen donors but also as carbon sources. Obtained xerogels were subjected to two different heat treatments, *i.e.* calcination in air against pyrolysis under argon. All samples led to pure anatase TiO₂ nanocrystals. As for pyrolysis, the texture, TiO₂ crystallite size, carbon content and carbon coating thickness can be controlled by simply changing the ether. To assess the impact of such coating, electrochemical performances of both TiO₂ and TiO₂/C composites were studied as anode materials for lithium-ion batteries. An insight into the role of intrinsic carbon (*i.e.* ether-derived pyrolytic carbon) *versus* extrinsic carbon additives (*i.e.* acetylene black) towards electrochemical performances of TiO₂ was presented. Despite the fact that intrinsic carbon enhanced the electronic conductivity of the electrode and improved the electrochemical performances as compared to the uncoated TiO₂ nanoparticles, electrodes formed with extrinsic carbon lead to better electrochemical performances (*i.e.* higher capacities). In fact, the amorphous carbon coating may form an artificial SEI that blocks the further lithiation of the TiO₂ core.

The catalytic graphitization of xerogel byproducts in presence of FeCl₃ was investigated. Two different concentrations of iron salt solutions and two pyrolysis atmospheres were explored on the THF xerogel. Samples exhibit the TiO₂ anatase crystal phase, one sample also evidences traces of TiO₂ rutile, and more surprisingly traces of Fe₂O₃ maghemite. The iron salt pretreatment does not modify the amount of carbon obtained after pyrolysis, but also does not significantly improve the graphitization degree as observed by Raman spectroscopy. These samples exhibit a practically identical Raman spectra behavior as the one observed for the TiO₂/C nanocomposites without any FeCl₃ impregnation treatment. It suggests a major presence of amorphous carbon because the pyrolysis temperature was not high enough to activate the catalytic process.

Even though these samples exhibit similar textural characteristics to those observed for the TiO₂/C nanocomposites without any iron treatment, a small amount of iron was beneficial for the electrochemical performances. Capacity was improved with 0.5 mmol of Fe per gram of carbon source; this sample reaches similar capacities as those obtained for the TiO₂/C-IPE-12CB electrode, containing both intrinsic and extrinsic carbon.

General Conclusion

The main objective of this PhD thesis was to explore the potential of non-hydrolytic sol-gel chemistry for the synthesis of TiO₂-based electrode materials for lithium-ion batteries. Two different approaches were explored to try to improve the low electronic conductivity, which represents a major drawback of TiO₂ for this application. The first approach consisted in preparing TiO₂-V₂O₅ mixed oxides, the second one was the preparation of TiO₂/C nanocomposites.

TiO₂-V₂O₅ mixed oxides, containing different vanadium loading from 5 to 20 at%, were successfully prepared by solvent-free NHSG routes based on the reaction of TiCl₄ and VOCl₃ with ¹Pr₂O, followed by a calcination in air. At low V loadings, the only crystalline phase detected was TiO₂ anatase. Traces of V₂O₅ scherbinaite were detected only at high V loadings. The presence of vanadium influenced the texture of the materials, the general trend being that the specific surface area decreased with the increase of vanadium loading. The vanadium loading has additional effects such as promoting the anatase to rutile transformation at lower temperatures and facilitating the growth of the TiO₂ particles. All samples presented similar hierarchical structures, based on primary rounded-shape nanoparticles 15-20 nm in size, self-assembled into micron-sized spherical particles. At high vanadium loadings, micron-sized V₂O₅ crystals were observed growing from the TiO₂ particles.

The conductivity of the TiO₂-V₂O₅ mixed oxides was significantly higher than that of the pure TiO₂ sample, but no correlation between the vanadium content and the conductivity could be found. Despite this improved electronic conductivity, the reversible capacity of the electrodes after the first cycle was not improved. Apparently, increasing the vanadium loading above 5 at% mostly led in the growth of V₂O₅ crystals and in a decrease of the specific surface area of the electrode material, resulting in lower specific capacity.

The electrochemical behavior against sodium was more encouraging. Contrary to the evaluation of the electrodes against lithium, a 5 at% vanadium loading improved the performance compared to pure TiO₂ (128 mAh g⁻¹ and 110 mAh g⁻¹ with a current rate of 336 mA g⁻¹ respectively).

The second approach explored was based on the preparation of TiO₂/C nanocomposites. Mesoporous carbon-coated TiO₂ nanocomposites were successfully synthesized using an original, solvent-free NHSG route. We proposed to use simple ethers in a stoichiometric amount not only as oxygen donors but also as carbon sources. After pyrolysis at 750 °C, mesoporous TiO₂/carbon nanocomposites built of anatase nanocrystals coated by an amorphous carbon film were obtained, as shown by XRD, Raman spectroscopy, ¹³C CPMAS-NMR spectroscopies, and electron microscopy. The carbon content can be controlled by playing on the reaction temperature. The nature of the ether impacted the carbon content and the carbon coating thickness, as well as the texture of the nanocomposite and TiO₂ crystallite size. This simple NHSG approach should provide a general method to synthesize mesoporous metal oxide-carbon nanocomposites.

The electrochemical behavior of TiO₂/C nanocomposites and their TiO₂ counterparts (obtained by calcination in air) toward lithium insertion-desinsertion was investigated. The influence of the carbon coating on the electrochemical performances was evidenced and compared to that of a conventional carbon-black additive. However, as far as electrochemical

performances are concerned, carbon black appeared more effective than the intrinsic carbon coating. This could be ascribed to the more graphitic nature of the carbon black additive, and/or to the hindering of lithium ion diffusion toward the TiO_2 by the intrinsic carbon coating.

The catalytic graphitization was explored by impregnating xerogel byproducts by a FeCl_3 solution. The use of a lower pyrolysis temperature, as compared with those used in literature, did not allow for a significant improvement of the graphitization degree of the carbon in TiO_2/C nanocomposites.

Different directions can be proposed to continue this work. The influence of the calcination temperature on the electrochemical performances should be completed, using for instance *in situ* X-ray diffraction or *in situ* Fourier transform infrared spectroscopy. The stability of our TiO_2 materials over broad potential windows also deserve further investigations. The hierarchical TiO_2 obtained by the $^1\text{Pr}_2\text{O}$ route shows good electrochemical performances, which could be improved by preparing, for example, $\text{TiO}_2\text{-SnO}_2$ mixed oxides instead of $\text{TiO}_2\text{-V}_2\text{O}_5$.

Concerning the TiO_2/C nanocomposites, our results demonstrate that the approach is potentially attractive in terms of process and material. To improve the electrodes performance, researches should target the formation of mesoporosity in the carbon coating to allow a better diffusion of lithium ions. Besides, a careful tuning of the pyrolysis conditions, this could possibly be achieved by using other O-donors.

Moreover, this original and simple NHSG approach provides a general method to synthesize mesoporous metal oxide-carbon nanocomposites, and much remains to be done to explore different oxide and mixed oxide-carbon systems, different oxygen/carbon donors, and to investigate the potential applications of the resulting nanocomposites.

Résumé en Français

Synthèse par chimie sol-gel non-hydrolytique de matériaux d'électrodes pour batteries Li-ion à base de TiO₂

Les batteries lithium-ion (LIBs selon leurs sigles en anglais) sont des outils de stockage de l'énergie omniprésents pour des applications portables ou des véhicules hybrides et électriques. Cependant, pour des applications demandant une forte puissance énergétique, les performances des matériaux actuellement utilisés comme électrodes doivent être améliorées.

Les travaux les plus récents dans ce domaine portent sur l'utilisation d'oxydes métalliques. Ces composés, les plus abondants de la planète, sont des matériaux intéressants à étudier car ils présentent en plus des propriétés telles que le superparamagnétisme ou la piézoélectricité. Ces différentes propriétés ouvrent un éventail de possibilités pour des diverses applications dans des domaines technologiques tels que la catalyse, les colorants, des applications biomédicales et également pour des applications énergétiques.

Parmi ces oxydes, le dioxyde de titane (TiO₂) a été largement étudié pour trois raisons majeures : il possède un indice de réfraction élevé ($n=2.49$ à 589 nm pour TiO₂ anatase [160]), c'est un semiconducteur (une bande interdite de 3.2 eV pour TiO₂ anatase [157, 182, 209]) enfin, il présente aussi une activité photocatalytique (limite de bande à 387 nm pour TiO₂ anatase, proche du rayonnement ultraviolet [182]). La recherche a fait des progrès sur ce matériau en visant un contrôle de la morphologie, la cristallinité, la taille de particule et la porosité, tout cela en regard des applications spécifiques. Dans le domaine du stockage de l'énergie, le TiO₂ a attiré l'attention comme remplaçant potentiel du graphite des anodes des batteries Li-ion, notamment pour les applications à haute demande énergétique. Cela tient à la capacité spécifique théorique (335,6 mAh·g⁻¹) [91], sa stabilité chimique et son coût faible de production. À côté de ces avantages, le TiO₂ possède une faible conductivité électronique ($10^{-12} < \sigma < 10^{-7}$ S·cm⁻¹ [191]) et aussi un faible coefficient de diffusion ionique ($10^{-14} < D_c < 10^{-6}$ cm²·s⁻¹ [192-195]). Ces deux facteurs limitent les performances électrochimiques pour des applications en batteries au lithium qui ne sont pas aujourd'hui à des niveaux suffisants pour répondre aux demandes des industriels.

Cependant, tout n'est pas perdu pour le TiO₂ ; ils existent des approches permettant d'envisager une amélioration de ses propriétés électrochimiques. Tout d'abord, dans l'idée de palier le faible coefficient de diffusion, les recherches se sont orientées vers des matériaux nanostructurés et à porosité contrôlée ou hiérarchique [119, 121]. Cette approche vise la création de plus de surface et donc plus de sites d'entrée du lithium dans la structure du TiO₂, favorisant ainsi le flux des ions [119]. Parallèlement, le dopage du TiO₂ par des atomes métalliques vise à améliorer la conductivité par la modification de sa structure cristalline [143]. Une troisième approche cible l'utilisation de carbone avec le but d'améliorer la conductivité de l'électrode en général ; le carbone peut être présent sous forme de carbone amorphe [265], graphène [199-201, 264] ou nanotubes de carbone [150, 198] et forme soit un assemblage hybride de particules [198, 264], soit un revêtement [202, 208, 265].

De façon générale, les oxydes métalliques, TiO₂ inclus, sont produits par des méthodes de synthèse à des températures assez élevées et fréquemment des phénomènes de ségrégation sont observés. Ces méthodes rendent difficile l'obtention des oxydes complexes ou nanostructurés. Une première réponse a été trouvée par la « chimie douce », terme conçu par

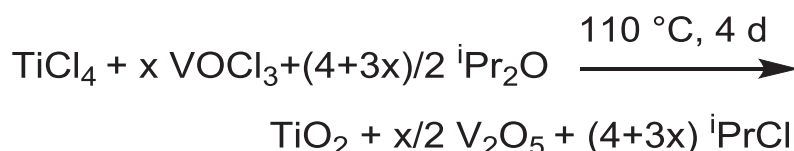
les chimistes français Jacques Livage et Jean Rouxel [2, 3]. La chimie douce regroupe un ensemble de réactions produites en solution, favorisant ainsi l'homogénéité et le contrôle de la réaction. Elles sont généralement réalisées à des températures faibles de l'ordre de 200 °C à 300 °C au maximum et plus généralement entre 100 °C et 200 °C. Les produits obtenus sont généralement métastables et sont susceptibles d'évoluer avec un traitement thermique, notamment par des processus de cristallisation et de frittage. La chimie du sol-gel non-hydrolytique (SGNH) représente une alternative aux voies conventionnelles de sol-gel car elle met en jeu des réactions entre des chlorures métalliques et des donneurs d'oxygène différents de l'eau tels que des éthers, des alcools ou encore des aldéhydes et des acides carboxyliques. Cette méthode de synthèse s'est révélée efficace pour la production des oxydes et des oxydes mixtes mésoporeux [4, 19, 22].

Dans ce contexte, l'objectif principal de ce travail de thèse a été le développement des matériaux à base de TiO_2 synthétisés par une méthode de sol-gel non-hydrolytique pour des applications comme électrodes des batteries Li-ion. Étant donné la nécessité de modifier les propriétés électrochimiques du TiO_2 , deux différentes approches ont été développées. Un premier ensemble de travaux porte sur la préparation des oxydes mixtes ($\text{TiO}_2\text{-V}_2\text{O}_5$). La voie éther du SGNH a été privilégiée avec notamment l'utilisation de ${}^i\text{Pr}_2\text{O}$ comme donneur d'oxygène. Il est important de noter que ces matériaux ont été obtenus sans l'ajout de solvants ni d'additifs, ceci permettant d'aller vers une approche plus « Verte » de la synthèse de ces matériaux. Un deuxième ensemble de travaux porte sur la réalisation de nanocomposites TiO_2/C . Cette approche reprend la voie de SGNH dont il avait été montré par le passé que la formation de l'oxyde métallique s'accompagne de celle de sous-produits carbonés. Ces derniers étaient jusqu'à présent éliminés par lavage ou consommés lors d'une étape de calcination. L'idée a été de préserver la présence de ces résidus carbonés et d'en faire la source du carbone qui est obtenu par une pyrolyse sous atmosphère inerte (Ar). Cela permet d'éliminer les étapes d'addition de sources externes de carbone pour l'obtention de ce type de composites et évite les étapes de lavage de l'oxyde. On rejoint ici encore les préoccupations de la chimie verte, notamment en terme d'économie d'atomes.

Les matériaux obtenus ont été caractérisés autant d'un point de vue structurale, texturale et morphologique (*i.e.* diffraction des rayons X, microscopie électronique, physisorption d'azote, spectroscopie Raman) que pour leurs performances électrochimiques (*i.e.* impédance et cyclages galvanostatiques). Concernant les nanocomposites TiO_2/C , le revêtement carboné a été analysé plus en détail en déterminant la quantité de carbone (*i.e.* analyse thermogravimétrique) et en essayant de comprendre la nature de ce carbone (*i.e.* résonance magnétique nucléaire solide du carbone).

Synthèse des oxydes mixtes ($\text{TiO}_2\text{-V}_2\text{O}_5$) par chimie sol-gel non-hydrolytique pour des applications comme matériaux d'anode de batteries Li-ion

Cette première partie est consacrée à la synthèse d'oxydes mixtes $\text{TiO}_2\text{-V}_2\text{O}_5$ en utilisant ${}^i\text{Pr}_2\text{O}$ comme donneur d'oxygène selon une méthode de synthèse sol-gel non-hydrolytique. Des poudres nanocristallines de TiO_2 et des $\text{TiO}_2\text{-V}_2\text{O}_5$ ont été préparées avec différentes proportions de vanadium : 5, 10, 15 et 20 at%. Le bilan réactionnel général est présenté dans le Schéma 1. La nomenclature adoptée, TiV_x , indique la valeur x du pourcentage atomique théorique de vanadium introduit dans l'échantillon (Tableau 1).

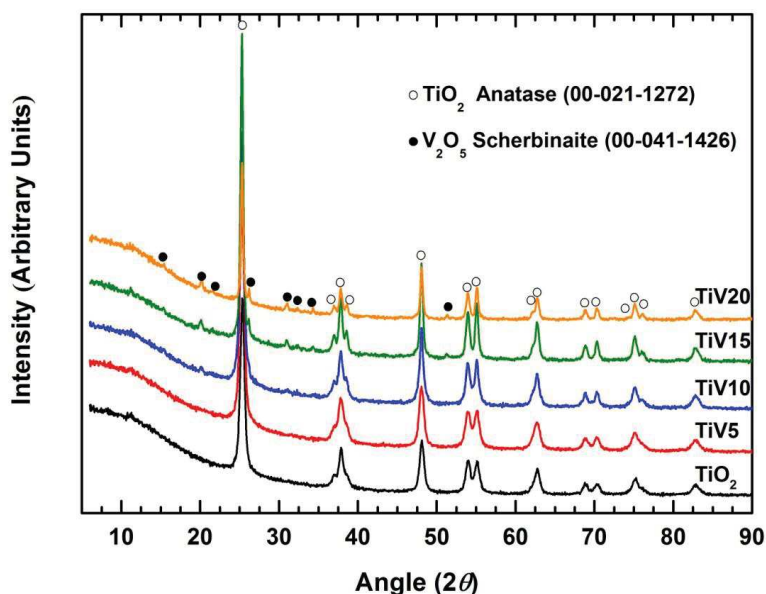
Schéma 1 Bilan réactionnel idéal de la synthèse d'oxydes mixtes $\text{TiO}_2\text{-V}_2\text{O}_5$.

L'analyse EDX montre que la composition en vanadium des échantillons est relativement proche des valeurs attendues pour ces produits, compte tenu de la composition en chlorure métallique de départ (Tableau 1).

Tableau 1 Contenu expérimental de vanadium, taille de cristallite et information de la texture du TiO_2 et des oxydes mixtes ($\text{TiO}_2\text{-V}_2\text{O}_5$).

Echantillon	Vanadium ^a (at%)	Taille de cristallite ^b (nm)	S _{BET} ^c (m ² /g)	V _p ^d (cm ³ /g)	D _p ^e (nm)
TiO ₂	0	13	68	0,17	5,7
TiV5	7,7	12	64	0,15	6,5
TiV10	8,4	17	58	0,16	7,9
TiV15	12,0	25	27	0,13	16,2
TiV20	17,0	25	15	0,09	20,2

^a D'après l'analyse EDX ; ^b selon l'analyse de DRX en appliquant l'équation de Scherrer ; ^c surface spécifique ; ^d volume poreux total ; ^e diamètre moyen BJH des pores calculé à partir de la courbe de desorption.

Figure R. 1 Diffractogrammes du TiO_2 et des oxydes mixtes ($\text{TiO}_2\text{-V}_2\text{O}_5$).

Les diffractogrammes de ces échantillons (Figure R. 1) montrent tous la formation de la phase cristalline anatase pour le TiO_2 (JCPDS 00-21-1272). Pour des faibles proportions de vanadium, l'absence d'un déplacement significatif des pics de diffraction peut être vue comme résultant de la solubilité du vanadium dans la structure cristalline du TiO_2 . Les échantillons avec une concentration plus élevée en vanadium montrent la présence de V_2O_5 scherbinaite (JCPDS 00-041-1426). La taille de cristallite, pour les cristaux de TiO_2 anatase, a été déterminée par l'équation de Scherrer et elle est comprise entre 13 et 25 nm. Elle devient plus importante avec l'augmentation de la proportion de vanadium (Tableau 1).

En microscopie MEB (Figure R. 2) les échantillons présentent dans tous les cas des morphologies hiérarchiques, résultant de l'aggrégation de nanoparticules primaires d'une taille autour des 15-20 nm (en corrélation avec les valeurs déterminées par DRX). Ces nanoparticules forment des agglomérats sphériques d'une taille qui atteint l'échelle de quelques microns qui, à leur tour, forment aussi des agglomérats de taille plus importante ($\approx 10-15 \mu\text{m}$). On remarquera que les particules secondaires dans le cas du TiO_2 sont plus petites, avec des tailles moyennes entre les $0,6 \mu\text{m}$ et $1,2 \mu\text{m}$; alors que les particules dans le cas des oxydes mixtes atteignent des tailles entre les $3 \mu\text{m}$ et $6 \mu\text{m}$. En outre, tel que les diffractogrammes l'avaient montré, les oxydes mixtes avec un contenu égal ou supérieur au 15 at% présentent des plaquettes cristallines de V_2O_5 imbriquées dans les particules de TiO_2 anatase.

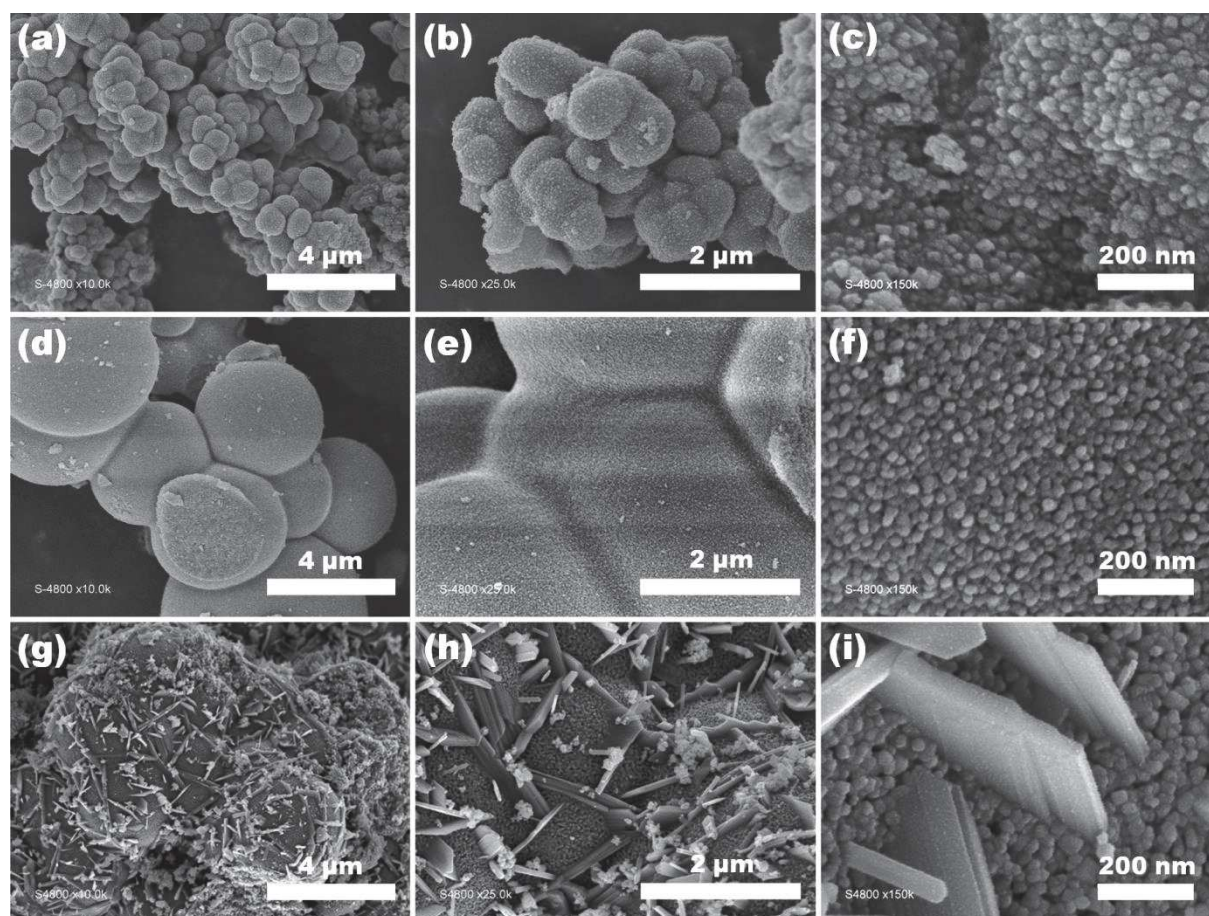


Figure R. 2 Micrographies MEB de TiO_2 (a-c), TiV5 (d-f) et TiV20 (g-i) à différents grossissements (x10k, x25k et x150k).

Les analyses texturales (isothermes d'adsorption-désorption d'azote Figure R. 3, Tableau 1) montrent pour les cinq échantillons des isothermes de type IV (IUPAC) caractéristique des solides mésoporeux. Ceci est confirmé par la distribution BJH de la taille des pores centrée entre 3-10 nm, pour le cas du TiO_2 et TiV5 et entre 10-40 nm pour TiV15 et TiV20 . L'échantillon TiV10 est un cas particulier, il présente une distribution bimodale avec des pores appartenant aux deux régions décrites précédemment. Selon une tendance générale, la surface spécifique des échantillons diminue avec l'augmentation de la proportion de vanadium passant de $68 \text{ m}^2 \cdot \text{g}^{-1}$ pour le TiO_2 à $15 \text{ m}^2 \cdot \text{g}^{-1}$ pour le TiV20 . Cette décroissance est attribuée à l'augmentation de la taille de cristallite et aux cristaux de V_2O_5 .

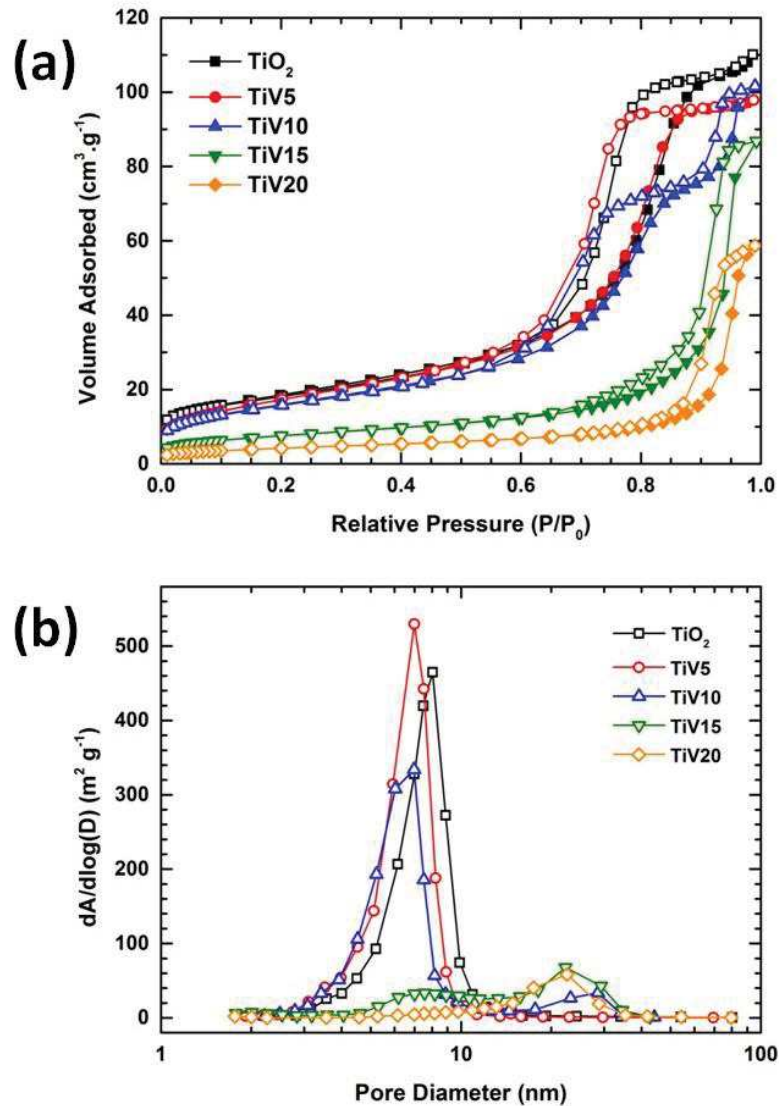


Figure R. 3 (a) Isothermes d'adsorption-désorption d'azote et (b) distribution BJH de la taille des pores déterminée à partir de la courbe de désorption du TiO₂ et des oxydes mixtes TiO₂-V₂O₅. Les symboles pleins et ouverts correspondent aux courbes d'adsorption et desorption respectivement.

Les profils galvanostatiques de charge-décharge correspondant au premier cycle sont présentés dans la Figure R. 4. Il est important prendre en compte que les capacités affichées n'ont pas été corrigées en fonction de la quantité de vanadium présente dans les oxydes mixtes. Les cinq matériaux présentent un comportement caractéristique de la phase anatase lors de l'insertion de lithium [184-186]. Tout d'abord, ils montrent la présence d'un plateau vers 1,7 V *versus* Li⁺/Li, lors de la première décharge, associé à la coexistence de la phase anatase du TiO₂ et d'une solution solide de titanate de lithium.

L'influence du vanadium est mise en évidence sur la première partie de la courbe de décharge (*i.e.* depuis le circuit ouvert jusqu'à 1,8 V *versus* Li⁺/Li). On constate l'apparition des épaulements vers 2,0-2,3 V *versus* Li⁺/Li, correspondant à des capacités de 50 à 100 mAh·g⁻¹. Ce comportement indique la présence d'activité électrochimique correspondant à un couple redox différent de celui lié au TiO₂ ; cette caractéristique est en accord avec le comportement des oxydes de vanadium par rapport au lithium [143]. L'absence de ce phénomène lors de la première charge met en évidence l'irréversibilité de l'insertion de lithium dans les vanadates.

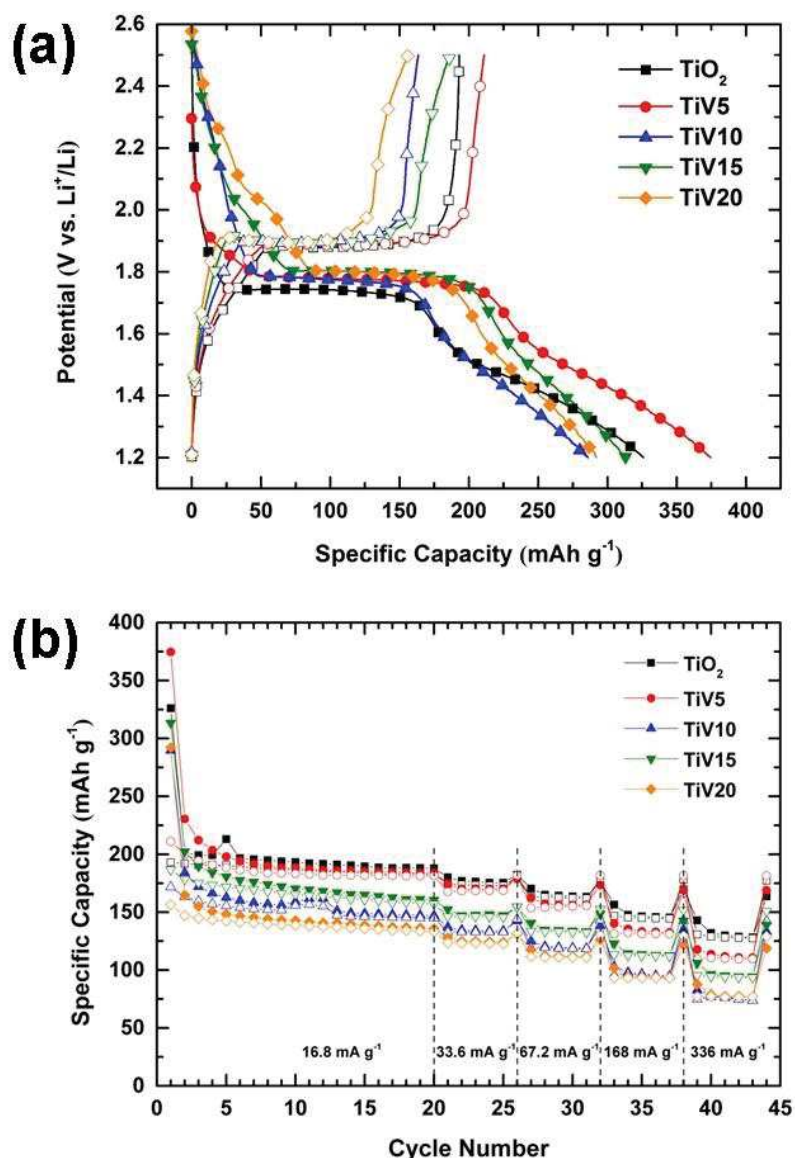


Figure R. 4 (a) Profils galvanostatiques correspondant au premier cycle (charge-décharge) des électrodes de TiO₂ et de TiO₂-V₂O₅ avec une densité de courant égal à 16,8 mA·g⁻¹ (C/20) par rapport au lithium ; (b) performances électrochimiques correspondant au cyclage avec différents densités de courant (C=335,6 mA·g⁻¹) pour une fenêtre de potentiel de 1,2-2,5 V versus Li⁺/Li (les symboles pleins et ouverts correspondent à la réduction -décharge- ou à l'oxydation -charge- respectivement).

La présence de vanadium modifie aussi le potentiel moyen du plateau lors de la première réduction. Il se voit augmenté de $\approx 0,04$ V versus Li⁺/Li pour TiV5 et TiV10, et de $\approx 0,1$ V versus Li⁺/Li for TiV15 and TiV20. Pour ce qui concerne la première oxydation, tous les échantillons montrent un potentiel de plateau identique ce qui se traduit par une amélioration de la polarisation avec l'augmentation du contenu vanadium. Ainsi, la capacité spécifique du plateau biphasique associé, à la formation de la phase Li_{0.5}TiO₂, est améliorée pour l'échantillon TiV5 (170 mAh·g⁻¹) par rapport au TiO₂ (150 mAh·g⁻¹) et cette valeur est proche de la valeur théorique (165,5 mAh·g⁻¹). Concernant les échantillons TiV10, TiV15 et TiV20, les capacités spécifiques du plateau biphasique sont inférieures à 150 mAh·g⁻¹ ce qui confirme la supériorité du TiV5 parmi les oxydes mixtes préparés. La cyclabilité de ces matériaux est présentée dans la Figure R. 4b. De façon générale, tous les échantillons présentent une bonne rétention de capacité tout au long du cyclage auquel ils ont été soumis, avec des augmentations progressives de densités de courant de C=16.8 mA·g⁻¹ à C=336 mA·g⁻¹. Lors

graphite dans tous les cas ; cela suggère que le carbone obtenu par pyrolyse possède une nature amorphe.

La taille de cristallite a été déterminée en utilisant l'équation de Scherrer avec la réflexion la plus intense du TiO_2 anatase (*i.e.* plan (101) ; $\approx 25,3^\circ 2\theta$, Tableau 2). Elle est comprise entre 7 et 20 nm et il est impossible de conclure à un effet de la nature du gaz de traitement thermique (air ou argon). En revanche, la taille des cristallites semble plus dépendante de la nature du donneur d'oxygène ; les cristallites de TiO_2/C -IPE étant plus grandes que celles de TiO_2/C -THF. Ce phénomène peut être dû à une quantité majeure de carbone dans ce dernier, empêchant ainsi sa croissance.

Tableau 2 Taille de cristallite et information de la texture du TiO_2 et des TiO_2/C nanocomposites.

Sample	Crystallite size ^a (nm)	S_{BET}^b ($\text{m}^2 \text{g}^{-1}$)	V_p^c (cm^3/g)	D_p^d (nm)
Xer-IPE	7	---	---	---
TiO_2/C -IPE	20	70	0.18	9.3
TiO_2 -IPE	16	50	0.17	9.3
Xer-THF	11	---	---	---
TiO_2/C -THF	13	75	0.21	10.2
TiO_2 -THF	14	63	0.23	10.3

^a Selon l'analyse de DRX en appliquant l'équation de Scherrer ; ^b surface spécifique ; ^c volume poreux total ; ^d diamètre moyen BJH des pores calculé à partir de la courbe de desorption.

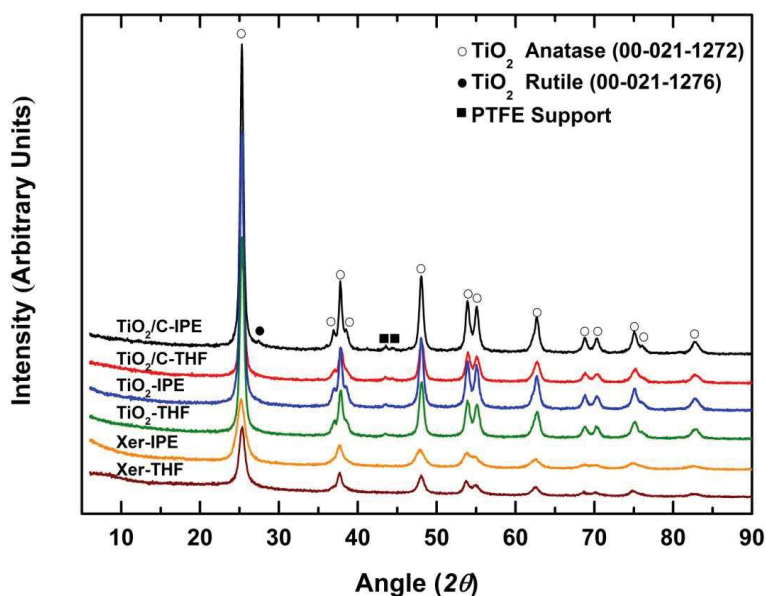


Figure R. 5 Diffractogrammes des xérogels, TiO_2 et TiO_2/C nanocomposites.

Les images MEB (Figure R. 6) des échantillons obtenues par la voie $^i\text{Pr}_2\text{O}$ montrent le même genre de structure hiérarchique que celle observée en absence de carbone : particules de taille micrométrique formées à partir de nanoparticules. Dans le cas du THF comme donneur d'oxygène, on observe aussi des nanoparticules formant des agglomérats, mais dans ce cas-ci, les agglomérats ne sont plus sphériques mais plutôt des blocs monolithiques. D'un point de vue générale, il n'y a pas de différences remarquables entre les morphologies obtenues par pyrolyse et calcination.

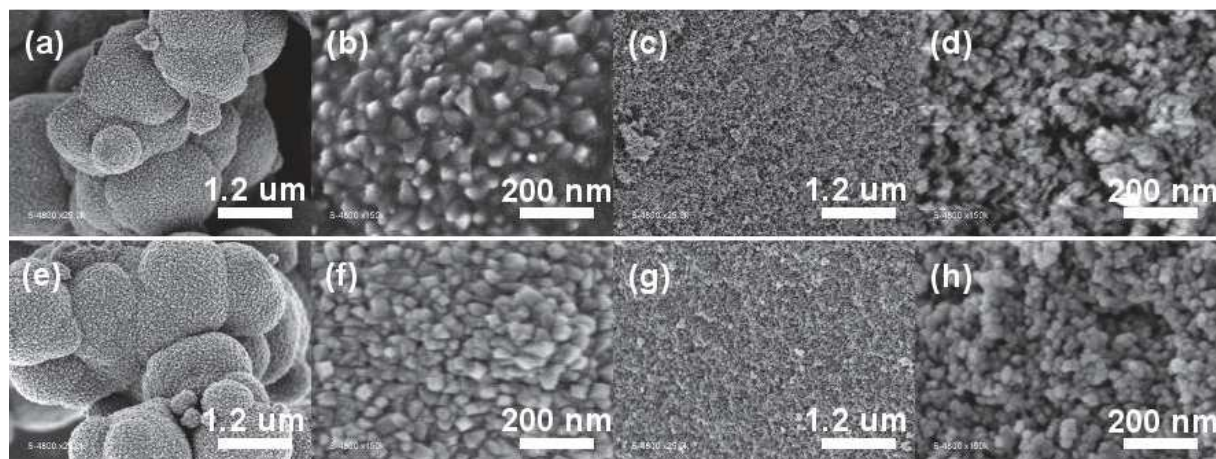


Figure R. 6 Micrographies MEB de TiO₂-IPE (a,b), TiO₂-THF (c,d), TiO₂/C-IPE (e,f), TiO₂/C-THF (g,h) à différents grossissements (x25k et x150k).

Les nanocomposites TiO₂/C ont été aussi analysés par MET (Figure R. 7). Ces micrographies mettent en évidence les plans correspondant au TiO₂ anatase et permettent de constater la taille des particules primaires, *i.e.* $16,2 \pm 5,7$ nm pour TiO₂/C-IPE et $12,5 \pm 3,3$ nm pour TiO₂/C-THF. Ces valeurs sont en accord avec la taille de cristallite déterminée par DRX. Cette analyse souligne aussi la nature et la structure du carbone vis-à-vis des nanoparticules de TiO₂. Dans les deux cas, les particules de TiO₂ sont recouvertes uniformément par un revêtement de carbone amorphe, ainsi la présence des agglomérats de carbone n'est pas observé. Pour les échantillons synthétisés à partir de THF, le revêtement de carbone présente une taille plus uniforme, par rapport à ceux obtenus par ¹Pr₂O.

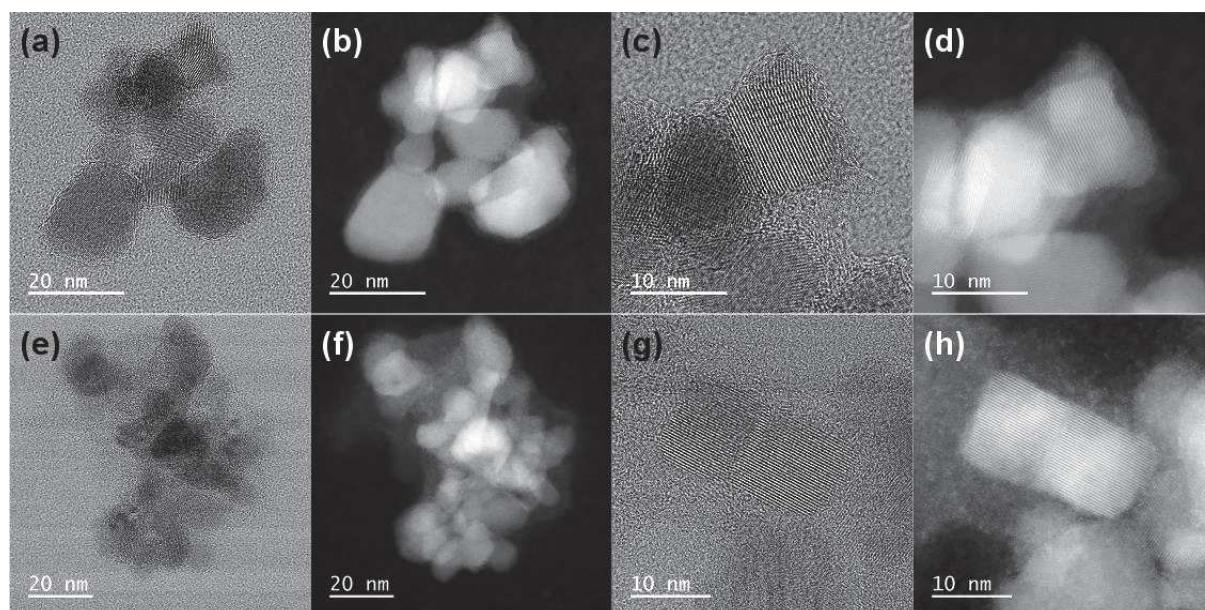


Figure R. 7 Micrographies MET de TiO₂/C-IPE (a-d) et TiO₂/C-THF (e-h) ; (b, d, f, h) ont été prises en champ noir annulaire à angle élevé.

Ces nanocomposites ont été étudiés par spectroscopie Raman (Figure R. 8) et ont été comparés à un noir de carbone, le même utilisé lors de la préparation des électrodes pour les cyclages électrochimiques. De façon générale, les deux échantillons présentent les bandes D et G, typiques des matériaux graphitiques ou partiellement graphitiques qui sont respectivement observées à 1350 cm^{-1} à 1580 cm^{-1} dans les cas classiques [278-280]. Pour les échantillons TiO₂/C-IPE et TiO₂/C-THF, ce n'est pas le cas. La bande G est centrée à *ca.*

1600 cm^{-1} et il y a la formation d'une bosse à 1200 cm^{-1} . Ce comportement a été rapporté par Sadezky *et al* [281] lors d'une étude sur la suie et des matériaux carbonés. D'autres publications démontrent que la bande D est composée de 4 bandes : D1, D2, D3 et D4 (1350; 1620; 1500 et 1200 cm^{-1} respectivement) [281-283], dont D3 correspond au carbone amorphe. La présence de ces bandes justifierait l'allure des spectres Raman obtenus. Ces analyses nous conduisent à conclure à la formation d'un carbone partiellement graphitisé, mais surtout très désordonné et amorphe.

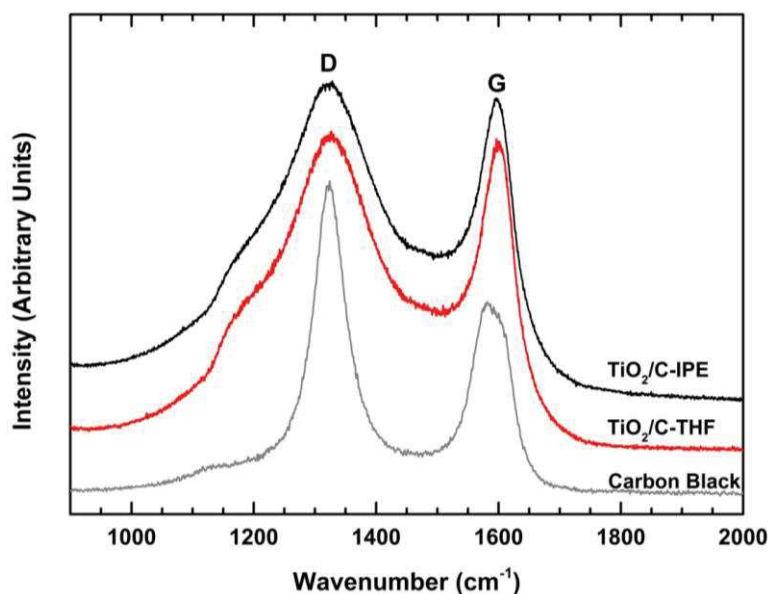


Figure R. 8 Spectre Raman des nanocomposites TiO_2/C dans la région de 900 à 2000 cm^{-1} .

Une analyse comparant le rôle de la présence de carbone intrinsèque (carbone issu de la pyrolyse) et extrinsèque (noir de carbone) lors de l'insertion de Li a été effectuée par un cyclage galvanostatique (Figure R. 9). Différentes compositions d'électrodes ont été évaluées ; dans tous les cas, le pourcentage de PVDF est resté le même (Tableau 3). Toutes les électrodes ont présenté le comportement classique d'insertion de lithium pour la phase anatase de TiO_2 .

Tableau 3 Composition des électrodes.

Echantillon	TiO_2 (wt %)	$\text{C}_{\text{extrinsèque}}$ (wt %)	$\text{C}_{\text{intrinsèque}}$ (wt %)	PVDF (wt %)
$\text{TiO}_2\text{-IPE-0CB}$	94	---	---	6
$\text{TiO}_2\text{-THF-0CB}$	94	---	---	6
$\text{TiO}_2\text{-IPE-18CB}$	76	18	---	6
$\text{TiO}_2\text{-THF-18CB}$	76	18	---	6
$\text{TiO}_2/\text{C-IPE-12CB}$	76	12	6	6
$\text{TiO}_2/\text{C-THF-0CB}$	76	---	18	6
$\text{TiO}_2/\text{C-IPE-0CB}$	88	---	6	6

Les électrodes de TiO_2 préparés sans aucun carbone, obtenus par calcination du xérogel (*i.e.* $\text{TiO}_2\text{-IPE-0CB}$ et $\text{TiO}_2\text{-THF-0CB}$) présentent une chute importante de capacité à des faibles densités de courant. Pour le cas de $\text{TiO}_2/\text{C-THF-0CB}$, le carbone intrinsèque, apporté par la pyrolyse du xérogel, améliore la capacité et la stabilité de l'échantillon par rapport aux derniers. Cependant, le carbone intrinsèque dans le $\text{TiO}_2/\text{C-IPE-0CB}$ n'apporte pas une

amélioration ; en effet, il montre des capacités semblables à celles obtenues par son homologue calciné. Cet effet peut être associé au taux de carbone dans cet échantillon, il contient seulement 1/3 de carbone par rapport à $\text{TiO}_2/\text{C-THF-0CB}$. Bien que le carbone intrinsèque montre une amélioration dans les performances électrochimiques, pour le cas du nanocomposites $\text{TiO}_2/\text{C-THF}$ vis-à-vis son homologue calciné ; les électrodes contenant du TiO_2 et du carbone extrinsèque montrent des meilleures capacités. Ce comportement suggère que ce revêtement carboné amorphe forme une couche de SEI qui empêcherait une majeure insertion de lithium.

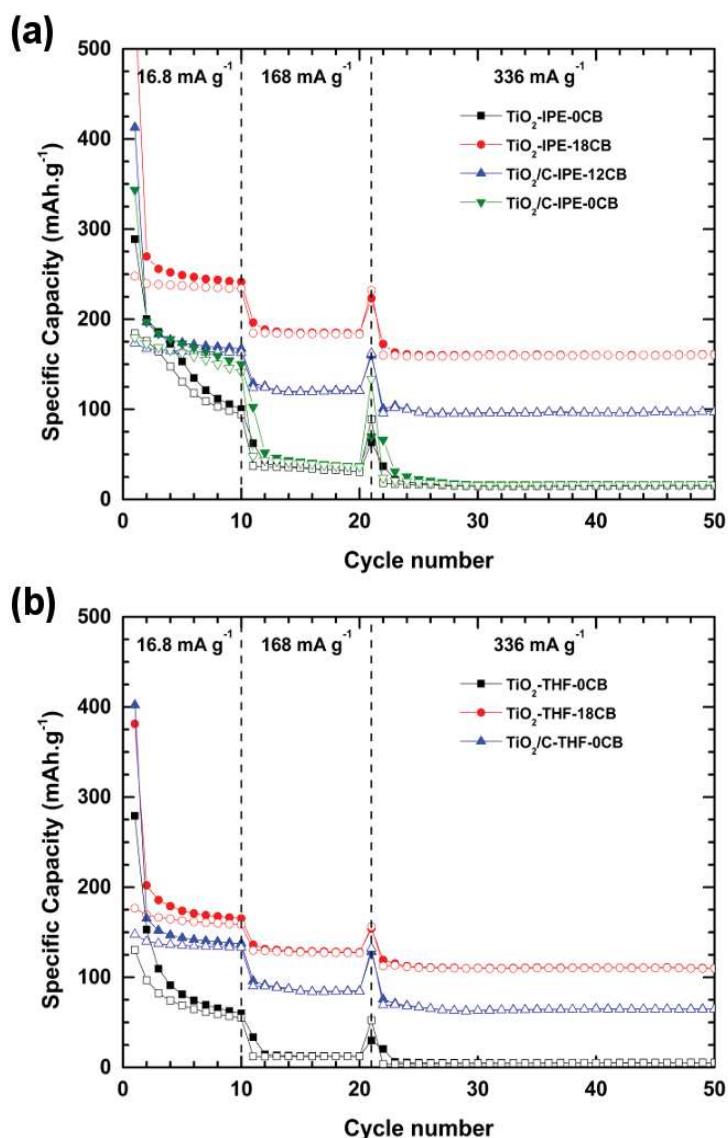


Figure R. 9 Performances électrochimiques correspondant au cyclage avec différentes densités de courant ($C=335.6 \text{ mA}\cdot\text{g}^{-1}$) pour une fenêtre de potentiel de 1.2-2.5 V *versus* Li^+/Li (les symboles pleins et ouverts correspondent à la réduction –décharge– ou à l’oxydation –charge– respectivement).

Conclusions

En résumé, des nanoparticules de TiO_2 anatase mésoporeux avec une structure hiérarchique ont été élaborées en utilisant la voie éther du sol-gel non-hydrolitique. Ces nanoparticules présentent des tailles moyennes entre les 10 et 25 nm et forment des agrégats sphériques qui atteignent la taille de quelques microns. Ces sphères microporeuses de TiO_2 montrent des

performance électrochimiques classiques. Des oxydes mixtes $\text{TiO}_2\text{-V}_2\text{O}_5$ ont été préparés de la même façon et conduisent à une amélioration de la conductivité électronique, mais la capacité réversible au-delà du premier cycle n'a pas été améliorée par rapport au TiO_2 . En plus, l'ajout de vanadium en quantités supérieures à 5 at% donne comme résultat la croissance des cristaux de V_2O_5 , une réduction de la surface spécifique et aussi de la capacité spécifique de ces matériaux.

Des nanocomposites TiO_2/C ont été obtenus par pyrolyse des xérogels en convertissant en carbone les sous-produits de la réaction de sol-gel non-hydrolytique utilisant $^i\text{Pr}_2\text{O}$ et THF. Ces matériaux présentent une structure composée des nanoparticules formant des agglomérats sphériques pour le cas de $^i\text{Pr}_2\text{O}$ et des blocs monolithiques pour le THF. Ils présentent une phase carbonée essentiellement amorphe avec certains domaines graphitisés désordonnés. Les cyclages galvanostatiques montrent une amélioration de la capacité et de la stabilité des électrodes formées à base des nanocomposites, par rapport aux analogues calcinés et sans ajout de source de carbone extrinsèque.

Il reste encore différentes approches à être développées telles que la formation d'autres oxydes mixtes, $\text{TiO}_2\text{-SnO}_2$ par exemple, ou encore l'utilisation d'autres donneurs d'oxygène/carbone pour la formation des nanocomposites $\text{TiO}_2/\text{carbone}$.

References

1. Escamilla-Perez, A.M., et al., *Lithium insertion properties of mesoporous nanocrystalline TiO₂ and TiO₂-V₂O₅ microspheres prepared by non-hydrolytic sol-gel*. J. Sol-Gel Sci. Technol., 2016. **79**(2): p. 270-278.
2. Gerand, B. and L. Seguin, *The soft chemistry of molybdenum and tungsten oxides: a review*. Solid State Ionics, 1996. **84**(3,4): p. 199-204.
3. Sanchez, C., et al., "*Chimie douce*": *A land of opportunities for the designed construction of functional inorganic and hybrid organic-inorganic nanomaterials*. C. R. Chim., 2010. **13**(1-2): p. 3-39.
4. Mutin, P.H. and A. Vioux, *Recent advances in the synthesis of inorganic materials via non-hydrolytic condensation and related low-temperature routes*. J. Mater. Chem. A, 2013. **1**(38): p. 11504-11512.
5. Gopalakrishnan, J., *Chimie Douce Approaches to the Synthesis of Metastable Oxide Materials*. Chem. Mater., 1995. **7**(7): p. 1265-75.
6. Makarova, M., et al., *Soft chemistry preparation methods and properties of strontium titanate nanoparticles*. Opt. Mater. (Amsterdam, Neth.), 2010. **32**(8): p. 803-806.
7. Liu, X., N. Fechner, and M. Antonietti, *Salt melt synthesis of ceramics, semiconductors and carbon nanostructures*. Chem. Soc. Rev., 2013. **42**(21): p. 8237-8265.
8. Mendelovici, E., *Thermal synthesis of inorganic materials*. Thermochim. Acta, 1989. **148**: p. 205-18.
9. Niederberger, M. and G. Garnweitner, *Organic reaction pathways in the nonaqueous synthesis of metal oxide nanoparticles*. Chem. - Eur. J., 2006. **12**(28): p. 7282-7302.
10. Brinker, C.J. and G.W. Scherer, *CHAPTER 1 - Introduction*, in *Sol-Gel Science*. 1990, Academic Press: San Diego. p. xvi-18.
11. Rechberger, F. and M. Niederberger, *Synthesis of aerogels: from molecular routes to 3-dimensional nanoparticle assembly*. Nanoscale Horiz., 2017. **2**(1): p. 6-30.
12. Livage, J., M. Henry, and C. Sanchez, *Sol-gel chemistry of transition metal oxides*. Prog. Solid State Chem., 1988. **18**(4): p. 259-341.
13. Livage, J. and C. Sanchez, *Sol-gel chemistry*. J. Non-Cryst. Solids, 1992. **145**(1-3): p. 11-19.
14. Livage, J., et al., *The chemistry of the sol-gel process*. Solid State Ionics, 1989. **32-33**(Pt. 2): p. 633-8.
15. Dearing, A.W. and E.E. Reid, *Alkyl orthosilicates*. J. Am. Chem. Soc., 1928. **50**: p. 3058-62.
16. Corriu, R., et al., *Preparation of monolithic binary oxide gels by a nonhydrolytic sol-gel process*. Chem. Mater., 1992. **4**(5): p. 961-3.
17. Corriu, R.J.P., et al., *Preparation of monolithic metal oxide gels by a non-hydrolytic sol-gel process*. J. Mater. Chem., 1992. **2**(6): p. 673-4.
18. Corriu, R.J.P., et al., *Preparation of monolithic gels from silicon halides by a non-hydrolytic sol-gel process*. J. Non-Cryst. Solids, 1992. **146**(2-3): p. 301-3.
19. Mutin, P.H. and A. Vioux, *Nonhydrolytic Processing of Oxide-Based Materials: Simple Routes to Control Homogeneity, Morphology, and Nanostructure*. Chem. Mater., 2009. **21**(4): p. 582-596.
20. Pinna, N. and M. Niederberger, *Surfactant-free nonaqueous synthesis of metal oxide nanostructures*. Angew. Chem., Int. Ed., 2008. **47**(29): p. 5292-5304.

21. Debecker, D.P. and P.H. Mutin, *Non-hydrolytic sol-gel routes to heterogeneous catalysts*. Chem. Soc. Rev., 2012. **41**(9): p. 3624-3650.
22. Debecker, D.P., V. Hulea, and P.H. Mutin, *Mesoporous mixed oxide catalysts via non-hydrolytic sol-gel: A review*. Appl. Catal., A, 2013. **451**: p. 192-206.
23. Garnweitner, G. and M. Niederberger, *Nonaqueous and surfactant-free synthesis routes to metal oxide nanoparticles*. J. Am. Ceram. Soc., 2006. **89**(6): p. 1801-1808.
24. Pinna, N., *The "benzyl alcohol route": an elegant approach towards organic-inorganic hybrid nanomaterials*. J. Mater. Chem., 2007. **17**(27): p. 2769-2774.
25. Bilecka, I. and M. Niederberger, *New developments in the nonaqueous and/or non-hydrolytic sol-gel synthesis of inorganic nanoparticles*. Electrochim. Acta, 2010. **55**(26): p. 7717-7725.
26. Bilecka, I., et al., *Microwave-assisted solution synthesis of doped LiFePO₄ with high specific charge and outstanding cycling performance*. J. Mater. Chem., 2011. **21**(16): p. 5881-5890.
27. Arnal, P., et al., *Preparation of anatase, brookite and rutile at low temperature by non-hydrolytic sol-gel methods*. J. Mater. Chem., 1996. **6**(12): p. 1925-1932.
28. Arnal, P., et al., *A Solution Chemistry Study of Nonhydrolytic Sol-Gel Routes to Titania*. Chem. Mater., 1997. **9**(3): p. 694-698.
29. Aboulaich, A., B. Boury, and P.H. Mutin, *Reactive and Organosoluble Anatase Nanoparticles by a Surfactant-Free Nonhydrolytic Synthesis*. Chem. Mater., 2010. **22**(16): p. 4519-4521.
30. Niederberger, M., M.H. Bartl, and G.D. Stucky, *Benzyl Alcohol and Titanium Tetrachloride-A Versatile Reaction System for the Nonaqueous and Low-Temperature Preparation of Crystalline and Luminescent Titania Nanoparticles*. Chem. Mater., 2002. **14**(10): p. 4364-4370.
31. Wang, J., et al., *Pseudocapacitive Contributions to Electrochemical Energy Storage in TiO₂ (Anatase) Nanoparticles*. J. Phys. Chem. C, 2007. **111**(40): p. 14925-14931.
32. Zhu, J., et al., *Nanocrystalline anatase TiO₂ photocatalysts prepared via a facile low temperature nonhydrolytic sol-gel reaction of TiCl₄ and benzyl alcohol*. Appl. Catal., B, 2007. **76**(1-2): p. 82-91.
33. Li, G., et al., *High Purity Anatase TiO₂ Nanocrystals: Near Room-Temperature Synthesis, Grain Growth Kinetics, and Surface Hydration Chemistry*. J. Am. Chem. Soc., 2005. **127**(24): p. 8659-8666.
34. Trentler, T.J., et al., *Synthesis of TiO₂ Nanocrystals by Nonhydrolytic Solution-Based Reactions*. J. Am. Chem. Soc., 1999. **121**(7): p. 1613-1614.
35. Xu, J., et al., *X-ray Diffraction and X-ray Absorption Spectroscopy Studies of Sol-Gel-Processed Zirconium Titanates*. Chem. Mater., 2000. **12**(11): p. 3347-3355.
36. Aboulaich, A., et al., *Surfactant-Free Organo-Soluble Silica-Titania and Silica Nanoparticles*. Chem. Mater., 2009. **21**(13): p. 2577-2579.
37. Bourget, L., et al., *Non-hydrolytic sol-gel routes to silica*. J. Non-Cryst. Solids, 1998. **242**(2,3): p. 81-91.
38. Hay, J.N., D. Porter, and H.M. Raval, *A versatile route to organically-modified silicas and porous silicas via the non-hydrolytic sol-gel process*. J. Mater. Chem., 2000. **10**(8): p. 1811-1818.
39. Acosta, S., et al., *Preparation of alumina gels by a non-hydrolytic sol-gel processing method*. Journal of Non-Crystalline Solids, 1994. **170**(3): p. 234-242.
40. De Hazan, Y., et al., *The evolution of microstructure in nonhydrolytic alumina xerogels*. J. Sol-Gel Sci. Technol., 1999. **14**(3): p. 233-247.
41. Grader, G.S., G.E. Shter, and Y. De Hazan, *Novel ceramic foams from crystals of AlCl₃(Pr₂iO) complex*. J. Mater. Res., 1999. **14**(4): p. 1485-1494.

42. Acosta, S., et al., *Novel non-hydrolytic sol-gel route to metal oxides*. J. Sol-Gel Sci. Technol., 1994. **2**(1/2/3): p. 25-8.
43. Harreld, J.H., J. Sakamoto, and B. Dunn, *Non-hydrolytic sol-gel synthesis and electrochemical characterization of tin-based oxide aerogels*. Journal of Power Sources, 2003. **115**(1): p. 19-26.
44. Aboulaich, A., B. Boury, and P.H. Mutin, *Reactive and organosoluble SnO₂ nanoparticles by a surfactant-free non-hydrolytic sol-gel route*. Eur. J. Inorg. Chem., 2011. **2011**(24): p. 3644-3649.
45. Wilkinson, A.P., C. Lind, and S. Pattanaik, *A New Polymorph of ZrW₂O₈ Prepared Using Nonhydrolytic Sol-Gel Chemistry*. Chem. Mater., 1999. **11**(1): p. 101-108.
46. Zhao, Z.W., Z.P. Guo, and H.K. Liu, *Non-aqueous synthesis of crystalline Co₃O₄ powders using alcohol and cobalt chloride as a versatile reaction system for controllable morphology*. J. Power Sources, 2005. **147**(1-2): p. 264-268.
47. Bilecka, I., I. Djerdj, and M. Niederberger, *One-minute synthesis of crystalline binary and ternary metal oxide nanoparticles*. Chem. Commun. (Cambridge, U. K.), 2008(7): p. 886-888.
48. Pinna, N., et al., *Magnetite Nanocrystals: Nonaqueous Synthesis, Characterization, and Solubility*. Chem. Mater., 2005. **17**(11): p. 3044-3049.
49. Petitto, C., H.P. Mutin, and G. Delahay, *A highly efficient silver niobium alumina catalyst for the selective catalytic reduction of NO by n-decane*. Chem. Commun. (Cambridge, U. K.), 2011. **47**(38): p. 10728-10730.
50. Alfenas, C.d.S., et al., *Antibacterial activity of Nb-aluminum oxide prepared by the non-hydrolytic sol-gel route*. J. Mol. Catal. A: Chem., 2011. **338**(1-2): p. 65-70.
51. Ricci, G.P., et al., *Iron-alumina materials prepared by the non-hydrolytic sol-gel route: Synthesis, characterization and application in hydrocarbons oxidation using hydrogen peroxide as oxidant*. Appl. Catal., A, 2010. **389**(1-2): p. 147-154.
52. Ciuffi, K.J., et al., *Eu³⁺ entrapped in alumina matrix obtained by hydrolytic and non-hydrolytic sol-gel routes*. Journal of Non-Crystalline Solids, 2002. **304**(1): p. 126-133.
53. de Lima, O.J., et al., *Sol-gel entrapped cobalt complex*. Mater. Charact., 2003. **50**(2/3): p. 101-108.
54. Silva, G.M., et al., *Synthesis of indium tin oxide nanoparticles by a nonhydrolytic sol-gel method*. Quim. Nova, 2012. **35**(3): p. 473-476.
55. Matias, C.R., et al., *Synthesis and characterization of Nb₂O₅:La³⁺,Eu³⁺ phosphors obtained by the non-hydrolytic sol-gel process*. J. Braz. Chem. Soc., 2015. **26**(12): p. 2558-2570.
56. Cestari, A., et al., *Preparation of calcium fluoroaluminosilicate glasses containing sodium and phosphorus by the nonhydrolytic sol-gel method*. J. Alloys Compd., 2009. **472**(1-2): p. 299-306.
57. Kaper, H., et al., *High-Surface-Area SiO₂-ZrO₂ Mixed Oxides as Catalysts for the Friedel-Crafts-Type Alkylation of Arenes with Alcohols and Tandem Cyclopropanation Reactions*. ChemCatChem, 2012. **4**(11): p. 1813-1818, S1813/1-S1813/3.
58. Andrianainarivelo, M., et al., *Mixed oxides SiO₂-ZrO₂ and SiO₂-TiO₂ by a non-hydrolytic sol-gel route*. J. Mater. Chem., 1996. **6**(10): p. 1665-1671.
59. Cojocariu, A.M., et al., *Non-hydrolytic SiO₂-TiO₂ mesoporous xerogels-Efficient catalysts for the mild oxidation of sulfur organic compounds with hydrogen peroxide*. Catalysis Today, 2010. **157**(1-4): p. 270-274.
60. Cojocariu, A.M., et al., *Mild oxidation of bulky organic compounds with hydrogen peroxide over mesoporous TiO₂-SiO₂ xerogels prepared by non-hydrolytic sol-gel*. Appl. Catal., B, 2010. **97**(3-4): p. 407-413.

61. Cojocariu, A.M., et al., *Non-hydrolytic synthesis of mesoporous silica-titania catalysts for the mild oxidation of sulfur compounds with hydrogen peroxide*. Chem. Commun. (Cambridge, U. K.), 2008(42): p. 5357-5359.
62. Lafond, V., P.H. Mutin, and A. Vioux, *Non-hydrolytic sol-gel routes based on alkyl halide elimination: toward better mixed oxide catalysts and new supports: Application to the preparation of a SiO₂-TiO₂ epoxidation catalyst*. Journal of Molecular Catalysis A: Chemical, 2002. **182-183**: p. 81-88.
63. Andrianainarivelo, M., et al., *Non-hydrolytic sol-gel process: zirconium titanate gels*. J. Mater. Chem., 1997. **7**(2): p. 279-284.
64. Andrianainarivelo, M., et al., *Nonhydrolytic sol-gel process: aluminum and zirconium titanate gels*. J. Sol-Gel Sci. Technol., 1997. **8**(1/2/3): p. 89-93.
65. Andrianainarivelo, M., et al., *Nonhydrolytic Sol-Gel Process: Aluminum Titanate Gels*. Chem. Mater., 1997. **9**(5): p. 1098-1102.
66. Linacero, R., M.L. Rojas-Cervantes, and J.D.D. Lopez-Gonzalez, *Influence of the synthesis methods on the physical and structural characteristics of 0.6TiO₂-0.4Al₂O₃ catalytic supports*. J. Mater. Sci., 2000. **35**(13): p. 3269-3278.
67. Mutin, P.H., et al., *Nonhydrolytic vanadia-titania xerogels: Synthesis, characterization, and behavior in the selective catalytic reduction of NO by NH₃*. Appl. Catal., B, 2006. **69**(1-2): p. 49-57.
68. Debecker, D.P., et al., *One-step non-hydrolytic sol-gel preparation of efficient V₂O₅-TiO₂ catalysts for VOC total oxidation*. Appl. Catal., B, 2010. **94**(1-2): p. 38-45.
69. Barbieri, F., et al., *Mixed-oxide catalysts involving V, Nb and Si obtained by a non-hydrolytic sol-gel route: preparation and catalytic behavior in oxidative dehydrogenation of propane*. Catal. Today, 2000. **61**(1-4): p. 353-360.
70. Debecker, D.P., et al., *Design of SiO₂-Al₂O₃-MoO₃ Metathesis Catalysts by Nonhydrolytic Sol-Gel*. Chem. Mater., 2009. **21**(13): p. 2817-2824.
71. Debecker, D.P., et al., *A non-hydrolytic sol-gel route to highly active MoO₃-SiO₂-Al₂O₃ metathesis catalysts*. Catal. Sci. Technol., 2012. **2**(6): p. 1157-1164.
72. Bouchmella, K., et al., *Olefin metathesis with mesoporous rhenium-silicium-aluminum mixed oxides obtained via a one-step non-hydrolytic sol-gel route*. J. Catal., 2013. **301**: p. 233-241.
73. Caetano, B.L., et al., *Cobalt aluminum silicate complexes prepared by the non-hydrolytic sol-gel route and their catalytic activity in hydrocarbon oxidation*. Appl. Catal., A, 2006. **311**: p. 122-134.
74. Matos, M.G., et al., *Synthesis and photoluminescent properties of yttrium vanadate phosphor prepared by the non-hydrolytic sol-gel process*. J. Lumin., 2014. **147**: p. 190-195.
75. Debecker, D.P., et al., *Total oxidation of benzene and chlorobenzene with MoO₃- and WO₃-promoted V₂O₅/TiO₂ catalysts prepared by a nonhydrolytic sol-gel route*. Catal. Today, 2010. **157**(1-4): p. 125-130.
76. Pereira, P.F.S., et al., *Red, green and blue (RGB) emission doped Y₃Al₅O₁₂ (YAG) phosphors prepared by non-hydrolytic sol-gel route*. J. Lumin., 2010. **130**(3): p. 488-493.
77. Pereira, P.F.S., et al., *Aluminate matrix doped with Tm³⁺/Tb³⁺/Eu³⁺ obtained by non-hydrolytic sol-gel route: White light emission*. J. Lumin., 2014. **146**: p. 394-397.
78. Pereira, P.F.S., et al., *Microwave synthesis of YAG:Eu by sol-gel methodology*. J. Lumin., 2007. **126**(2): p. 378-382.
79. Nassar, E.J., et al., *Eu(III) incorporation in sol-gel aluminum-yttrium matrix by non-hydrolytic route*. Journal of Luminescence, 2005. **111**(3): p. 159-166.

80. Nassar, E.J., et al., *Nonhydrolytic sol-gel synthesis and characterization of YAG*. J. Mater. Sci., 2007. **42**(7): p. 2244-2249.
81. Pereira, P.F.S., et al., *Study of the annealing temperature effect on the structural and luminescent properties of SrWO₄:Eu phosphors prepared by a non-hydrolytic sol-gel process*. J. Alloys Compd., 2012. **526**: p. 11-21.
82. Pereira, P.F.S., et al., *Rietveld refinement and optical properties of SrWO₄:Eu³⁺ powders prepared by the non-hydrolytic sol-gel method*. J. Rare Earths, 2015. **33**(2): p. 113-128.
83. Niederberger, M., et al., *Nonaqueous and Halide-Free Route to Crystalline BaTiO₃, SrTiO₃, and (Ba,Sr)TiO₃ Nanoparticles via a Mechanism Involving C-C Bond Formation*. J. Am. Chem. Soc., 2004. **126**(29): p. 9120-9126.
84. Di Vona, M.L., E. Traversa, and S. Licoccia, *Nonhydrolytic synthesis of NASICON of composition Na₃Zr₂Si₂PO₁₂: A spectroscopic study*. Chem. Mater., 2001. **13**(1): p. 141-144.
85. Styskalik, A., et al., *Non-hydrolytic synthesis of titanosilicate xerogels by acetamide elimination and their use as epoxidation catalysts*. J. Sol-Gel Sci. Technol., 2012. **63**(3): p. 463-472.
86. Skoda, D., et al., *Mesoporous titanosilicates by templated non-hydrolytic sol-gel reactions*. J. Sol-Gel Sci. Technol., 2015. **74**(3): p. 810-822.
87. Skoda, D., et al., *Templated non-hydrolytic synthesis of mesoporous zirconium silicates and their catalytic properties*. J. Mater. Sci., 2015. **50**(9): p. 3371-3382.
88. Skoda, D., et al., *Novel non-hydrolytic templated sol-gel synthesis of mesoporous aluminosilicates and their use as aminolysis catalysts*. RSC Adv., 2016. **6**(29): p. 24273-24284.
89. Skoda, D., et al., *Mesoporous SnO₂-SiO₂ and Sn-silica-carbon nanocomposites by novel non-hydrolytic templated sol-gel synthesis*. RSC Adv., 2016. **6**(73): p. 68739-68747.
90. Ozawa, K. and Editor, *Lithium Ion Rechargeable Batteries*. 2009: Wiley-VCH Verlag GmbH & Co. KGaA. 336 pp.
91. Scrosati, B. and J.r. Garche, *Lithium batteries: Status, prospects and future*. Journal of Power Sources, 2010. **195**(9): p. 2419-2430.
92. Palacin, M.R., *Recent advances in rechargeable battery materials: a chemist's perspective*. Chemical Society Reviews, 2009. **38**(9): p. 2565-2575.
93. Guyomard, D. and J.M. Tarascon, *Rocking-chair or lithium-ion rechargeable lithium batteries*. Adv. Mater. (Weinheim, Ger.), 1994. **6**(5): p. 408-12.
94. Xu, W., et al., *Lithium metal anodes for rechargeable batteries*. Energy & Environmental Science, 2014. **7**(2): p. 513-537.
95. Goodenough, J.B. and K.-S. Park, *The Li-Ion Rechargeable Battery: A Perspective*. J. Am. Chem. Soc., 2013. **135**(4): p. 1167-1176.
96. Tarascon, J.M. and M. Armand, *Issues and challenges facing rechargeable lithium batteries*. Nature (London, U. K.), 2001. **414**(6861): p. 359-367.
97. Choi, N.-S., et al., *Challenges Facing Lithium Batteries and Electrical Double-Layer Capacitors*. Angewandte Chemie International Edition, 2012. **51**(40): p. 9994-10024.
98. Zhang, S.S., *A review on electrolyte additives for lithium-ion batteries*. J. Power Sources, 2006. **162**(2): p. 1379-1394.
99. Goriparti, S., et al., *Review on recent progress of nanostructured anode materials for Li-ion batteries*. Journal of Power Sources, 2014. **257**: p. 421-443.
100. Nitta, N., et al., *Li-ion battery materials: present and future*. Materials Today, 2015. **18**(5): p. 252-264.

101. Reddy, M.V., G.V. Subba Rao, and B.V.R. Chowdari, *Metal Oxides and Oxysalts as Anode Materials for Li Ion Batteries*. Chem. Rev. (Washington, DC, U. S.), 2013. **113**(7): p. 5364-5457.
102. Shi, W., et al., *Design of Nanostructured Hybrid Materials Based on Carbon and Metal Oxides for Li Ion Batteries*. J. Phys. Chem. C, 2012. **116**(51): p. 26685-26693.
103. Cabana, J., et al., *Beyond Intercalation-Based Li-Ion Batteries: The State of the Art and Challenges of Electrode Materials Reacting Through Conversion Reactions*. Advanced Materials, 2010. **22**(35): p. E170-E192.
104. Poizot, P., et al., *Nano-sized transition-metal oxides as negative-electrode materials for lithium-ion batteries*. Nature, 2000. **407**(6803): p. 496-9.
105. Szczech, J.R. and S. Jin, *Nanostructured silicon for high capacity lithium battery anodes*. Energy Environ. Sci., 2011. **4**(1): p. 56-72.
106. Lou, X.W., et al., *Template-free synthesis of SnO₂ hollow nanostructures with high lithium storage capacity*. Adv. Mater. (Weinheim, Ger.), 2006. **18**(17): p. 2325-2329.
107. Park, C.-M., et al., *Li-alloy based anode materials for Li secondary batteries*. Chemical Society Reviews, 2010. **39**(8): p. 3115-3141.
108. Winter, M., et al., *Insertion electrode materials for rechargeable lithium batteries*. Adv. Mater. (Weinheim, Ger.), 1998. **10**(10): p. 725-763.
109. Zhang, W.-J., *Lithium insertion/extraction mechanism in alloy anodes for lithium-ion batteries*. Journal of Power Sources, 2011. **196**(3): p. 877-885.
110. Nitta, N. and G. Yushin, *High-Capacity Anode Materials for Lithium-Ion Batteries: Choice of Elements and Structures for Active Particles*. Particle & Particle Systems Characterization, 2014. **31**(3): p. 317-336.
111. Winter, M. and J.r.O. Besenhard, *Electrochemical lithiation of tin and tin-based intermetallics and composites*. Electrochimica Acta, 1999. **45**(1): p. 31-50.
112. Idota, Y., et al., *Tin-based amorphous oxide: a high-capacity lithium-ion-storage material*. Science (Washington, D. C.), 1997. **276**(5317): p. 1395-1397.
113. Zhang, W.-J., *A review of the electrochemical performance of alloy anodes for lithium-ion batteries*. Journal of Power Sources, 2011. **196**(1): p. 13-24.
114. Wu, H. and Y. Cui, *Designing nanostructured Si anodes for high energy lithium ion batteries*. Nano Today, 2012. **7**(5): p. 414-429.
115. Kaskhedikar, N.A. and J. Maier, *Lithium Storage in Carbon Nanostructures*. Advanced Materials, 2009. **21**(25-26): p. 2664-2680.
116. Kavan, L., *Electrochemistry of titanium dioxide: some aspects and highlights*. The Chemical Record, 2012. **12**(1): p. 131-142.
117. Yi, T.-F., et al., *Recent development and application of Li₄Ti₅O₁₂ as anode material of lithium ion battery*. J. Phys. Chem. Solids, 2010. **71**(9): p. 1236-1242.
118. Wang, Z., L. Zhou, and X.W. Lou, *Metal Oxide Hollow Nanostructures for Lithium-ion Batteries*. Advanced Materials, 2012. **24**(14): p. 1903-1911.
119. Wang, J., et al., *Preparation and electrochemical properties of TiO₂ hollow spheres as an anode material for lithium-ion batteries*. Journal of Power Sources, 2009. **191**(2): p. 614-618.
120. Yu, L., H.B. Wu, and X.W.D. Lou, *Self-Templated Formation of Hollow Structures for Electrochemical Energy Applications*. Acc. Chem. Res., 2017. **50**(2): p. 293-301.
121. Shen, J., et al., *Hollow mesoporous frameworks without the annealing process for high-performance lithium-ion batteries: A case for anatase TiO₂*. Chemical Engineering Journal, 2013. **228**: p. 724-730.
122. Song, B., et al., *Electrochemical properties of TiO₂ hollow microspheres from a template-free and green wet-chemical route*. Journal of Power Sources, 2008. **180**(2): p. 869-874.

123. Bruce, P.G., B. Scrosati, and J.-M. Tarascon, *Nanomaterials for rechargeable lithium batteries*. *Angew. Chem., Int. Ed.*, 2008. **47**(16): p. 2930-2946.
124. Armstrong, G., et al., *Nanotubes with the TiO₂-B structure*. *Chemical Communications*, 2005(19): p. 2454-2456.
125. Armstrong, A.R., et al., *Lithium-Ion Intercalation into TiO₂-B Nanowires*. *Advanced Materials*, 2005. **17**(7): p. 862-865.
126. Park, M.-S., et al., *Preparation and Electrochemical Properties of SnO₂ Nanowires for Application in Lithium-Ion Batteries*. *Angewandte Chemie*, 2007. **119**(5): p. 764-767.
127. Chan, C.K., et al., *Fast, Completely Reversible Li Insertion in Vanadium Pentoxide Nanoribbons*. *Nano Letters*, 2007. **7**(2): p. 490-495.
128. Nam, K.T., et al., *Virus-Enabled Synthesis and Assembly of Nanowires for Lithium Ion Battery Electrodes*. *Science*, 2006. **312**(5775): p. 885-888.
129. Hasegawa, G., et al., *Synthesis and electrochemical performance of hierarchically porous N-doped TiO₂ for Li-ion batteries*. *New J. Chem.*, 2014. **38**(4): p. 1380-1384.
130. Zhao, H., et al., *Structural and electrochemical characteristics of Li_{4-x}Al_xTi₅O₁₂ as anode material for lithium-ion batteries*. *Electrochim. Acta*, 2008. **53**(24): p. 7079-7083.
131. Fang, J., et al., *Fe, S co-doped anatase TiO₂ nanotubes as anodes with improved electrochemical performance for lithium ion batteries*. *RSC Adv.*, 2016. **6**(74): p. 70133-70140.
132. Anh, L.T., et al., *Improving the electrochemical performance of anatase titanium dioxide by vanadium doping as an anode material for lithium-ion batteries*. *J. Power Sources*, 2013. **243**: p. 891-898.
133. Bi, Z., et al., *High performance Cr, N-codoped mesoporous TiO₂ microspheres for lithium-ion batteries*. *J. Mater. Chem. A*, 2014. **2**(6): p. 1818-1824.
134. Andriamiadamanana, C., et al., *Room-temperature synthesis of iron-doped anatase TiO₂ for lithium-ion batteries and photocatalysis*. *Inorg. Chem.*, 2014. **53**(19): p. 10129-10139.
135. Robertson, A.D., et al., *New inorganic spinel oxides for use as negative electrode materials in future lithium-ion batteries*. *J. Power Sources*, 1999. **81-82**: p. 352-357.
136. Chen, C., et al., *Copper-Doped Dual Phase Li₄Ti₅O₁₂-TiO₂ Nanosheets as High-Rate and Long Cycle Life Anodes for High-Power Lithium-Ion Batteries*. *ChemSusChem*, 2015. **8**(1): p. 114-122.
137. Ali, Z., et al., *Design and evaluation of novel Zn doped mesoporous TiO₂ based anode material for advanced lithium ion batteries*. *J. Mater. Chem.*, 2012. **22**(34): p. 17625-17629.
138. Du, G., et al., *Br-Doped Li₄Ti₅O₁₂ and Composite TiO₂ Anodes for Li-ion Batteries: Synchrotron X-Ray and in situ Neutron Diffraction Studies*. *Adv. Funct. Mater.*, 2011. **21**(20): p. 3990-3997.
139. Gnednikov, S.V., et al., *Nanostructured zirconia-doped titania as the anode material for lithium-ion battery*. *Russ. J. Inorg. Chem.*, 2015. **60**(6): p. 658-664.
140. Fehse, M., et al., *Nb-Doped TiO₂ Nanofibers for Lithium Ion Batteries*. *J. Phys. Chem. C*, 2013. **117**(27): p. 13827-13835.
141. Aldon, L., et al., *Size Particle Effects on Lithium Insertion into Sn-doped TiO₂ Anatase*. *Chem. Mater.*, 2006. **18**(6): p. 1401-1406.
142. Wolfenstine, J. and J.L. Allen, *Electrical conductivity and charge compensation in Ta doped Li₄Ti₅O₁₂*. *J. Power Sources*, 2008. **180**(1): p. 582-585.

143. Reddy, M.V., et al., *Evaluation of undoped and M-doped TiO₂, where M = Sn, Fe, Ni/Nb, Zr, V, and Mn, for lithium-ion battery applications prepared by the molten-salt method.* RSC Adv., 2015. **5**(37): p. 29535-29544.
144. Yen, Y.-C., et al., *Study on solid-electrolyte-interphase of Si and C-coated Si electrodes in lithium cells.* J. Electrochem. Soc., 2009. **156**(2): p. A95-A102.
145. Dimov, N., et al., *Characterization of carbon-coated silicon Structural evolution and possible limitations.* J. Power Sources, 2003. **114**(1): p. 88-95.
146. Dimov, N., S. Kugino, and M. Yoshio, *Carbon-coated silicon as anode material for lithium ion batteries: advantages and limitations.* Electrochimica Acta, 2003. **48**(11): p. 1579-1587.
147. Yang, X.-Q., et al., *Structural studies of the new carbon-coated silicon anode materials using synchrotron-based in situ XRD.* Electrochemistry Communications, 2002. **4**(11): p. 893-897.
148. Lee, H.-Y. and S.-M. Lee, *Carbon-coated nano-Si dispersed oxides/graphite composites as anode material for lithium ion batteries.* Electrochemistry Communications, 2004. **6**(5): p. 465-469.
149. Luo, H., et al., *Carbon coated Li₄Ti₅O₁₂ nanorods as superior anode material for high rate lithium ion batteries.* J. Alloys Compd., 2013. **572**: p. 37-42.
150. Liu, X.-M., et al., *Carbon nanotube (CNT)-based composites as electrode material for rechargeable Li-ion batteries: A review.* Compos. Sci. Technol., 2012. **72**(2): p. 121-144.
151. Zhang, H.-L., et al., *Electrochemical performance of pyrolytic carbon-coated natural graphite spheres.* Carbon, 2006. **44**(11): p. 2212-2218.
152. Liu, S.-h., et al., *Improving the electrochemical properties of natural graphite spheres by coating with a pyrolytic carbon shell.* New Carbon Materials, 2008. **23**(1): p. 30-36.
153. Han, Y.-S. and J.-Y. Lee, *Improvement on the electrochemical characteristics of graphite anodes by coating of the pyrolytic carbon using tumbling chemical vapor deposition.* Electrochimica Acta, 2003. **48**(8): p. 1073-1079.
154. Guo, S. and S. Dong, *Graphene nanosheet: synthesis, molecular engineering, thin film, hybrids, and energy and analytical applications.* Chem. Soc. Rev., 2011. **40**(5): p. 2644-2672.
155. Zhang, J., et al., *CNFs@CNTs: superior carbon for electrochemical energy storage.* Adv. Mater. (Weinheim, Ger.), 2008. **20**(8): p. 1450-1455.
156. Song, Y.-Y., et al., *Facile method to synthesize a carbon layer embedded into titanium dioxide nanotubes with metal oxide decoration for electrochemical applications.* J. Mater. Chem. A, 2015. **3**(47): p. 23754-23759.
157. Dahl, M., Y. Liu, and Y. Yin, *Composite Titanium Dioxide Nanomaterials.* Chem. Rev., 2014. **114**(19): p. 9853-9889.
158. Mei, Y., Y. Huang, and X. Hu, *Nanostructured Ti-based anode materials for Na-ion batteries.* J. Mater. Chem. A, 2016. **4**(31): p. 12001-12013.
159. de Caritat, P. and C. Reimann, *Comparing results from two continental geochemical surveys to world soil composition and deriving Predicted Empirical Global Soil (PEGS2) reference values.* Earth Planet. Sci. Lett., 2012. **319-320**: p. 269-276.
160. Yao, J.K., et al., *High refractive index TiO₂ film deposited by electron beam evaporation.* Surf. Eng., 2009. **25**(3): p. 257-260.
161. Zhou, W., et al., *Novel multi-layer cross-linked TiO₂/C nanosheets and their photocatalytic properties.* New J. Chem., 2014. **38**(4): p. 1647-1654.

162. Li, H., et al., *Synthesis of highly efficient C-doped TiO₂ photocatalyst and its photo-generated charge-transfer properties*. J. Colloid Interface Sci., 2011. **354**(1): p. 175-180.
163. Lin, Y.-T., et al., *Effect of C content and calcination temperature on the photocatalytic activity of C-doped TiO₂ catalyst*. Sep. Purif. Technol., 2013. **116**: p. 114-123.
164. Levinson, R., P. Berdahl, and H. Akbari, *Solar spectral optical properties of pigments-Part I: model for deriving scattering and absorption coefficients from transmittance and reflectance measurements*. Sol. Energy Mater. Sol. Cells, 2005. **89**(4): p. 319-349.
165. Sun, Z., et al., *A carbon-coated TiO₂(B) nanosheet composite for lithium ion batteries*. Chem. Commun. (Cambridge, U. K.), 2014. **50**(41): p. 5506-5509.
166. Song, T. and U. Paik, *TiO₂ as an active or supplemental material for lithium batteries*. J. Mater. Chem. A, 2016. **4**(1): p. 14-31.
167. Hanaor, D.A.H. and C.C. Sorrell, *Review of the anatase to rutile phase transformation*. Journal of Materials Science, 2011. **46**(4): p. 855-874.
168. Aravindan, V., et al., *TiO₂ polymorphs in 'rocking-chair' Li-ion batteries*. Mater. Today (Oxford, U. K.), 2015. **18**(6): p. 345-351.
169. Zachau-Christiansen, B., et al., *Lithium insertion in different titanium dioxide modifications*. Solid State Ionics, 1988. **28-30**(Pt. 2): p. 1176-82.
170. Pfanzelt, M., P. Kubiak, and M. Wohlfahrt-Mehrens, *Nanosized TiO₂ Rutile with High Capacity and Excellent Rate Capability*. Electrochem. Solid-State Lett., 2010. **13**(7): p. A91-A94.
171. Yang, Z., et al., *Nanostructures and lithium electrochemical reactivity of lithium titanates and titanium oxides: A review*. Journal of Power Sources, 2009. **192**(2): p. 588-598.
172. Kubiak, P., et al., *Electrochemical evaluation of rutile TiO₂ nanoparticles as negative electrode for Li-ion batteries*. J. Power Sources, 2009. **194**(2): p. 1099-1104.
173. McNulty, D., E. Carroll, and C. O'Dwyer, *Rutile TiO₂ Inverse Opal Anodes for Li-Ion Batteries with Long Cycle Life, High-Rate Capability, and High Structural Stability*. Adv. Energy Mater., 2017: p. Ahead of Print.
174. Pfanzelt, M., et al., *TiO₂ rutile—An alternative anode material for safe lithium-ion batteries*. Journal of Power Sources, 2011. **196**(16): p. 6815-6821.
175. Qiao, H., et al., *Electrochemical charge storage of flowerlike rutile TiO₂ nanorods*. Chem. Phys. Lett., 2010. **490**(4-6): p. 180-183.
176. Qiao, H., et al., *High lithium electroactivity of hierarchical porous rutile TiO₂ nanorod microspheres*. Electrochem. Commun., 2008. **10**(9): p. 1280-1283.
177. Yoganarasimhan, S.R. and C.N.R. Rao, *Mechanism of crystal structure transformations. III. Factors affecting the anatase-rutile transformation*. Trans. Faraday Soc., 1962. **58**: p. 1579-89.
178. Shannon, R.D. and J.A. Pask, *Kinetics of the anatase-rutile transformation*. J. Am. Ceram. Soc., 1965. **48**(8): p. 391-8.
179. Sabyrov, K., N.D. Burrows, and R.L. Penn, *Size-Dependent Anatase to Rutile Phase Transformation and Particle Growth*. Chemistry of Materials, 2012. **25**(8): p. 1408-1415.
180. Reidy, D.J., J.D. Holmes, and M.A. Morris, *The critical size mechanism for the anatase to rutile transformation in TiO₂ and doped-TiO₂*. Journal of the European Ceramic Society, 2006. **26**(9): p. 1527-1534.
181. Hoffmann, M.R., et al., *Environmental Applications of Semiconductor Photocatalysis*. Chem. Rev. (Washington, D. C.), 1995. **95**(1): p. 69-96.

182. Sun, B., P.G. Smirniotis, and P. Boolchand, *Visible Light Photocatalysis with Platinized Rutile TiO₂ for Aqueous Organic Oxidation*. Langmuir, 2005. **21**(24): p. 11397-11403.
183. Kerisit, S., et al., *Computer Simulation of the Phase Stabilities of Lithiated TiO₂ Polymorphs*. J. Phys. Chem. C, 2010. **114**(44): p. 19096-19107.
184. Wagemaker, M., W.J.H. Borghols, and F.M. Mulder, *Large Impact of Particle Size on Insertion Reactions. A Case for Anatase Li_xTiO₂*. J. Am. Chem. Soc., 2007. **129**(14): p. 4323-4327.
185. Lafont, U., et al., *In Situ Structural Changes upon Electrochemical Lithium Insertion in Nanosized Anatase TiO₂*. J. Phys. Chem. C, 2010. **114**(2): p. 1372-1378.
186. Froeschl, T., et al., *High surface area crystalline titanium dioxide: potential and limits in electrochemical energy storage and catalysis*. Chem. Soc. Rev., 2012. **41**(15): p. 5313-5360.
187. Marchand, R., L. Brohan, and M. Tournoux, *TiO₂(B) a new form of titanium dioxide and the potassium octatitanate K₂Ti₈O₁₇*. Mater. Res. Bull., 1980. **15**(8): p. 1129-33.
188. Ge, M., et al., *A review of one-dimensional TiO₂ nanostructured materials for environmental and energy applications*. J. Mater. Chem. A, 2016. **4**(18): p. 6772-6801.
189. Dylla, A.G., G. Henkelman, and K.J. Stevenson, *Lithium Insertion in Nanostructured TiO₂(B) Architectures*. Accounts of Chemical Research, 2012. **46**(5): p. 1104-1112.
190. Liu, Z., et al., *Nanostructured TiO₂(B): the effect of size and shape on anode properties for Li-ion batteries*. Progress in Natural Science: Materials International, 2013. **23**(3): p. 235-244.
191. Liu, Y. and Y. Yang, *Recent progress of TiO₂-based anodes for Li ion batteries*. J. Nanomater., 2016. **2016**: p. 8123652/1-8123652/15.
192. Nguyen, L.H., et al., *Self-Assembled Ultrathin Anatase TiO₂ Nanosheets with Reactive (001) Facets for Highly Enhanced Reversible Li Storage*. ChemElectroChem, 2014. **1**(3): p. 539-543.
193. Gligor, F. and S.W. de Leeuw, *Lithium diffusion in rutile structured titania*. Solid State Ionics, 2006. **177**(26-32): p. 2741-2746.
194. Bach, S., J.P. Pereira-Ramos, and P. Willman, *Investigation of lithium diffusion in nano-sized rutile TiO₂ by impedance spectroscopy*. Electrochim. Acta, 2010. **55**(17): p. 4952-4959.
195. Koudriachova, M.V., N.M. Harrison, and S.W. de Leeuw, *Effect of Diffusion on Lithium Intercalation in Titanium Dioxide*. Phys. Rev. Lett., 2001. **86**(7): p. 1275-1278.
196. Mauger, A., H. Xie, and C.M. Julien, *Composite anodes for lithium-ion batteries: status and trends*. AIMS Mater. Sci., 2016. **3**(3Spec.Iss.): p. 1054-1106.
197. Zhi, M., et al., *Nanostructured carbon-metal oxide composite electrodes for supercapacitors: a review*. Nanoscale, 2013. **5**(1): p. 72-88.
198. Cao, F.F., et al., *Symbiotic Coaxial Nanocables: Facile Synthesis and an Efficient and Elegant Morphological Solution to the Lithium Storage Problem*. Chemistry of Materials, 2010. **22**(5): p. 1908-1914.
199. Chen, C.J., et al., *Na⁺ intercalation pseudocapacitance in graphene-coupled titanium oxide enabling ultra-fast sodium storage and long-term cycling*. Nature Communications, 2015. **6**.
200. Qin, G.H., X.Y. Zhang, and C.Y. Wang, *Design of nitrogen doped graphene grafted TiO₂ hollow nanostructures with enhanced sodium storage performance*. Journal of Materials Chemistry A, 2014. **2**(31): p. 12449-12458.

201. Qin, G., X. Wu, and H. Zhang, *Rational design of TiO₂-V₂O₅-C nanostructure grafted by N-doped graphene with enhanced photocatalysis and lithium ion store performances*. RSC Adv., 2014. **4**(94): p. 52438-52450.
202. Tahir, M.N., et al., *Extraordinary Performance of Carbon-Coated Anatase TiO₂ as Sodium-Ion Anode*. Adv. Energy Mater., 2016. **6**(4): p. 1501489.
203. Oschmann, B., et al., *Polyacrylonitrile Block Copolymers for the Preparation of a Thin Carbon Coating Around TiO₂ Nanorods for Advanced Lithium-Ion Batteries*. Macromol. Rapid Commun., 2013. **34**(21): p. 1693-1700.
204. Mueller, F., et al., *Influence of the carbonaceous conductive network on the electrochemical performance of ZnFe₂O₄ nanoparticles*. J. Power Sources, 2013. **236**: p. 87-94.
205. Wan, G., et al., *Preparation and microwave absorption properties of uniform TiO₂@C core-shell nanocrystals*. RSC Adv., 2015. **5**(94): p. 77443-77448.
206. Kim, K.-T., et al., *Carbon-coated anatase titania as a high rate anode for lithium batteries*. J. Power Sources, 2015. **281**: p. 362-369.
207. Ulissi, U., et al., *Investigation of the electrochemical features of carbon-coated TiO₂ anode for application in lithium-ion battery using high voltage LiNi_{0.5}Mn_{1.5}O₄ spinel cathode*. Electrochim. Acta, 2016. **201**: p. 158-164.
208. Fu, L.J., et al., *Novel TiO₂/C nanocomposites for anode materials of lithium ion batteries*. Journal of Power Sources, 2006. **159**(1): p. 219-222.
209. Mai, L., et al., *Effect of C doping on the structural and optical properties of sol-gel TiO₂ thin films*. Appl. Surf. Sci., 2009. **255**(22): p. 9285-9289.
210. Xiao, Q., et al., *Solar photocatalytic degradation of methylene blue in carbon-doped TiO₂ nanoparticles suspension*. Sol. Energy, 2008. **82**(8): p. 706-713.
211. Zhang, J.-J., et al., *Carbon coated TiO₂-SiO₂ nanocomposites with high grain boundary density as anode materials for lithium-ion batteries*. J. Mater. Chem. A, 2013. **1**(25): p. 7360-7369.
212. Oh, S.-M., et al., *High electrochemical performances of microsphere C-TiO₂ anode for sodium-ion battery*. ACS Appl. Mater. Interfaces, 2014. **6**(14): p. 11295-11301.
213. Pham-Cong, D., et al., *Enhanced electrochemical performance of carbon-coated TiO₂ nanobarbed fibers as anode material for lithium-ion batteries*. Electrochem. Commun., 2015. **60**: p. 204-207.
214. Bai, X., et al., *Simple fabrication of TiO₂/C nanocomposite with enhanced electrochemical performance for lithium-ion batteries*. Electrochim. Acta, 2015. **169**: p. 241-247.
215. Ge, Y., et al., *High cyclability of carbon-coated TiO₂ nanoparticles as anode for sodium-ion batteries*. Electrochim. Acta, 2015. **157**: p. 142-148.
216. Tan, L., et al., *Nitrogen-doped carbon coated anatase TiO₂ anode material for lithium-ion batteries*. Materials Letters, 2013. **109**: p. 195-198.
217. Guo, S., et al., *Porous ternary TiO₂/MnTiO₃@C hybrid microspheres as anode materials with enhanced electrochemical performances*. J. Mater. Chem. A, 2015. **3**(47): p. 23895-23904.
218. Henry, A., et al., *Conversion of Nanocellulose Aerogel into TiO₂ and TiO₂@C Nanothorns by Direct Anhydrous Mineralization with TiCl₄. Evaluation of Electrochemical Properties in Li Batteries*. ACS Appl. Mater. Interfaces, 2015. **7**(27): p. 14584-14592.
219. Memon, N.K., D.H. Anjum, and S.H. Chung, *Multiple-diffusion flame synthesis of pure anatase and carbon-coated titanium dioxide nanoparticles*. Combust. Flame, 2013. **160**(9): p. 1848-1856.
220. Wang, X., et al., *Multi-type carbon doping of TiO₂ photocatalyst*. Chemical Physics Letters, 2007. **444**(4-6): p. 292-296.

221. Cullity, B.D. and S.R. Stock, *Elements of X-Ray Diffraction, 3rd Edition*. 2001: Prentice Hall. 664 pp.
222. Broll, N., *Caractérisation des solides cristallisés par diffraction X*. Techniques de l'Ingénieur, traité Analyse et Caractérisation, 1996: p. PE1080-1 - PE1080-17.
223. Rouquerol, F., et al., *Texture des matériaux pulvérulents ou poreux*. Techniques de l'Ingénieur, traité Analyse et Caractérisation, 2003: p. P1050-1 - P1050-24.
224. Sing, K.S.W., et al., *Reporting physisorption data for gas/solid systems with special reference to the determination of surface area and porosity (Recommendations 1984)*. Pure Appl. Chem., 1985. **57**(4): p. 603-19.
225. Brunauer, S., et al., *A theory of the van der Waals adsorption of gases*. J. Am. Chem. Soc., 1940. **62**: p. 1723-32.
226. Emmett, P.H. and S. Brunauer, *The use of low-temperature van der Waal adsorption isotherms in detg. the surface area of iron synthetic ammonia catalysts*. J. Am. Chem. Soc., 1937. **59**: p. 1553-64.
227. Brunauer, S., P.H. Emmett, and E. Teller, *Adsorption of gases in multimolecular layers*. J. Am. Chem. Soc., 1938. **60**: p. 309-19.
228. Pyun, S.-I., et al., *Electrochemistry of Insertion Materials for Hydrogen and Lithium*. Monographs in Electrochemistry, ed. F. Scholz. 2012: Springer Berlin Heidelberg.
229. Bard, A.J. and L.R. Faulkner, *Electrochemical Method: Fundamentals and Applications*. 2nd ed, ed. J.W. Sons. 2001, New York: John Wiley & Sons.
230. Shin, J.-Y., D. Samuelis, and J. Maier, *Sustained Lithium-Storage Performance of Hierarchical, Nanoporous Anatase TiO₂ at High Rates: Emphasis on Interfacial Storage Phenomena*. Advanced Functional Materials, 2011. **21**(18): p. 3464-3472.
231. Koivumaki, J. and J.V. Seppala, *Comparison of ethylene-propylene copolymers obtained with titanium, vanadium and zirconium catalyst systems*. Polym. Bull. (Berlin), 1993. **31**(4): p. 441-8.
232. Zhang, S., et al., *Ethylene/propylene copolymerization catalyzed by vanadium complexes containing N-heterocyclic carbenes*. Dalton Trans., 2015. **44**(34): p. 15264-15270.
233. Haag, M.C., et al., *Residual metal content in ethylene-propylene-diene monomers synthesized using vanadium- and zirconocene-based catalysts*. J. Appl. Polym. Sci., 1999. **74**(8): p. 1997-2003.
234. Zhang, Y.-H. and A. Reller, *Phase transformation and grain growth of doped nanosized titania*. Materials Science and Engineering: C, 2002. **19**(1): p. 323-326.
235. Balikdjian, J.P., et al., *Sintering and phase transformation of V-loaded anatase materials containing bulk and surface V species*. J. Phys. Chem. B, 2000. **104**(38): p. 8931-8939.
236. Gallardo Amores, J.M., V. Sanchez Escribano, and G. Busca, *Anatase crystal growth and phase transformation to rutile in high-area TiO₂, MoO₃-TiO₂ and other TiO₂-supported oxide catalytic systems*. J. Mater. Chem., 1995. **5**(8): p. 1245-9.
237. Gouma, P.I. and M.J. Mills, *Anatase-to-rutile transformation in titania powders*. J. Am. Ceram. Soc., 2001. **84**(3): p. 619-622.
238. Liu, D., et al., *TiO₂ Nanotube Arrays Annealed in N₂ for Efficient Lithium-Ion Intercalation*. J. Phys. Chem. C, 2008. **112**(30): p. 11175-11180.
239. Goodenough, J.B. and Y. Kim, *Challenges for Rechargeable Li Batteries*. Chem. Mater., 2010. **22**(3): p. 587-603.
240. Zhang, X., et al., *Electrochemical and infrared studies of the reduction of organic carbonates*. Proc. - Electrochem. Soc., 2001. **2000-21**(Rechargeable Lithium Batteries): p. 280-289.

241. Haregewoin, A.M., et al., *Comparative Study on the Solid Electrolyte Interface Formation by the Reduction of Alkyl Carbonates in Lithium ion Battery*. *Electrochimica Acta*, 2014. **136**: p. 274-285.
242. Dacher, P., *A promising new prototype of battery*, C. press, Editor. 2015.
243. Anon, *CRC Handbook of Chemistry and Physics, 84th Edition, Edited by David R. Lide*. *J. Am. Chem. Soc.*, 2004. **126**(5): p. 1586.
244. Vignarooban, K., et al., *Current trends and future challenges of electrolytes for sodium-ion batteries*. *Int. J. Hydrogen Energy*, 2016. **41**(4): p. 2829-2846.
245. Nithya, C. and S. Gopukumar, *Sodium ion batteries: a newer electrochemical storage*. *Wiley Interdiscip. Rev.: Energy Environ.*, 2015. **4**(3): p. 253-278.
246. Hwang, J.-Y., S.-T. Myung, and Y.-K. Sun, *Sodium-ion batteries: present and future*. *Chem. Soc. Rev.*, 2017. **46**(12): p. 3529-3614.
247. Dahbi, M., et al., *Negative electrodes for Na-ion batteries*. *Phys. Chem. Chem. Phys.*, 2014. **16**(29): p. 15007-15028.
248. Yabuuchi, N., et al., *Research Development on Sodium-Ion Batteries*. *Chem. Rev.* (Washington, DC, U. S.), 2014. **114**(23): p. 11636-11682.
249. Louvain, N., et al., *On the electrochemical encounter between sodium and mesoporous anatase TiO₂ as a Na-ion electrode*. *CrystEngComm*, 2016. **18**(23): p. 4431-4437.
250. Wu, L., et al., *Unfolding the Mechanism of Sodium Insertion in Anatase TiO₂ Nanoparticles*. *Adv. Energy Mater.*, 2015. **5**(2): p. n/a.
251. Li, W., et al., *A Reversible Phase Transition for Sodium Insertion in Anatase TiO₂*. *Chem. Mater.*, 2017. **29**(4): p. 1836-1844.
252. Mao, M., et al., *Pipe-Wire TiO₂-Sn@Carbon Nanofibers Paper Anodes for Lithium and Sodium Ion Batteries*. *Nano Lett.*, 2017. **17**(6): p. 3830-3836.
253. Bommier, C. and X. Ji, *Recent Development on Anodes for Na-Ion Batteries*. *Isr. J. Chem.*, 2015. **55**(5): p. 486-507.
254. Li, S., et al., *Alternating voltage induced ordered anatase TiO₂ nanopores: An electrochemical investigation of sodium storage*. *J. Power Sources*, 2016. **336**: p. 196-202.
255. Longoni, G., et al., *Shape-Controlled TiO₂ Nanocrystals for Na-Ion Battery Electrodes: The Role of Different Exposed Crystal Facets on the Electrochemical Properties*. *Nano Lett.*, 2017. **17**(2): p. 992-1000.
256. Shi, X., et al., *Anatase TiO₂@C composites with porous structure as an advanced anode material for Na ion batteries*. *J. Power Sources*, 2016. **330**: p. 1-6.
257. Ortiz, G.F., et al., *Alternative Li-Ion Battery Electrode Based on Self-Organized Titania Nanotubes*. *Chem. Mater.*, 2009. **21**(1): p. 63-67.
258. Arena, F., R. Di Chio, and G. Trunfio, *An experimental assessment of the ammonia temperature programmed desorption method for probing the surface acidic properties of heterogeneous catalysts*. *Appl. Catal., A*, 2015. **503**: p. 227-236.
259. Manriquez, M.E., et al., *Preparation of TiO₂-ZrO₂ mixed oxides with controlled acid-basic properties*. *Journal of Molecular Catalysis A: Chemical*, 2004. **220**(2): p. 229-237.
260. Li, Y., et al., *Li-ion and Na-ion transportation and storage properties in various sized TiO₂ spheres with hierarchical pores and high tap density*. *J. Mater. Chem. A*, 2016: p. Ahead of Print.
261. Su, X., et al., *Advanced titania nanostructures and composites for lithium ion battery*. *Journal of Materials Science*, 2012. **47**(6): p. 2519-2534.
262. Hong, Z., et al., *Hierarchical rutile TiO₂ with mesocrystalline structure for Li-ion and Na-ion storage*. *Electrochim. Acta*, 2016. **202**: p. 203-208.

263. Marinaro, M., et al., *Low temperature behaviour of TiO₂ rutile as negative electrode material for lithium-ion batteries*. Journal of Power Sources, 2011. **196**(22): p. 9825-9829.
264. Cai, D., et al., *High specific capacity of TiO₂-graphene nanocomposite as an anode material for lithium-ion batteries in an enlarged potential window*. Electrochimica Acta, 2012. **74**: p. 65-72.
265. Zhang, J., T. Huang, and A. Yu, *Synergistic effect of amorphous carbon coverage and enlarged voltage window on the superior lithium storage performance of nanostructured mesoporous anatase TiO₂: Emphasis on interfacial storage phenomena*. J. Alloys Compd., 2014. **606**: p. 61-67.
266. Yang, X., et al., *Nanosized anatase titanium dioxide loaded porous carbon nanofiber webs as anode materials for lithium-ion batteries*. Electrochem. Commun., 2011. **13**(10): p. 1098-1101.
267. Antic, Z., et al., *Multisite luminescence of rare earth doped TiO₂ anatase nanoparticles*. Mater. Chem. Phys., 2012. **135**(2-3): p. 1064-1069.
268. Zhu, J., et al., *Low temperature synthesis of anatase rare earth doped titania-silica photocatalyst and its photocatalytic activity under solar-light*. Colloids Surf., A, 2010. **355**(1-3): p. 178-182.
269. Sevilla, M. and A.B. Fuertes, *Catalytic graphitization of templated mesoporous carbons*. Carbon, 2006. **44**(3): p. 468-474.
270. Sevilla, M., et al., *Direct synthesis of graphitic carbon nanostructures from saccharides and their use as electrocatalytic supports*. Carbon, 2008. **46**(6): p. 931-939.
271. Maldonado-Hodar, F.J., et al., *Catalytic graphitization of carbon aerogels by transition metals*. Langmuir, 2000. **16**(9): p. 4367-4373.
272. Han, S., et al., *Simple solid-phase synthesis of hollow graphitic nanoparticles and their application to direct methanol fuel cell electrodes*. Adv. Mater. (Weinheim, Ger.), 2003. **15**(22): p. 1922-1925.
273. Marsh, H., D. Crawford, and D.W. Taylor, *Catalytic graphitization by iron of isotropic carbon from poly(furfuryl alcohol), 725-1090 K. A high-resolution electron microscope study*. Carbon, 1983. **21**(1): p. 81-7.
274. Pradeep, V.S., et al., *Influence of pyrolysis atmosphere on the lithium storage properties of carbon-rich polymer derived SiOC ceramic anodes*. Solid State Ionics, 2014. **262**: p. 22-24.
275. Iida, Y. and S. Ozaki, *Grain growth and phase transformation of titanium oxide during calcination*. J. Am. Ceram. Soc., 1961. **44**: p. 120-7.
276. Hoekstra, J., et al., *Carbon-Supported Base Metal Nanoparticles: Cellulose at Work*. ChemSusChem, 2015. **8**(6): p. 985-989.
277. Ohsaka, T., F. Izum, and Y. Fujiki, *Raman Spectrum of Anatase, TiO₂*. J. Raman Spectrosc., 1978. **7**(6): p. 321-324.
278. Ferrari, A.C. and J. Robertson, *Interpretation of Raman spectra of disordered and amorphous carbon*. Phys. Rev. B: Condens. Matter Mater. Phys., 2000. **61**(20): p. 14095-14107.
279. Tuinstra, F. and J.L. Koenig, *Raman spectrum of graphite*. J. Chem. Phys., 1970. **53**(3): p. 1126-30.
280. Matthews, M.J., et al., *Origin of dispersive effects of the Raman D band in carbon materials*. Phys. Rev. B: Condens. Matter Mater. Phys., 1999. **59**(10): p. R6585-R6588.

-
281. Sadezky, A., et al., *Raman microspectroscopy of soot and related carbonaceous materials: Spectral analysis and structural information*. Carbon, 2005. **43**(8): p. 1731-1742.
 282. Ivleva, N.P., et al., *Raman Microspectroscopic Analysis of Size-Resolved Atmospheric Aerosol Particle Samples Collected with an ELPI: Soot, Humic-Like Substances, and Inorganic Compounds*. Aerosol Sci. Technol., 2007. **41**(7): p. 655-671.
 283. Dippel, B., H. Jander, and J. Heintzenberg, *NIR FT Raman spectroscopic study of flame soot*. Phys. Chem. Chem. Phys., 1999. **1**(20): p. 4707-4712.

Non-hydrolytic sol-gel synthesis of TiO₂-based electrode materials for Li-ion batteries

Non-hydrolytic sol-gel (NHSG) provides useful alternatives to conventional sol-gel routes. In particular, the ether route based on the reaction of chloride or oxychloride precursors with ether oxygen donors is a well-established method for the preparation of mesoporous oxides and mixed-oxides. Li-ion batteries are ubiquitous in the field of electrochemical energy storage, from mobile devices to electric and hybrid vehicles. However, commercial electrode materials do not fulfill all the requirements needed for high-power applications. TiO₂ is as a promising material to replace graphite anodes in high-power Li-ion batteries, despite its poor electronic conductivity, which must be improved. In this context, the objective of this PhD thesis is the conception of different TiO₂-based electrode materials benefitting from NHSG advantages. Two different approaches were developed, using the ether route in the absence of any solvent or additive. First, hierarchical mesoporous oxides, TiO₂ and TiO₂-V₂O₅, were synthesized by calcination of xerogels in air. Secondly, mesoporous nanocomposites built of carbon-coated TiO₂ nanoparticles were obtained by pyrolysis under argon of the xerogels; in this case, the ether is used for the first time as both as an oxygen donor and a carbon source. The texture and the structure of the resulting materials were characterized by N₂ physisorption, electron microscopy, XRD, and Raman spectroscopy. TiO₂/C samples were further analyzed by TGA and ¹³C CPMAS-NMR. Galvanostatic cycling at different current rates was performed to determine the electrochemical performances in lithium insertion-deinsertion.

Keywords : Non-hydrolytic sol-gel ; Mesoporous materials ; TiO₂-V₂O₅ mixed oxides ; TiO₂/C nanocomposites ; TiO₂ anatase ; Lithium-ion batteries

Synthèse par chimie sol-gel non-hydrolytique de matériaux d'électrodes pour batteries Li-ion à base de TiO₂

Le procédé sol-gel non-hydrolytique (SGNH) offre une alternative intéressante au procédés sol-gel classiques. Notamment, la « voie éther », impliquant la réaction de précurseurs chlorures ou oxychlorures avec un éther comme donneur d'oxygène, est une méthode simple et efficace pour la préparation d'oxydes et d'oxydes mixtes mésoporeux. Les batteries Li-ion sont omniprésentes aussi bien dans des applications portables que pour des véhicules électriques ou hybrides. Cependant, les performances des électrodes commerciales sont insuffisantes pour des applications haute puissance. TiO₂ est un candidat prometteur pour remplacer les anodes de graphite dans les batteries Li-ion, mais sa conductivité électronique doit être améliorée. L'objectif de ce travail de thèse est d'utiliser les avantages du procédé SGNH pour préparer des matériaux d'électrodes à base de TiO₂. Deux approches ont été explorées, mettant en jeu la voie éther en l'absence de tout solvant ou additif. Premièrement, des oxydes mésoporeux à structure hiérarchique, TiO₂ et TiO₂-V₂O₅, ont été synthétisés par calcination des xérogels. Deuxièmement, des nanocomposites mésoporeux constitués de nanoparticules de TiO₂ recouvertes d'un film de carbone ont été obtenus par pyrolyse sous atmosphère d'argon, l'éther jouant le rôle de donneur d'oxygène et aussi, pour la première fois, de source de carbone. Les matériaux ont été caractérisés par physisorption d'azote, microscopie électronique, DRX, spectroscopie Raman, ATG ainsi que par RMN ¹³C CPMAS pour les nanocomposites. Les performances en insertion-désinsertion du lithium ont été étudiées par cyclage galvanostatique à différentes densités de courant.

Mots clés : Sol-gel non-hydrolytique ; Matériaux mésoporeux ; Oxydes mixtes TiO₂-V₂O₅ ; Nanocomposites TiO₂/C ; TiO₂ anatase ; Batteries lithium-ion